Finanziato dall'Unione europea NextGenerationEU
Ministero dell'Università e della Ricerca
Italiadomani PIANO NAZIONALE DI RIPRESA E RESILIENZA

multi-Risk sciEnce for resilienT commUnities undeR a changiNgclimate

Codice progetto MUR: **PE00000005** – CUP LEAD PARTNER: D33C22001290002

Report and scenarios for multi-risk, cascading and compounding effects and emerging risks

DV 5.3.1

Finanziato dall'Unione europea NextGenerationEU
Ministero dell'Università e della Ricerca
Italiadomani PIANO NAZIONALE DI RIPRESA E RESILIENZA

CONTRIBUTORS

Antonella Peresan, Hany M. Hassan Elsayed, Hazem Badreldin, Chiara Scaini, Elisa Zuccolo (OGS);
Francesca Borghi, Erika Brattich, Francesco Decataldo, Andrea Faggi, Francesca Ferretti, Tiziano Maestri, Eva Vanna Lorenza Negri, Luca Pozza (University of Bologna);
Maria Grazia Badas (Task Co-Leader), Gianluca Gatto, Amit Kumar, Sabrina Lai, Federica Leone, Santhosh Paramasivam, Giorgio Querzoli, Corrado Zoppi (University of Cagliari);
Chiara Arrighi, Gianni Bartoli, Simona Francalanci, Federico Gusella, Barbara Pintucchi, Marco Uzielli (University of Florence);
Giovanni Besio, Rosella Bovolenta, Federico Canepa, Serena Cattari, Arianna Cauteruccio, Francesco De Leo, Sergio Lagomarsino, Andrea Lira Loarca, Dario Massabò, Federico, Mazzei, Luisa Pagnini, Giuseppe Piccardo (Task Leader), Margherita Rago, Paola Salmona (University of Genoa);
Roberto Castelluccio, Maria Fabrizia Clemente, Valeria D'Ambrosio, Carlo Del Gaudio, Federica dell'Acqua, Mariano Di Domenico, Mariacarla Fraiese, Rossella Marmo, Ferdinando Di Martino, Vittorio Miraglia, Maria Polese, Chiara Russo, Antonio Sferratore, Gabriella Tocchi, Gerardo Verderame, Cristina Visconti (University of Napoli Federico II)

1. Technical References

Project Acronym	RETURN
Project Title	multi-Risk sciEnce for resilienT commUnities undeR a changiNg climate
Project Coordinator	Domenico Calcaterra UNIVERSITA DEGLI STUDI DI NAPOLI FEDERICO II domcalca@unina.it
Project Duration	December 2022 – November 2025 (36 months)

Deliverable No.	DV 5.3.1
Dissemination level*	PU
Work Package	WP3 – Multi-risk vulnerability and impact assessment and forecasting
Task	Complex and emerging risks for urban and metropolitan areas
Lead beneficiary	UNIGE
Contributing beneficiary/ies	OGS, UNIBO, UNICA, UNIFI, UNIGE, UNINA

* PU = Public

PP = Restricted to other program participants (including the Commission Services)

RE = Restricted to a group specified by the consortium (including the Commission Services)

CO = Confidential, only for members of the consortium (including the Commission Services)

2. Technical References

Version	Date	Lead contributor	Description
1.0	30/08/2024	UNIGE	First release

Summary

List of Figures

List of Tables

1. Introduction

The use of risk and multi-risk scenarios has become increasingly prevalent in risk assessment studies, as they provide a structured approach to evaluate the impacts of one or multiple hazardous events within a specific context. A scenario, in this context, is a specific realization of single- or multi-hazard processes, serving as the foundation for conducting a comprehensive risk or multi-risk assessment.

Within the framework of the Transversal Spoke TS1 of the RETURN project, particularly in Work Package 5.3, several risk scenarios will be proposed and analyzed to assess multi-risk in urban and metropolitan areas. To effectively address these complex challenges, besides the characterization and description of single and multiple hazards, a matrix approach is being developed within Work Package 5.3 to identify and clarify the key relationships between different hazards and the exposed elements of the urban environment. This approach is essential for understanding how multiple hazards can interact and compound their effects, which is particularly relevant in densely populated and infrastructurally complex areas.

Given the inherent challenges and limitations associated with rigorous probabilistic modeling for multi-risk assessment, the concept of storylines is introduced as an alternative and complementary approach. An event-based risk storyline can be described as a physically self-consistent sequence of past or plausible future events and their consequences. This method allows for the exploration of complex scenarios where traditional probabilistic methods may not be feasible or sufficient, especially in cases where uncertainties are significant, and data is limited.

To develop consistent and realistic multi-risk scenarios and storylines tailored to specific urban contexts, it is crucial to define all the elements involved—namely, hazard, exposure, vulnerability, and their potential interactions. The objective of Deliverable 5.3.1, which represents the first deliverable of Work Package 5.3, can be summarized into the following key components, each of which corresponds to a section within this deliverable:

- Section 2. Outline the initial steps of the matrix approach, providing a framework for identifying and analyzing the interactions between hazards and exposed elements in urban environments.
- Section 3. Identify and catalog the individual hazards that can contribute to the development of multi-risk scenarios, with essential contributions from the Vertical Spokes (VS) of the RETURN project.
- Section 4. Begin addressing multi-hazard issues specific to urban and metropolitan areas, with a particular focus on challenges related to climate change and its impact on hazard interactions.
- Section 5. Propose and describe the initial set of storylines developed by researchers involved in Work Package 5.3, which will serve as the basis for further scenario analysis and risk assessment.

Future deliverables within Work Package 5.3 will build on this foundation by focusing on different aspects of multi-hazard and multi-risk modeling. Deliverable 5.3.2 will develop a modeling approach to assess the physical and functional vulnerability of urban areas to multiple hazards. Following this, Deliverable 5.3.3 will address systemic vulnerability modelling, including socio-economic and health aspects together with physical, safety and environmental issues, examining their interdependencies within urban systems.

Finally, Deliverable 5.3.4 will focus on multi-hazard impact and risk modeling, aiming to create rapid forecasting methodologies to support timely decision-making in complex multi-risk scenarios.

Through these deliverables, Work Package 5.3 aims to provide a comprehensive and integrated approach to multi-risk assessment, contributing to the resilience and sustainability of urban and metropolitan areas in the face of emerging and compounding risks.

Note 1: This document is to be intended as part of an ongoing iterative process. As such it will be subject to further updates and modifications in the following phases of the project, also according to the feedback and consultations among the project partners and with the stakeholders.

Note 2: To **promote** the use of consistent and shared definitions for key concepts relevant to the RETURN project, the deliverables of Work Package 3 largely adopt definitions from the Glossary provided in Appendix B – Dictionary of Terms (Preliminary Glossary) of Deliverable 5.2.1, "Risk-Oriented Taxonomy and Ontology of Urban Subsystems and Functional Models".

2. Analysis of the relationships between hazards and exposure for the definition of multi-risk scenarios

According to UNISDR terminology (UNISDR, 2009), risk assessment can be intended as a methodology to determine the nature and extent of risk by analyzing potential hazards and evaluating existing conditions of vulnerability that together could potentially harm exposed people, property, services, livelihoods and the environment on which they depend. Therefore, there is the need of evaluating the characteristics of hazards (i.e., location, intensity, frequency and probability) and of identifying the elements exposed to those hazards, their characteristics together with their vulnerability. More specifically, in terms of vulnerability and with reference to urban and metropolitan areas, it is important to include different dimensions, i.e., the physical, social, economic, environmental and institutional dimensions (Pittore and Griffo, 2023). It should also be highlighted that hazards, exposure and vulnerability may each be subject to uncertainty in terms of magnitude and likelihood of occurrence, and each may change over time and space due to socio-economic changes and human decision-making (IPCC, 2022b).

As a result of risk assessment, impacts of specific events occurring in a territory can be evaluated, which are the consequences of realized risks on natural and human systems (IPCC, 2022b). Impacts can also be referred to as losses, consequences or outcomes and they have been documented after disasters mainly in terms of numbers of people killed, injured or affected, and in terms of physical losses and damages across the social, infrastructure and productive sectors and their economic equivalencies (WMO, 2014b). More in general, impacts can be either adverse or beneficial and they refer to effects on lives, livelihoods, health and well-being, ecosystems and species, economic, social and cultural assets, services (including ecosystem services), and infrastructure (IPCC, 2022b).

In the last decades, it has become evident how a multi-hazard perspective is essential for efficient and effective disaster risk reduction practices (UNISDR, 2015). Countries can indeed face multiple hazards, which might be correlated or interacting with one another and have potential interrelated effects (UNDRR, 2020). Considering one geographic area, multi-risk assessment is intended to be the overall risk arising from a series of possible adverse events and their interactions with the different specific vulnerabilities of the exposed elements. A multi-risk approach implies not only a multi-hazard perspective, but also a dynamic multi-vulnerability (Versace et al., 2023).

Making use of risk or multi-risk scenarios has become increasingly common within risk assessment studies since they allow to evaluate impacts of one or multiple events in a specific context and they are useful to support risk-communication (Gomez-Zapata et al., 2021). A scenario can be intended as a given realization of single- or multi-hazard processes, thus it represents a starting point of a risk or multi-risk assessment (Sadegh et al., 2018, Gomez-Zapata et al., 2023).

In the framework of the Transversal Spoke TS1 of the RETURN project, and, more specifically, in the Work Package 5.3, several risk scenarios will be proposed and analyzed with the objective of assessing multi-risk in different urban environments. Moreover, given that a rigorous probabilistic modelling for multi-risk assessment is very challenging and might not be always applicable, the concept of storylines is introduced: an event-based risk storyline can be described as a physically self-consistent unfolding of past or plausible future events and their consequences (Sillmann et al., 2021).

In order to develop consistent multi-risk scenarios and storylines for a specific urban context, as will be also analyzed in Section 5, there is the need to define all the elements at play, i.e., hazard, exposure, vulnerability, and their possible interactions. To this aim, a matrix approach is being proposed in the framework of the Work Package 5.3 to identify the main relationships between the hazards and the exposed elements of the urban environment. In more detail, three different matrix types are introduced:

- **Hazard *vs* hazard matrix** (a first version is presented in Figure 1. Hazard vs hazard matrix for definition of multi-hazard relationships.
-) to describe multi-hazard relationships, which, according to definitions reported in Pittore and Griffo (2023), can be classified as:
  - Independence: it implies a spatial and temporal overlapping of the impact of multiple hazards without any dependence or triggering relationship.
  - Triggering or cascading: it implies a primary and a secondary hazard, the latter caused by the occurrence of an event related to the primary hazard.
  - Change conditions: they relate to one hazard altering the disposition of a second hazard by changing environmental conditions.
  - Compound hazard: different hazards are the results of the same primary event or large-scale processes.
  - Mutual exclusion: negative dependence between hazards.

In Figure 1, the listed hazards are the ones considered in the RETURN project within the activities of the Vertical Spokes (VS), but the list may be also expanded, depending on the scope of the study, considering hazards as defined by UNDRR (2020).

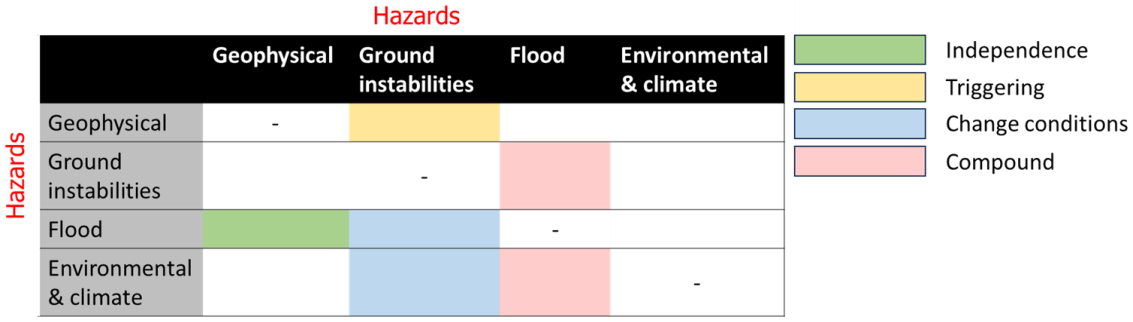

Figure 1. Hazard vs hazard matrix for definition of multi-hazard relationships.

- **Exposure *vs* exposure matrix** to describe relationships between the elements of an urban system. This matrix allows to highlight dependencies (or non-dependencies) among the different components and makes it possible to identify the most critical elements at risk.

  It should be highlighted that the conceptual model of the urban system, reported in Figure 2, has been developed within the Work Package 5.2 of TS1 and is considered here for sake of consistency. Similarly, in the following, the taxonomies for Urban Systems defined in WP 5.2 (Pittore and Grifo, 2023) will be used. From Figure 2, it can be seen that the urban system is subdivided into several subsystems, which can further include subcomponents, according to the mentioned taxonomy. It is

worth mentioning that the adopted model will not include all possible details and features of the physical world, but only those that are relevant to fulfill the scope of multi-risk assessment.

The version of the exposure *vs* exposure matrix proposed in the RETURN Deliverable 5.2.1 (Pittore and Griffo, 2023) is reported in Figure 3. Exposure vs exposure matrix for description of interdependencies among elements of the urban system.

.

By explicating the relationships between the exposed elements, also functional and systemic aspects could be more easily identified, contributing to a proper investigation of functional and systemic vulnerabilities, which is among the objectives of Tasks 5.3.2 and 5.3.3 of the Work Package 5.3.

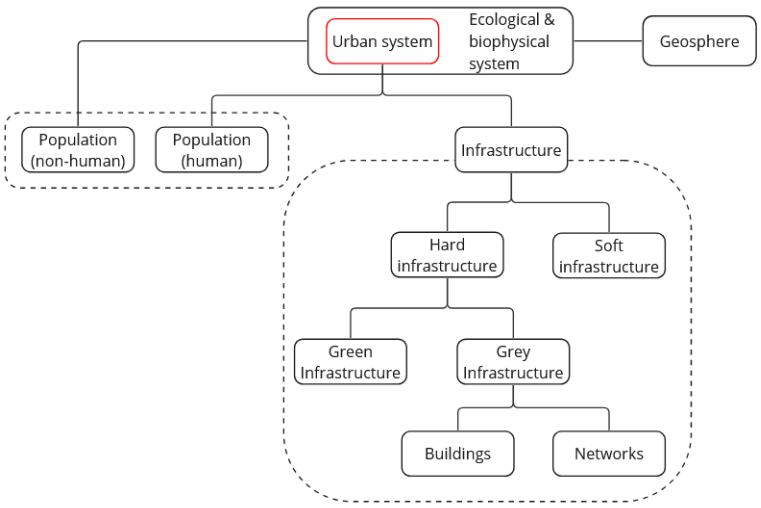

Figure 2. Conceptual model of urban system and corresponding subsystems (Pittore and Grifo, 2023).

- **Exposure *vs* hazard matrix** to highlight relationships between the exposed elements and the different hazards. A first version of the matrix has been developed (Figure 4) considering, for the exposure, the conceptual model of the urban system, previously introduced, and the taxonomy defined in the Work Package 5.2 of TS1. In terms of hazards, a more detailed classification is taken into account, with respect to what presented in Figure 1. Both lists are currently under review and will be updated in the following phases of the project.

  To fill the matrix, as a first assessment, based on expert judgment, it is necessary to identify which elements are vulnerable to a specific hazard. The assessment is binary at this stage (vulnerable or not vulnerable). In this way, on the one hand, by reading the table vertically (i.e., for a single hazard) it is possible to have a clear idea about how many and which elements of the taxonomy should be modeled to assess the impacts of a specific hazardous event; moreover, this visualization can contribute to the definition of the scale at which the analyses have to be carried out. On the other hand, by reading the table horizontally, elements on which multi-risk assessment is crucial are highlighted.

Afterwards, the exposure *vs* hazard matrix can also include further information, e.g., related to the multi-dimensional nature of vulnerability or to the possible impacts and consequences of the hazardous event. An example is reported in Figure 5, where different vulnerability types are also included, according to the following definitions:

- Physical vulnerability: propensity of the elements to suffer physical impacts of a hazardous event (Douglas, 2007; Birkmann et al., 2013).
- Functional vulnerability: propensity of the elements to suffer impacts (also physical) which impair their function.
- Systemic vulnerability: it includes social, economic and environmental vulnerability, therefore: (i) the propensity of human well-being to suffer harm due to disruption of individual and collective social systems (Birkmann et al., 2013); (ii) the propensity of economic assets and processes to be harmed by exogenous shocks (Cardona et al., 2012); (iii) the potential natural resource depletion and resource degradation following a hazardous event (UNEP, 2021).

If more than one vulnerability dimension is applicable for a specific element, “mix vulnerability” can be used in the matrix. It should be mentioned that the definitions of the dimensions of vulnerability, partially taken from Pittore and Grifo (2023), are currently under review within the activities of the Transversal Spoke TS1.

Dependencies ("row X" depends on "column Y")						Tourists	Residents	Building green	Urban agricultural land	Urban green area	Residential Buildings	Educational buildings	Health buildings	Assembly buildings	Industrial buildings	Storage buildings	Hazardous buildings	Roads	Railway/Subway	Power	Water	Communication	Sewage	Sea	Water bodies	Wetlands	Swales	Filter stripes	Educational System	Water system	Health service	Financial System	Emergency System	Law enforcement system	Recreational system
Population	Non-resident				Tourists			x	x	x			x	x				x	x	x	x	x	x	x					x	x	x	x	x	x
	Resident				Residents			x	x	x	x	x	x	x	x	x	x	x	x	x	x	x	x	x	x	x	x	x	x	x	x	x	x	x
Infrastructure	Hard infrastructure	Green infrastructure			Building green	x	x			x	x	x	x	x				x	x	x	x	x	x	x	x	x	x	x	x	x				x
					Urban agricultural land		x			x	x	x								x	x		x		x	x	x	x	x						x
					Urban green area	x	x	x			x	x	x	x						x	x			x	x	x	x	x	x						x
		Gray infrastructure	Buildings		Residential buildings		x	x	x	x			x					x	x	x	x	x	x						x						x
					Educational buildings	x	x	x	x	x				x				x	x	x	x	x	x					x	x	x	x					x
					Health buildings	x	x	x		x	x	x		x				x	x	x	x	x	x						x	x	x	x	x			x
					Assembly buildings	x	x	x		x		x						x	x	x	x	x	x					x	x	x						x
					Industrial buildings		x	x	x							x	x	x	x	x	x	x						x		x		x				
					Storage buildings		x	x	x						x		x	x	x	x	x	x	x	x				x		x				x		
					Hazardous buildings		x		x						x	x		x	x	x	x	x	x							x				x		
			Networks	Transportation	Roads	x	x	x	x	x	x	x	x	x	x	x	x		x	x		x	x						x	x	x			x	x	x
					Railways/subways	x	x	x		x	x	x	x	x	x	x	x	x		x	x	x							x	x	x	x		x	x	x
				Utilities	Power	x	x	x	x	x	x	x	x	x	x	x	x	x	x		x	x	x	x	x				x	x	x		x	x	x
					Water	x	x	x	x	x	x	x	x	x	x	x	x	x	x	x		x	x	x	x	x	x	x	x	x	x		x	x	x
					Communication	x	x	x	x	x	x	x	x	x	x	x	x	x	x	x									x		x	x	x	x	x
					Sewage	x	x	x	x	x	x	x	x	x	x	x	x	x	x	x	x		x					x	x	x	x		x	x	x	x
		Blue Infrastructure	Blue Area		Sea	x	x								x		x	x	x	x	x		x							x					x
					Water bodies	x	x			x			x		x		x						x								x					x
					Wetlands	x	x			x					x		x														x					x
			Blue-green area		Swales	x	x			x					x		x														x					x
					Filter stripes	x	x	x		x	x	x	x		x	x	x						x								x					x
	Soft infrastructure				Educational system		x	x	x	x		x	x	x				x	x	x	x	x	x							x	x		x	x	x
					Water system	x	x	x		x	x	x	x	x	x	x	x			x	x	x	x					x			x		x	x	x	x
					Health service	x	x	x				x	x	x				x	x	x	x	x	x							x			x	x	x	x
					Financial system	x	x	x												x		x								x	x					
					Emergency system	x	x	x					x	x			x	x	x	x	x	x								x				x	x	x
					Law enforcement system	x	x	x										x	x	x	x	x								x			x			
					Recreational system	x	x	x	x	x	x	x		x				x	x	x	x	x	x	x	x				x	x	x	x	x	x		
						22	28	23	14	21	14	17	17	17	15	11	16	21	21	25	22	21	21	8	9	5	5	12	14	28	15	6	14	15	24

Figure 3. Exposure vs exposure matrix for description of interdependencies among elements of the urban system.

	Hazard / Exposure	Slope and ground instabilities	Earthquake	Tsunami	Volcanic hazard	Fluvial floods	Pluvial floods	Coastal floods	Coastal erosion	Extreme winds	Air quality	Heat waves	Chemical	Biological
Population	Population	X	X	X	X	X	X	X	X	X	X	X	X	X
Green infrastructure	Green buildings	X	X	X	X	X	X	X	X		X	X		
	Urban agricultural land	X	X	X	X	X	X	X		X	X	X	X	X
	Urban green area	X	X	X	X	X	X	X		X	X	X		
Buildings	Residential buildings	X	X	X	X	X	X	X	X					
	Educational buildings	X	X	X	X	X	X	X	X			X		X
	Health buildings	X	X	X	X	X	X	X	X				X	X
	Assembly buildings	X	X	X	X	X	X	X	X	X		X	X	X
	Industrial buildings	X	X	X	X	X	X	X	X	X		X	X	X
	Storage buildings	X	X	X	X	X	X	X	X	X		X	X	X
Transportation	Roads	X	X	X	X	X	X	X	X					
	Railways	X	X	X	X	X	X	X	X	X				
	Subways	X	X			X	X	X						
Utility networks	Power network	X	X	X	X	X	X	X		X		X		
	Water supply network	X	X	X	X				X			X	X	X
	Telecommunication network	X	X	X	X					X				
	Sewage network	X	X			X	X	X					X	X
	Sea		X	X				X		X			X	
	Water bodies	X	X	X		X	X					X	X	X
	Open spaces - no green	X	X	X	X	X	X	X		X	X	X		X
Soft infrastructure	Educational system	X	X	X	X	X	X	X				X		X
	Water system	X	X	X									X	
	Health service	X	X	X	X	X	X	X				X		X
	Financial system													
	Emergency system	X	X	X	X	X	X	X				X		
	Law enforcement system	X	X	X	X	X	X	X						
	Recreational system	X	X	X	X	X	X	X		X	X	X		X

Figure 4. Exposure vs hazard matrix.

	Exposure \ Hazard	Slope and ground instabilities	Earthquake	Tsunami	Volcanic hazard	Fluvial floods	Pluvial floods	Coastal floods	Coastal erosion	Extreme winds	Air quality	Heat waves	Chemical	Biological
Population	Population	X	X	X	X	X	X	X	X	X	X	X	X	X
Green infrastructure	Green buildings	X	X	X	X	X	X	X	X		X	X		
	Urban agricultural land	X	X	X	X	X	X	X		X	X	X	X	X
	Urban green area	X	X	X	X	X	X	X		X	X	X		
Buildings	Residential buildings	X	X	X	X	X	X	X	X					
	Educational buildings	X	X	X	X	X	X	X	X			X		X
	Health buildings	X	X	X	X	X	X	X	X				X	X
	Assembly buildings	X	X	X	X	X	X	X	X	X		X	X	X
	Industrial buildings	X	X	X	X	X	X	X	X	X		X	X	X
	Storage buildings	X	X	X	X	X	X	X	X	X		X	X	X
Transportation	Roads	X	X	X	X	X	X	X	X					
	Railways	X	X	X	X	X	X	X	X	X				
	Subways	X	X			X	X	X						
Utility networks	Power network	X	X	X	X	X	X	X		X		X		
	Water supply network	X	X	X	X				X			X	X	X
	Telecommunication network	X	X	X	X					X				
	Sewage network	X	X			X	X	X					X	X
	Sea		X	X				X		X			X	
	Water bodies	X	X	X		X	X					X	X	X
	Open spaces - no green	X	X	X	X	X	X	X		X	X	X		X
Soft infrastructure	Educational system	X	X	X	X	X	X	X				X		X
	Water system	X	X	X									X	
	Health service	X	X	X	X	X	X	X				X		X
	Financial system													
	Emergency system	X	X	X	X	X	X	X				X		
	Law enforcement system	X	X	X	X	X	X	X						
	Recreational system	X	X	X	X	X	X	X		X	X	X		X

Physical vulnerability | Systemic vulnerability | Functional vulnerability | Mix vulnerability

Figure 5. Exposure vs hazard matrix with focus on multi-dimensional vulnerability.

3. Single-hazard description focusing on emerging risks in urban and metropolitan areas

In rapidly evolving urban and metropolitan landscapes, the identification and understanding of single hazards, particularly emerging hazards and subsequent risks, are crucial for effective risk management and resilience planning. This Section delves into the distinct characteristics and implications of various hazard types that are increasingly relevant in urban and metropolitan areas. As cities continue to grow and face complex interdependencies, the need to address these risks proactively becomes paramount.

The following sub-sections systematically explore each category of hazards that pose potential threats to urban environments:

- geophysical hazards: examining risks such as slope and ground instabilities, earthquakes and volcanic activities and tsunamis, all of which can have catastrophic impacts on urban infrastructure and populations.
- Hydraulic hazards: focusing on risks associated with water bodies, including fluvial and pluvial flooding as well as coastal vulnerability in urban areas, which can critically influence urban planning and safety regulations in coastal and riverine cities.
- Meteorological hazards: analyzing hazards like storms and extreme precipitations that are becoming more intense and frequent due to changing climate patterns, impacting urban life and infrastructure.
- Climate hazards: discussing long-term climate changes and their acute effects on urban areas, such as urban heat islands, sea-level rise, storm surges and extreme wave events, which require innovative adaptation strategies.
- Chemical hazards: addressing risks related to air pollution from gases and aerosols in urban environments, as well as interactions between urbanization, air quality, and atmosphere, factors that can contribute to severe health and environmental crises in urban settings.
- Biological hazards: considering the effects of climate change on both the general population and those occupationally exposed and assessing the potential impact of particles and contaminants on human tissues and their implications for health.

3.1 Geophysical hazards

3.1.1 Slope and Ground Instabilities

Urban areas have more and more often to cope with slope instability, a critical factor for the lives of residents, as well as the safety and longevity of urban infrastructures. Ground instabilities, such as landslides and subsidence phenomena, can pose significant risks, especially in areas where urban development has altered the natural landscape. These risks are exacerbated by climate change, which introduces new challenges for managing and mitigating slope instability in urban and metropolitan environments.

Climate change is intensifying extreme weather events such as heavy rainfall, and prolonged dry spells, which have direct consequences on slope stability. Increased rainfall, in particular, leads to higher levels of soil saturation, which weakens the cohesion of slopes, making them more susceptible to landslides and

other forms of ground instability. Urban areas are particularly vulnerable because the presence of impervious surfaces, such as roads and buildings, can alter natural drainage patterns, causing water to accumulate in unexpected areas. This runoff can exacerbate erosion processes, increasing the risk of slope failure. On the other hand, prolonged dry spells can cause soil desiccation and cracking, which reduces soil cohesion and makes slopes more vulnerable to instability when heavy rains eventually occur. This is particularly problematic in urban areas where the soil structure has already been compromised by construction and other human activities.

Hilly urban areas face unique challenges. The construction of buildings, roads, and other infrastructure can disrupt the natural equilibrium of slopes, leading to ground instability. While retaining walls and other slope stabilization structures, are intended to mitigate these risks, they can introduce new hazards if not properly designed or maintained. The combined effect of climate change and urban development often necessitate innovative approaches to slope management and the prevention of ground instability.

In urban and metropolitan areas, slope instabilities can lead to disastrous consequences. Landslides, for instance, can damage buildings, roads, and utility lines, leading to costly repairs and disruptions to daily life. The high population density in urban areas significantly increases the risk of casualties in the event of ground instability. Furthermore, slope failures can have a cascading effect, triggering additional hazards such as floods or the collapse of nearby infrastructure.

Mitigating slope instability in urban areas requires a multidisciplinary approach, combining engineering solutions with careful urban planning and environmental management. Understanding the geomorphological, hydrological and anthropic features of the area is essential in predicting where instabilities are most likely to occur. Furthermore, with the added uncertainty brought by climate change, it is crucial to adopt adaptive strategies that can respond to changing environmental conditions.

One effective technique for analyzing slope instabilities in urban and metropolitan areas is the implementation of statistical methods, such as Logistic Regression, within Geographic Information Systems (GIS). It allows to process large amounts of geospatial data and provides detailed maps indicating which areas are most likely to develop ground instability events, specifically landslides. Combining geomorphological, climate and anthropological factors, such GIS-based models can generate susceptibility maps that identify instability prone areas within urban environments, helping urban planners and engineers make informed decisions about where to focus mitigation efforts. Moreover, by incorporating climate change projections and other dynamic factors, these models can be continuously updated to reflect new hazard conditions, making them a valuable tool for long-term urban resilience planning.

Liguria region serves as a paradigmatic case due to its orographic complexity and high susceptibility to landslides. The territory steep morphology, combined with possible intense rainfall and urban development, makes Liguria particularly vulnerable to slope instability. Over the years, the region has experienced numerous landslides, causing damage to infrastructure and disrupting daily life. The region's unique combination of natural and human factors makes it an ideal case study for understanding the challenges of managing slope instabilities in urban and metropolitan areas.

In summary, addressing slope and ground instabilities in urban areas, particularly in the context of climate change, requires an integrated approach that combines engineering, urban planning, and advanced data analysis techniques. The use of GIS and logistic regression offers a promising solution for identifying and

mitigating risks in urban environments, with Liguria region providing a valuable case study for understanding the complexities of slope management in areas prone to landslides.

3.1.1.1 Processing of Landslide Susceptibility Maps in GIS Environment Using Logistic Regression

As part of Spoke V2 of the Extended Partnership RETURN, the UNIGE1 - DICCA working group is developing a statistically-based methodology for elaborating landslide susceptibility maps, indicating the likelihood of an area to experience landslides. Starting from the assumption that landslides are more likely to occur in areas with similar characteristics to those where they have already occurred, various factors that characterize a territory (predisposing factors) are analyzed and related to actual landslides through statistical processing in a GIS (Geographic Information System) environment. GIS is particularly well-suited for statistical analysis due to its ability to manage large amounts of georeferenced data, accurately characterize an area, and perform both general and specific analyses. In this context, a Logistic Regression process relates the dichotomous variable (landslide/no landslide) to various factors characterizing an area, assigning each factor a different weight.

The result of this analysis is a probability map, which is subsequently divided into qualitative classes, identifying areas with low, medium, and high susceptibility to landslides.

The aforementioned methodology has been tested in a Learning Case as part of VS2 and is currently under further development and validation on more different case studies to improve its reliability and make it transferable to other areas and scales.

It is important to note that a susceptibility map provides a geographical indication of a hazard of landslide triggering, but it does not indicate when the event might occur. Therefore, it is preparatory and functional for direct investigation, identifying the most problematic areas where intervention might be prioritized if critical issues are identified.

Tools Used

The work conducted within VS2 was primarily carried out using the Open Source GIS application GRASS. The operations performed primarily involve functions such as:

- Classification
- Vector geoprocessing (buffer, intersection, feature extraction)
- Data conversion (from vector to raster format and vice versa)
- Map Algebra
- Hydrological modeling (specific commands for basin and hydrological network analysis)
- Interpolation
- Statistical analysis

Study area

The Learning Case focuses on a coastal area of approximately 1,550 km², with elevations exceeding 1,000 meters, predominantly covered by forests and natural areas, with a smaller percentage of agricultural and urbanized land. The nominal scale of 1:100,000 with a resolution of 20 meters was chosen for the study. To ensure that the proposed procedure can be replicated in other areas of Italy with similar characteristics, Open data accessible across the entire Italian territory have been selected.

Additionally, by using base data with a higher level of detail (e.g., data downloadable from various regional or municipal cartographic portals) and adjusting the reference values of the considered parameters, the level of detail can be increased, up to a peri-urban scale. This is particularly useful for highlighting potential instability situations along the connecting routes between urban areas and smaller settlements, along "transit" infrastructures (e.g., highways, railways, or high-voltage networks...), and in peripheral areas where natural and anthropic elements often alternate in a "disordered" manner.

For the delineation of the study area, it is generally advisable to choose a natural boundary rather than an administrative one, provided data access is possible. In particular, in the case of small areas (e.g., areas near infrastructure or settlements), it is preferable to consider a larger territory than strictly necessary to obtain a statistically significant sample.

Identification of Predisposing Factors

The first phase of the work involved identifying the relevant factors for landslide susceptibility (Table 1). The territorial characteristics considered include:

- Morphology
- Geology, lithology, and land use
- Climatic aspects
- Anthropogenic aspects

A literature review was then conducted to identify a set of factors:

- Identified as certainly relevant
- Describable using Open data
- Independent of specific situations (e.g., presence of large hydroelectric plants, presence of faults, etc.)

By cross-referencing the findings from the literature review with the data actually accessible at the national level or common to all regions, a set of data base was selected.

For the Learning Case, all maps were converted to raster format with a resolution of 20 meters.

Table 1. Predisposing factors considered in the case study.

Predisposing Factors	Description	Source data	Data Used in the Learning Case	Type of data
Accumulation	Number of areal units drained by each unit	Processing from the Digital Terrain Model	DTM – Digital Terrain Model – Liguria ed. 2023 (Geoportale Regione Liguria, 2024)	Raster
Climatic aggressiveness	Concentration of precipitation compared to the annual average	Processing of rainfall cumulate data	ARPAL (Ligurian Regional Agency for Environment Protection) Data (ARPAL, 2013)	Raster
Exposure	Orientation relative to the North of the steepest slope direction	Processing from the Digital Terrain Model	DTM - Digital Terrain Model - Liguria ed. 2023 (Geoportale Regione Liguria, 2024)	Raster
Lithology	Type of rocky substrate	Geological map	Geological map of Italy (INSPIRE Geoportal, 2020)	Vector
Slope	Inclination of the slopes relative to the horizontal plane	Processing from the Digital Terrain Model	DTM – Digital Terrain Model - Liguria ed. 2023 (Geoportale Regione Liguria, 2024)	Raster
Elevation	Altitude relative to sea level	Digital Terrain Model	DTM – Digital Terrain Model - Liguria ed. 2023 (Geoportale Regione Liguria, 2024)	Raster
Distance from transport networks	Distance bands from main roads, secondary roads, and railways	Regional Technical Cartography	Regional Technical map 1:5000 - 2007/2013 - II Edition 3D / Topographic database (Geoportale Regione Liguria, 2024)	Vector
Land use and coverage	Vegetation or artificial land coverage	CORINE Land Cover maps or regional land use cartography	Land use map sc. 1:10000 - ed. 2019 (Geoportale Regione Liguria, 2024)	Vector

Historically and Currently Active Landslide Areas

The data reported in the Inventory of Landslide Phenomena in Italy (IFFI, Inventory of Landslide Phenomena in Italy - IFFI) are considered as "ground truth." The IFFI cartography is frequently updated, but it does not represent real-time situations. In the latest edition, updated to 2022, the following types of landslides are identified, each associated with its respective identification code:

- Undefined landslide (0)
- Fall/Topple (1)
- Rotational/Translational Slide (2)
- Spread (3)
- Slow Flow (4)
- Fast Flow (5)
- Subsidence (6)
- Complex (7)
- DPGV Deep-Seated Gravitational Slope Deformations (8)
- Areas with widespread falls/topples (9)
- Areas with widespread subsidence (10)
- Areas with widespread shallow landslides (11)

The proposed methodology for developing the susceptibility map was applied only to earth landslides, specifically rotational/translational slides, slow flows, and fast flows. Additionally, undefined landslides and complex landslides were also categorized under this category.

Regarding "areas with widespread shallow landslides," these represent areas where multiple shallow landslide events have occurred, but do not indicate the precise boundaries of each landslide. The data reported in the IFFI cartography come from various sources and have different scales of origin compared to the working scale. For statistical analysis purposes, this may lead to non-negligible inaccuracies. Furthermore, each type of landslide phenomenon is influenced differently by the predisposing factors. Therefore, it would be advisable to evaluate the susceptibility of an area relative to each type of landslide separately. However, in some cases, this could result in a statistically hardly significant sample.

Data Preparation /1 - Classification

It is possible to apply the logistic regression method using continuous, ordinal, or binomially distributed data sets. In this work, all predisposing factors were converted into ordinal data through reclassification and aggregation operations, describing each factor by a discrete number of classes, ordered from 1 to *n* (in the case study $n < 10$). This makes it possible to compare qualitative and quantitative data.

Accumulation

The accumulation value is expressed as log(abs(accumulation_map) + 1). The values reported in the resulting raster map, are greater than 0 and are grouped into 6 classes as follows:

Range	Class
0 - 1	1
1 - 2	2
2 - 3	3
3 - 4	4
4 - 5	5
> 5	6

Values between 0 and 1 indicate a watershed or ridge, while higher values indicate valleys or other accumulation areas. In the literature, the presence of soil moisture or surface runoff is considered an important factor and is also described using other indices (e.g., Topographic Wetness Index...), which are also derived from the Digital Terrain Model. However, in peri-urban areas, water runoff is often altered by the presence of retaining structures that obstruct the natural flow along the slopes, by drainage works, and by soil impermeabilization. Therefore, this parameter should be reconsidered. For example, it might be more relevant to identify situations where there is a convergence of uncovered or culverted historic streams, retaining walls, and multi-story buildings, and to classify areas based on their proximity to these features.

Climatic Aggressiveness

Rainfall is certainly a relevant factor to take into consideration in assessing susceptibility to landslides, both in terms of cumulative precipitation and concentrated rainfall events. In the Learning Case, this aspect was considered by including the Climatic Aggressiveness parameter, calculated using the Arnoldus Index (Arnoldus H. M. J., 1980):

$$AC = \sum_{i=1}^{12} \frac{p_i^2}{P}$$

where p_i = cumulative rainfall for each month, P = average annual rainfall.

Based on the literature and as observed in the Learning Case, Climatic Aggressiveness has proven to be a determining factor for various types of landslides (Commission of European Communities, 1992). However, at the same time, it is one of the most challenging factors to accurately represent in the model.

Precipitation data, in fact, refer either to the stations where they were recorded (when considering local data) or to continuous data maps (global, European, or national data) but at a much lower resolution than the data used to describe other predisposing factors (e.g., 1 km compared to 20 m). In the first case, it is necessary to interpolate the point data to build a continuous map; in the second case, it is advisable to resample the map, also interpolating the value of each cell. This inevitably leads to approximations that vary depending on the interpolation method used.

The most suitable method would be kriging, based on the definition of the semivariogram, which is the function that describes how the correlation between spatial data changes with the distance between them. Several algorithms exist to develop this function, but in general, they require the "manual" input of various parameters, which presupposes the operator's knowledge of the territory. To promote the transferability of the proposed methodology, deterministic interpolation methods were preferred, which rely solely on the geometric arrangement of known points, including Inverse Distance Weighted (IDW), Triangulated Irregular Network (TIN), and Regularized Spline with Tension (RST). Regardless of the method used, it is also important to remember that precipitation data should be collected over an area larger than the study area to ensure accurate processing, even in "border" areas.

Another important factor in evaluating the influence of precipitation is the temporal aspect. In climate studies, a reference period of 30 years is considered significant. Therefore, it was decided to create a "general" Climatic Aggressiveness map for the study area using accessible digital data, from the earliest available period to the present day.

$$\frac{\sum_{1}^{n}\sum_{i=1}^{12}\frac{p_i^2}{P_{tot}}}{n}$$

where p_i = cumulative rainfall for each month for each year considered, P_{tot} = total rainfall for each year considered, n = number of years considered.

Since precipitation data prior to the early 2000s are often difficult to obtain, incomplete, or available in formats that are hard to use (e.g., scans of paper records), the map can be updated annually or seasonally using the Arnoldus index as described above.

As an example, in the Learning Case, the baseline map was created by interpolating the Climatic Aggressiveness data collected by ARPAL (Ligurian Regional Agency for Environment Protection) at individual stations for the 1980–2010 period.

For the subsequent years, aggressiveness was calculated by directly interpolating the cumulative monthly precipitation data for the various stations, both for the 2010–2020 decade and seasonally for the years after 2020.

The values reported in the resulting Climatic Aggressiveness map for the Learning Case have eventually divided into classes according to the guidelines provided by the European Commission in 1992 (CEC, 1992).

Range	Class	Description
< 60	1	Low
60 - 90	2	Medium-Low
60 -120	3	Medium
120 160	4	Medium-High
> 160	5	High

This classification method is suitable for rather large areas, but when working at a municipal scale or in relatively small territories (less than 100 km²), the entire study area may fall into a single class. Since constant factors cannot be included in the next phase of multivariate analysis, either Climatic Aggressiveness is not considered, or the single represented class must be subdivided into "subclasses," particularly in the case of the "High" or "Low" classes. This situation could be due to the fact that, during the period considered, no particularly intense localized precipitation occurred in the area, or that the rain data collection points are very far apart, preventing the recording of phenomena in intermediate areas.

Orientation

Slope orientation values, ranging from 0° to 360°, have been grouped into 4 classes (North, West, South, East). The classes are divided as follows:

North: 0° to 45°

East: 45° to 135°

South: 135° to 225°

West: 225° to 315°

North: 315° to 360°

so that each cardinal direction is at the center of its respective class.

Range	Class	Direction
0 - 45	1	North
45 - 135	2	East
135 - 225	3	South
225 - 315	4	West
315 - 360	1	North

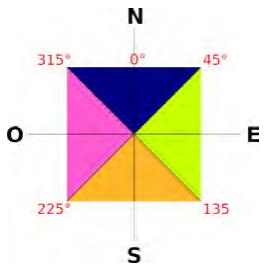

For smaller areas or areas with very complex morphology, it may be more appropriate to group the orientation values into 8 classes.

Lithology

In the Learning Case, the different geological units have been grouped into 5 classes based on their origin. As an example, the table used is provided, which only considers the formations present in the studied area (description corresponding to the "Name" column of the Geological Map of Italy, as mentioned above).

The map used has a nominal scale of 1:100,000, suitable for regional or basin-scale extensions, and the most general classification method was used. Certainly, for peri-urban scales, the classification should take into account a higher level of detail, especially in cases where the area contains formations particularly prone to the development of landslide phenomena.

Formation	Class
deposits	1
magmatic rocks	2
metamorphic rocks	3
sedimentary rocks	4
other	5

Slope

The slope of an area can be expressed in degrees (from 0 to 90°) or as a percentage, calculated as the ratio between the vertical and horizontal distance between two points (from 0 to ∞). In this work, it was calculated in degrees, and the values for individual points were grouped into 8 classes of 5° up to a slope of 40°, with an additional single class for all values between 40° and 90° (Table 5). However, in mountainous areas, it may be useful to add more classes (between 40° and 90°), and in smaller areas where minor differences are more significant, it might be more practical to use percentage values.

Range	Class
0 - 5	1
5 - 10	2
10 - 15	3
15 - 20	4
20 - 25	5
25 - 30	6
30 - 35	7
35 - 40	8
40 - 90	9

Elevation

In the Learning Case, elevation values have been grouped into 250-meter classes, starting from the lowest value in the study area. In the case of a coastal area, the value 1 is assigned to the elevation class between 0 and 250 meters. In hilly or mountainous areas, the value 1 is assigned to the range of values where the lower limit corresponds to the lowest elevation in the study area.

In smaller areas or areas with minor elevation differences, it may be important to use smaller classes, for example, every 100 meters.

Range	Class
0 - 250	1
250 - 500	2
500 - 750	3
750 - 1000	4
1000 - 1250	5
1250 - 1500	6
1500 - 1750	7
1750 - 2000	8

Distance from Transport Infrastructure (Road Network and Railways)

Transport infrastructure includes vehicular roads (highways, extra-urban and urban thoroughfares, extra-urban and urban service roads), secondary roads (trails, stairways, dirt roads...), railways, and their related accessory spaces. For the purposes of this analysis, the focus is not on the importance of the infrastructure itself but rather on its impact on the morphology of the considered area.

Bridges, viaducts, and tunnels, which do not directly affect the terrain, have been excluded. To define the area affected by the presence of the infrastructures, some buffer areas have considered: 50 meters (including the road axis), 100, 150, 200, and beyond 200 meters from the axis. Indeed, at a distance of 200 meters, the influence of a road, especially a narrow one, may already be negligible (Brenning et al., 2015). However, since in a GIS environment, map algebra operations that involve continuous and discontinuous maps result in discontinuous maps, it has been decided to create a class that encompasses all areas more than 200 meters away from the road axis.

For the analysis of urban and peri-urban areas, it would be advisable to directly use the cartography of road and railway areas and their related service areas (for Liguria and most regions, available as a layer in the Regional Technical Map, CTR), where these infrastructures are represented as polygons with their actual dimensions.

Distance	Class
0 - 50	1
50 - 100	2
100 - 150	3
150 - 200	4
beyond 200	5

Land Use

The land use map can vary significantly depending on how certain classes are defined (for example, how infrastructure areas or green spaces within an urban area are considered).

At a regional or basin scale, with a resolution of 20 meters, it is advisable to use land use maps produced by the regions, which provide a relatively high level of detail, and then group the different types of use into macro-classes. The criterion chosen for the grouping of uses is the Land Cover Classification System (LCCS) developed by the United Nations (UN) Food and Agriculture Organization (FAO) and used to classify the ESA maps for 2020–2021 (ESA, 2021). This classification is based on actual land cover rather than land use (for example, a chestnut grove is considered "tree vegetation" as land cover, while as land use it falls under "agricultural areas") and can also be used for smaller areas (such as municipal or slope-scale), for which it might be convenient to derive land use through photointerpretation.

Land Cover	Class
Built-up	1
Crops	2
Tree cover	3
Shrubland	4
Grassland	5
Bare – Sparse vegetation	6
Water	7
Herbaceous wetland	8

Landslide Areas

In the IFFI inventory (IFFI, 2024), each landslide is represented both as a polygon and as a point. The polygon encompasses the entire area affected by the landslide, including both the detachment area and the area where the landslide materials are deposited. The point, on the other hand, is located within the polygon at the highest elevation and approximates the location of the detachment point.

Based on the experience gained from analyzing the Learning Case, it is not considered correct to use the entire extent of a polygon for statistical analysis because this includes parts of the territory that are not actually affected by the landslide, which adds confusion to the model being developed. On the other hand, considering only the detachment points would be more accurate, but the sample size is often too small and therefore not very significant.

It is often necessary to use adjustments to optimize the data. From observations in the Learning Case, in general, the larger the area being studied, the smaller the error introduced by using the "complete" areas, and beyond a certain extent, it may be convenient to consider them as they are. For smaller areas, a good compromise could be to use, for landslides larger than the pixel size (400 m² in the Learning Case), clusters of predefined points (e.g., 3 x 3) placed within the polygon at an elevation equal to or lower than the detachment point.

Certainly, in the case of peri-urban areas or areas adjacent to infrastructure or particularly vulnerable elements, determining the actual landslide areas becomes very important. However, considering that these areas are generally not very extensive, it may be worth identifying them through photointerpretation or direct surveying, using the IFFI inventory as a base.

The identified landslide areas, which make up the statistical sample, are then represented on a raster map with a value of 1, while the rest of the territory is assigned a value of 0.

Data Preparation /2 - Reordering of Classes Based on Conditional Probability

The number assigned to each class during the data preparation phase is not necessarily correlated with the progression of susceptibility to landslides. Therefore, it is necessary to reorder them so that they exhibit a monotonic trend. Through bivariate statistical analysis, the maps of each factor are reclassified, assigning each class an increasing number based on the conditional probability of landslides.

$P_{cond} = P(f|k) = \frac{P(f \cap k)}{P(k)}$

where $P(f \cap k)$ = probability that a point is in a landslide $= \frac{landslide\ area}{total\ area}$, $P(k)$ = probability that a point belongs to a class k = $\frac{area \in k}{total\ area}$.

The value 1 is assigned to the class with the lowest probability of a landslide. If one or more classes have no pixels in a landslide (conditional probability = 0), the value 1 is assigned to that class (or those classes).

Multivariate Analysis Using Logistic Regression

Considering Landslide Probability = 1 where a landslide has already occurred and Landslide Probability = 0 where a landslide event is not possible, the probability can be expressed using the logit function defined as:

logit (Y) = $z = \ln\frac{P(Y=1)}{1-P(Y=1)}$ con $P(Y=1)$ = probability that a landslide occurs.

The Logistic Regression model is then applied as a Generalized Linear Regression model by setting:

$z_i = \beta_0 + \beta_1(x_1) + \beta_2(x_2) + \beta_2(x_2)... + \beta_i(x_i)$

where x_1, x_2, x_i are the classified and reordered maps of the different predisposing factors, β_0 is the intercept value, β_1, β_2, … β_i are the weights assigned to the different factors.

This process leads to the creation of a map of expected values. Through the inverse operation, a map is generated that expresses, for each point, the probability of being involved in a landslide event, that is, the susceptibility.

$P(Y_i = 1) = \frac{e^{z_i}}{1+e^{z_i}}$

Model Reliability

A preliminary assessment of the model's reliability is obtained by calculating the Area Under the ROC (Receiver Operating Characteristic) Curve (Fawcett, 2006).

This method evaluates the accuracy of the landslide susceptibility map. It is a very useful step because it helps to determine whether the considered factors and the used data are adequate (Figure 6). A low AUC value, in fact, could be due to the quality of the input data, but also to the inclusion of irrelevant or non-independent factors in the model, or to the omission of specific elements of the considered area that are of particular importance (e.g., erosion conditions, presence of faults, soil type, etc.).

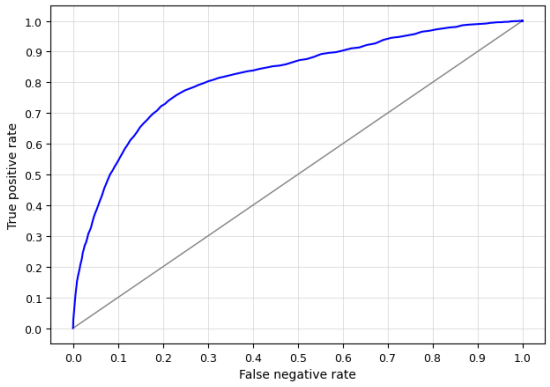

Figure 6. ROC curve related to fast flows in the Learning Case area.

The ability provided by the AUC to easily compare different models also allows for identifying the truly relevant elements and arriving at the definition of the set of predisposing factors that, for a specific area and a particular type of landslide, lead to the best model.

In this regard, the "Leave One Out Cross Validation" method can be used (Figure 7). The logistic regression model is applied to the study area multiple times, removing a different predisposing factor each time. When the AUC obtained by excluding a specific factor is higher than that of the general model, it means that the factor worsens the model. The model should then be recalculated considering only the factors that do not add confusion. At this point, the situation can be reassessed, and a decision can be made on whether to include other previously omitted factors.

acc aggr orient lith slope Q net use

--- aggr orient lith slope Q net use

acc ---- orient lith slope Q net use

acc aggr ---- lith slope Q net use

acc aggr orient ---- slope Q net use

acc aggr orient lith ---- Q net use

acc aggr orient lith slope - net use

acc aggr orient lith slope Q ---- use

acc aggr orient lith slope Q net ---

Figure 7. Scheme of the "Leave One Out" Cross Validation.

In the area chosen for the Learning Case, the best results were obtained for slow flows, fast flows, and undefined landslides, with AUC > 80%.

In the case of fast flows, it was possible to further improve the model by excluding two factors.

Identification of Susceptibility Classes

Once the best model for the study area has been defined, it is necessary to make the maps produced by the model understandable even to non-experts. The values shown on the susceptibility maps should therefore be grouped into classes, allowing for a qualitative assessment: 1 = low, 2 = medium, and 3 = high.

There is no universal criterion for determining the classes. They can be identified by dividing the values into equal intervals, based on the distribution of the values (e.g., based on percentiles or Natural Breaks), by taking into account the need to include a larger or smaller safety margin, or by using other criteria.

As an example, the classification method used in the Learning Case is provided:

- Lower value of the high class = average value of the landslide areas
- Lower value of the medium class = (average value of the landslide areas - minimum value of the entire area) / 2 + minimum value of the entire area

Validation

The model validation process is still ongoing. To date, for some small sample areas, the model's accuracy has been tested by using 70% of the areas for calibration and the remaining 30% for validation, observing a good match.

The more homogeneous an area is, the more accurate the model. This makes it especially important to choose a physical rather than administrative boundary to avoid including areas with very different characteristics.

For peri-urban areas or those adjacent to large infrastructure, using IFFI data (IFFI, 2024) as the calibration set, it would be advisable to use survey or aerial photo data during the validation phase. The IFFI inventory, in fact, provides a relatively "static" situation and does not fully reflect a constantly evolving reality.

3.1.2 Seismic hazard

Seismogenic hazards, commonly referred to as earthquakes, give rise to specific hazards such as ground shaking, subsidence or ground rupture, but can also trigger hazards such as tsunami or rockfall (UNDRR, 2020). Seismic hazard is related to the potential risk posed by earthquakes to human life, infrastructure, and the built environment. It is one of the most important issues for the vulnerability assessment of urban and metropolitan area due to their dense population, complex infrastructure, and the concentration of essential services. In Italy, which is one of the most seismically active regions in Europe, the risks associated with seismic events are significant. Understanding seismic hazard in this context is critical for effective disaster management, urban planning, and resilience-building.

Hazard analysis encompasses a range of physical phenomena triggered by earthquakes. The most immediate effect of an earthquake is the generation of seismic waves, which propagate through the Earth's crust, causing ground shaking in the affected region. Additionally, earthquakes can induce permanent ground displacements, such as surface fault ruptures, uplift, subsidence, and folding. These ground-shaking events and permanent displacements are considered primary hazards, with ground shaking being particularly critical, as it accounts for the majority of structural damage and human casualties during an earthquake.

Moreover, these primary hazards can give rise to secondary hazards, compounding the destructive potential of an earthquake. Earthquake-induced ground shaking and displacements can lead to the formation of tsunamis, trigger landslides, cause soil liquefaction, and even result in flooding. These secondary hazards often expand the impact zone and contribute to long-term devastation, making comprehensive hazard analysis vital for effective disaster mitigation and preparedness.

Seismic hazard is typically defined as the probability of exceeding a certain level of ground motion (e.g., shaking intensity) at a specific location over a given return period. The assessment of seismic hazard involves the analysis of several factors, including the frequency and magnitude of potential earthquakes and the geological characteristics of the area. Climate change, though primarily associated with weather-related events, also has indirect implications for seismic hazard, especially through its influence on secondary hazards such as landslides and soil liquefaction.

The seismic hazard is particularly significant in urban and metropolitan areas, where population density and infrastructure concentration increase the potential for catastrophic outcomes. Since 1900, earthquakes have killed approximately 8.5 million people and caused $2 trillion of damage 1 (Daniell et al., 2011). In regions with a history of seismic activity, such as Italy, understanding and mitigating seismic risk is critical for disaster preparedness and resilience. Italy is located on the convergence zone of the African and Eurasian tectonic plates, making it one of the most seismically active regions in Europe. The country has experienced several devastating earthquakes, with significant events including the 1908 Messina earthquake, the 2009 L'Aquila earthquake, the 2012 Emilia earthquake and the 2016 Central Italy earthquakes. These events have highlighted the vulnerability of Italy's urban areas, where historical buildings, aging infrastructure, and dense populations contribute to the risks associated with seismic hazard.

Seismic hazard is assessed using probabilistic methods, which estimate the likelihood of different levels of ground motion occurring at a given site. This assessment typically involves the creation of seismic hazard maps that incorporate data on historical earthquake activity, fault lines, and local soil conditions. These maps provide a crucial tool for urban planning and structural design, helping to guide building codes and land-use decisions in areas at risk of earthquakes. For example, Italy's national seismic hazard map categorizes regions based on their expected seismic activity and provides guidance for earthquake-resistant construction standards.

In urban and metropolitan areas, seismic hazard poses unique challenges. The concentration of people and buildings in these areas means that an earthquake can have widespread and severe impacts. The risk is further exacerbated by the presence of older buildings that may not comply with modern seismic codes, as well as critical infrastructure such as bridges, tunnels, and utility networks that are vulnerable to earthquake damage.

In addition to structural measures, urban areas must also focus on emergency preparedness and disaster response planning. Ensuring that evacuation routes, emergency services, and communication systems remain operational during and after an earthquake is critical to minimizing the impact of a seismic event. Public education campaigns about earthquake preparedness, including drills and information on safe practices, are also essential components of urban seismic hazard mitigation.

While seismic activity is primarily driven by geological processes, climate change can influence seismic hazard in indirect but significant ways. One of the key connections between climate change and seismic hazard is through the increased risk of secondary hazards, such as landslides, soil liquefaction, and tsunamis, which can be triggered by earthquakes. In Italy, climate change is intensifying extreme weather events, such as heavy rainfall and prolonged droughts, both of which can exacerbate ground instability. For instance, increased rainfall can lead to soil saturation, which weakens slopes and makes them more susceptible to landslides during an earthquake. Coastal areas are also at greater risk due to rising sea levels and the potential for more frequent and severe tsunamis triggered by underwater seismic activity. These climate-related factors add a layer of complexity to seismic hazard assessment and necessitate the integration of climate adaptation strategies into seismic risk management. Urban areas in Italy must not only plan for seismic events but also account for the compounded risks posed by climate change, ensuring that buildings and infrastructure can withstand both primary and secondary hazards.

In summary, seismic hazard in urban and metropolitan areas is a complex and multifaceted challenge, particularly in seismically active regions like Italy. The combination of dense populations, aging infrastructure, and the added risks posed by climate change makes seismic hazard assessment and mitigation a top priority for urban planners and policymakers. Through the use of seismic hazard assessments, building codes, retrofitting efforts, and emergency preparedness planning, cities can enhance their resilience to earthquakes. Given Italy's history of seismic activity and its vulnerability to future events, ongoing efforts to improve seismic safety are crucial to protecting lives and preserving the built environment in the face of this persistent natural hazard.

3.1.2.1 Significant measures in seismic hazard assessment

The intensity of an earthquake and the potential damage it may cause are measured using various scales. The two most widely recognized measures are the Richter scale and Peak Ground Acceleration (PGA). The Richter scale quantifies the energy released by an earthquake, while PGA measures the intensity of ground shaking at a specific location. PGA is of particular importance in seismic hazard assessments because it directly correlates with the forces that can cause structural damage to buildings and infrastructure.

The United States Geological Survey developed an instrumental Intensity scale, which maps peak ground acceleration and peak ground velocity on an intensity scale similar to the Mercalli scale. These values are used to create shake maps by seismologists around the world (see, e.g., Wald et al., 1999). Table 2 compares seismic intensities using the Richter scale and PGA values, providing a first reference for understanding the potential impact of earthquakes of different magnitudes.

Table 2. Comparison between Richter magnitude and PGA.

Richter Scale	PGA (g)	Description
0 - 2.9	< 0.02	Minor earthquakes, generally not felt
3.0 - 3.9	0.02 - 0.04	Light shaking, minimal damage

4.0 - 4.9	0.04 - 0.1	Moderate shaking, potential damage to weak structures
5.0 - 5.9	0.1 - 0.2	Strong shaking, damage to buildings (light)
6.0 - 6.9	0.2 - 0.4	Very strong shaking, damage to buildings (moderate)
7.0-7.9	0.4-0.7	Severe earthquake, damage to buildings (moderate to heavy)
8.0 +	> 0.7	Violent and extreme earthquake, significant destruction over a wide area

Another significant measure used in engineering is the Pseudo-Spectral Acceleration (Sa or PSA). Unlike PGA, which reflects the maximum acceleration at a specific location, PSA provides a more detailed measure of the response of a structure. It represents the maximum acceleration experienced by a Single Degree of Freedom (SDOF) system, with a specified vibration period and damping ratio, subjected to earthquake-induced ground motion. PSA is particularly useful in seismic design and analysis because it accounts for how different structures, depending on their natural frequencies and damping characteristics, will respond to seismic forces.

The shape of earthquake spectra is influenced by a range of factors that are closely related to the characteristics of earthquake ground motion. These factors include (Elnashai and Di Sarno, 2015):

- magnitude;
- source mechanism and characteristics;
- distance from the energy release source;
- wave travel path;
- rupture directivity;
- local geology and site conditions.

While all of these factors play a role in shaping earthquake spectra, some have a more significant impact than others. The three primary parameters that fundamentally influence earthquake spectra are magnitude, distance, and site conditions. For example, Figure 8 illustrates spectra generated for different earthquake magnitudes, as derived from two different ground-motion models (also known as attenuation relationships). These models are analytical expressions that describe how ground motion varies based on factors such as earthquake magnitude, source characteristics, and site conditions. By comparing the spectra across different ground-motion models, we can observe how these factors influence the expected seismic response at a given location.

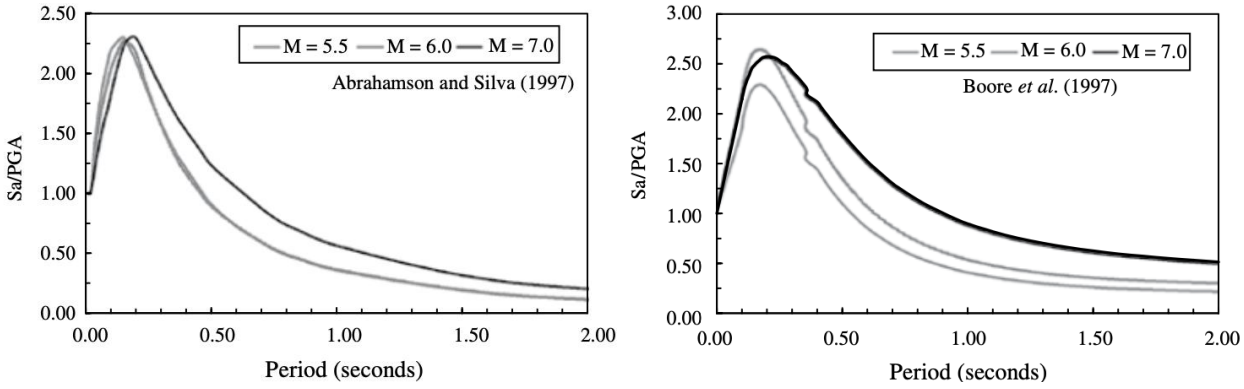

Figure 8. Effects of magnitude on spectral shape using different attenuation relationships (Elnashai and Di Sarno, 2015).

To evaluate the risk posed to a structure by ground-motion shaking, it is essential to determine the annual rate (or probability) of exceeding various levels of shaking at a given site, across a spectrum of intensity levels. This information can be visually represented in a plot, as shown in Figure 9, which illustrates that lower intensity levels are exceeded more frequently, whereas higher intensity levels occur much less often. This type of plot is known as a ground-motion hazard curve, or simply a hazard curve. The mathematical methodology used to generate these curves is called Probabilistic Seismic Hazard Analysis (PSHA). PSHA provides a rigorous framework for quantifying seismic hazard by integrating uncertainties related to earthquake magnitude, location, and ground-motion characteristics, offering a comprehensive assessment of seismic risk at a particular site.

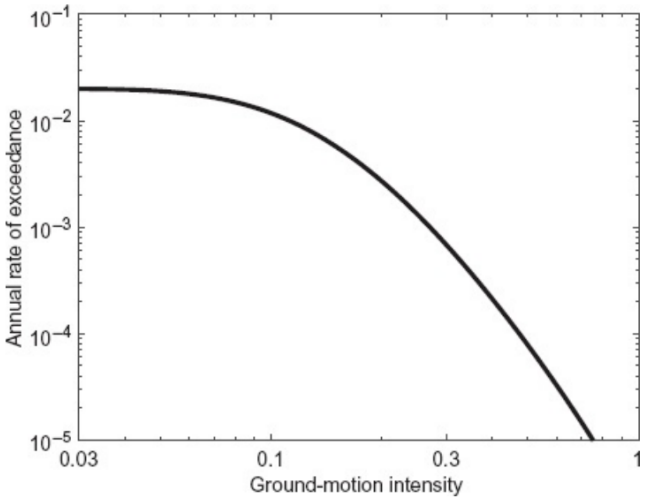

Figure 9. Ground-motion hazard curve illustrating the probability of exceeding various levels of ground shaking at a specific site (Baker et al., 2021).

At its core, PSHA involves five key steps (Baker et al., 2021; Figure 10):

- specify the ground-motion intensity measure (IM) of interest;
- identify the site properties that help predict ground-motion intensity;
- compute the locations, characteristics, and occurrence rates of all rupture scenarios capable of producing damaging ground motions;
- predict the resulting distribution of ground-motion intensity as a function of the site characteristics and each rupture scenario's properties;
- consider all possible ruptures, and uncertainty in resulting ground-motion intensity.

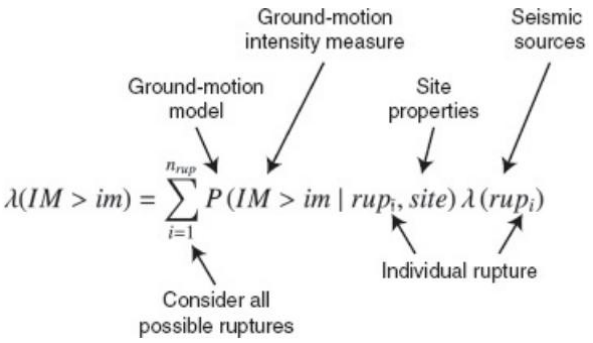

Figure 10. Inputs to a probabilistic seismic hazard analysis calculation (Baker et al., 2021).

The outcome of these calculations is a ground-motion hazard curve, which quantifies the complete distribution of intensity measure (IM) levels and their corresponding rates of exceedance. The PSHA approach, which integrates numerous models and data sources to produce results like those depicted in Figure 5, could appear complex and opaque. However, a closer examination reveals that the method is actually quite intuitive. Once fully understood and applied, PSHA offers significant flexibility, allowing it to meet the diverse needs of various users. Moreover, it is a quantitative method, capable of incorporating all available knowledge about seismic activity and the resulting ground shaking at a given site. This adaptability makes PSHA an essential tool for accurately assessing seismic hazard across different contexts and applications.

One might ask why PSHA stops at calculating ground-motion hazard before moving on to risk analysis (Baker et al., 2021). Practically, this separation allows different specialists to handle each stage, focusing on their expertise. Additionally, many applications, like building codes, only require hazard information to set design forces, without needing a full risk analysis. Hazard analysis can be conducted independently of specific structures, while risk analysis also requires detailed knowledge of the system in question. Therefore, hazard and risk calculations are often distinct processes, allowing flexibility and modularity in how seismic hazard information is used.

Once a hazard curve is selected to represent the seismic hazard at a specific site, a vulnerability assessment can be performed to evaluate how increasing intensity measure (IM) values affect the structures. This assessment, often using a probabilistic approach, relates IM levels to potential damage outcomes for structures, ranging from minor or no damage to complete collapse. Damage thresholds are typically defined in terms of Engineering Demand Parameters (EDP), such as top displacement or interstorey drift, which are determined through experimental or mechanical studies (e.g., Elnashai and Di Sarno, 2015).

Vulnerability reflects the susceptibility of individuals, communities, infrastructure, or systems (including ecosystems) to adverse effects from hazards (UNDRR, 2020). In probabilistic seismic design, it is critical to quantify EDPs for specific shaking levels to estimate potential damage (structural, non-structural, or content-related). A comprehensive vulnerability study should consider a wide range of structures and utilize computationally efficient analysis models to ensure accurate and scalable results.

Exposure analysis focuses on linking the exceedance of specific damage levels (e.g., deaths, injuries, economic losses) to the impacts of an earthquake. Seismic risk is then quantified by combining hazard, vulnerability, and exposure analyses. This provides estimates of the probability of experiencing certain consequences, such as fatalities, injuries, displaced populations, or financial costs for recovery, resulting from an earthquake's impact on structures.

The Global Earthquake Model (GEM) Foundation (https://www.globalquakemodel.org/) has developed a comprehensive global map of earthquake hazard and risk, which was first released in 2018. This map synthesizes data from national and regional seismic hazard models, many of which were developed in collaboration with national governments and research institutions. These models are specifically designed to inform seismic design regulations within building codes, ensuring that structures are built to withstand the specific seismic threats in their regions. The 2023 version of the GEM Global Seismic Hazard Map (version 2023.1) depicts the geographic distribution of the PGA with a 10% probability of being exceeded in 50 years, computed for reference rock conditions (Johnson et al., 2023). The map was created by collating maps computed using national and regional probabilistic seismic hazard models developed by various institutions and projects, in collaboration with GEM Foundation scientists. This version represents an update from the previous release from 2018 and features improvements in most regions of the world, as well as a higher spatial definition compared to the previous version.

3.1.3 Tsunami hazard

Lessons learned from recent devastating tsunamis (e.g. Japan 2011 and Sumatra 2004 earthquake generated tsunamis) dramatically evidenced that tsunami hazard assessment is an essential element to improve risk mitigation plans in coastal urban/metropolitan settlements. Obtaining accurate and detailed information on tsunami hazard parameters (e.g., the height the waves may reach, the speed that may produce drag forces, and the impact that may be triggered in the coastal areas), is critical in view of the high population density, infrastructures, lifelines and other major structures (e.g. ports or plants) that are situated along the coast. In this framework, tsunami modeling is a promising tool, which may help simulating a comprehensive set of possible tsunami scenarios for the area of interest, joining together source information and topo-bathymetric data with the physical knowledge about waves propagation, to assess their possible impacts in the areas of interest. In the framework of disaster risk mitigation, high-resolution inundation maps and high-resolution vulnerability analysis are the essential requirements for the development of tsunami emergency plans for coastal communities.

Three essential components are required for the simulation of tsunami events: a) the process of the earthquake rupture (information about the source); b) the bathymetry of the path to the target location (information about the path); c) the topography of the location (inland propagation). The reliability of tsunami hazard estimates based on scenarios simulations, besides depending on the capacity of the adopted numerical model to reliably reproduce the complexity of tsunami wave interactions in the coastal areas, is also strongly influenced by the quality of the input data. Therefore, detailed and accurate information about potential sources, local topographic and bathymetric data, are essential ingredients for effective tsunami site-specific analysis.

The accurate characterization of tsunami hazard at urban scale, in particular, requires detailed bathymetry and coastal topography data to accurately estimate tsunami wave amplitudes and inundation depths. The

local topography and the propagation direction of tsunami waves significantly influence the run-up effect of earthquake-induced tsunamis. Also, the presence of buildings and/or natural barriers (e.g. dunes and trees) may significantly affect the tsunami waves ingression, thus evidencing a relevant interconnection between hazard and exposure, which is critical for the adequate planning of metropolitan coastal areas. For further details about tsunami risk assessment for coastal infrastructures and urban settlements see Reis et al. (2022) and Hassan et al. (2020) and references therein.

3.1.3.1 Tsunami scenarios for the Adriatic sea

Tsunami hazard analysis, based on physical-numerical modelling of wide set of scenarios, is carried out for Italian coasts with the purpose of contributing to tsunami risk assessment and emergency management for selected urban and metropolitan areas. This research is developing in the framework of the RETURN project and, so far, it resulted in two scientific publications as Peresan and Hassan, (2022; 2024). These studies aim to update the existing tsunami hazard models for selected coastal cities; the obtained results can contribute to the definition of related emergency plans and can provide, in combination with other hazards (e.g. earthquakes), plausible scenarios as the base for developing storylines.

As far as tsunami emergency management is concerned, it is worth to recall that a National Alert System for earthquake generated tsunamis (SiAM – "Sistema Allertamento Maremoti") has been established in 2017 (Directive of the President of the Council of Ministers, 17 February 2017). Within this formal framework, the CAT-INGV ("Centro Allerta Tsunami", managed by INGV) operates at the Italian national level, with the aim of disseminating alert messages to the territory, including local authorities. Since 2017, various tsunamis have been assigned a "watch" alert level (i.e. red alert, with an offshore wave amplitude estimate >50 cm, and a run-up >1 m) by the CAT-INGV system, (e.g. 2nd May 2020, Crete; 30th October 2020, Aegean Sea; 6th February 2023, Turkey). Though ultimately resulting in false alarms, these alerts call for the need of developing suitable emergency plans, based on adequate tsunami inundation maps.

Such maps, however, are not yet available for several tsunami prone areas situated along the Italian coastal zone, particularly the Northeast Adriatic coasts between Trieste and Lignano, due to their peculiar bathymetric and topographic setting. The available tsunami probabilistic hazard estimates (e.g. NEAMTHM18 maps, Basili et al., 2020), in fact, are provided for sites located along the 50m depth isobaths. Usually, in order to calculate the run-up to the coastline (i.e. the maximum topographic height, compared to the mean sea level, reached by the tsunami wave during its ingression), an empirical coefficient (i.e. a multiplication factor) is applied to the maximum amplitude of the tsunami wave estimated along the 50 m isobaths (Tonini et al., 2021). In the Northern Adriatic and similar coasts, where the bathimetry is extremely shallow (well below 50 meters), the distance between these isobaths and the coastline is very large, and such an empirical relationship may well turn out inadequate. In addition, in the alert messages, an upper bound is not provided for the tsunami wave amplitude (or a run-up) in the area of interest. According to the mentioned SiAM directive, the accuracy and reliability of inundation data derived from existing probabilistic tsunami hazard estimates, can be improved by carrying out detailed investigations at local scale (e.g., municipal level and port areas), integrating its results with detailed studies through physical-numerical modelling. This is especially important for critical areas, which are characterised by the presence of strategic infrastructures, high population density, etc.

To assess tsunami hazard for the urban cities located along the northeast Adriatic coastal zone, a wide set of tsunami scenarios has been computed, considering the possible tsunamigenic sources as defined in the most updated database of seismogenic sources. Parametric tests have been performed as well, to account for seismic source variability and a localized high-resolution Digital Terrain Model (DTM), with a spatial resolution of 20 m, has been used as topographic and bathymetry dataset for the tsunami simulations. Specifically, these recent studies have been accomplished accounting for the recently updated DISS database of seismogenic sources in the Adriatic Sea, and considering different potential tsunamigenic sources of tectonic origin, located in three distance ranges from the areas of interest (namely at Adriatic-wide, regional and local scales). A nested grid of different resolution domains (i.e. 450m, 115m, and 20m) of topographic-bathymetric data have been adopted from open access and local sources. The large domain, with coarse bathymetry is taken from GEBCO-2020, while the smaller domain is taken from EMODnet and the 20m domain from Trobec et al., (2018).

The study by Peresan and Hassan (2024) aims to provide physically consistent tsunami hazard estimates, based on the modelling of tsunami waves propagation from a wide set of possible sources, to be considered in case an alert is issued by the CAT-INGV tsunami warning system. Accordingly, this multi-scenario analysis, which has been carried out for the Northeast Adriatic region, consists of two main parts.

In the first part only the possible tsunamigenic earthquake sources located within the Adriatic Sea have been considered, based on the recently updated DISS database (DISS-3.3 http://diss.rm.ingv.it/diss/) and following the tsunami decision matrix developed by CAT-INGV. According to the decision matrix, a seismogenic source is considered tsunamigenic, of potential weak local tsunami (distance ≤ 100 km), if it is capable of producing shallow offshore earthquakes of magnitude M≥6. Therefore, a database of local tsunamigenic earthquake sources of Mmax≥6 relative to our area of interest (i.e. the coastal area between Lignano and Trieste) and Mmax≥6.5 for regional (100 km < distance ≤ 400) and basin-wide (distance > 400 km) tsunamis, has been extracted from the DISS-3.3 database. The compilation of a related database of tsunami scenarios allows us to evaluate the potential tsunami hazard at different distances and serves as pre-computed scenarios in case a future tsunami alert is activated. In this way, in case of tsunamigenic earthquake occurrence, the results for best matched pre-computed scenario (in location and magnitude) can be identified, extracted and used for a quick response (see, for example, Figure 11). It is worth noting that, the maximum magnitude of most seismogenic sources within the DISS-3.3 was upgraded (i.e. generally increased), in a range of 0-1.7 magnitude unit relative to the previous DISS-3.2.1 version. Therefore, according to the updated DISS-3.3 a larger number of seismogenic sources turn out to be capable of generating tsunami, compared to the former DISS version used by Peresan and Hassan (2022), because magnitude increased for several sources. This might be regarded as a warning about the uncertainty on the magnitude of future events.

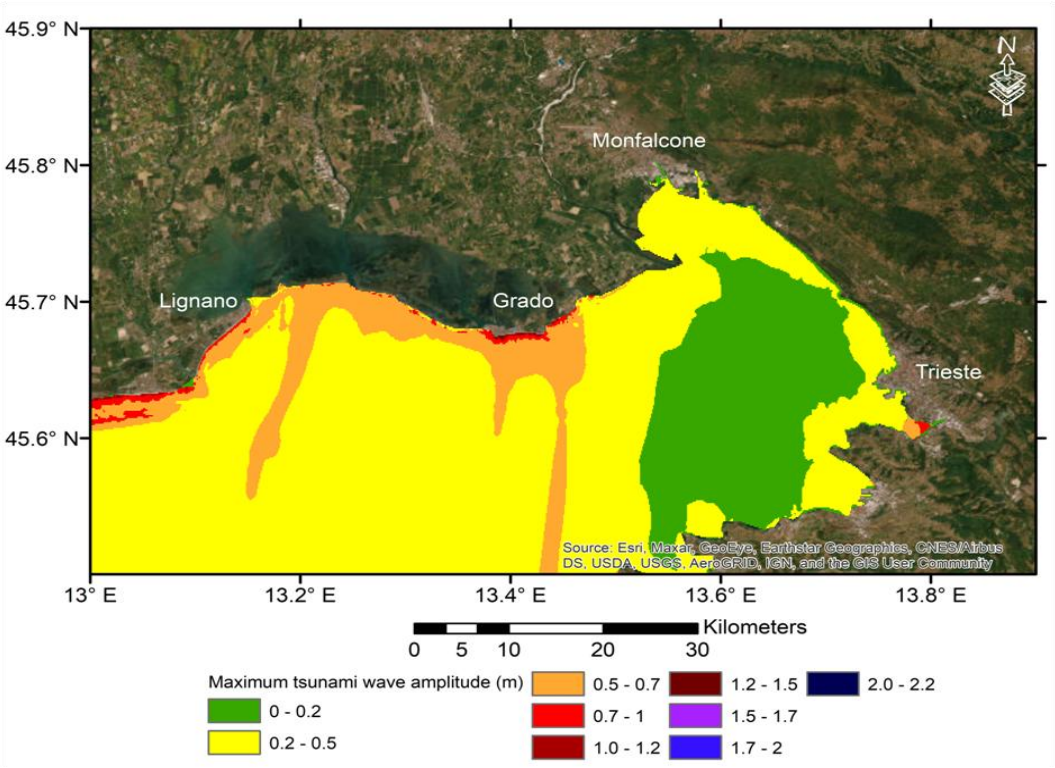

Figure 11. Map of the maximum tsunami wave amplitude computed for the regional tsunamigenic sources (Peresan and Hassan, 2024).

In the second part, the tsunami scenarios for possible very distant sources, located outside the Adriatic Sea, have been computed (hereinafter called basin-wide sources), from five main tsunamigenic earthquake zones: West Greece, Calabrian, West Hellenic, East Hellenic and Cyprian Arcs. The tsunami scenarios of maximum expected earthquake (based on historical seismicity or geological surveys) within each of these sources have been computed and an aggregated scenario has been extracted. Maps of maximum wave amplitude for aggregated scenarios at basin and area of interest scales are given for each tsunamigenic earthquake zone.

The obtained results show that basin-wide tsunamis from West Greece, Calabrian Arc and West Hellenic Arc should be carefully considered, because tsunamigenic earthquakes of Mmax>7.5 turn out capable to impact the Northeast Adriatic coast zone at orange alert level (amplitude up to 0.5 m) and even at red alert level (up to 0.8 m for a magnitude M=8.5 earthquake in the West Hellenic Arc), as inferred from the modelling. The scenarios computed for the East Hellenic and Cyprian Arcs, instead, provide amplitudes corresponding to information level (green alert level).

Further studies have been carried out recently for possible tsunamigenic earthquakes in Southern Adriatic, with a focus on the Montenegro-Albania source zones, and aimed at the assessment of expected inundation (Xhafaj et al. 2024) in Durres and other coastal municipality's locations in Albania. Tsunamigenic earthquake sources, associated with large events (M>7.5) in Southeastern Adriatic may have a significant impact also on Italian coasts (e.g. Apulia), with detectable ground-shaking and tsunami waves.

3.1.4 Volcanic hazard

Volcanic hazards pose significant risks to both human populations and infrastructure, particularly in regions with active or dormant volcanoes. These hazards encompass a range of phenomena, including lava flows, pyroclastic flows, ash fall, volcanic gas emissions, and lahars (see, for example, Papale, 2015). In addition to these immediate threats, volcanic activity can trigger long-term environmental changes, such as alterations in climate and ecosystems. Recent archaeology has revealed the dramatic impact of volcanic eruptions on civilizations throughout history (e.g., Donovan, 2012).

Italy, situated on the collision boundary of the African and Eurasian tectonic plates, is home to several active volcanic systems, including Mount Etna, Stromboli, Vesuvius, and Campi Flegrei, making it one of the most volcanically active countries in the world. The country has experienced numerous eruptions throughout history, some of which have had devastating effects on populations and the environment. Mount Vesuvius, which famously destroyed the cities of Pompeii and Herculaneum in AD 79, remains a constant threat to the densely populated Naples metropolitan area. Similarly, Mount Etna, located on the island of Sicily, is one of the most active volcanoes in the world, with frequent eruptions that impact both local populations and air travel across Europe.

One of the most concerning volcanic systems in Italy is the Campi Flegrei caldera, located just west of Naples. This large volcanic area is known for its potential to produce highly explosive eruptions, with the last significant eruption occurring nearly 500 years ago in 1538. Campi Flegrei's activity is closely monitored by scientists, as the caldera has shown signs of unrest in recent decades, including ground deformation and increased seismicity. An eruption from Campi Flegrei could have catastrophic consequences for the millions of people living in the Naples region, as well as for the broader Mediterranean area.

Campi Flegrei is a supervolcano, a type of volcanic system capable of producing eruptions that are orders of magnitude larger than typical volcanic events. The caldera has a history of producing massive eruptions, with the most significant occurring around 39,000 years ago, known as the Campanian Ignimbrite eruption. This event is considered one of the largest volcanic eruptions in Europe and had a profound impact on the region, covering vast areas with volcanic ash and affecting the climate.

Today, the potential for another large-scale eruption at Campi Flegrei is a major concern. The caldera is located beneath densely populated urban areas, and even a moderate eruption could result in widespread destruction, loss of life, and economic disruption. Furthermore, the volcanic gases released during an eruption could contribute to atmospheric pollution, exacerbating air quality issues in the region. Given the potential scale of impact, Campi Flegrei is considered one of the most dangerous volcanic systems in the world, and continuous monitoring is essential for early warning and evacuation planning.

Monitoring volcanic activity has greatly advanced with the use of radar and satellite remote sensing technologies (Singh and Bartlett, 2018). Synthetic Aperture Radar (SAR), particularly through Interferometric SAR (InSAR), enables precise measurement of ground deformation by detecting surface changes, even in cloud-covered or remote regions. These surface deformations often indicate magma movement beneath a volcano, helping predict potential eruptions. Satellite remote sensing extends this capability by using various sensors to monitor volcanic gases, thermal emissions, and ash plumes. Thermal Infrared (TIR) sensors detect heat anomalies, while multispectral and hyperspectral imaging captures gas

emissions like sulfur dioxide (SO_2). This data is crucial for monitoring volcanic activity and assessing associated risks. Combining radar monitoring with satellite data allows for continuous observation of volcanoes worldwide, even in challenging environments. The ability to monitor deformation, thermal activity, and gas emissions from space, regardless of weather conditions, enhances early warning systems and disaster preparedness in volcanic regions. These technologies work together to provide a comprehensive understanding of volcanic behavior, supporting effective hazard assessment and timely responses.

While volcanic activity is primarily driven by geological processes, climate change can influence volcanic hazards in indirect ways. For instance, climate change can exacerbate the secondary effects of volcanic eruptions, such as landslides and lahars. Melting glaciers and permafrost can destabilize volcanic slopes, increasing the likelihood of landslides during or after an eruption. Additionally, changes in precipitation patterns due to climate change can enhance the potential for lahars, which are destructive mudflows composed of volcanic material and water. This is particularly relevant for volcanic regions like Italy, where shifts in climate could affect the behavior of volcanic systems and the severity of volcanic hazards. Furthermore, large volcanic eruptions can have significant effects on the global climate. The release of sulfur dioxide and ash into the atmosphere during a major eruption can lead to a temporary cooling effect, known as volcanic winter, as these particles reflect sunlight away from the Earth's surface. Historical examples include the eruption of Mount Tambora in 1815, which caused the "Year Without a Summer," leading to widespread crop failures and food shortages. In the context of climate change, understanding the interplay between volcanic activity and atmospheric processes is crucial for predicting and mitigating the broader environmental impacts of volcanic eruptions.

Volcanic hazards present a serious risk to Italy, particularly in regions like Campi Flegrei, where the potential for a large-scale eruption poses a significant threat to millions of people. The intersection of volcanic activity with climate change adds complexity to hazard assessments, as changing environmental conditions can influence both the frequency and severity of volcanic events. Continuous monitoring, risk assessment, and preparedness planning are essential for mitigating the impacts of volcanic hazards and protecting communities in Italy and beyond. The ongoing study of volcanic systems, such as Campi Flegrei, is critical for advancing our understanding of these powerful natural phenomena and enhancing resilience in the face of future eruptions.

3.1.4.1 The Campi Flegrei case study: monitoring and simulation strategies

Volcanic eruptions pose significant risks to life, infrastructure, and the environment. In response to these challenges, the project leverages state-of-the-art technologies and methodologies to enhance the monitoring and assessment of volcanic hazards, including short-term and long-term monitoring strategies, probabilistic hazard assessments, and the development and application of sophisticated numerical simulations.

The Campi Flegrei caldera, located near Naples, Italy, represents one of the most hazardous volcanic regions in the world due to its potential for catastrophic eruptions and its proximity to densely populated areas. Detailed monitoring and advanced simulation techniques are essential for mitigating the risks posed by this supervolcano. To address these challenges, a combination of real-time monitoring strategies and advanced simulation tools, such as the SPEED platform, are being employed to assess and predict volcanic hazards in the Campi Flegrei area.

The monitoring strategies for Campi Flegrei employ an integrated approach that utilizes a variety of tools and methodologies to form a comprehensive understanding of ongoing volcanic activity. The main components of this strategy include:

- Areal Monitoring (short term activity). Short-term monitoring focuses on immediate, real-time data acquisition to detect early signs of volcanic activity that could lead to eruptions. This aspect of the project utilizes drones equipped with sensors to measure gas emissions and radionuclide levels at active fumaroles. These drones offer a versatile and dynamic method to access difficult terrains and provide continuous monitoring. This method allows for the collection of detailed data on volcanic gases, which are key indicators of volcanic unrest (e.g., Figure 12). By analyzing gas species and radionuclides, scientists can detect changes in the volcanic system that may precede an eruption.

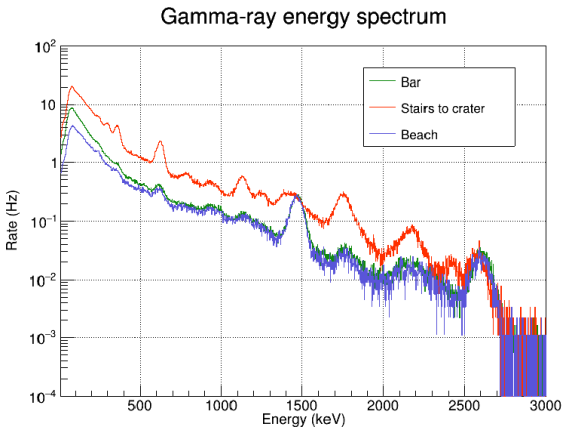

Figure 12. Example of results from aerial monitoring activities.

- Probabilistic Hazard Mapping (long term activity). In contrast to the immediate focus of short-term monitoring, long-term strategies involve the creation of detailed hazard maps and the development of models that predict the likelihood of various volcanic impacts over extended periods (e.g., Figure 13). These maps are based on historical eruption data from active volcanoes and are crucial for community planning and long-term risk management. They include maps displaying exceedance percentiles of impact parameters, offering a probabilistic assessment that helps in understanding the range and likelihood of potential hazards, and a high-resolution grid system that models impact parameters at a 250-meter resolution, providing unparalleled detail that aids in precise planning and response strategies.

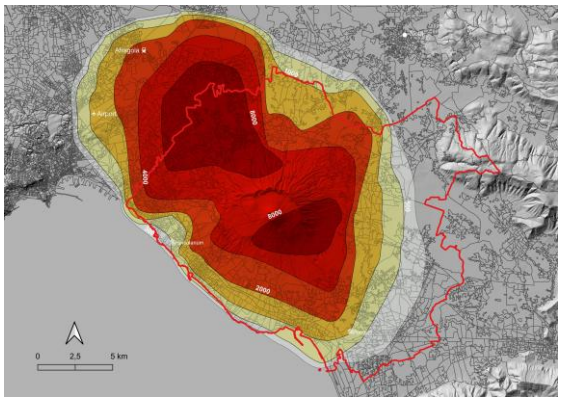

Figure 13. Example of maps of exceedance percentile of impact parameters from past eruptions.

- Transfer to Vulnerability: this activity serves as a critical link between volcanic hazard assessments and the broader Transversal Spoke 1 (TS1) objectives. It aims to produce high-resolution grid maps (250-meter resolution) that illustrate potential impacts from volcanic hazards, such as structural damage, economic losses, and infrastructure disruptions (see, for example, Figure 14). By translating volcanic intensity measures into actionable impact parameters, these maps support disaster preparedness and risk mitigation. This activity integrates data from various sources, contributing to dynamic vulnerability models, which are essential for TS1's goal of enhancing community resilience and guiding decision-making processes.

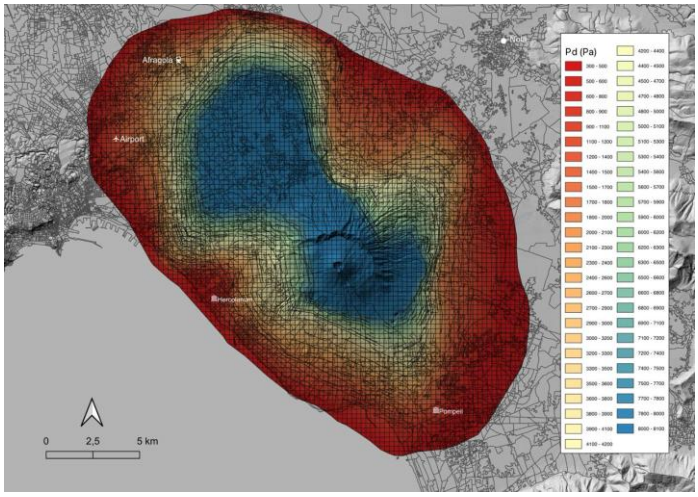

Figure 14. Example of high-resolution grid maps illustrating potential impacts from volcanic hazards.

The SPEED (SPectral Elements in Elastodynamics with Discontinuous Galerkin; https://speed.mox.polimi.it/) simulation platform plays a crucial role in enhancing the understanding of seismic and volcanic hazards in the Campi Flegrei region. Physics-Based Simulations (PBS) performed by SPEED are "source-to-site" numerical simulations that model the propagation of seismic waves from the earthquake source to the affected site. These simulations take into account various factors, including seismic source, the propagation path, and localized geological features or/and structures.

SPEED is a physics-based numerical simulation tool designed to model seismic wave propagation from the earthquake source to the affected area, considering various geological features and structures along the way (e.g., Smerzini et al., 2024). The development of numerical models for simulating wave propagation in seismic regions has tremendously evolved in the past ten years. SPEED is a certified and rigorous numerical software for the reliable prediction of near-fault ground motions and seismic response of strategic structures in complex three-dimensional scenarios. It is based on the Discontinuous Galerkin Spectral Element method, a non-conforming domain decomposition technique combining the flexibility of discontinuous Galerkin finite elements with the accuracy of spectral techniques. SPEED naturally allows a non-uniform polynomial degree distribution (p-adaptivity), as well as a locally varying mesh size (h-adaptivity). Such a built-in flexibility is mandatory in complex two- and three-dimensional problems featuring multi-scale phenomena.

The use of PBS is motivated by the need to address limitations in traditional seismic data, such as: incomplete datasets, with limited or sparse accelerometric records that do not fully capture all potential seismic scenarios; area-specific ground motions, with the need to include both source characteristics and local geological features (e.g., volcanic areas, deep basins, near-source). PBS appears able to provide detailed ground motion predictions, including time-histories (recorded ground motions over time), spatial variability (changes in ground motion intensity across different areas), and permanent ground displacement (long-term changes in the ground due to seismic events).

Starting with the hypocentral locations and focal mechanisms of earthquakes in the Campi Flegrei area (Figure 15), a detailed numerical model is constructed using the SPEED platform. This model integrates three-dimensional velocity structures (Vp and Vs), which are derived from tomography data (Figure 16), offering a detailed representation of the subsurface geology. The numerical model incorporates all available geophysical and seismotectonic information, ensuring a comprehensive and accurate simulation environment (Figure 17).

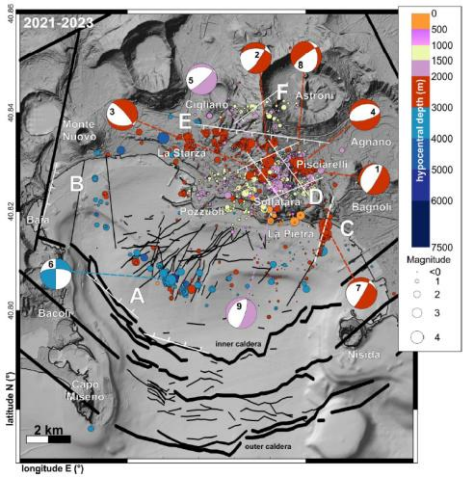

Figure 15. Example of map concerning hypocentral location and focal mechanisms of earthquakes in the Campi Flegrei area.

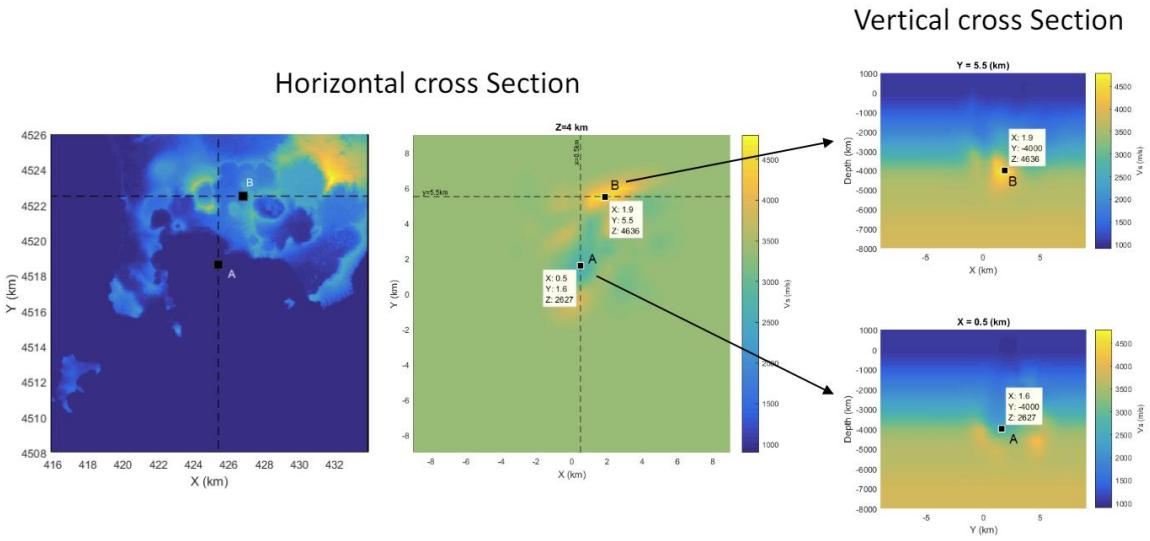

Figure 16. Example of a numerical map depicting 3-D velocity structures from tomography data.

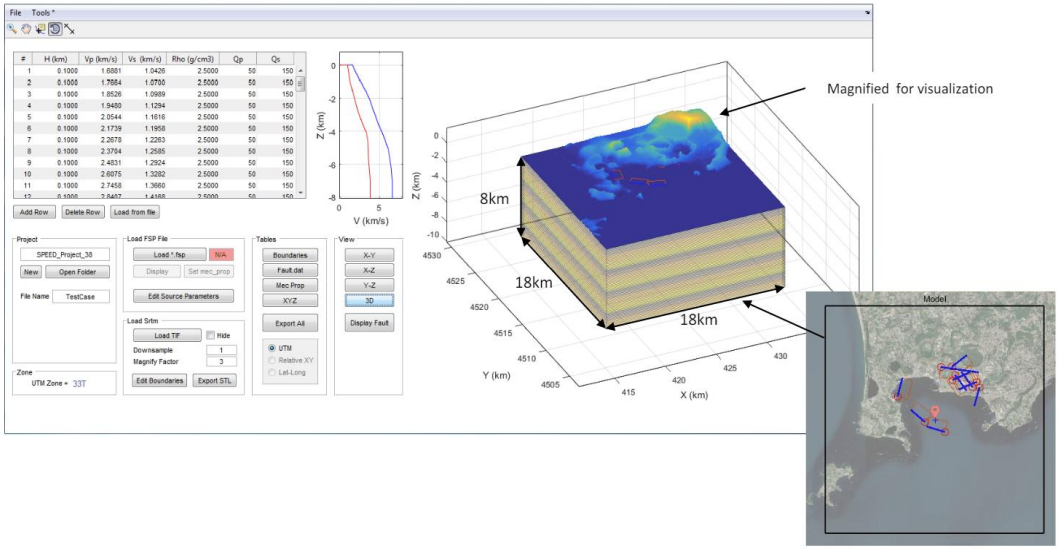

Figure 17. Illustration of the development for the SPEED numerical model.

To validate the simulations, the results are compared against recorded seismic events, which helps refine the model and enhance its reliability. Once validated, the SPEED platform allows for the simulation of larger magnitude earthquakes, providing critical insights into potential future seismic hazards. Additionally, SPEED enables the simulation of earthquake sequences (i.e., clusters of related seismic events that occur over short periods). These sequences are particularly significant in volcanic regions like Campi Flegrei, where seismic activity often precedes or accompanies volcanic eruptions. This capability is crucial for understanding the complex interactions between seismic and volcanic processes, ultimately supporting risk assessments and emergency preparedness efforts in this highly dynamic region.

The SPEED platform is integrated with real-time hazard assessment systems, enabling operational earthquake forecasting and early warning systems (EEW). By simulating earthquake scenarios and sequences in real-time, the platform helps authorities predict the impact of seismic events and make informed decisions about evacuations and other protective measures. One of the challenges in seismic hazard assessment is accounting for uncertainties in the data and models. The SPEED platform incorporates uncertainty analyses by using a probabilistic approach to seismic hazard modeling. This allows for a range of possible outcomes to be considered, providing a more robust assessment of the risks. In addition to hazard assessment, SPEED can be used to develop dynamic vulnerability models that consider area-specific ground motion inputs and earthquake sequences. These models help assess the structural response of buildings and infrastructure to seismic events, providing critical information for risk and resilience assessments.

The integration of detailed monitoring strategies with advanced simulation platforms like SPEED is essential for managing the complex volcanic and seismic risks in the Campi Flegrei region. By combining real-time data collection with sophisticated numerical modeling, these tools provide a comprehensive approach to hazard assessment and disaster preparedness, helping to protect the millions of people living in the shadow of this supervolcano.

3.2 Hydraulic hazards

3.2.1 Coastal vulnerability in urban areas

Coastal cities are among the most exposed areas to climate change, as they may suffer from several effects it triggers, such as rising sea levels (Frederikse, 2020), more frequent storms (Lira-Loarca, 2022), and increasing coastal erosion (Ranasinghe R. , 2016) threatening their infrastructures and communities. Besides, coastal population have constantly growth over the past decades (e.g., (Rodriguez, 2020)), and such trend is expected to hold in the future (Neumann, 2015). The combination of increasing human pressure and the exacerbation of the environmental stressors make coastal settlements extremely vulnerable, and require to undertake proper countermeasures with the utmost urgency.

The major threats to coastal assets and urban areas can be grouped into “hydrodynamic” and “morpho-dynamic” processes, i.e., physical processes that ultimately shape the land-sea interface. The former concern the analysis of wave-related phenomena and currents, wave propagation from offshore to nearshore, mass and energy fluxes, and wave-structure interactions. Coastal morpho-dynamic, on the other hand, is associated to the evolution of coastal and seafloor morphology, sediment erosion and deposition processes, and the complex interactions between waves and sediments. Alle these processes evolve on various spatial and temporal scales, in response to forcing factors such as wind, tides, and sea-level variations and, being closely tied to coastal flooding and erosion events, are addressed below.

Ocean waves

Ocean waves are initially triggered by the stress exerted by the wind over the sea surface. If the processes is free to evolve over a long enough time span, a full wave is generated and put into motion, i.e., it starts to propagate along the wind direction in the generation area. The simplest way to describe a sea wave is through the Airy model, which assumes that a wave profile (η) can be described through a linear first-order sinusoidal function, as the one shown in Figure 18.

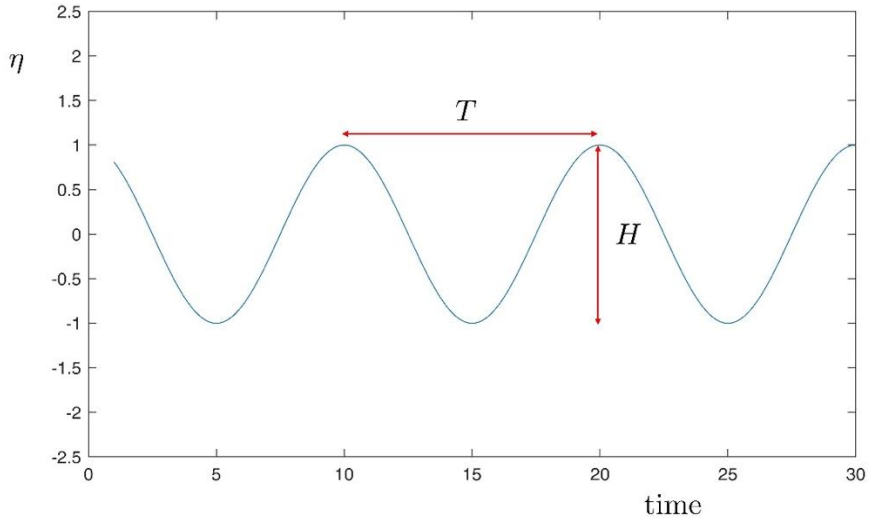

Figure 18. Water level profile (η) according to the Airy wave theory.

The main parameters describing the wave profile are:

- wave height: it is defined as the distance between the wave crest and the wave through (*H* in the sketch of Figure 18); it is measured in m.
- Wave period: is the time elapsed between the passage of two successive crests (or, equivalently, two successive throughs; note the Airy wave is symmetric); it is usually referred to as *T* and it is measured in seconds.
- Wave direction: usually expressed according to the Nautical convention, i.e., directions are defined clock-wise starting from 0°N (or 360°N), which indicate waves travelling south.

All secondary parameters, such as wave celerity, wave energy, etc., relevant for coastal processes, can be derived based on the above mentioned quantities.

As waves propagate from deep water towards the shore, they encounter gradually shallower depths; such interaction can affect both wave directions and wave heights. Indeed, owing to wave refraction wave crests tend to orientate parallel to the shore regardless the off-shore incoming direction; on the other hand, through the shoaling effect the wave height is increased in the very proximity of the water edge foreshore (Sorensen, 1993). The above effects are crucial, as they eventually trigger the wave breaking, which occur when the wave becomes unstable and therefore dissipates its energy. Wave breaking can take place in different forms, depending on both waves and seabed characteristics, as shown in Figure 19.

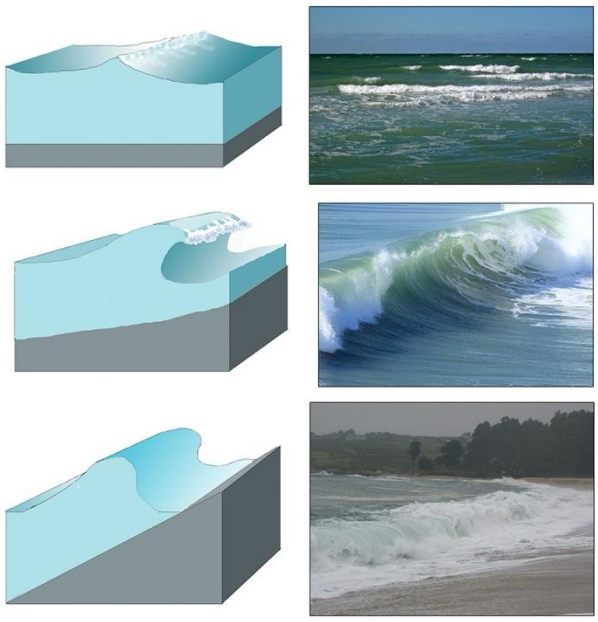

Figure 19. Three different types of breaking. From top to bottom: spilling; plunging; surging. Adapted from Introduction to Oceanography by Paul Webb under a Creative Commons Attribution 4.0 International License.

The breaking condition associated to the local bathymetry is usually estimated via a simple parametric formula (M'Cowan, 1893):

$$\frac{H}{h} = 0.78 \quad (1)$$

In other wors, Eq. (1) states that e.g., a wave exceeding 80 cm at 1 m local depth (referred to as *h*) will break. While the model above is rather simple and cannot describe in full details the breaking phenomena, it helps to derive a prompt estimate of the breaking locations depending on local bathymetry and waves characteristics, which is crucial in turn for a plethora of reasons. First, breaking triggers set-up and run-up on the coast, which are key processes influencing shoreline flooding. The former is the increase in mean water level due to the onshore transport of mass by breaking waves, that push the water column piling up water in front of the breaking section; the latter refers instead to the maximum vertical extent of wave action on a beach or coastal structure, occurring when waves rush up the shore after breaking. The resulting water level elevation define how far inland the wave can reach, and it is therefore pivotal in assessing flooding hazard (Bosboom, 2021).

Second, wave breaking is responsible of the generation of littoral currents, also known as long-shore currents, which transport sediments along the shore and ultimately influence the morphology of beaches and dunes. As a matter of fact, the dynamics of littoral currents and sediment transport have various consequences on coasts. For example, coastal erosion can occur in some areas where the littoral current removes sediments more rapidly than they are deposited, leading to land loss and coastline regression, which endangers infrastructure and natural habitats. In this respect, beaches can be extremely vulnerable to changes in external sediment inputs, which may occur in particular when river discharges are impeded or sediments are trapped either for mining activities or hydropower production (see for instance (De Leo,

2017)). This particularly applies to beach that are naturally *erosive*, meaning that they tend to retreat if not properly nourished. A easy-to-use criteria to establish the trend of a coast is provided by (Larson, 1989), as outlined in the sketch below (Figure 20):

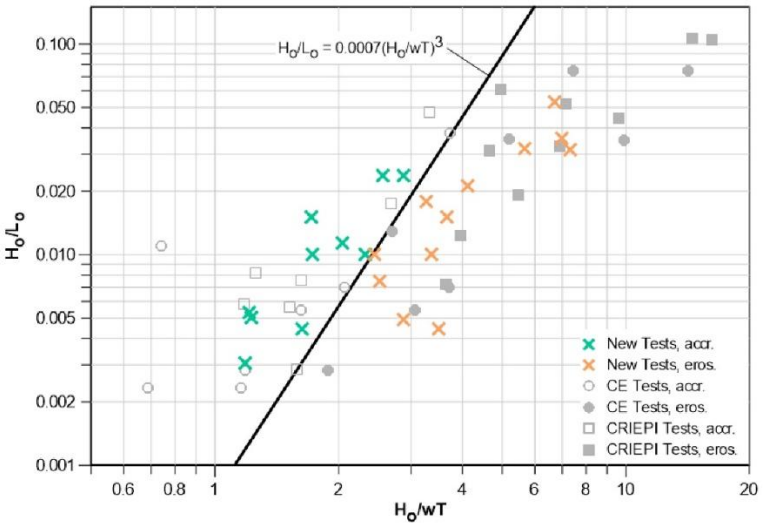

Figure 20. Larson and Kraus criterion. Points on the left (right) side of the solid black line indicate an accretive (erosive) beach. Adapted from (Samaras, 2024) under the CC BY 4.0 license.

where L_0 indicate the average wave length off-shore (the subscript 0 denotes off-shore conditions), while w is the settling velocity that embeds the local grain size distribution.

In other words, if a beach is erosive, the lack of sediment inputs will inevitably yield a shoreline retreat, especially in the case of increased environmental stressors, undermining in turn the coastal assets and infrastructures.

Sea Level Rise

While the processes above naturally occur along the shores, the extent to which they can endanger the coastal settlements can be greatly magnified by effect of sea level rise. Imagine a coastal section characterized by a certain slope, referred to as $\tan\beta$, and assume that wave breaking usually occur at a distance x from the shoreline edge. It is easy to demonstrate that, for a Δs increase in water level, the breaking section will lie closer to the coast, by an amount equal to $\Delta s/\tan\beta$. For a 10:1 slope, a 50 cm increase would lead to a 20 m shift of the breaking section toward the coast. In turn, this would greatly amplify the risk of flooding for coastal assets and settlements.

In addition, the increase in mean sea level drives a reshaping of coastal section, with increasing erosion in the proximity of the shoreline edge (see Figure 21).

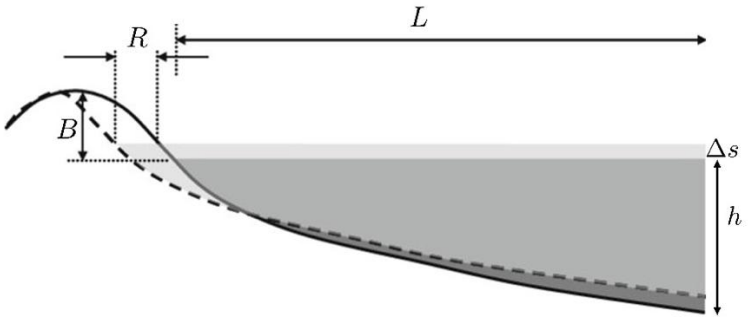

Figure 21. Schematic representation of the Bruun rule. Adapted from (Ranasinghe R. C., 2012) under the terms of the Creative Commons Attribution Noncommercial License (https://creativecommons.org/licenses/by-nc/2.0).

The easiest model aimed at describing this effect is the Brunn rule (Bruun, 1988) , which reads:

$$R = \frac{\Delta s \times L}{h+B} \quad (2)$$

Where R is the shoreline recession; h is the depth beyond which no sediment transport occurs and B is the berm or dune height above the mean sea level. Eq. (2) allows to promptly understand the coastal section realignment due to sea level rise, although it should not be used quantitatively owing to its simplicity (Cooper, 2004).

There is a wide consensus among the scientific community on the main causes of sea level rise, i.e., the melting of glaciers and ice sheets, and the thermal expansion of seawater, the discussion of which falls beyond the scope of the present document. Table 3 and Figure 22 report the SLR change estimates for the Mediterranean region under the SSP5-8.5 scenario for different temporal periods.

Table 3. SLR change in meters under SSP5-8.5 relative to 1995-2004 in the Mediterranean Region (source: IPCC WG1 Atlas).

Period	Scenario	Median (meters)	P25 | P75	P10 | P90	P5 | P95
Near Term (2021-2040)	SSP5-8.5	0.1	0.1 | 0.2	0.1 | 0.2	0.0 | 0.2
Medium Term (2041-2060)	SSP5-8.5	0.3	0.2 | 0.3	0.1 | 0.4	0.1 | 0.4
Long Term (2081-2100)	SSP5-8.5	0.7	0.5 | 0.8	0.4 | 1.0	0.4 | 1.0

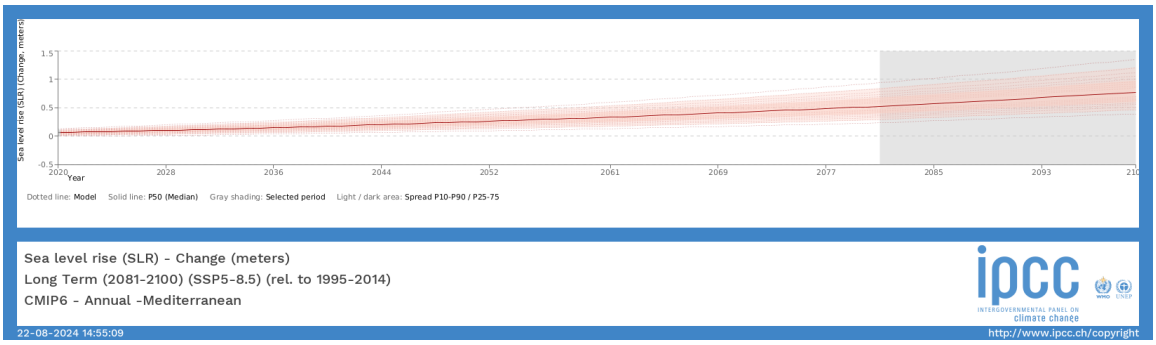

Figure 22. SRL change in meters for the scenario SSP5-8.5 and period 2020-2100 with the long-term projection highlighted. Source: IPCC WG1 Atlas

For more details and the state-of-the-art worldwide projections according to different emission scenarios, the reader is referred to https://interactive-atlas.ipcc.ch and https://sealevel.nasa.gov/ipcc-ar6-sea-level-projection-tool

Tides

Tides are the regular rise and fall of sea levels caused primarily by the gravitational forces exerted by the celestial bodies along with the rotation of the Earth. Being deterministic signals, tidal waves can be easily predicted (Codiga, 2011), and are therefore not directly relatable to climate change, even though significant though small trends in the astronomic forcing have been quantified in previous literature (Woodworth, 2010). However, tidal amplitudes can be greatly modified by anthropogenic activity that has led worldwide to wetland reclamation, channel dredging, and other environmental changes often modifying the tide damping (Talke, 2020) and tidal regimes. This can affect flooding hazard to a great extent (Li, 2021), and therefore implies to carefully account for tidal contribution as well.

All the above stressors feedback in a nonlinear manner, hence they can lead to extreme outcomes that wouldn't be predicted by looking at individual hazards in isolation. The frequency of occurrence of storm events is another crucial aspect, which can increase the disruptive potential of extreme phenomena (). Even more so in the framework of climate change, which is expected to increase the frequency and intensity of hazards, such as storms and heavy rainfall, and potentially exacerbate the occurrence of compound events making this a growing concern.

3.2.1.1 Coastal risk definition

Risk is the potential for adverse consequences for human or ecological systems, recognising the diversity of values and objectives associated with such systems and it is the result of the combination of a hazard, the vulnerability of a system, and the level of exposure to it (Figure 23).

Risk provides a framework for understanding the increasingly severe, interconnected and often irreversible impacts of climate change on ecosystems, biodiversity, and human systems; differing impacts across regions, sectors and communities; and how to best reduce adverse consequences for current and future generations.

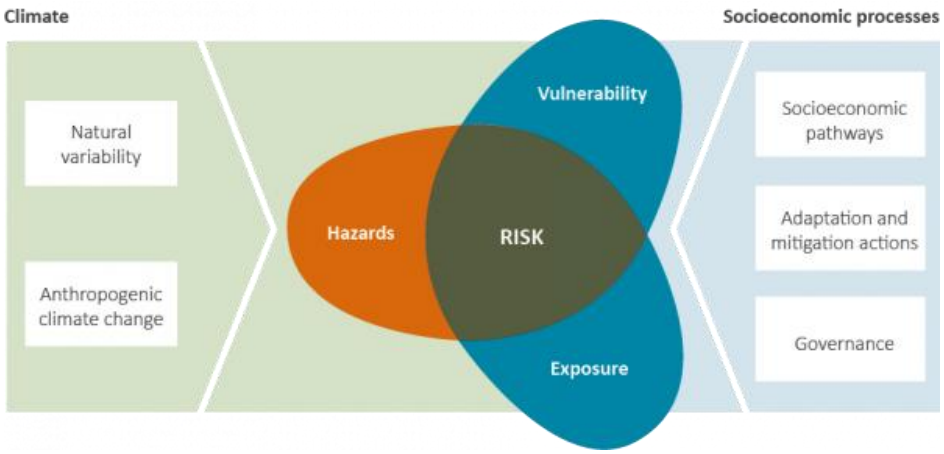

Figure 23. Risk definition (source: IPCC WG2)

Regional risks for increasing levels of global warming: Europe and Mediterranean

The main identified risks for the Europe and Mediterranean regions, under a changing climate, can be summarized as (Figure 24):

- Risks to people, economies and infrastructures due to coastal and inland flooding.
- Stress and mortality to people due to increasing temperatures and heat extremes.
- Marine and terrestrial ecosystems disruptions.
- Water scarcity to multiple interconnected sectors.
- Losses in crop production, due to compound heat and dry conditions, and extreme weather.

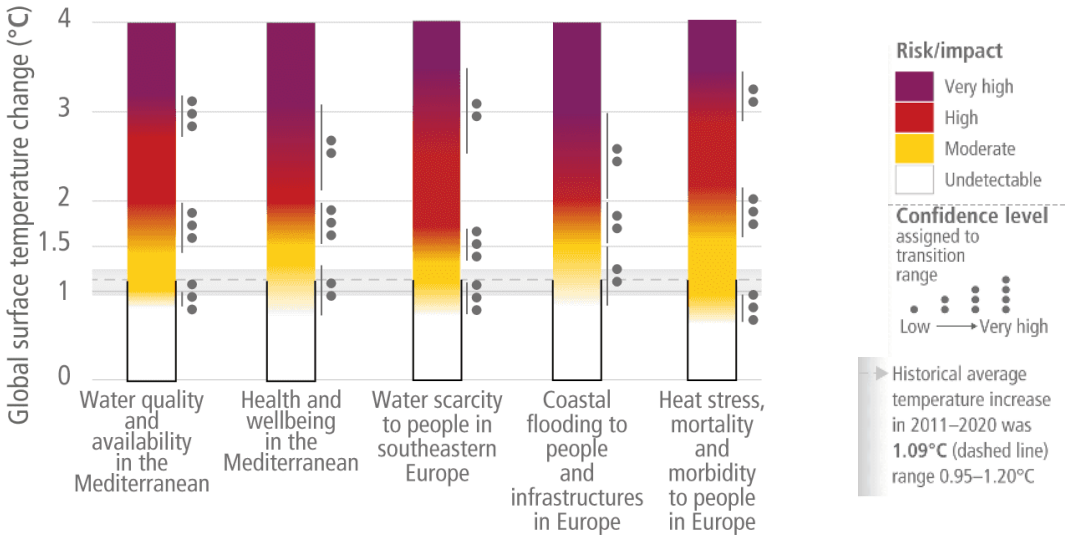

Figure 24. Main risks in the European and Mediterranean region according to different global surface temperature change levels. (source: IPCC WG2)

3.2.2 Fluvial floods

Fluvial floods, which occur when rivers overflow their banks due to excessive water from rainfall or snowmelt, are a significant threat to urban areas. Urbanization intensifies these hazards by altering natural hydrological processes, while climate change exacerbates the frequency and severity of flood events.

Fluvial floods pose high socio-environmental impacts. In peri-urban areas, floods can inundate farmlands, resulting in crop loss, soil erosion, and reduced agricultural productivity. Although agriculture is less prominent in urban cores, urban flooding can still impact food supply chains (Jonkman & Kelman, 2005). Floodwaters can destroy roads, bridges, buildings, and utilities, disrupting daily life and economic activities. Urban areas, with their dense infrastructure, are particularly vulnerable to such damage (Kundzewicz et al., 2013). Flooding can also modify habitats, affecting flora and fauna. In urban areas, this might involve green spaces, parks, and riverbanks that serve as important ecological niches (Tockner et al., 2002). Moreover, flooding can also affect water quality, since floods can transport pollutants, including sediments, nutrients, and contaminants, into water bodies. Urban runoff often contains higher levels of pollutants due to industrial and residential waste (Meybeck, 2003).

The text below summarizes findings from relevant literature on the complex factors contributing to fluvial flood hazards. It also emphasizes the importance of adopting a multifaceted and adaptive approach to flood risk management. This approach aims to enhance urban resilience in response to the increasing environmental challenges.

3.2.2.1 Urbanization and Fluvial Flood hazards

Impact of Impervious Surfaces on Hydrology

Urbanization leads to the creation of impervious surfaces such as roads, rooftops, and pavements, which dramatically reduce the infiltration of rainwater into the soil. The increased runoff flows directly into river systems, raising water levels more quickly than in natural environments. According to Ochoa-Rodríguez et al. (2015), in urbanized catchments, the peak discharge can increase by 30-50% compared to natural catchments, significantly heightening the risk of fluvial floods . These effects are particularly pronounced in densely populated cities where impervious surfaces cover a large proportion of the land.

Urban Expansion and Loss of Natural Floodplains

The expansion of urban areas often encroaches upon natural floodplains, which serve as critical buffers during flood events by temporarily storing excess water. When these areas are developed, their ability to mitigate flood risks is diminished. The conversion of floodplains into urban land uses not only increases the volume of water flowing into rivers but also reduces the overall storage capacity of the watershed (Patro et al., 2019). This combination of factors leads to higher and more frequent flooding in urbanized regions.

Bates et al (2015) showed how land use and land cover (LULC) changes have influenced flood risk in the U.S. over time, increasing flood frequency and severity and called for sustainable land-use practices and better urban planning to mitigate these impacts.

Effect of Urban Heat Islands on Localized Rainfall

Urban heat islands (UHIs), where cities are significantly warmer than their surrounding rural areas, can influence local weather patterns, including rainfall intensity (UHIs are described in Section 2.4.1). According to Zhang et al. (2018), UHIs can increase the likelihood of heavy localized rainfall, contributing to a higher hazard of urban flooding. The study also pointed out that the interaction between UHIs and fluvial systems can exacerbate flooding by increasing the volume and intensity of runoff entering rivers.

Channelization and River Engineering

Urban development frequently involves the modification of river channels to protect infrastructure, control water flow, and prevent floods. However, these interventions often disrupt natural hydrological processes, leading to unintended consequences. For instance, channelization, which involves straightening and deepening river channels, can increase the speed of water flow, reducing the time available for flood warnings and increasing the severity of downstream flooding (He et al., 2018). Wohl et al. (2015) emphasized that engineered rivers lose their natural ability to dissipate flood energy, resulting in more destructive floods downstream.

Complex Urban Hydrology

Urban hydrology is complex due to the interplay between natural watercourses and man-made drainage systems. This complexity can make it difficult to predict and manage flood risks effectively. The work by Roux et al. (2017) underscores the challenges of managing urban watercourses that have been heavily modified by infrastructure such as storm drains, culverts, and levees. These structures can create bottlenecks during heavy rainfall, leading to unexpected flooding in otherwise considered low-risk areas.

3.2.2.2 Climate change and Fluvial Flood hazards

Increased Precipitation Intensity and Frequency

Climate change alters global precipitation patterns, leading to more intense and frequent rainfall events. The IPCC reports that many regions, particularly those in mid to high latitudes, are experiencing increased extreme precipitation events, directly contributing to fluvial flooding risks. Arnell and Gosling (2016) examined the implications of these changes on river flood risks globally, noting that urban areas are particularly vulnerable due to their high population densities and economic importance. The study emphasized that even small increases in rainfall intensity could lead to significant flooding in cities with inadequate drainage systems.

Rising Temperatures and Snowmelt-Driven Floods

In addition to precipitation, rising global temperatures are causing earlier and more rapid snowmelt in mountainous regions, contributing to fluvial floods. Sorg et al. (2014) investigated the impacts of climate-induced snowmelt on river flooding, particularly in urban areas downstream of mountain ranges. The study found that cities reliant on snow-fed rivers are likely to experience earlier and more severe flooding events as snowmelt occurs earlier in the year, coinciding with spring rains. This overlap can overwhelm river systems, leading to significant urban flooding.

Sea Level Rise and Compound Flooding

Coastal cities are facing the dual threat of fluvial flooding and sea level rise, which can exacerbate the impacts of river floods. A study by Brown et al. (2018) highlighted the phenomenon of compound flooding, where high river flows coincide with storm surges or high tides, leading to severe floods in urban coastal areas. The research indicated that as sea levels continue to rise, the risk of compound flooding will increase, posing a significant threat to low-lying urban areas.

3.2.2.3 Case studies of Fluvial Flooding

Urban Flooding in Asia

Southeast Asia is one of the most flood-prone regions in the world, with urban areas such as Bangkok, Jakarta, and Manila frequently experiencing severe fluvial floods. A study by Tanoue et al. (2016) explored the socio-economic impacts of fluvial flooding in these cities, finding that rapid urbanization and poor land-use planning are significant contributors to the region's flood risk . The study also highlighted that many of these cities lack adequate infrastructure and flood management systems, exacerbating the impacts of floods on vulnerable populations.

The annual monsoon season in South Asia often leads to severe river flooding. The 2017 South Asian floods affected millions of people, demonstrating the need for improved flood forecasting and infrastructure resilience (Hirabayashi et al., 2013).

In July 2021, the city of Zhengzhou in Henan province experienced record-breaking rainfall, leading to severe urban flooding. The flooding disrupted public transportation, caused extensive damage to infrastructure, and resulted in numerous fatalities. The event underscored the challenges of managing urban floods in rapidly growing cities and the importance of resilient urban planning (Wu et al., 2021).

Fluvial Flooding in US

The 2008 Mississippi River floods were one of the most significant flood events in recent U.S. history. Extensive flooding affected several states, including Iowa, Illinois, and Missouri, leading to widespread damage to agriculture, infrastructure, and communities. Neal et al (2013) analyzed the hydrological and meteorological conditions leading to the 2008 floods. The study highlighted that a combination of above-average precipitation, rapid snowmelt, and saturated soils contributed to the severity of the flooding.

Houston, Texas, has experienced frequent and severe urban flooding due to its flat topography, extensive urbanization, and complex river systems. The 2015 Memorial Day flood was a particularly devastating event, with significant rainfall leading to the overflow of the Buffalo Bayou and other local rivers. Brody et al. (2018) found that rapid urbanization, including the construction of impervious surfaces, had significantly increased the flood risk in Houston.

The Northeast U.S. has seen an increase in the frequency and intensity of flood events, driven in part by changing climate conditions. Cities like New York, Boston and New Orleans are increasingly vulnerable to both fluvial and coastal flooding. Research by Brody et al. (2013) focused on the 2011 Mississippi River floods, which caused widespread damage in cities along the river. The study emphasized the role of urbanization and floodplain development in exacerbating flood risks and called for more integrated flood management strategies that consider both structural and non-structural measures.

The Red River Basin, spanning North Dakota, Minnesota, and parts of Canada, is highly susceptible to flooding due to its flat topography and snowmelt-driven river systems. The region has experienced several major flood events, including the catastrophic 1997 Red River flood. Pinter et al. (2015) examined the long-term flood management strategies in the Red River Basin, focusing on the balance between structural defences, such as levees, and non-structural measures, like floodplain restoration. The study found that levees provide short-term protection but can also exacerbate downstream flooding, while a more integrated floodplain management approach that combines both structural and ecological solutions is needed.

Flood Risk in European Cities

The 2002 and 2013 floods in Central Europe highlighted the vulnerability of the region to fluvial flooding. These events caused billions of euros in damage and led to significant changes in flood management policies (Kundzewicz et al., 2013).

European cities, particularly those along major rivers such as the Rhine, Danube, and Thames, are also at significant risk of fluvial flooding. A detailed analysis by Pinter et al. (2015) examined flood trends in European cities over the past century, noting an increase in flood frequency and severity due to a combination of climate change and urban expansion. The study pointed out that while European cities have invested heavily in flood defences, such as levees and flood walls, these structures may not be sufficient to cope with future flood risks without additional measures.

In July 2021, catastrophic flooding affected parts of Germany and Belgium, resulting from unprecedented rainfall. Rivers such as the Ahr and the Meuse overflowed, causing widespread destruction. This event highlighted the vulnerabilities of urban areas, where dense infrastructure exacerbated the damage. The floods resulted in over 200 deaths and significant economic losses, emphasizing the need for robust flood management and early warning systems (Kreibich et al., 2021).

Fluvial floods in Italy

The 2023 Emilia-Romagna Floods

In May 2023, the Emilia-Romagna region in northern Italy experienced one of the most devastating flood events in recent history. A combination of persistent heavy rainfall and the overflow of major rivers such as the Savio, Lamone, and Montone resulted in widespread flooding, leading to significant loss of life, displacement of thousands of people, and extensive damage to infrastructure and agriculture. Bianchi et al. (2024) analyzed the hydrological and meteorological factors contributing to the 2023 Emilia-Romagna floods. The study highlighted that the region received over 200 mm of rainfall in just 48 hours, which overwhelmed the capacity of local rivers and flood defenses. The researchers pointed out that the extreme weather conditions were exacerbated by climate change, with the region experiencing a trend towards more intense and frequent rainfall events. The study also emphasized the role of human activities, such as urbanization and land use changes, in increasing the flood risk by reducing the natural absorption capacity of the land. This analysis highlights the need for urgent measures to improve flood risk management in the region, including restoring natural floodplains, better land use planning, and enhancing early warning systems.

The 2020 Piedmont Floods

The Piedmont region in northwest Italy experienced severe flooding in October 2020, with heavy rainfall leading to the overflow of several rivers, including the Sesia, Tanaro, and Po rivers. This event was one of the most significant flood events in the region in decades, resulting in widespread damage and several fatalities. Pasquale et al. (2021) found that the floods were driven by a combination of extreme rainfall, which exceeded 600 mm in some areas over 48 hours, and the already saturated soil conditions from previous rains. The study highlighted the increasing frequency of such extreme weather events in the region, likely due to climate change, and emphasized the need for improved flood forecasting and early warning systems.

The 2014 Parma Floods

In October 2014, the Parma River in northern Italy overflowed its banks following an intense storm, leading to severe flooding in the city of Parma and surrounding areas. The floodwaters caused extensive damage to infrastructure, including roads, bridges, and residential buildings, and resulted in significant economic losses. A detailed case study by Rossi et al. (2016) revealed that the flood was exacerbated by inadequate maintenance of riverbanks and floodplains, as well as the lack of coordinated flood management across regional and local authorities. The authors recommended the implementation of integrated flood risk management strategies, including the restoration of natural floodplains and improved urban planning.

The 2018 Calabria Flash Floods

Southern Italy, particularly the Calabria region, is susceptible to flash floods due to its mountainous terrain and Mediterranean climate. In August 2018, a flash flood in the Raganello Gorge, caused by sudden torrential rain, led to the deaths of ten hikers and severe environmental damage. A study by Esposito et al. (2019) emphasized the role of intense, localized rainfall in triggering the flash flood, compounded by the region's steep topography. The study also highlighted the lack of effective early warning systems and public awareness, contributing to the high casualty rate. The authors suggested that better monitoring of meteorological conditions and developing real-time warning systems could help reduce the risk of similar disasters in the future.

The 2016 Florence Floods

In November 2016, the city of Florence experienced severe flooding due to the overflow of the Arno River, reminiscent of the devastating 1966 flood. The 2016 event, though less severe, still caused significant damage to the city’s historical heritage sites and infrastructure. Bonaccorso et al. (2017) focused on the hydrological response of the Arno River basin to prolonged heavy rainfall, which exceeded 200 mm in some areas. They concluded that while flood defenses have improved since 1966, the city remains vulnerable to extreme weather events, particularly in light of climate change. The authors recommended further strengthening of flood defenses and the implementation of adaptive management practices to protect the city's cultural heritage.

The 2013 Sardinian Floods

In November 2013, Sardinia experienced one of its most severe flood events in recent history, primarily affecting the northeastern part of the island. The flood, caused by the passage of Cyclone Cleopatra,

brought unprecedented rainfall to the region, with some areas receiving more than 450 mm of rain in less than 24 hours, resulting in the deaths of 18 people and widespread destruction of property, infrastructure, and agriculture. Mossa and Rulli (2014) highlighted how the extreme rainfall led to the overflow of rivers causing significant flash flooding, also due to inadequate drainage systems, deforestation, and urban expansion in flood-prone areas.

The 2011 Liguria Floods

The Liguria region in northwest Italy was hit by severe flooding in October 2011, particularly affecting the Cinque Terre and the towns of Monterosso and Vernazza. The floods were caused by an intense storm that produced over 500 mm of rain in less than 6 hours, leading to flash floods and landslides. Cavaliere et al. (2013) identified the combination of extreme rainfall, steep terrain, and human activities, such as deforestation and unregulated construction, as key factors that exacerbated the flood's impact. The authors stressed the importance of sustainable land use practices and the restoration of natural vegetation to reduce flood risk in the region.

3.2.2.4 Mitigation and Adaptation strategies

Addressing fluvial flood hazards in urban areas requires an integrated approach:

1. Green Infrastructure and Nature-Based Solutions. Urban areas need to prepare for more frequent and severe flooding events due to climate change (Kundzewicz et al., 2019). Green infrastructure, including green roofs, rain gardens, permeable pavements, and urban wetlands, offers a sustainable approach to managing urban runoff and reducing flood risks. By enhancing the natural absorption of rainwater, these systems help delay and reduce the runoff volume entering rivers. Research by Fletcher et al. (2015) demonstrated that green infrastructure could reduce peak flood flows by 20-40% in some urban settings, making it an essential component of flood risk management in cities. Additionally, these solutions provide environmental co-benefits, such as improving urban air quality and biodiversity.
2. Enhancing Urban Drainage Systems. Updating and expanding urban drainage systems to handle the increased volume of water associated with extreme weather events is critical for reducing flood risks. Ochoa-Rodríguez et al. (2015) discussed the importance of using high-resolution rainfall data and advanced hydrological models to design more resilient urban drainage systems that can cope with contemporary and future flood scenarios. The study suggested that incorporating real-time monitoring and adaptive management strategies into drainage systems could significantly improve their effectiveness in managing urban floods.
3. Urban Planning and Zoning. Strategic urban planning that restricts development in flood-prone areas and promotes flood-resilient construction practices is essential for reducing urban flood risks. Di Baldassarre et al. (2018) emphasized the need for cities to adopt zoning regulations that reflect current and projected flood risks, including setting aside floodplains for water storage and prohibiting construction in high-risk area. The study also highlighted the role of adaptive land-use planning in accommodating the dynamic nature of flood risks due to climate change.
4. Community-Based Flood Management. Engaging communities in flood risk management is crucial for building resilience at the local level, since well-prepared communities are better equipped to respond to and recover from flood events, reducing both economic losses and human casualties. Public awareness and participation are crucial for effective flood risk management, and they have

recently deserved attention in the literature (Scolobig et al., 2015). Kreibich et al. (2017) discussed how community-based approaches, such as public awareness campaigns, flood emergency planning, and the promotion of flood insurance, can significantly reduce floods' impacts on urban populations.

5. Integrated Flood Management. An integrated approach to flood management that combines structural measures, such as levees and flood barriers, with non-structural measures, like early warning systems and land-use planning, is essential for managing flood risks in urban areas. Climate projections should be incorporated into flood risk management to account for increased variability and intensity of precipitation. Carter et al. (2017) explored the benefits of integrated flood risk management, noting that this approach allows for more flexible and adaptive responses to changing flood risks. Cities should invest in combining traditional flood defenses and innovative solutions, such as floodable parks and temporary flood storage areas, to enhance their resilience to fluvial floods.
6. Enhance Modelling capability and Technology Integration. Analyzing past flood events to understand frequency, magnitude, and impacts provide insights into patterns and help in preparing for future floods (Merz et al., 2010). Hydrological and hydraulic models can simulate river flow and floodplain dynamics under various scenarios and help predict flood extents and impacts, providing crucial data for urban planning (Beven, 2012). The modelling capabilities have dramatically improved in the last decade thanks to the availability of computational resources, detailed input data and new monitoring techniques, such as remote sensing technologies that offer real-time data and enhance monitoring capabilities (Schumann et al., 2009). Smith et al. (2019) proposed a new approach to flood risk assessment by integrating both spatial and temporal data, resulting in more accurate flood hazard models. They emphasized the importance of high-resolution data in capturing the complexities of flood events, particularly in urban settings and showed that combining various data sources, such as satellite imagery, river flow measurements, and topographic data, can create more reliable flood risk maps for better planning and decision-making. Leveraging advancements in remote sensing, artificial intelligence, and big data analytics for real-time monitoring and predictive modelling can provide actionable insights and improve urban flood management (DeVries et al., 2020). In this perspective, urban flood monitoring networks can provide insightful data (see Section 4.1.1).

In conclusion, the above recent fluvial flood events in Italy have demonstrated the country's vulnerability to extreme weather events and the challenges of managing flood risks in diverse and complex landscapes. They have also highlighted the need for improved flood forecasting, better maintenance of flood defenses, and the adoption of integrated flood risk management strategies. As climate change continues to influence weather patterns, Italy must enhance its preparedness and resilience to mitigate the impact of future fluvial flood events.

A complex interplay of factors, including urbanization, climate change, and inadequate infrastructure drives fluvial flood hazards in urban areas. The risks associated with these floods are expected to increase as cities continue to grow and as climate change leads to more extreme weather patterns. To effectively

manage these hazards, cities must adopt a comprehensive and integrated approach to flood risk management, including green infrastructure, enhanced drainage systems, strategic urban planning, and community engagement. Ongoing research and adaptation will be critical to ensuring that urban areas remain resilient to the challenges posed by fluvial floods.

3.2.3 Pluvial floods

Pluvial floodings typically affect the urban environment with the potential to produce extensive damages depending on the vulnerability of the exposed assets. The increase in the degree of imperviousness in cities enhances the formation of runoff, distressing the capacity of the stormwater drainage system (both in terms of inlets and pipes) even for shorter return periods than the design ones (Aronica and Lanza, 2005).

The pluvial flooding results from rainfall-generated overland flow and ponding before the runoff enters any watercourse, drainage system or sewer, or cannot enter it because the network is full to capacity (Falconer et al., 2009). It generally derives from rainfall rates exceeding the infiltration capacity of soils and the drainage capacity of stormwater infrastructure, resulting in ponding and overland flow (Rosenzweig et al. 2018).

Pluvial flooding is often confused with urban flash flooding or surface water flooding. Urban flash floods are caused by the overtopping of natural watercourses flowing through urbanised areas, which are sometimes covered and become part of the urban stormwater drainage system, while “surface water flooding” is a more general terminology covering different sources of flooding (Falconer et al., 2009). Fluvial flooding occurs when water routed by streams, rivers or equivalent water bodies overflows their banks, inundating the adjacent floodplain area (Rosenzweig et al. 2018).

Pluvial flooding is caused by localized intense rainfall and the flood models used to assess the related hazard are applied on a city (or part of a city) scale using local rainfall records and a high-resolution digital elevation model (DEM) (Guerreiro et al., 2017). Both the temporal scale of rainfall records and the spatial resolution of the DEM play a key role in the modelling of the associated flood hazard.

A certain spatial and temporal resolution of the input data can be assumed as representative of a given urban context, while it may result totally inadequate for a different urban context. In the work of Guerreiro et al. (2017), an attempt to assess pluvial flooding hazard on a continental scale was performed for Europe by assuming a return period of the rainfall event equal to 10-years and the hourly temporal resolution for rainfall data. A spatial resolution of 25 m was used for the DEMs. The authors confirm, as expected, that further updating of the results is necessary by using input data with a proper spatial and temporal resolution. Nevertheless, even under such a generalized approach they managed to identify areas within the European territory that are significantly prone to pluvial flooding (i.e. the Mediterranean region), including the Italian territory.

An accurate assessment of the hazard related to pluvial flooding requires high-resolution rainfall data, a comprehensive knowledge of the surface drainage system and of the underground drainage network, a detailed representation of the topographic characteristics of the urban environment (including the microtopography features, basements, and underpasses), as well as the infiltration capacity of urban surfaces. This optimal scenario is nowadays still a challenge, and research is ongoing to assess the

minimum suitable resolution of the underlying information that is sufficient to fully characterise urban flooding events (Cristiano et al. 2017, Fewtrell et al. 2008). A more comprehensive state of the art is available for the case of fluvial floods and the associated spatial scale (see e.g., Savage et al 2016).

In the literature many hydrologic/hydraulic models are available, despite some approximations, to reproduce the surface propagation of flooding and the flow within the elements of the underground drainage network. The main Achille's heel in the modelling of pluvial flooding is related to the accuracy and resolution of the input data in terms of rainfall, description of the urban drainage network (surface and underground) and the topographic representation of the territory. The two-dimensional simulation of the pluvial flooding in terms of both flow velocity and water depth is strictly affected by the presence of obstacles that can divert the flow. As an example, the DEMs available for the Italian territory at National, Regional and Municipality levels are usually characterized by spatial resolution from 10 to 0.5 m that – depending on the size, steepness and degree of imperviousness of the urban catchment – usually appears insufficient to reproduce the real pattern of the pluvial flooding in the investigated area. The extension of the flooded area, as well as the maps of water depth and velocity, obtained from the modelling chain, are the most largely used indicators of the hazard for both pluvial al fluvial flood studies. A proper validation of modelled results can be obtained with dedicated post-flood survey.

3.2.3.1 Rainfall data

In-situ rainfall measurements at the ground from traditional rain gauges are assumed as representative of a portion of the territory, and their accuracy (Cauteruccio et al., 2021) play a key role in the modelling of flood events in urban areas. An example about the impact of the accuracy of rainfall measurements in the assessment of the hazard related to pluvial flooding for the Italian territory is described in the work of Lombi et al. (2022). In that work, results using observed (uncorrected) and corrected annual maxima rainfall as meteorological forcing were compared showing how the design of rainfall events with a duration of 30 minutes or shorter is significantly affected by the temporal aggregation, highlighting the importance of correcting annual maxima rainfall for a proper evaluation.

The relationship between the required temporal resolution of rainfall measurements and the extension of the urban catchment area to conduct pluvial flooding studies is not unique. Radar measurements can be exploited to estimate the relationship between the spatial and temporal scales that characterize the hydraulic/hydrologic response of an urban area. Despite radar measurements have the disadvantage to provide rainfall estimation at a spatial resolution comparable with the size of the urban catchment they have the potential to observe the dynamic evolution of precipitation events. By exploiting historical series of rainfall maps, the predominant combinations of rainfall intensity and duration (associated to a specific rainfall climatology) having the potential to result in critical conditions causing pluvial floodings can be established.

A multi-sensor approach can help to characterize the precipitation event in terms of rainfall intensity and spatial and temporal resolution. With the objective to increase the spatial resolution of the rainfall data, citizen science rain gauge stations can be used despite potentially affected by a lower quality and accuracy compared with authoritative monitoring networks. In the work of Loglisci et al. (2024) it was demonstrated that for a pluvial flooding event occurred in a Mediterranean city the role of rainfall

measurements provided by citizen science rain gauge station was crucial to better understand the spatiotemporal structure of the phenomena causing urban flooding in the study area.

The multi-sensor approach can also exploit the availability of opportunistic sensor that allow to increase the spatial coverage of the study area if compared with traditional rain gauge networks. The development of opportunistic sensors is a recent innovation in the measurement of precipitation intensity (Giannetti and Lanza, 2023), suggesting a high potential for large-scale application due to the low cost of their installation and operation. Already existing, but usually unrelated, microwave (MW) or millimeter wave (mmW) links are used to infer the rainfall amount or intensity by interpreting the extra attenuation induced by the precipitation on the received signal level. Various communication technologies can be exploited, such as commercial MW links (CMLs) of cellular phone networks, satellite MW links (SMLs), including broadcast satellite links (BSLs), but also wireless sensor networks (WSNs), e.g., for Internet of things (IoT) applications, moving vehicles, surveillance cameras, etc. (see, e.g., Uijlenhoet et al. 2018, Giannetti et al. 2019, Haberlandt and Sester 2010, and Allamano et al. 2015).

The Smart Rainfall System (SRS) was developed at the Polytechnic School, University of Genoa, as a cooperation between the Department of Civil, Chemical and Environmental Engineering (DICCA) and the Electrical, Electronics and Telecommunication Engineering and Naval Architecture Department (DITEN) to estimate rainfall intensity in real time by processing the attenuation of microwave satellite link signal measured by low-cost sensors (Federici et al., 2014). By processing the attenuation of the satellite microwave link signal, each SRS sensor produces an estimate of the rainfall amount at the temporal resolution of one minute. When a set of microwave links are placed on the field of interest and connected to a central processing and analysis node, a map of the estimated rain field can be obtained. The computation of the rainfall intensity based on the one-minute attenuation measurements made by the SRS sensors includes the application of a digital denoising filtering of the received signal to eliminate any spurious high-frequency fluctuation. The integral attenuation due to the presence of rain as measured by the microwave sensor is the result of the attenuation that occurs in the portion of the microwave link that is crossed by precipitation. Since the actual space distribution of the rainfall field is not known a priori, the method is based on the simplified assumption that the rainfall intensity is uniform along the microwave link.

Although in principles these sensors are suitable for large-scale installation and coverage of wide areas, the availability of comprehensive and convincing validation exercises is still scarce (see, e.g., Colli et al., 2019) and assessing their accuracy is difficult.

3.2.3.2 Spatial description of the territory

One of the major challenges in modelling rainfall–runoff in urbanized areas is related to the influence of the complex overland surface, with particular focus on the spatial resolution that characterizes the urban surfaces and influences the dynamic evolution of the flooding water flow. As summarized by Papaioannou et al. (2016), an important factor to assess and map the extension of the flooding areas, especially in complex terrain, is the accuracy of the digital elevation model (DEM) (Bates et al. 2003, Tsubaki and Ichiro 2010). Photogrammetric techniques (Teng et al. 2015), terrestrial laser scanners (TLS) or airborne light detection and ranging (LIDAR) could support the production of high-resolution DEMs. The mentioned works are mainly focused on fluvial flooding, where a coarser spatial resolution of the topographic information than in case of pluvial flooding is acceptable.

Moreover, accurate knowledge of the surface and underground drainage networks plays a key role in the assessment of the hazard related to pluvial flooding. A detailed description of each drainage element (type, geometrical characteristics, position, material) is rarely available. Due to the difficulties in collecting a detailed description of the urban drainage network, since a limited knowledge of the dimension and location of storm drain inlets, manholes and pipes is common, an exhaustive knowledge of these elements for the modelling of pluvial flooding is nowadays still a challenge.

To overstep this drawback, in the work of Bertsch et al. (2017) an automated GIS (Geographic Information System) routine to generate synthetic storm drain inlet locations was developed. To validate the obtained results a detailed field survey was conducted by recording the actual storm drain inlet locations for a sample urban catchment located in Scotland. An initial version of the GIS routine was developed by forcing all inlets to be positioned along roads and to be of the same grating type, spaced at an equal distance and close to the existing pipe network. The initial GIS routine produced 85% of the number of total storm water inlets surveyed. Authors ascribe this difference to two main reasons: a recently built area with a much greater density of storm drain inlets in comparison to the overall catchment, and small-scale terrain depressions which results in an accumulation of surface water where additional inlets had been installed. The drainage efficiency was assessed by calculating the inflow volumes for the network at each time step using the CityCAT model (Glenis et al., 2018) for rainfall intensity values associated with return periods of 20 and 50 years. The trueness of the synthetic inlet drainage network was examined in relative terms by comparing the flow hydrograph, the total volume discharged by each inlet, and the surface water depth in the flooded areas obtained with the surveyed inlets and the synthetic ones, while the accuracy and limitations of the CityCAT model were not addressed in that paper.

Results obtained by the initial GIS routine show a significant underestimation of the flow rate captured by the synthetic inlets if compared with the surveyed ones, therefore improvements were applied to consider terrain information and increase the density of inlets in newly built areas and in terrain depressions. Results obtained after applying the adaptation procedure reproduced 99% of the number of the surveyed inlets. A significant improvement was reached in terms of the drainage efficiency, especially after incorporating the terrain information to re-position the inlets. Overall, the differences in surface water depth vary from – 0.01m to 0.01 m and are scattered across the whole investigated area. Details about the spatial resolution of the terrain and the size of the various buffer layers are described in the paper. These are site dependent and refer to a flat urban area with an extension of 2.1 km^2. The transferability of this procedure requires appropriate rescaling according to the geometric characteristics of the study area.

The procedure described above can be considered as a useful tool to reconstruct the position of the storm drain inlets in the urban environment when a dedicated survey is not available or financial resources and timing requirement make a detailed survey unfeasible. The reproducibility of the proposed procedure in a different urban environment can be supported by a partial survey limited to a portion of the investigated urban area to extract the main features of the inlets (relative distance, main types, extension of the buffer layers around the street and the pipes, inlet density in terrain depressions and new built areas). This characterization can be extended to the whole investigated urban basin to apply the developed GIS routine and derive the position of the inlets for the modelling of pluvial flooding.

After estimating the characteristics of the surface drainage network from dedicated surveys or by means of the application of appropriate procedure, the role of the operational conditions of storm water inlets in the modelling of pluvial flooding must be considered. Indeed, the hydraulic performance of the entire drainage system can be dramatically affected by the operational conditions of inlets, these being the route for surface storm-water runoff to enter the underground drainage network (ten Veldhuis and Clemens, 2011). The inlet capacity and efficiency were defined in the work of Despotovic et al. (2005) and their relationship with relevant parameters (approaching flow, longitudinal and lateral street slopes) was established through laboratory experiments with the aim to explain the reason of the surplus of water runoff in the urban environment. Moreover, the effects of clogging of inlets on the capacity of the surface drainage system to convey rainfall into the underground drainage network was also investigated. The capacity is defined as the quantity of water captured by the inlet, while the inlet efficiency depends on the approaching runoff rate and is defined as the captured percentage of the approaching flow rate. The maintenance conditions of the inlet affect its capacity and result in decreasing its efficiency when a portion of the approaching flow is not captured by the inlet and produce the so-called pass-over flow. Based on the laboratory results, in the mentioned paper, the pass-over flow was calculated, for a sample case study, considering numerous inlets positioned along a street.

In the work of Palla et al. (2018) the efficiency of the surface drainage network under various operational conditions (degree of clogging) was investigated by using a hydrodynamic model that considers only overland (pluvial) propagation while the interaction with the subsurface drainage network is not simulated (it is assumed to receive all water drained by inlets). Inlet operational conditions were varied stochastically using a Monte Carlo approach and the flood propagation was modelled using the FLURB-2D model (Aronica et al. 1998). A case study in the city of Genoa (Italy) was chosen, the catchment area (80 ha) is completely urbanised with very limited pervious areas and equipped with about 250 inlets. Chicago hyetographs for return periods (T) equal to 2, 5 and 10 years were adopted. Simulation results allowed to identify local flood prone areas due to the failure of the surface drainage system for all precipitation events, showing that topographic effects have the potential to produce local flooding with significant water depth and that local inlet operational conditions may affect the behaviour of the whole urban drainage system. Pluvial flooding due to the inefficiency of the surface drainage system is shown to be independent on the conditions of the underground drainage network.

Lanza et al. (2023) investigated the impact of the inlet number, positioning, and efficiency on the risk of pluvial flooding. Detailed information about the inlet characteristics, including the potential degree of clogging, were obtained from the archives of the company in charge of the street and inlet maintenance, corroborated by a dedicated survey in the study area. This allowed obtaining a complete definition of the geometric and hydraulic characteristics of the stormwater inlets. It was assumed that the capacity of the storm sewers is sufficient to drive away the water conveyed through the inlets, therefore no backflow is considered. Hydraulic modelling is performed by using the HEC-RAS 2D software code (v. 6.3.1) (USACE, 2021) and inlets are simulated as pumping stations with a customised stage-discharge relationship based on the available literature studies. Results are presented in the form of maps of the water depth and velocity over the study areas, and critical regions are identified based on the observed frequency (return period) of the expected flooding. This study aimed at providing suitable information to plan priorities in the maintenance interventions (cleaning and repairing of inlets) and possible expansion of the surface drainage system. The model is applied to a case study of an urban district of the town of Genoa (Italy), to

support the activities of the project RUN – "Urban Resilience: Now-casting of the risk of flooding with IoT sensors and Open Data", funded within the ROP-ERDF (Regional Operational Programme of the European Regional Development Fund).

3.2.3.3 Modelling of pluvial flooding

The hazard related to pluvial flooding is traditionally described using as indicators the extension of the flooded area, the water depth and velocity and a combination of these two latter indicators to derive the conditional hazard classes (see Maranzoni et al., 2022 for a review of the flood hazard classification methods available in the literature). A variety of stormwater drainage models and software codes are available in the literature. In the following, a brief description of the main typologies of models employed for research purposes is reported.

Stormwater drainage models are characterized by two main steps: the first concerns the hydrologic processes where rainfall is transformed into runoff, the second concerns the flow propagation along the drainage network. Following these steps, the modelling of the propagation of the flood volume on the investigated catchment area is required to obtain a comprehensive assessment of the flood hazard. The one-dimensional (1D) approach is usually sufficient to characterize the second step of the analysis, related to the flow routing within the pipes. The first step, based on the quantification of the runoff volume, is preferably modelled using a two-dimensional (2D) distributed approach but in some cases the conceptual model simplification is assumed. Finally, a fully 2D approach is fundamental to reproduce the propagation of flood volumes over the catchment surface and derive the associated flood hazard maps.

The drainage network is typically conceptualized as a set of nodes, corresponding to manholes, and connections/links between them, representing pipes. The runoff generated in a defined portion of the catchment is assigned to an entry node and is then conveyed along the drainage network by solving the Saint-Venant equations. The Storm Water Management Model (SWMM) is a hydrologic and hydraulic model developed by the United States Environment Protection Agency (EPA) (EPA 1971) to solve the 1D steady or unsteady flow equations within connections/links (the pipes of the drainage network). The model was progressively upgraded and in 2022 a new feature of a 1D/1D explicit approach allowing users to define inlet devices that capture the surface runoff (Rossman and Simon, 2022) and convey the collected volume within the pipes.

The modelling of floods in urban areas requires the exchange discharges between the surface and subsurface flow to be considered. Therefore, various studies proposed combined 1D/2D models to address this issue. Bazin et al. (2014) validated, for a specific case study, the hydrodynamic simulations carried out by solving the 2D and 1D shallow water equations for the surface and subsurface flow, respectively, against measurements from an experimental facility available at the Jigawa Open Laboratory of Kyoto University. In Barreiro et al. (2023) a 1D/2D urban flood model based on an offline coupling procedure between the 1D model SWMM and the 2D model MOHID Land is presented. Manholes and inlet devices act as interface connectors between the two models. Inlet devices are responsible for capturing runoff and conveying it to manholes (2D to 1D), while manholes can return excessive flows to the surface when the sewer system is pressurized (1D to 2D). The interchange of data between the two models (coupling procedure) is set offline at the end of the run of each model.

Computational and numerical stability aspects are also addressed; for instance, in Fan et al. (2017) a coupled model for urban flood inundation was developed by using an implicit dual time stepping method (DTS) to improve the run time efficiency. The method is fully implicit and can be run in parallel computing mode. The implicit scheme ensures a greater stability and is therefore particularly suitable for urban flood simulations where a complex underlying surface dictates the propagation of flooding.

Software tools like HEC-RAS 2D (USACE 2021) allow modelling the surface propagation of flood due to both the river overflow inundation (using the combined 1D/2D model) and pluvial flooding phenomena (using the 2D model capability alone). The HEC-RAS software was developed by the U.S. Army Corps of Engineers and allows to set a variety of simulations schemes from steady to unsteady flow by solving the Shallow Water equations or the Diffusion Wave equations (less accurate). A similar 1D/2D approach is used by the Kalypso software (https://kalypso.bjoernsen.de/index.php?id=470&L=1 last access 24/07/2024). Kalypso solves the unsteady coupled 1D/2D flows for surface waters by connecting a one-dimensionally modelled river section with another section modelled using the 2D model. The two components are coupled by means of appropriate boundary conditions. The mathematical basis of the computation module is formed by the Saint-Venant equations and the shallow water equations, respectively.

Equivalent to the HEC-RAS software is MOHID Land developed by the MARETEC (Marine and Environmental Thecnology Research Center) at the Instituto Superior Técnico of the University of Lisbon. It is a hydrologic/hydraulic integrated model with four compartments: the atmosphere, porous media, surface land, and river drainage network. The surface runoff is 2D modelled setting the kinematic wave or the diffusion wave approximation while within the river network the 1D Saint-Venant equations are solved. This model was coupled in the work of Barreiro et al. (2023) with SWMM to reach a complete modelling framework to accounting for the various steps affecting flooding scenarios.

3.2.3.4 Post-flood survey strategies in urban areas

The main reason why it is worth performing a post-flood survey arises from the need of improving our understanding of the flood phenomenon and increase the resilience of the anthropic environment. Resilience, defined as “the ability of people or things to recover quickly after something unpleasant, such as shock, injury, etc.” (Oxford Learners dictionary), can be improved by learning in advance the characteristics and expected evolution of a flood event, the expected damages, and the possible countermeasures, to be ready to reasonably face the next event. The concept is well synthesised by Szoenyi et al. (2017) in the title of their chapter, reading “After the flood is before the next flood”.

Post-flood survey places the basis for the calibration and validation of flood models with the objective to single out the main critical issues and plan mitigation strategies.

Within this general framework, multiple objectives can be supported by the information collected during the post-flood survey and, though the overall survey is generally a multipurpose activity, identifying the specific aims is useful to plan and adopt optimal methods of investigation.

The most common post-flood survey actions aim at readily assessing the damages to relevant infrastructure, buildings, commercial and industrial premises, private and public properties, etc. The

transportation network is generally impacted by the flood and detailed identification of the damages to roads and railways is a primary objective.

This is generally performed in the immediate aftermath of the event (few hours or days), or even during the event, by the civil protection as the basis for organizing rescue actions and supporting the provision of rapid funding from the (local or national) government in the emergency phases. Rapid assessment of the damages for emergency support can be later followed by a more detailed assessment to quantify the precise amount of compensation funding for citizens and companies.

Damage assessment is also important in view of conducting investigations, usually activated by the Public Prosecutor Office following complaints from citizens, to assess possible responsibilities of the various regional planning and land protection authorities, or public and private actors as well. Following Szoenyi et al. (2017) “conducting a forensic post-event study is similar to detective work in that it needs an experienced team of experts, a consistent and iterative meta-structure, and guidance on how to pursue leads and new information”.

Among the most difficult elements to quantify in relation to flood events, knowledge of the vulnerability of the anthropic and natural settlements is also one of the most important factors to support resilience. Indeed, vulnerability quantifies the level of damage that is expected for a generic asset when it is exposed to a flood event of a given magnitude and may vary widely with the type of asset at risk, the age, the maintenance conditions, and with the physical characteristics of the flood (including hydrodynamics, duration, sediment transport, pollution, etc.).

A non-negligible application of the results of a post-flood survey resides in the validation of flood propagation models. The hydrodynamic parameters and simplifying hypotheses adopted in the simulation of flooding scenarios using numerical models always requires, indeed, careful validation. However, while flow rate data from instrumented river sections are commonly available for validating hydrological rainfall-runoff models, quantitative information about the flow depth and velocity occurring in urban areas in the event of pluvial flooding are rarely found.

The extent of urban flooded areas is the main relevant parameter, whether monitored from remote satellite platforms or recorded as a site survey action. The information can be detected also from the analysis of photographs and videos taken by experts or citizens during or in the immediate aftermath of the event. Comparison of simulated versus recorded flood extent data is the most common form of validation of flood propagation models.

As an example, in Figure 25, two photographs (taken by a private citizen) of the runoff occurred during the rainfall event on August 28th, 2023, in the town of Genoa are reported. As a confirmation of the analysis reported in the work of Loglisci et al. (2024), where merged radar maps and rain gauge measurements demonstrated that the rainfall climatology of the Genoa territory is characterized by short duration and very localized events, the rapid evolution of the flooding can be extrapolated from these pictures. In the left-hand panel, significant runoff covers the whole road from one side to the other, while after 10 minutes the runoff decreased and was soon confined to a small portion of the road.

(a) (b)

Figure 25. Dynamic evolution of runoff during the event of August 28th, 2023, in Genoa. Panel a) refers to 02:07 CET while panel b) refers to 10 minutes later (photographs were provided by a private citizen).

3.2.3.5 The case study of the RETURN project

This section summarizes the research conducted within the activity of the RETURN project, Vertical Spoke 1 (VS1) "Water", Work Package 2 (WP2) "Flood risk under environmental and climatic changes" by the research team of the University of Genova, Department of Civil, Chemical and Environmental Engineering (DICCA) composed by Dr. Cauteruccio Arianna, Prof. Boni Giorgio and Prof. Gnecco Ilaria. The input data availability issue, with specific focus on the spatial resolution, is addressed by means of a comparison of pluvial flooding scenarios using rain gauges and opportunistic sensors for an urban case study.

The case study is a densely built urban area within the Metropolitan area of Genoa (Italy), that was recently (September 24th, 2022) affected by pluvial flooding associated with a rainfall event characterized by a low return period (T between 1.5 and 3 years). The investigated urban area is in the West part of Genoa, in the Sampierdarena district, and is characterized by a flat zone of about 1 km2 (see red area in Figure 26). It is equipped with a traditional tipping-bucket rain gauge station (named Arpal-FI) managed by the environmental protection agency of the Liguria region (ARPAL) and one SRS (named SRS-SA). Two further SRSs are available close to the investigated area: in Borzoli (named SRS-BO) and in Castelletto (named SRS-CA) positioned 2.7 km and 4.0 km far from Arpal-FI, respectively. In the analysis, other two rain gauges managed by ARPAL are considered, the Castellaccio (Arpal-CA) and Centro Funzionale (Arpal-CF) located at 5.1 km and 4.5 km far from the Arpal-FI. The position of each instrument is shown in Figure 26. Measurements from the ARPAL rain gauges are available at 5 minutes resolution while SRSs provide measurements at 1 minute resolution.

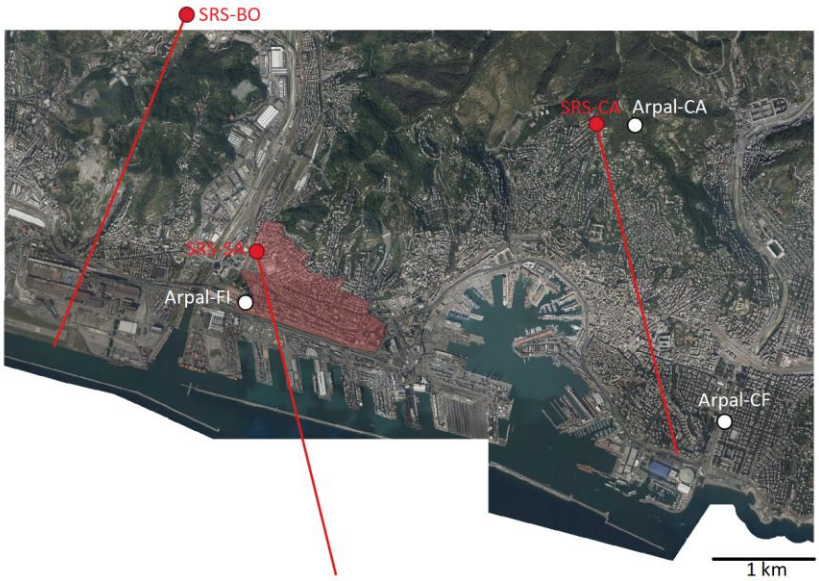

Figure 26. Overview of the investigated urban area with indicated the position of the three rain gauges (white circles) and the three SRSs (red circles) with the associated satellite links (red lines).

Assuming the Arpal-FI rain gauge as the reference instrument for the present study (since it is located within the investigated urban area) the ratio between the rainfall amount measured by each instrument and the reference one, as well as the peak ratio, are summarised in Table 4. The comparison of the investigated rainfall event as measured by each instrument is shown in Figure 27a. It is evident that the two Arpal rain gauges positioned outside of the study area do not capture the magnitude and the duration of the rainfall event measured at the reference station. On the contrary, the SRSs, despite some underestimation of the peak rainfall, provide a good representation of the temporal evolution and total volume of the reference rainfall event. This can be ascribed to the larger spatial representativeness of the SRS with respect to the traditional rain gauge. The satellite link may indeed cross the bulk of the rainfall event even though the precise location of the sensor is not immersed in the rain field.

Table 4. Rainfall event and flooding parameters as a comparison with the reference instrument (Arpal-FI).

Instrument	Rainfall amount ratio	Peak ratio	Volume ratio condit. on h>5cm	Max Depth ratio
Arpal-CA/Arpal-FI	0.62	0.59	0.54	0.91
Arpal-CF/Arpal-FI	0.64	0.55	0.50	0.91
SRS-SA/Arpal-FI	1.07	0.56	0.90	1.02
SRS-CA/Arpal-FI	1.02	0.38	0.84	1.01
SRS-BO/Arpal-FI	1.08	0.45	0.79	1.03

Pluvial flooding scenarios were modelled based on the rainfall measurements obtained from the various sensors using the HEC-RAS 2D software (USACE 2021), solving the shallow water equations (SWE-EM stricter momentum) at fixed time steps of 0.5s. The connection with the subsurface drainage network is neglected in this study since in Lanza et al. (2023) it is shown that flooding in the study area is ascribable to a complete clogging of stormwater inlets meaning that the subsurface drainage network is inefficient.

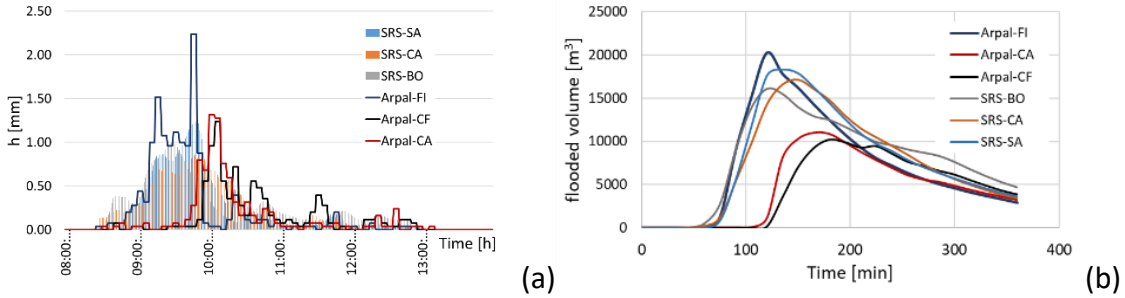

Figure 27. (a) Temporal evolution of the investigated rainfall event as measured by the various sensors, (b) temporal evolution of the modelled flood volume (conditional on a minimum water depth h = 5 cm) obtained when using as input the rainfall measurements from various sensors.

The results of the modelled scenarios are reported in terms of maps of the maximum water depth (see Figure 28) and the ratios between the flooded volume (conditional on a minimum water depth h = 5 cm) and maximum water depth obtained in each scenario and the reference values obtained using the rainfall measured at Arpal-FI (see Table 4). The temporal evolution of the modelled flood volume (conditional on a minimum water depth h = 5 cm) is reported in Figure 27b. Both the maps and the ratios indicate that differences are limited when SRSs are employed, either when positioned in the same urban area or at few kilometres far from the area. The point nature of measurements taken at rain gauge stations outside of the study area reduces to a half the flooded volume and by 10% the maximum water depth. In all cases a reduction of the extension of the flooded area is shown indicating an underestimation of the flood hazard. The temporal evolution of the modelled flood volume reflects the differences already observed in the temporal evolution of the rainfall event as measured by the various sensors, including the shift in time of the core of the event in case of the two rain gauge stations located outside of the study area. The significant underestimation of the rainfall peak experienced by the SRS measurements does not result into a corresponding reduction of the peak of the flood volume probably because of the accumulation of flooded water in the depressed areas of the domain.

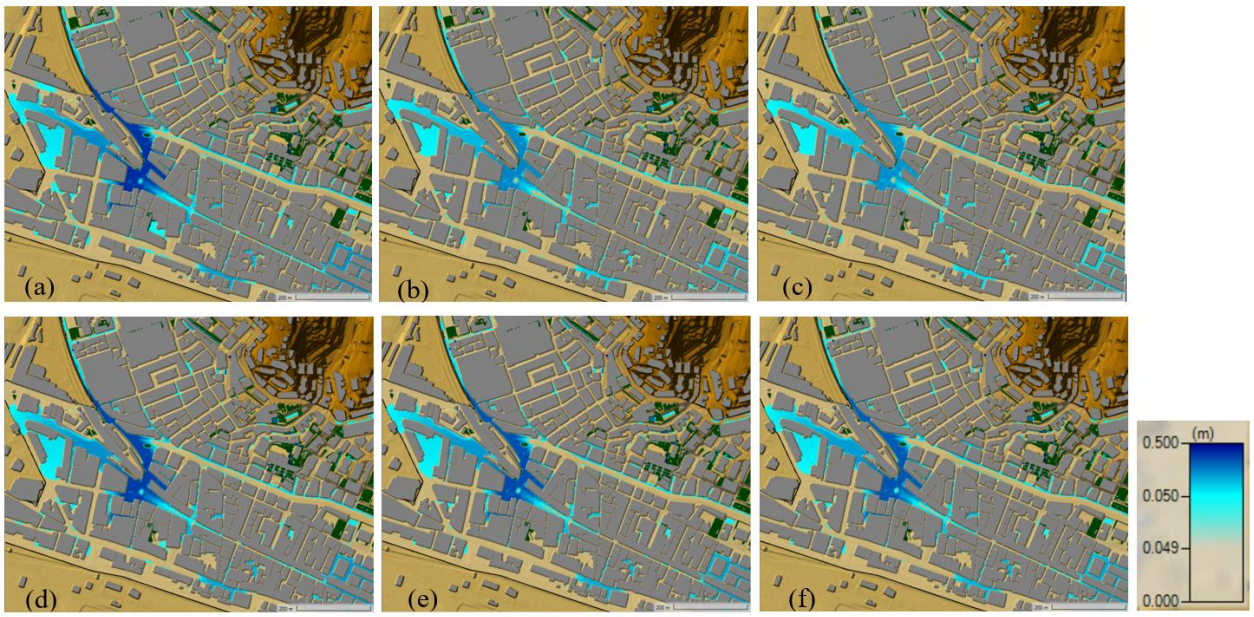

Figure 28. Maps of the maximum water depth for the investigated rainfall event using measurements from: (a) Arpal-FI, (b) Arpal-CA, (c) Arpal-CF, (d) SRS-SA, (e) SRS-CA and (f) SRS-BO.

In conclusion, various pluvial flooding scenarios were simulated in the present work to highlight the impact of data availability and reliability over the assessment of the flood hazard in a highly urbanised district of the town of Genoa. Significant differences were observed and quantified between flooding scenarios obtained by simulating the distribution of excess rainwater when various rainfall data are considered. A real-world event measured by rain gauge stations and opportunistic sensors is used to compare the results. Although the overall flooding conditions are captured in all the examined cases, due to the simplification adopted in the flow modelling approach, it is evident from the results that significant differences in the expected flood volumes and maximum water depth are obtained when using various sources of the rainfall information. In the case of the simulated event, the role of opportunistic sensors located within or in the proximity of the study area largely outperforms the contribution of nearby rain gauge data when these are located even only 5 km far from the study area, and this was shown to hold for both the total flooded volume and the maximum water depth.

This work, published as a part of the short paper by Cauteruccio et al. (2024), highlighted the relevance of the input rainfall pattern on the modelling of pluvial flooding scenarios for a specific case study characterized by a rapidly evolving event with a limited spatial coverage, suggesting that the input information plays a central role, even prevailing with respect to details of the flood modelling approach.

3.3 Meteorological hazards

3.3.1 Extreme wind events under climate change and multi-risk perspective

The Mediterranean basin, although relatively small, has unique and complex orographic features, such as sharp land-sea transitions. The wind climate of the mid-latitudes of Europe, particularly in the Mediterranean basin, which spans the entire vertical extent of the Italian peninsula, is primarily influenced by two phenomena: extra-tropical cyclones and thunderstorm downbursts. Understanding the physical

mechanisms behind these phenomena is essential for characterizing their spatio-temporal behavior and assessing the associated risks to both the built and natural environments.

These two phenomena differ significantly in their temporal and spatial characteristics. Extra-tropical cyclones, which are cyclonic winds that develop outside the tropical regions, are extensive and long-lasting events. They typically span around 1,000 kilometers and can persist for several days. These cyclones originate at subpolar low-pressure centers, formed by the convergence of cold winds from the north pole and warm air from the tropics. The polar front is the transition zone between these two air masses. The cyclonic system derives its energy from the horizontal thermal contrast in the atmosphere.

Bjerknes and Solberg (1921) first described the evolution mechanism of this phenomenon, known as cyclogenesis. As the horizontal wind's rotation (vorticity) around the low-pressure center increases, so does the updraft (the upward movement of vertical wind above the low-pressure center). This process reduces surface pressure, and the resulting pressure gradient between the cyclone's center and its outer region generates horizontal wind. The Coriolis force, caused by Earth's rotation, creates spiral winds around the low-pressure center (Figure 29). Over time intervals ranging from 10 minutes to 1 hour, the winds from extra-tropical cyclones are stationary flows, and their velocity distribution can be accurately represented by a Gaussian distribution.

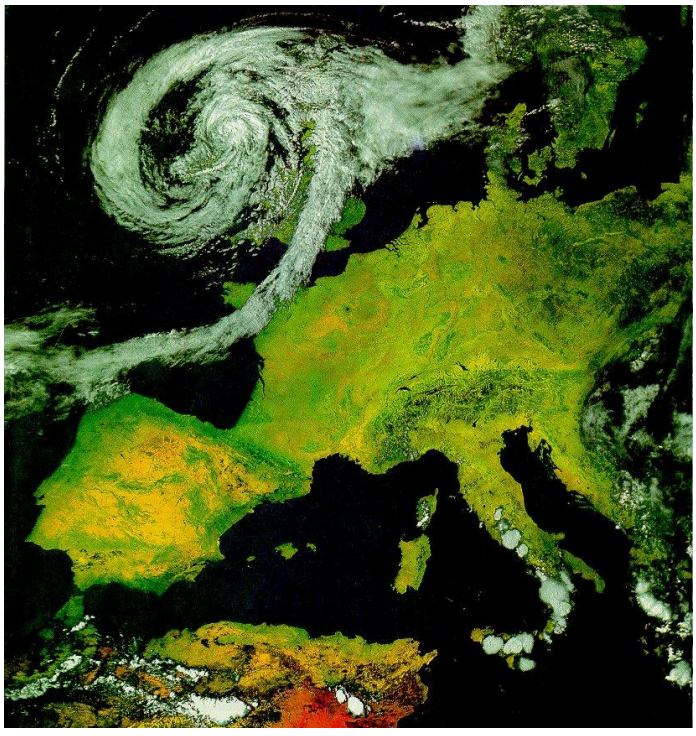

Figure 29. Satellite image of extra-tropical cyclone above United Kingdom.

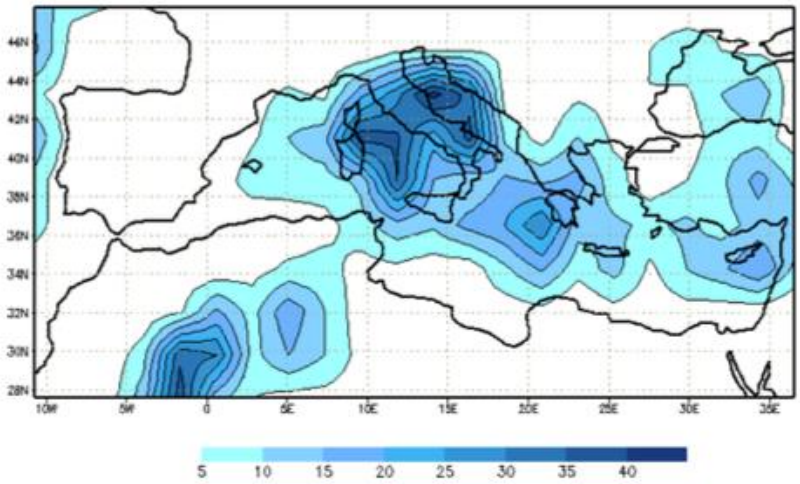

Figure 30. Number of intense cyclones over the 45 years of the ERA-40 period at mature stage per squares 2.25° x 2.25° (Flaounas et al., 2022).

Cyclones in the Mediterranean basin can also exhibit tropical-like characteristics (Figure 30). In recent decades, these tropical-like cyclones have become increasingly common at our latitudes. These events have recently been given a specific name by the scientific community: Medicanes, a portmanteau of "Mediterranean hurricanes" (Flaounas et al., 2022; Figure 31). Unlike extra-tropical cyclones, Medicanes typically feature a warm, clear, cloudless core, devoid of strong winds. They initially form as baroclinic phenomena due to the misalignment between pressure and density gradients. As they mature, they intensify through convective processes, such as extracting latent heat from warm sea temperatures. Recent climatic studies suggest that while their frequency may decrease, their intensity is likely to increase.

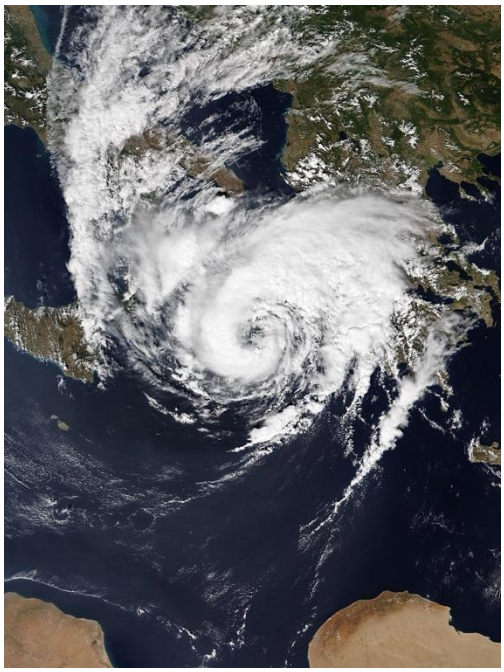

Figure 31. A satellite image of a Medicane over south of Italy.

However, the mid-latitude climate of the Mediterranean Basin is also governed by thunderstorm phenomena. They originate from the convective updraft of air from the lower tropospheric levels. The updraft of air can occur mainly following three distinct mechanisms: (i) forced mechanism – air clashes against an obstacle (mountain/hill prominence) that forces it to move upward; (ii) frontal mechanism – a front between cold and warm air forces the latter to uplift; (iii) natural convection – warmer and humid air tends to rise. Upon reaching condensation, the thunderstorm cloud (i.e., cumulonimbus) forms and, depending on the strength of the vertical air updraft, extends up to the tropopause (i.e., 10-12 km above the ground level, AGL). If the updraft intensity is particularly violent, the cumulonimbus can trespass at the lower stratosphere. Typically, the thunderstorm cloud extends vertically for about 10 km in the troposphere, starting about 1-2 km AGL, and it is thus quite recognizable among the other clouds.

The cold air inside the cloud now buoyantly falls to the ground through gravity. This creates the so-called downdraft, namely a vertical descent column of cold air. Upon impingement on the ground, the flow changes momentum from vertical to horizontal and expands in an ideally radial-symmetric structure on the horizontal at the near-ground levels (Canepa et al., 2022b, 2020; Solari et al., 2015). The thunderstorm dynamics described above can be summarized in mainly three stages (cumulus, mature, and dissipating stages) schematized in Figure 32.

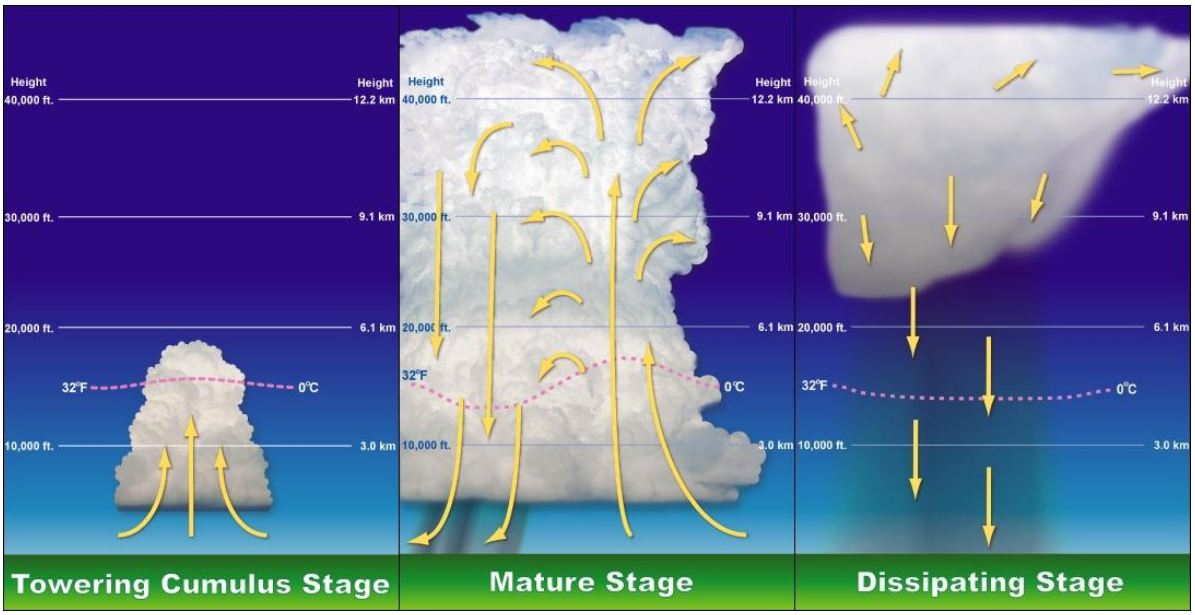

Figure 32. Schematic of thunderstorm phenomenon.

Different typologies of thunderstorms exist in nature. A short list is reported here below and in Figure 33, while the reader can refer to the vast literature on this topic:

1. Single cell
2. Supercell
3. Multi-cell
4. Mesoscale convective systems
   a) Squall line (thunderstorm front)
   b) Bow echoes (Arc-resonance type)

c) Line echo

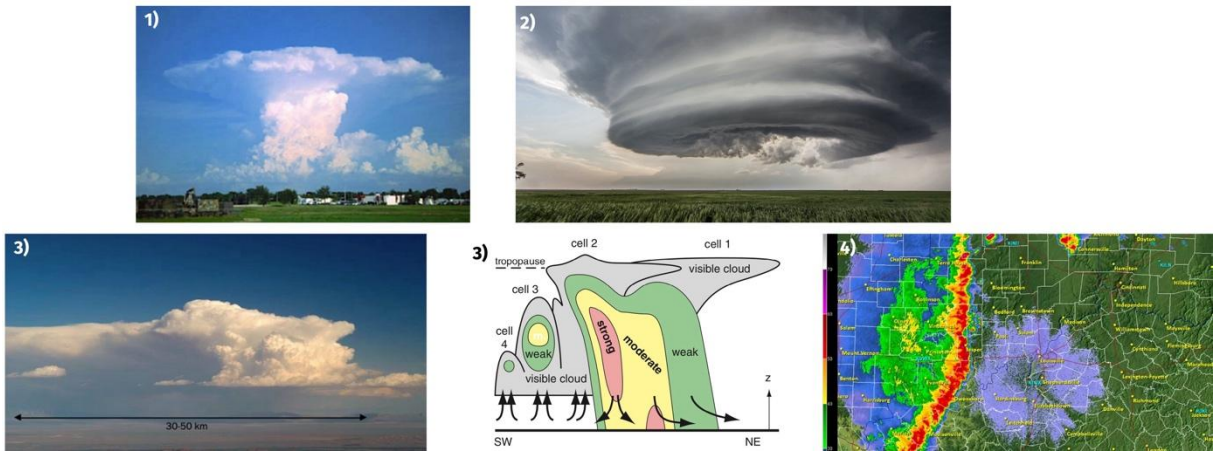

Figure 33. Thunderstorm typologies.

Contrary to cyclones, thunderstorms are very small phenomena, extending for a few km on the horizontal and lasting few tens of minutes. This, along with their highly non-stationary and transient wind characteristics (see, for example, Figure 34), makes them very difficult to record at full-scale and to build simple and physically reliable models as in the case of extra-tropical cyclones. These latter phenomena are still the reference flow to calculate wind-induced effects on structures within the design codes and standards. Thunderstorms, in turn, exhibit unique characteristics, as highlighted in Figure 34, including sudden changes in direction and speed (with flow acceleration) and mean wind speed profiles characterized by a typical "nose" shape, with maximum values closer to the ground. These features are now starting to be simulated in wind tunnels, often using specialized facilities. The paper by Aldereguía Sánchez et al. (2023), developed within the framework of the RETURN project, shows the possibility of using a passive device, such as a specially designed grid, to replicate the nose-shaped mean wind speed profile even in a conventional wind tunnel.

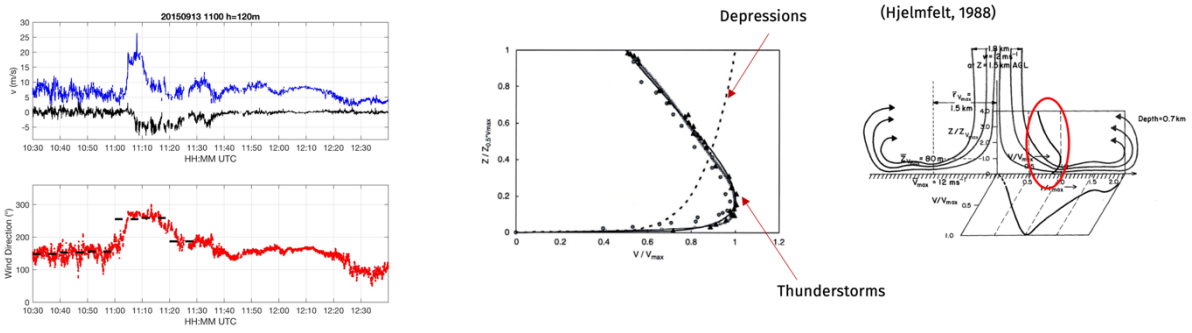

Figure 34. Wind speed and direction time series (left); extra-tropical cyclone and thunderstorm wind profiles (middle); vertical-view schematic of thunderstorm downburst wind (right).

A wide range of weather-induced natural hazards and multi-hazards in the Mediterranean are related to Mediterranean cyclones and thunderstorms with severe socio-economic consequences. In the natural hazards report of Munich Re at global scales for 2019, the Mediterranean region was pointed out because

of the storms that produce flash floods and inundation. Such storms have recurrently affected Italy, inflicting damage and billions of Euros in losses (Munich Re, 2022). Mediterranean cyclones with strong circulation, embedded convection and frontal structures produce high-impact weather including heavy rainfall and flooding, thunderstorms with intense lightning activity, windstorms and dust storms, tornadoes, storm surges, and landslides, including compounding effects.

The compounding interaction among these weather components will be treated more extensively in Section 4.2.2.

3.3.1.1 Statistical analysis of extreme winds

Probabilistic analysis of the data population

Let N_t be the number of pairs of the average values of wind speed and direction (V, α) that form the corrected dataset; let N_0 be the number of pairs of null values relative to wind calms; Let $N = N_t - N_0$ be the number of pairs of non-zero values.

From the N pairs of non-zero values of (V, α) S sub-datasets are extracted, the j-th of which includes the N_j speed values V associated with the j-th sector of incoming wind ($j = 1, 2, \ldots, S$, $N = N_1 + N_2 + \cdots + N_S$). Each sector is $\alpha = 360°/S$ wide and centered on the angle $\alpha_j = \frac{(2j-1)\Delta\alpha}{2}$, being 0° the direction of the wind coming from the north and $\Delta\alpha$ the sector width. The probability that the wind comes from the j-th sector is given by the formula:

$$f_{V_j}(v) = A_j f_{V_j}^S(v) \quad (v > 0;\ \ j = 1,2,\ldots,S) \tag{1}$$

being A_j the probability, conditional on $V > 0$, that the wind comes from the j-th sector (note that $\sum_{j=1}^{S} A_j = 1$); v is the state variable of V; $f_{V_j}^S(v)$ is the probability density function of the 10-min average wind speed coming from j-th sector, expressed in the form proposed by Weibull (Weibull, 1951):

$$f_{V_j}^S(v) = \frac{k_j}{c_j}\left(\frac{v}{c_j}\right)^{k_j-1} \exp\left[-\left(\frac{v}{c_j}\right)^{k_j}\right] \qquad (v \geq 0;\ \ j = 1,2,\ldots,S) \tag{2}$$

where k_j and c_j are the so-called shape and scale, respectively, parameters of the model. Distributions calculated on the basis of N_j values less than 1% of the available non-zero N_t values are considered to be limitedly reliable.

Starting from this setting, the overall probability density function $f_v(v)$ and the data population distribution function $F_v(v)$ are provided by the expressions (Solari, 1996):

$$f_v(v) = P_0\delta(v) + (1 - P_0)\sum_{j=1}^{S} A_j \frac{k_j}{c_j}\left(\frac{v}{c_j}\right)^{k_j-1} \exp\left[-\left(\frac{v}{c_j}\right)^{k_j}\right] \qquad (v \geq 0) \tag{3}$$

$$F_v(v) = 1 - (1 - P_0)\sum_{j=1}^{S} A_j \exp\left[-\left(\frac{v}{c_j}\right)^{k_j}\right] \qquad (v \geq 0) \tag{4}$$

where P_0 is the probability that $V = 0$, δ is the Dirac operator.

As an alternative to Eq. (3) and (4), $f_v(v)$ and $F_v(v)$ and can be expressed using formulas (Solari, 1996):

$$f_v(v) = P_0\delta(v) + (1-P_0)\frac{K}{C}\left(\frac{v}{C}\right)^{K-1}\exp\left[-\left(\frac{v}{C}\right)^{K}\right] \qquad (v \geq 0) \tag{5}$$

$$F_v(v) = P_0 + (1-P_0)\left\{1-\exp\left[-\left(\frac{v}{C}\right)^{K}\right]\right\} \qquad (v \geq 0) \tag{6}$$

in which K and C are the parameters of the distribution of the global dataset.

Probabilistic analysis of the extreme values

The procedure assigns to the first *r* annual maxima of *V* the asymptotic distribution of type I of Gumbel (Gumbel, 1958). The distribution function of the maximum annual value of *V* is given by the formula:

$$F_M(v) = e^{\left\{-e^{[-A(v-U)]}\right\}} \quad (v \geq 0) \tag{7}$$

where *v* is the state variable of *V*. *A* and *U* are the model parameters. By inverting Eq. (7) we obtain:

$$v = U - \frac{1}{A}\ln\left[-\ln\left(1-\frac{1}{R}\right)\right] \quad (R>1) \tag{8}$$

being

$$R(v) = \frac{1}{1-F_M(v)} \tag{9}$$

the mean return period, namely the average duration that elapses between the recurrence of events of intensity equal to or greater than *v*.

3.3.1.2 Case study – Analysis of the station Genoa – Porto Antico (GEPOA) (period 03/2016 – 10/2023)

Analysis of wind speed and direction timeseries

This section shows the analysis of the wind speed and direction timeseries recorded by the ARPAL met-station of Genoa – Porto Antico (see Section 2.3.1, code GEPOA) in the period from 4 March 2016 to 30 October 2023. The dates used in this report all refer to the UTC (Coordinated Universal Time) standard, which corresponds to Greenwich Standard Time, at 0° longitude.

The data analyzed are values of wind speed and direction averaged over 10 minutes, recorded continuously in the aforementioned period. The dataset has been checked for incorrect values, according to the procedures indicated in Section 3.3.3. No incorrect measurements were found during the period considered, so the dataset was analysed as a whole. Some intervals of the wind direction signals were disregarded in the directional analysis due to poor resolution of direction measurements. This allowed to make the datasets homogeneous and therefore idoneous to undergo a directional statistical analysis.

Table 5 provides a summary of the characteristics of the analysed dataset. The value of the potential measurements refers to the maximum number of measurements available (at the sampling frequency of the station for the length of the measurement period) if the dataset had no missing data. For the GEPOA dataset, this is 402688 values. The valid measurements, corresponding to the potential measurements excluding missing data, are 393542 overall (97.7%). These can in turn be divided between wind calms (wind speed less than or equal to 0.5 m/s), equal to 29238 values (7.2%), and non-zero speeds (greater than 0.5 m/s), equal to 364304 (90.5%). The number of missing data is 9146 (2.3%).

Table 5. Total number and percentage of missing, valid, null and non-zero measurements for the GEPOA dataset in the period 04/03/2016 – 30/10/2023.

Potential measuremens	*Missing measurements*	*Valid measurements*	*Wind calms*	*Non-zero values*
402688	9146	393542	29238	364304
100.0%	2.3%	97.7%	7.2%	90.5%

Figure 35 shows the Gantt chart of valid measurements, which allows to identify the periods in which the instrument has not measured.

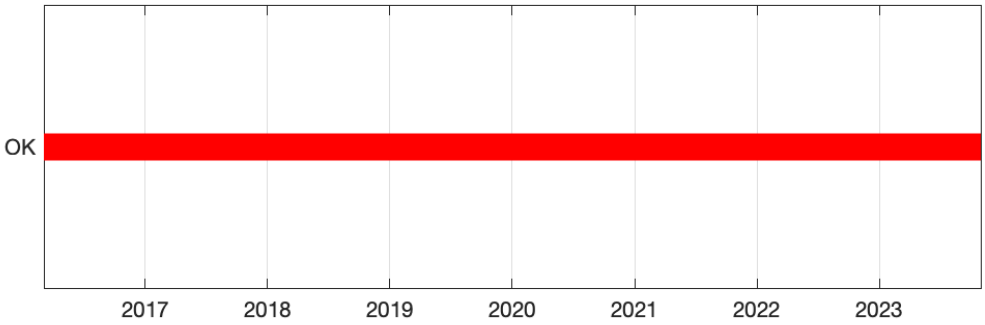

Figure 35. Temporal distribution of the measurements valid in the period 04/03/2016 – 30/10/2023 for the GEPOA dataset.

Figure 36 diagrams show the trend of the wind speed (a) and direction (b) timeseries over the measurement period. From the graph of the wind speed timeseries it can be seen that the values have never exceeded 17 m/s (10-min average values).

To get a more detailed picture of the data, Table 6 summarizes, for each of the 12 directional sectors analyzed (from 0° to 360° with step 30°), the recurrence of the wind speed divided into intervals of 1 m/s. Due to the poor resolution of direction measurement between 21/07/2022 and 20/03/2023, this time interval was removed from the analysis. From here the high number of wind speed values that falls in the column “undefined direction”. The last column shows the count in non-directional (i.e., aggregated) form. The last row shows the total of non-zero values of wind speed, sector by sector and for the entire dataset.

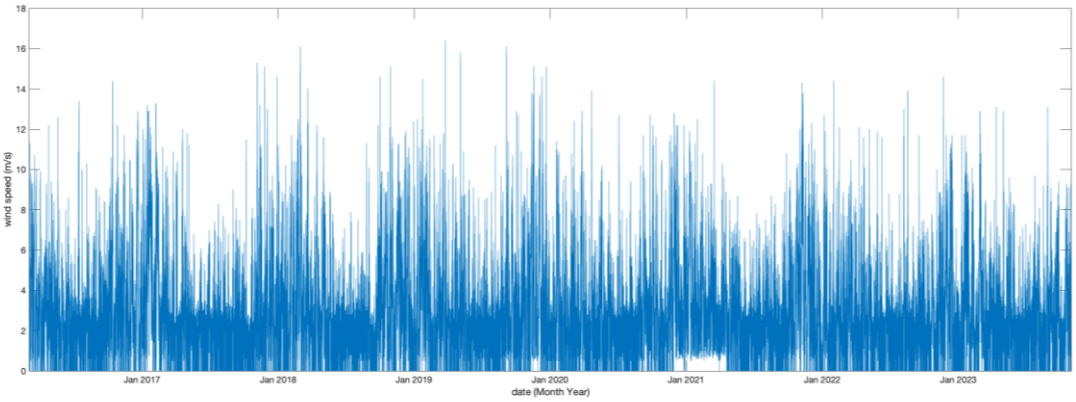

(a)

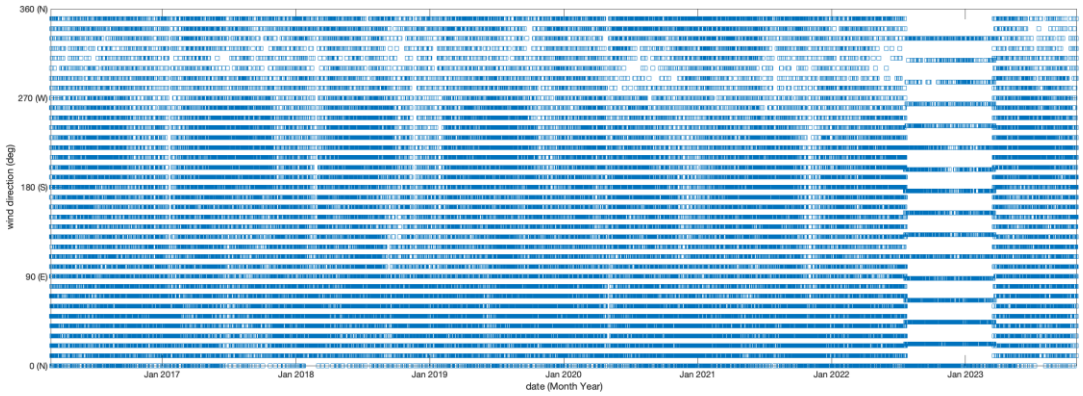

(b)

Figure 36. Timeseries of measurements (average over 10 minutes) valid in the period 04/03/2016 – 30/10/2023 for the GEPOA dataset: (a) wind speed; (b) wind direction.

Table 6. Count of measurements (averages over 10 minutes) valid in the period 04/03/2016 – 30/10/2023 for the GEPOA dataset divided into classes of 1 m/s of wind speed and 12 sectors of incoming wind direction, of amplitude 30°. The second-last column shows measurements for which only wind speed was recorded, if any. The last column shows the total of the measurements.

Number of processed data	393542
Number of wind calms	29238

Speed	**Direction sector – θ**													
U	**0-30**	**30-60**	**60-90**	**90-120**	**120-150**	**150-180**	**180-210**	**210-240**	**240-270**	**270-300**	**300-330**	**330-360**	**Undef**	**Total**
0.5-1	4305	5097	7731	8175	4527	1937	2310	2574	1432	1040	940	2690	4197	46955
1-2	4837	9423	11974	5922	5759	6165	11035	15714	6304	2065	1335	3235	8229	91997
2-3	3057	7226	7335	1540	3766	9893	17075	17164	6668	2069	841	1175	6457	84266
3-4	3861	7714	5801	556	3003	9566	7916	2657	1602	942	234	993	4002	48847
4-5	4185	8300	3866	123	2104	5684	3017	828	319	151	75	740	2627	32019
5-6	3617	7804	2363	24	1114	2492	1151	500	122	51	26	372	1906	21542
6-7	2833	6947	1494	4	351	714	392	270	43	7	8	171	1423	14657
7-8	2012	5415	935	1	73	247	160	110	11	3	2	65	960	9994
8-9	1422	3521	468	0	30	91	67	43	2	0	0	32	705	6381
9-10	827	2124	230	0	20	46	26	16	0	0	0	11	346	3646
10-11	442	1342	101	0	15	13	13	8	0	1	0	6	163	2104
11-12	227	738	65	0	13	4	8	2	0	0	0	0	85	1142
12-13	68	314	30	0	2	3	7	2	0	0	0	0	26	452
13-14	29	147	6	0	0	2	7	1	0	0	0	0	3	195
14-15	2	65	6	0	0	0	1	0	0	0	0	0	5	79
15-16	0	22	2	0	0	0	0	1	0	0	0	0	0	25
16-17	0	3	0	0	0	0	0	0	0	0	0	0	0	3
Total	31724	66202	42407	16345	20777	36857	43185	39890	16503	6329	3461	9490	31134	364304

Wind calm is defined $U < 0.5$ m/s
Wind speed classes: $Lower\ bound \leq U < Upper\ bound$
Wind direction sectors: $Lower\ bound \leq \theta < Upper\ bound$

A more immediate visualization of the data reported in Table 6 is possible via the polar diagram of Figure 37, which represents the wind rose corresponding to the measurements recorded in the GEPOA met-station. In this figure, the distance from the center of the graph indicates the frequency of the wind coming from a certain direction. Directions are divided into 12 sectors 30° wide. For each sector, different colors distinguish classes of increasing wind speed, as shown in the legend. Figure 37 shows a wind rose in which the prevailing directions (sectors with greater radius and therefore area) correspond to the wind coming from the north-eastern quadrant (mainly from 0° to 60°) and, to a lesser extent, from the southern quadrant (from 150° to 210°). The most intense winds (yellow) come mainly from the sectors from 0° to 60°.

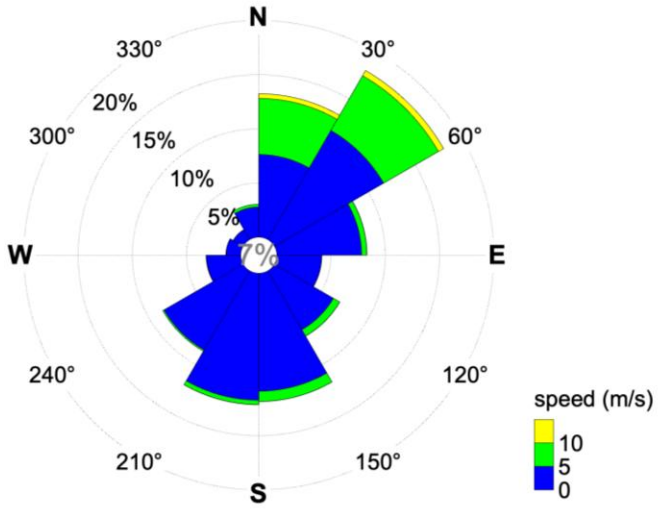

Figure 37. Wind rose for the measurement period 04/03/2016 – 30/10/2023 of the GEPOA dataset. The value at the center of the polar diagram (7%) corresponds to the percentage of wind calms (average wind speed over 10 minutes < 0.5 m/s) recorded.

Probabilistic analysis of wind speed and direction timeseries

This section reports the results of the probabilistic analysis performed on wind speed and direction measurements (averages over 10 minutes) of the GEPOA dataset for the period 04/03/2016 – 30/10/2023.

The present probabilistic analysis was performed both on the overall time series (population) of the wind speed (non-directional analysis), for both data population and extreme values, and subdividing it according to the incoming wind direction (directional analysis), considering 12 sectors 30° wide (from 0° to 360° with step 30°), only for the data population. For this latter analysis, the wind values between 21/07/2022 and 20/03/2023 were disregarded due to poor resolution of direction measurements.

Details of the probabilistic analysis of the data population performed in non-directional and directional form are reported above.

The results of the data population analysis are summarised in Table 7. The first 12 rows of the table refer to the directional analysis, while the last row shows the results of the non-directional analysis. On the left side (columns 2-6) for each directional sector, and in the last row for the whole population, the mean value and standard deviation of wind speed (average values over 10 minutes), the coefficient A_j and parameters k_j (shape parameter) and c_j (scale parameter) of the Weibull model, estimated by the resistant method (see above). The last line of the Table 7 reports the same estimates in non-directional form.

The regressions corresponding to the application of equation (4) (blue line) and equation (6) (cyan line) to the measured data are given in Figure 38 and, in terms of exceeding probability, in Figure 39.

Details of the probabilistic analysis of the extreme values performed in non-directional form are given above. The asymptotic distribution of the type I (Gumbel, 1958) was used to carry out the analysis.

The regression of Eq. (7) using the robust method (Hoaglin et al., 1983) allows for the derivation of the parameters of the Gumbel distribution.

Table 7. Parameters of directional and non-directional probability distributions (last line) for the wind speed timeseries (10-minute averages). Measurement period 04/03/2016 – 30/10/2023 for the GEPOA dataset.

Genoa – Porto Antico (GEPOA), 04/03/2016-30/10/2023 — Months 1-12

						Speed corresponding to exceedance probability 10**(-P)									
Sector	**Mean**	**StDev**	**A**	**K**	**C**	**1**	**2**	**3**	**4**	**5**	**6**	**7**	**8**	**9**	**10**
0- 30	4.097	2.692	0.081	1.469	4.545	8.018	12.852	16.936	20.598	23.976	27.144	30.146	33.014	35.770	38.429
30- 60	4.602	2.782	0.168	1.637	5.149	8.569	13.086	16.763	19.982	22.900	25.597	28.124	30.513	32.789	34.968
60- 90	2.702	1.993	0.108	1.636	2.948	4.909	7.498	9.607	11.454	13.128	14.675	16.125	17.497	18.803	20.054
90-120	1.200	0.754	0.042	2.224	1.343	1.954	2.669	3.203	3.645	4.029	4.374	4.688	4.978	5.249	5.503
120-150	2.378	1.603	0.053	1.705	2.629	4.287	6.437	8.165	9.665	11.017	12.260	13.420	14.513	15.551	16.542
150-180	3.088	1.423	0.094	2.390	3.476	4.928	6.586	7.804	8.802	9.664	10.430	11.125	11.765	12.359	12.916
180-210	2.562	1.210	0.110	2.617	2.864	3.939	5.133	5.993	6.689	7.285	7.810	8.284	8.718	9.119	9.494
210-240	2.115	0.990	0.101	2.862	2.356	3.153	4.017	4.629	5.118	5.533	5.897	6.223	6.521	6.794	7.049
240-270	2.064	0.883	0.042	2.784	2.310	3.116	3.997	4.624	5.127	5.555	5.931	6.269	6.577	6.861	7.126
270-300	2.034	1.011	0.016	2.245	2.288	3.318	4.518	5.412	6.151	6.794	7.369	7.893	8.376	8.827	9.251
300-330	1.696	0.980	0.009	2.095	1.898	2.826	3.935	4.775	5.478	6.094	6.648	7.156	7.627	8.068	8.484
330-360	2.090	1.618	0.024	1.621	2.278	3.811	5.845	7.506	8.964	10.287	11.512	12.661	13.748	14.785	15.778
0-360	3.004	2.158	0.926	1.714	3.285	5.344	8.009	10.146	12.001	13.670	15.205	16.636	17.984	19.263	20.485
Frequency of wind calms			0,070												

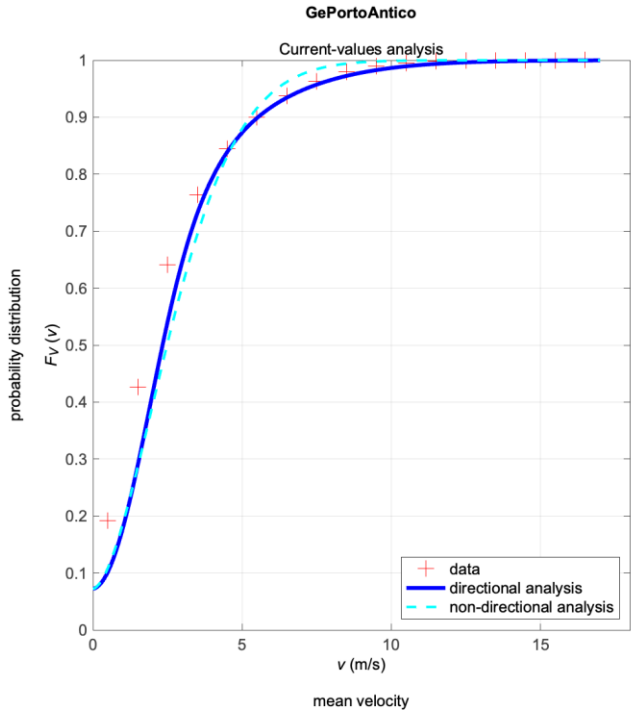

Figure 38. Cumulative distribution of wind speed (average over 10 minutes). Measurement period 04/03/2016 – 30/10/2023 for the GEPOA dataset.

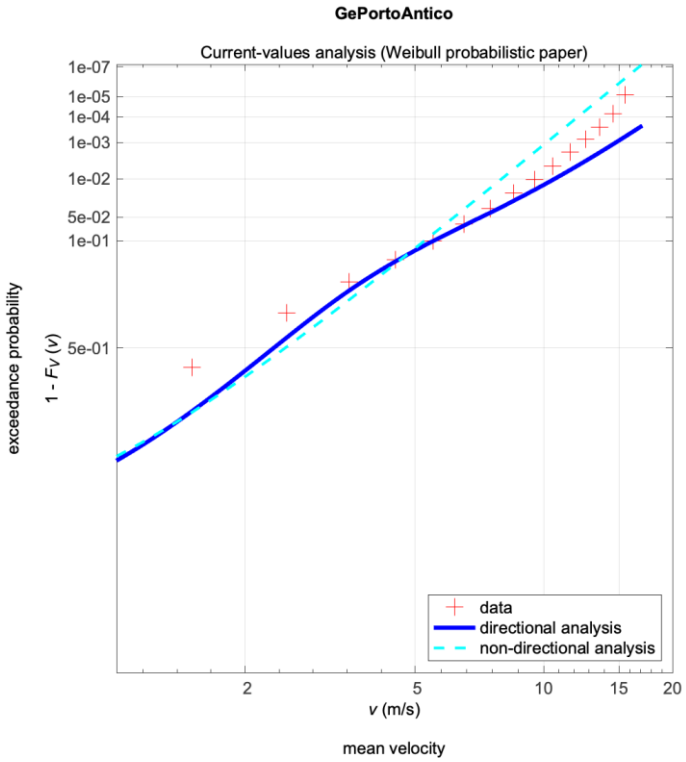

Figure 39. Exceeding probability of wind speed (average over 10 minutes). Measurement period 04/03/2016 – 30/10/2023 for the GEPOA dataset.

Figure 40 shows the joint density function of wind speed and direction (the values of which are listed on the right side of the Table 7) in polar form: the points in the innermost diagram correspond to the average wind speed coming from sectors 30° wide, with exceeding probability equal to 1% (10-2), while the points of the outermost diagrams correspond to exceeding probabilities of up to 0.001‰ (10-6). The diagram shows that the highest wind speeds, which correspond to the rarest events, are associated with the directions coming from the north-northeast.

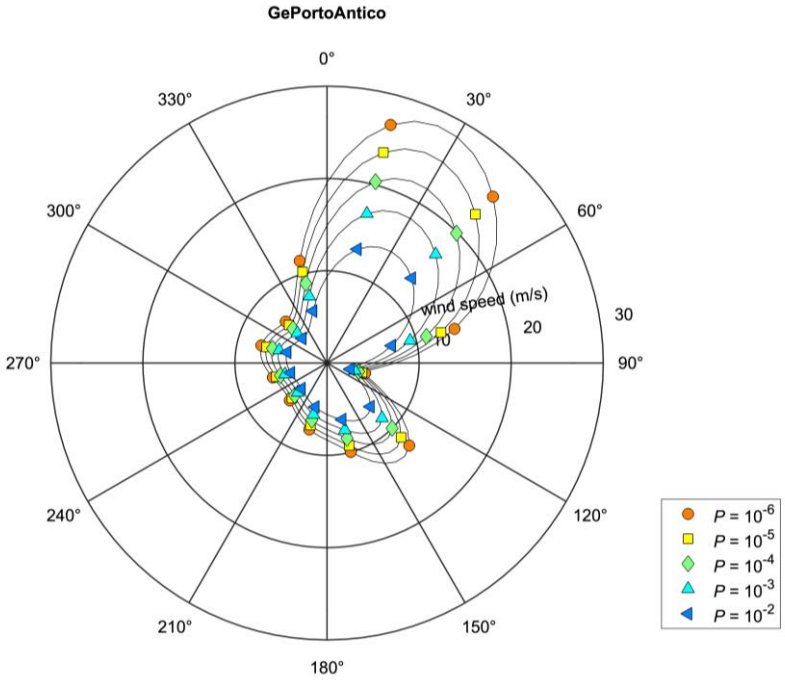

Figure 40. Polar diagram of probability distributions of directional wind speed (average over 10 minutes) for the GEPOA dataset.

Figure 41 shows the extreme value (EV) asymptotic distribution of type I (Gumbel distribution) (Gumbel, 1958) applied on the yearly maxima in non-directional form. Table 8 shows the estimated velocity maxima $V_{\max}$ associated with different return periods T_{R}.

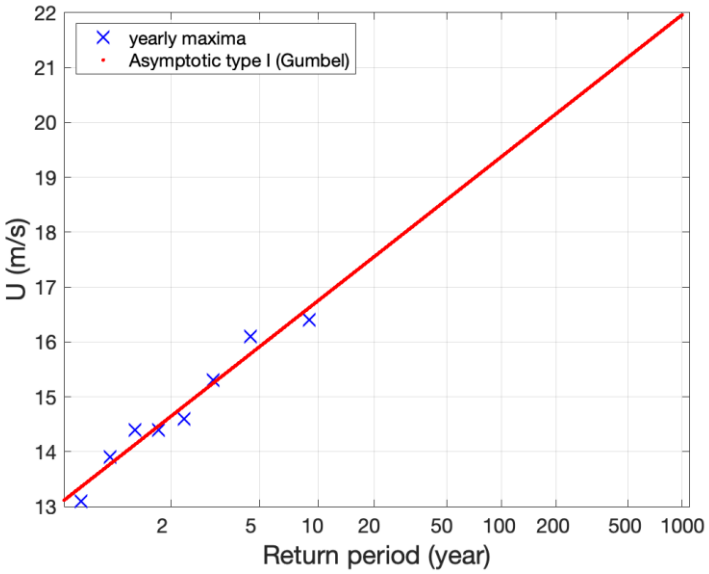

Figure 41. Type I EV distribution applied on the measured yearly maxima for the GEPOA dataset.

Table 8. Velocity maxima V_{max} associated with different return periods T_R for the GEPOA dataset.

T_R (years)	V_{max} (m/s)
2	14.64
5	15.91
10	16.75
20	17.56
50	18.60
100	19.38
200	20.16
500	21.18

Extreme wind speed values

Following Eq. (8), Table 9 reports the extreme wind speed values associated with different return period for the eight met-stations analyzed.

Table 9. Velocity maxima V_{max} associated with different return periods T_R for all datasets analyzed.

T_R (years)	V_{max} (m/s)							
	GEPOA	FFRES	RIGHI	GECER	GEPVA	STILA	MOPEN	PTURC
2	14.64	28.64	14.62	10.78	17.94	9.28	25.76	17.19
5	15.91	34.14	15.88	12.05	21.38	10.10	28.74	20.02
10	16.75	37.78	16.71	12.90	23.66	10.64	30.72	21.89
20	17.56	41.28	17.51	13.71	25.85	11.15	32.61	23.68
50	18.60	45.80	18.55	14.76	28.68	11.82	35.06	26.00
100	19.38	49.19	19.33	15.54	30.80	12.32	36.90	27.74
200	20.16	52.56	20.10	16.33	32.91	12.82	38.72	29.48
500	21.18	57.02	21.12	17.36	35.69	13.48	41.14	31.77

Figure 42 shows the map of extreme wind speed values corresponding to a return period T_R = 50 years for the met-stations of the ARPAL network. The wind speed contour covers the portion of the Municipality of Genoa defined by the locations of the met-stations. The maps were generated through bilinear interpolation of the values presented in Table 9. However, the comparison of wind speed values across different met-stations and, consequently, the interpretation of the maps themselves, proves to be rather misleading. This is due to the unique characteristics of the sites where each met-station is situated, including the orography (roughness and topography) as well as the installation height above sea level (ASL), both of which significantly influence the intensity of the recorded wind speeds.

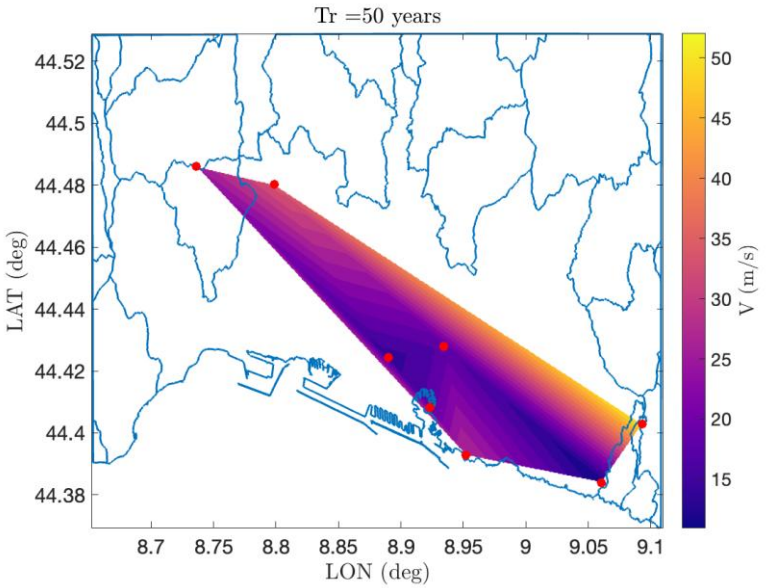

Figure 42. Map of bi-linearly interpolated extreme wind speed values in the Municipality of Genoa, for return period T_R = 50 years. Red circles indicate the locations of the met-stations.

3.3.1.3 Extraction of thunderstorm events

A series of thunderstorm wind events was extracted from ultrasonic anemometers and LiDAR Profilers installed within the WP and WPS wind monitoring network described in Section 3.3.3.

When handling vast amounts of data, it is essential to establish an analytical criterion for extracting and classifying wind speed records into homogeneous categories. For the wind speed database recorded during the WP and WPS projects, De Gaetano et al. (2014) developed a semi-automated procedure applied to records with a peak wind speed $\hat{V}$ greater than 15 m s-1. This threshold aligns with numerous studies in the literature (Choi, 2000, 2004; Durañona et al., 2007) and was chosen to enhance the statistical representation of the results. In contrast, other researchers have set higher peak wind speed thresholds (Canepa et al., 2020; Geerts, 2001; Lombardo et al., 2014) to increase the engineering relevance of the information.

The semi-automated algorithm involves systematic quantitative control followed by qualitative expert judgment. The quantitative control is primarily based on the gust factor, defined as the ratio between the peak $\hat{V}$ and mean $\bar{V}$ wind speeds in a time interval $\Delta t = 10$ min, $G_{10} = \hat{V}_{10}/\bar{V}_{10}$. The records that presented gust factors $G_{10} > 1.5$, indicating relatively low mean wind speeds and large isolated peaks, were initially identified as potential thunderstorm outflows. These records were then qualitatively double-checked to confirm if they exhibited a characteristic downburst-like time series, typically marked by a rapid increase in wind speed, a distinct isolated peak, and a subsequent period of relatively stable velocity, followed by a return to low values as the storm dissipates (Burlando et al., 2018; Canepa et al., 2020).

Full-scale signals are characterized by significant variability and complexity, mainly due to interactions between the downburst and background horizontal wind in the atmospheric boundary layer (ABL). The mutual positioning of the downburst and measuring instruments, especially during a storm, significantly influences the signals recorded at the anemometric station. Ground roughness also affects the downburst outflow at low heights above ground level (AGL). Recently, these interactions were thoroughly investigated experimentally on a large scale by Canepa et al. (2022a, 2022b, 2022c, 2023; Canepa et al., 2024).

The extracted events varied in the duration of the downburst-related portion of the wind speed record. Burlando et al. (2018) classified these events into three categories based on the time scale revealing the wind speed ramp-up and peak (10 minutes, 1 hour, and 10 hours). While the 10-minute and 1-hour records typically reflect the downburst nature of the events, the 10-hour signals are more likely to be thunderstorm-like severe gust fronts originating from extra-tropical cyclone windstorms.

Meteorological Feedback

All extracted records were cross-checked with meteorological information provided by the International Center for Environmental Monitoring (CIMA Research Foundation). The following meteorological data were analyzed for each event:

- Cloud top height distribution [m] from cloud analysis by Eumetsat, based on infrared measurements from SEVIRI onboard Meteosat second-generation satellites.
- Cloud hydrometeor reflectivity [dBZ] from radar analysis performed by:
- Constant-Altitude Plan Position Indicator (CAPPI), which provides reflectivity at several horizontal planes (2 – 8 km above ground).
- Vertical Maximum Intensity (VMI), which shows the maximum reflectivity value on the vertical plane above each point in the domain.

- Lightning map based on the SFLOC (spheric location) method, which gauges atmospheric electrical discharges by measuring the travel time of electromagnetic waves between clouds and the ground. Using ad hoc sensors, it identifies the strike position with an accuracy of 0.5 km.

This information is crucial for verifying the nature of the phenomenon. Downbursts originate from cumulonimbus clouds that can extend to high altitudes AGL, often reaching the tropopause at approximately 11 km AGL. Satellite imagery is vital for identifying potential thunderstorms. Additionally, wet downbursts are common in the Mediterranean (Burlando et al., 2018), and data on precipitation intensity, linked to measured air parcel reflectivity, provide essential insights. Lightning occurrences also uniquely detect thunderstorm activity.

3.3.1.4 Anemometric Database

The comprehensive extraction procedure described above identified 29 verified thunderstorm events that occurred between 2010 and 2015 in the Northern Tyrrhenian Sea.

Specifications of Measuring Instruments Involved

Wind signals were recorded using ultrasonic anemometers (Gill Instruments Limited) located at the ports of Genoa, Livorno, and La Spezia. The port of Livorno is equipped with tri-axial anemometers (Gill WindMaster Pro), except for biaxial anemometers LI06 and LI07, which also retrieve the vertical wind speed component (w). Genoa and La Spezia are equipped with biaxial anemometers (Gill WindObserver II), providing the two horizontal wind speed components (u and v), where u is the west-to-east component and v is the south-to-north component. Figure 43 shows the two types of anemometers used during the campaign. The acquisition frequency of all instruments was 10 Hz, with a wind speed measurement sensitivity of 0.01 m/s, except for LI06 and LI07, which had a sensitivity of 0.1 m/s, in a wind speed range of 0–65 m/s. Ultrasonic anemometers measure instantaneous wind speeds by recording the travel time of an ultrasonic pulse between pairs of transducers, providing precise information on the airspeed along the instrument's principal axes.

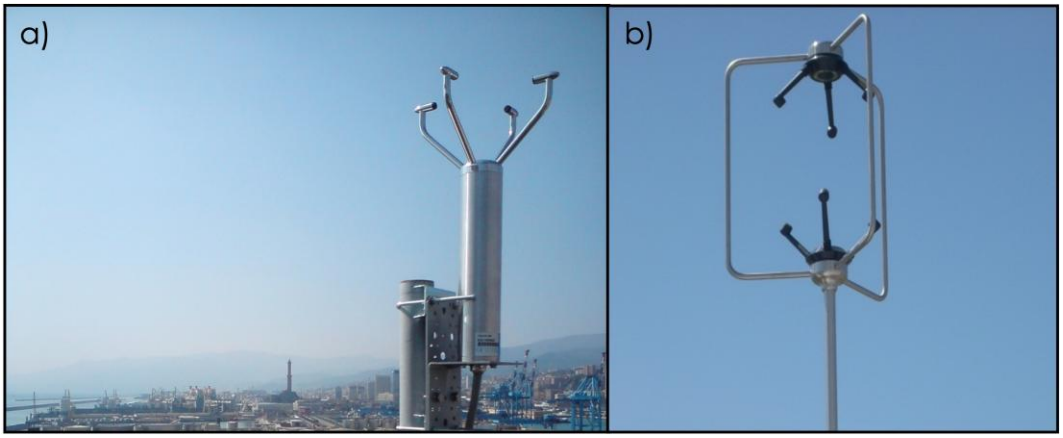

Figure 43. Bi-axial Gill WindObserver II anemometer in the port of Genoa (a) and tri-axial Gill WindMaster Pro anemometer in the port of Livorno (b).

Figure 44 illustrates the geographical distribution of the ultrasonic anemometers used in this study. Table 10outlines the specifications of these instruments, highlighting their varying installation heights, ranging from 13.0 to 75.0 m AGL. Owing to malfunctioning, maintenance activities, offline status, and various operational reasons by port authorities, the number of functioning anemometers varied from event to event.

Table 10. Specifications of ultrasonic anemometers involved: port code (GE – Genoa, LI – Livorno, SP – La Spezia); anemometer ID; geographical coordinates (latitude – Lat., longitude – Lon., height above ground level – h AGL) referred to WGS84 reference system; instrument type.

Port code	Anemometer ID	Lat. (°) WGS84	Lon. (°) WGS84	h AGL (m)	Ultrasonic anemometer type
GE	01	44.399494	8.924961	61.4	Bi-axial
GE	02	44.417539	8.776983	13.3	Bi-axial
GE	03	44.399638	8.925033	32.0	Bi-axial
LI	01	43.569594	10.301397	20.0	Tri-axial
LI	02	43.582747	10.307178	20.0	Tri-axial
LI	03	43.557986	10.290489	20.0	Tri-axial
LI	04	43.541456	10.293517	20.0	Tri-axial
LI	05	43.580178	10.31855	75.0	Tri-axial
LI	06	43.549286	10.296181	12.0	Bi-axial
LI	07	43.553862	10.306564	23.8	Bi-axial
SP	01	44.106000	9.829990	15.5	Bi-axial
SP	02	44.110120	9.838980	13.0	Bi-axial
SP	03	44.097330	9.857890	10.0	Bi-axial
SP	04	44.067030	9.816420	11.0	Bi-axial
SP	05	44.081300	9.881460	10.0	Bi-axial
SP	06	44.073333	9.840923	16.0	Bi-axial

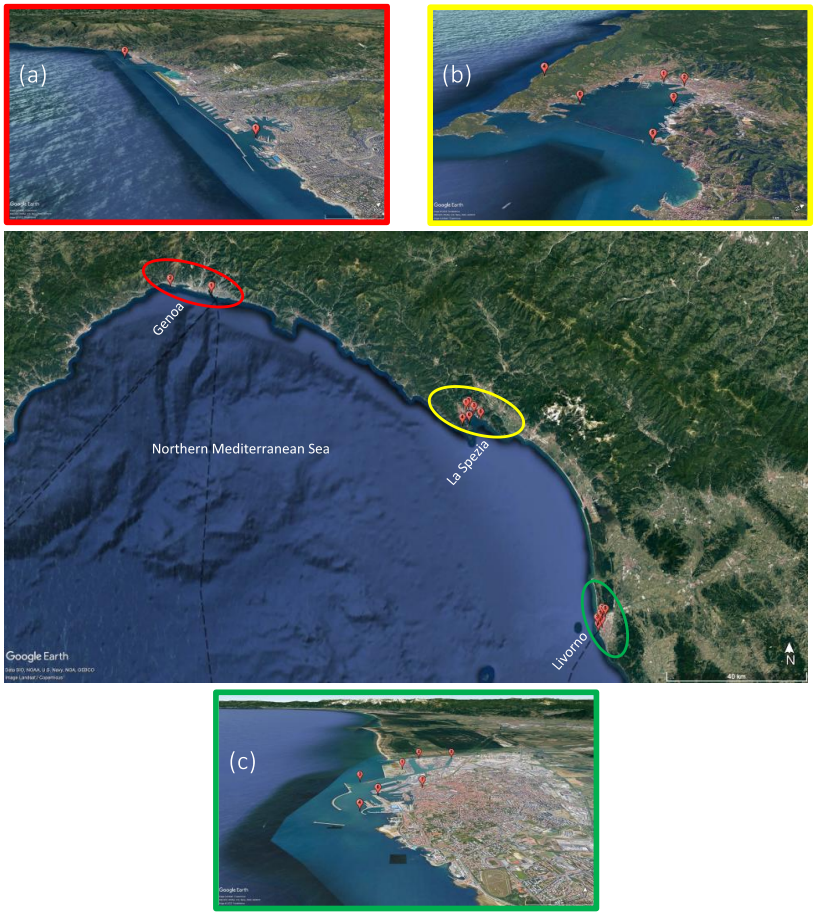

Figure 44. Location map of anemometers involved in the study. Closer view of the port areas of (a) Genoa, (b) La Spezia, and (c) Livorno. Images sourced from Google Earth Pro.

Thunderstorm events included in the database

The downburst measurement database consists of 99 ASCII text files, each representing a 10-hour recording from a single anemometer. This means the database includes more files than the number of extracted events, allowing users to perform cross-correlation analyses in space and time, even with a limited number of points (anemometers) for a specific event in a port area. This method facilitates the investigation of the three-dimensional characteristics of the phenomenon, potentially uncovering important details such as storm size, position, and trajectory.

Further details on the anemometric database of thunderstorm wind events are extensively documented in Canepa et al. (2024).

3.3.1.5 LiDAR Database

This section investigates three LiDAR wind profilers installed at the ports of Genoa, Livorno, and Savona. These profilers measure the three components of wind velocity at 12 heights above ground level (AGL) (40, 50, 60, 80, 90, 100, 120, 140, 160, 180, 200, and 250 meters) with a sampling rate of 1 Hz, allowing for a continuous reconstruction of the wind speed vertical profile. An ultrasonic anemometer, typically positioned at about 10 meters AGL, is always located near the LiDAR system to provide wind field data from the lower levels.

Specifications of Measuring Instruments Involved

The LiDARs (codes GE.51, LI.51, and SV.51) were installed between 2014 and 2015. The first LiDAR was installed in Savona in the second quarter of 2014, with the ones in Genoa and Livorno following approximately a year later. The measurement databases for these LiDARs cover periods from their respective installation dates until August 31, 2018, which is the last date considered in this analysis. Data acquisition discontinuities are attributed to malfunctions, routine maintenance, and, in the case of LI.51, vandalism. Other data gaps are due to heavy precipitation, which reduces the maximum measurement height because of scattering from raindrops.

Each LiDAR is a ground-based pulsed coherent system manufactured by Leosphere, commercially known as "WindCube V2." It emits highly collimated light energy pulses at regular intervals (pulse length). For each azimuth angle, the line-of-sight (radial) velocity v_r is calculated based on the Doppler shift principle, or the time shift of the backscattered light.

At a fixed vertical angle, typically 30°, the LiDAR measures four sequential radial velocities $v_{r,\theta}$ around the circle formed by a conical scanning, i.e. θ = 0°, 90°, 180° and 270°, plus one vertical measurement above the LiDAR. The time step between two subsequent pulses is 1 second, resulting in a complete conical scan every 5 seconds. The three wind velocity components are derived from these measurements, and assuming horizontal homogeneity of the wind field over the sensed height, the wind velocity vector can be considered representative of the central point of the scan circle (Figure 45).

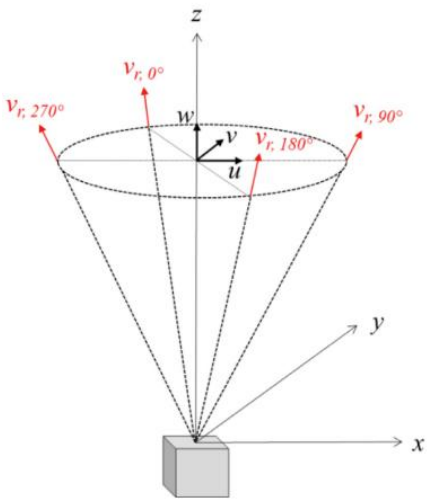

Figure 45. Scheme of the LiDAR and scanning method.

All wind speed measurements at a given azimuth angle are acquired simultaneously along the vertical profile due to the pulsed nature of the system. In contrast, other commercial LiDAR profilers, such as the ZephIR system, perform continuous conical scans from bottom to top. However, the non-simultaneity of the recorded profiles makes this type of LiDAR less suited for engineering purposes, especially for reconstructing transient events like downbursts. The LiDARs in this study measure with a sensitivity of 0.1

m/s for wind speed and 2° for wind direction. The variance in the recorded velocity is influenced by the volume filtering performed by the system, which can be predicted and partially corrected theoretically.

LiDAR reconstructs the wind speed at each sensed height by averaging five 1-Hz measurements, considering the width and depth of the resulting cone of measurements, which increases with elevation. A limitation of LiDAR is the non-independence of these measurements, as each azimuthal measurement is combined with the four previous ones. Therefore, none of the radial velocities can be considered independent of the preceding and following measurements. However, comparison between anemometric and LiDAR time series shows very good agreement at time scales of about two seconds.

Thunderstorm events included in the database

Following an automated control process similar to that used to create the anemometric database, visual and qualitative inspections of the signals were conducted to verify whether they resembled the typical pattern of downburst time histories, characterized by a sudden ramp-up of velocity followed by a peak and dissipation stage. Finally, interpretations and cross-check analyses with meteorological information were performed. This process allowed the selection and examination of a subset of 10 downbursts from the entire dataset of events extracted with the automated procedure. The related parameters, shown in Table 11, are based on a time period $\Delta t = 10$ min, containing the development of the storm, in agreement to the analytic criterion of extraction.

Table 11. Downburst events extracted: port, date and time of occurrence; maximum gust factor and its height, $G_{10_{max}}$ and $z(G_{10_{max}})$; maximum 1-Hz wind speed $U_{max,10}$ at the height $z(G_{10_{max}})$; absolute maximum 1-Hz wind speed $U_{max,10}$ and its height $z(U_{max,10})$; gust factor G_{10} at the height $z(U_{max,10})$.

Port	Date (YYYYMMDD)	Time (hh:mm) UTC	$G_{10_{max}}$	$z(G_{10_{max}})$ [m]	$U_{max,10}$ [m/s] at $z(G_{10_{max}})$	$U_{max,10}$ [m/s]	$z(U_{max,10})$ [m]	G_{10} at $z(U_{max,10})$
GE	20150814	22:15	2.46	100	21.2	21.4	90	2.37
GE	20150815	19:55	2.53	200	24.9	31.8	60	1.84
GE	20160305	08:15	1.53	80	22.9	23.1	200	1.33
GE	20160503	18:15	2.87	80	21.3	24.3	140	2.82
GE	20180412	16:20	1.64	80	18.3	19.4	200	1.56
GE	20180513	18:40	1.59	180	19.0	19.0	180	1.59
LI	20150725	09:50	2.00	40	21.6	21.6	40	2.00
LI	20150913	11:10	1.82	120	26.3	26.3	120	1.82
LI	20151028	19:30	1.67	40	20.3	22.4	250	1.44
LI	20180604	10:10	1.65	250	18.8	19.4	100	1.53

Figure 46 depicts, at the height of $G_{10_{max}}$ defined in Table 1, the 20-min time histories of the slowly-varying mean wind speed $\overline{U}(t)$ (Eq. (2)) and direction $\overline{\alpha}(t)$ (Eq. (4)) for the 10 events extracted and classified as thunderstorms.

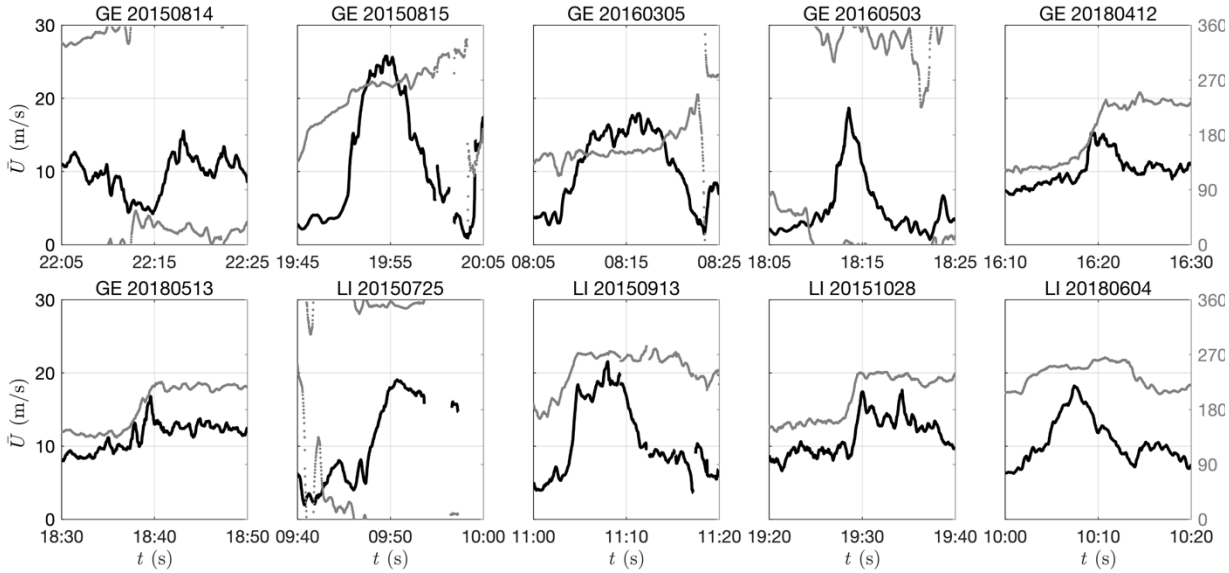

Figure 46. Downburst events extracted: slowly-varying mean wind speed (black line) and direction (gray line) time histories. Event names are given in terms of station, SS, year, YYYY, month, MM, and day, DD.

Table 12 presents the key meteorological information extracted from the corresponding diagrams, providing a quantitative basis for defining the subset of events. According to Fujita and Wakimoto (1983), a downburst event is classified as wet if the 1-hour cumulative precipitation exceeds 0.01 inch/h (0.254 mm/h). Cumulative precipitation data were collected from stations at Madonna delle Grazie (Genoa) and Stagno (Livorno), located approximately 3.15 km northwest and 7.10 km northeast of the LiDARs in the ports of Genoa and Livorno, respectively.

Table 12. Main meteorological characteristics of the 10 downburst events according to radar (reflectivity [dBZ]), satellite (cloud top height [m]), lightning (strikes [Y/N]), and rain rate (ground cumulated precipitation [mm/h]) measurements, and corresponding downburst classification between wet and dry. Radar measurements were not available (NA) in 2015 in Livorno.

Port	Date (YYYYMMDD)	Time UTC	Reflectivity [dBZ]	h_{cloud} [km]	Lightnings (yes [Y], no [N])	1-h precipitation [mm/h]	Downburst type
GE	20150814	22:15	50	12	Y	13.4	Wet
GE	20150815	19:55	48	11	Y	5.4	Wet
GE	20160305	08:15	27	11.5	N	9.5	Wet
GE	20160503	18:15	22	7.5	N	0	Dry
GE	20180412	16:20	31	9	N	4.4	Wet
GE	20180513	18:40	24	9.5	N	3	Wet
LI	20150725	09:50	NA	15	Y	6.4	Wet
LI	20150913	11:10	NA	12.5	Y	14	Wet
LI	20151028	19:30	NA	12	Y	9.2	Wet
LI	20180604	10:10	18	12	Y	0	Dry

Details on the thunderstorm extraction from the analyzed LiDAR Profilers can be found in the paper by Canepa et al. (2020) along with a thorough analysis of their physical characteristics in the view of structural applications.

3.3.2 Extreme precipitations

This section synthesizes recent results obtained in two main research fields related to pluvial flooding hazard assessment in urban areas addressing, in particular, the enhanced accuracy required for the knowledge of the rainfall input in terms of intensity, frequency and spatial/temporal distribution of the phenomenon. The first part deals with rainfall measurement issues, and the text is largely derived from the book chapter by Lanza and Cauteruccio (2022). The second part describes the role of extreme rainfall events relevant for pluvial flooding and their space/time patterns and was recently published in the paper by Loglisci et al. (2024).

3.3.2.1 The accuracy of rainfall data

In situ liquid and solid precipitation measurements are the essential source of information about the precipitation process, its spatiotemporal variability, and observed frequency. Two main classes of in situ measurement instruments can be identified: catching gauges (CGs), collecting precipitation into a container before the accumulated volume of water is measured over a given period using various principles, and non-catching gauges (NCGs), requiring no container to collect precipitation. Most NCGs (called disdrometers) detect the size and fall velocity of each single hydrometeor in flight through the sensing area, while some of them derive this information from the dynamic action of hydrometeors when impacting the surface of the sensor. All instruments are subject to measurement biases and uncertainties but, due to the specificity of the precipitation process (typically an ensemble of hydrometeors falling to the ground with varying size, shape, density, and velocity), the quantification and adjustment of such biases are more complex than for other essential environmental variables (e.g., air temperature and atmospheric pressure). High-resolution measurements, even down to the scale of the single hydrometeor in some cases, are the way to achieve better knowledge of the precipitation process and to increase the confidence of users in the accuracy of their basic source of information. The most relevant biases indeed arise at the finest scales of the precipitation process and/or are determined by the response of each single hydrometeor to the potentially disturbing factors at the measurement site.

Precipitation measurements obtained from both CGs and NCGs are affected by systematic biases due to instrumental and environmental sources. These can be classified into two main categories: catching and counting biases. Catching biases derive from the difficulty of the instrument to collect/detect (for CG and NCG, respectively) the exact amount of water falling over the projection of the measurement area on the ground and are caused by wind (recognized as the main factor, see Cauteruccio et al., 2024 and Chinchella et al., 2024 for CGs and NCGs, respectively), evaporation, and the splashing and wetting phenomena. Counting biases depend on the ability of the instrument to correctly quantify the amount of water that is collected/detected by the instrument. They depend on the inherent characteristics of the counting device: the mechanics of the tipping-bucket rain gauges (TBRGs), the filtering algorithm used to remove the signal noise from weighing gauges (WGs) raw data, and the interpretation algorithm characterizing each measurement principle exploited by NCGs (optical, microwave-, and impact-based principles are mostly used). Counting biases have a strong influence on CG rainfall measurements, being generally a function of the RI. The calibration procedure described in the Italian standard (UNI, 2012) and in the recent

European standard (CEN, 2019), to be performed in controlled laboratory conditions, allows to quantify the counting biases and to derive calibration curves to adjust RI measurements. Calibration is performed by comparing the gauge measurement with a known flow rate obtained by using a precision pump and checked by employing a high-resolution weighing device.

A systematic mechanical bias characterizes the mechanics of TBRG, the most used type of CG worldwide, since they increasingly underestimate rainfall as the RI increases. This underestimation is due to the water amount that is lost during the tipping movement of the bucket, as described by Marsalek (1981). This bias is gauge dependent and varies with RI. It can be adjusted by means of laboratory calibration, that must be periodically repeated during the service life of the instrument, to remove any possible additional source of error. Between two subsequent laboratory tests, the calibration of CGs can be verified in the field by using a portable field calibration device (see WMO, 2014), allowing rapid calibration tests.

For the laboratory calibration of NCGs (Lanza et al., 2021) recently, the European project INCIPIT – "Calibration and accuracy of non-catching instruments to measure liquid/solid atmospheric precipitation", funded by the European Association of Metrology Institutes (EURAMET) under the European Metrology Programme for Innovation and Research, has developed and proposed a metrologically sound calibration procedure (Merlone et al., 2022). The procedure has now been adopted by the Technical Committee TC318 of CEN (the European Committee for Standardization) as the normative project prEN 18097:2024. The proposed normative procedure also allows the classification of non-catching precipitation measurement instruments based on their calibration results, like the existing standard EN 17277:2019 on the calibration of CGs.

The calibration of NCGs is based on the comparison of measured water drop size and fall velocity values with the reference ones. If the raw data are not provided in output by the instrument, derived quantities such as the precipitation intensity and kinetic energy can be used. The calibration tests are carried out through the generation of sets of water drops with specific controlled diameter which are released at a fixed heigh over the sensing area or volume of the instrument. The drop size and fall velocity reproduced by the generator of drops are measured independently, before reaching the disdrometer, using a photogrammetric method (see Baire et al., 2021) and then compared with the output of the disdrometer.

3.3.2.2 Research conducted within the RETURN project

The research described below is published in Loglisci et al. (2024) and was conducted as a collaboration among the Department of Civil, Chemical and Environmental Engineering - DICCA (University of Genova – Unige, Italy) the Department of Earth, Environment and Life Sciences – DISTAV (Unige, Italy), CIMA Research Foundation (Savona, Italy), National Research Council - Research Institute for Geo-Hydrological Protection CNR-IRPI (Turin, Italy) and Geographical Information Systems International Group - GISIG (Genoa, Italy) within the activities of the RETURN project (Vertical Spoke 1 - VS1 "Water", Work Package 2 - WP2 "Flood risk under environmental and climatic changes" by Dr. Cauteruccio Arianna, Prof. Boni Giorgio) and the Horizon H2020 project I-CHANGE (Individual Change of HAbits Needed for Green European transition) (grant no. 101037193).

The Mediterranean region is characterized by a rainfall regime with short-duration and high-intensity events, which typically show a quite limited spatial extension and very rapid evolution and are therefore, in some cases, difficult to capture by traditional monitoring networks due to the too coarse spatial

coverage. Urban areas are affected by pluvial flooding resulting from the inefficiency of urban drainage systems and by riverine floods, from the overtopping of small streams (often covered and/or with narrowing sections) in orographically complex and steep areas. Since storm water drainage in the urban texture is structured in a great number of small-size catchments, usually smaller than the typical spacing of rain gauge stations, urban catchments are often ungauged.

Depth–duration–frequency (DDF) relationships derived from a rain gauge positioned in a contiguous urban catchment could estimate a return period associated with a specific rainfall depth that would affect the design of the pipe size or of potential structural adjustments of the drainage network. The temporal resolution of rainfall measurements also plays a key role in the study of flood events: the faster the hydrological response of the basin, the finer the required resolution of the supporting data. The World Meteorological Organization (WMO) developed the Observing Systems Capability Analysis and Review (OSCAR) tool (https://space.oscar.wmo.int/, last access: 12 July 2024) that contains quantitative user-defined requirements for observation of physical variables related to weather, water, climate, and other application areas. Regarding the variable precipitation intensity and the nowcasting/very-short-range forecasting application area, which can be considered relevant for small catchments, OSCAR reports that the highest performance level (indicated with the term “goal”) can be reached using measurements at a spatial resolution of up to 1 km and a temporal resolution of 5 min.

The case study of this work is the occurrence of pluvial flooding in the historic centre of the city of Genoa (Italy). Both the accuracy of rain gauge measurements and the spatial distribution of rain gauges are discussed in the analysis of rainfall extremes relevant for pluvial flooding in the study region. The large spatial variation in rainfall intensity, especially for short-duration events, is shown below to arise from the analysis of rainfall statistics obtained from rainfall records of contiguous rain gauge stations in the city of Genoa. A reference station was selected because of the high accuracy and fine resolution of the available data. Four other rain gauge stations were selected within a radius of 1.5 to 8.0 km from the reference station. Monthly rainfall totals and extreme value statistics of short-duration/high-intensity events were compared to show that, even within such a short distance, the variation in the expected maximum rainfall is significant.

Three stations are managed by the environmental protection agency of the Liguria region (ARPAL) and are equipped with the FAK010AA rain gauge manufactured by Mtx s.r.l, which provides measurements of the rainfall intensity (RI) with a temporal resolution of 5 min. They are called Castellaccio (AR-2), Centro Funzionale (AR-3), and Sant’Ilario (AR-4). Two other rain gauge stations, owned by the University of Genova are indicated in the following with the abbreviations GU and DICCA. The first (now equipped with a SIAP UM7525 rain gauge) is the source of a quasi-bicentennial rainfall time series and has been providing RI measurements with an hourly resolution since 2002 (Cauteruccio and Lanza, 2023). The DICCA station (manufactured by CAE S.p.A) is managed by the Department of Civil, Chemical and Environmental Engineering (DICCA) and has been providing RI measurements with a resolution of 1 min since 1988. The geographical coordinates (WGS84) and altitude above mean sea level of the rain gauge stations are listed in Table 13.

The time series of about 30 years of rainfall intensity measurements (from 1 January 1988 to 31 December 2021) at 1 min resolution available from the DICCA tipping-bucket rain gauge was here assumed as a

reference data set. Both raw and corrected data are available, after application of appropriate calibration curves, as derived at the laboratory of the World Meteorological Organization (WMO) Measurement Lead Centre on Precipitation Intensity. The calibration and adjustments applied are in accordance with the European standard EN 17277/2019 (CEN, 2019).

The other three rainfall time series analysed in this paper were obtained from stations AR-2, AR-3, and AR-4 for 12 years of high-resolution data (2011 to 2022). Finally, hourly rainfall data for the same period were also obtained from the GU station.

DDF curves were derived using the 30-year time series of corrected 1 min RI measurements from the DICCA reference rain gauge. A typical power law expression was used for the DDF curves, where the rainfall depth for a given duration and return period, T, is expressed as a scale coefficient, a(T), multiplied by the rainfall duration to the power of the shape coefficient, b.

Table 13. Geographical coordinates (WGS84) and altitude above mean sea level of the rain gauge stations.

Station code	N [°]	E [°]	Altitude [m]
DICCA	44.40	8.96	45
GU	44.42	8.93	58
AR-2	44.43	8.93	360
AR-3	44.40	8.94	30
AR-4	44.38	9.06	174

Due to the relatively short duration of the time series available from the nearby stations, only the DDF curves associated with return periods T = 1.5, 2.32, and 5 years were used in the analysis. These are also typical values of the return periods assumed in the design of urban drainage networks, beyond which the failure of the drainage system is accepted. Note that a return period of 2.32 years was chosen because it is associated with the mean value of the sample of annual maxima calculated for each event duration under the hypothesis of an underlying Gumbel distribution of rainfall extremes (Gumbel, 1941). For sub-hourly rainfall, the coefficient b is equal to 0.57, while a(T) is equal to 46.67, 62.53, and 84.59 mm h^{-b} for the three return periods used.

The year-to-year variability of monthly precipitation for 12 years of records at the four rain gauge stations studied is shown in Figure 47. The boxes and whiskers cover the central 50% and 80% of the data set, respectively. The mean and median values are indicated in each box by the horizontal red and black lines, respectively. The mean values, the extremes, and the annual variability observed at AR-4 are systematically higher than at the other stations. In the dry summer months, the relative difference between the mean precipitation at two neighbouring stations is limited, but in the wet months (autumn and spring), when intense precipitation is usually expected, this difference is greater, despite the short distance between them. Especially in autumn, the mean and the annual variability of precipitation are systematically lower at GU than at the other stations.

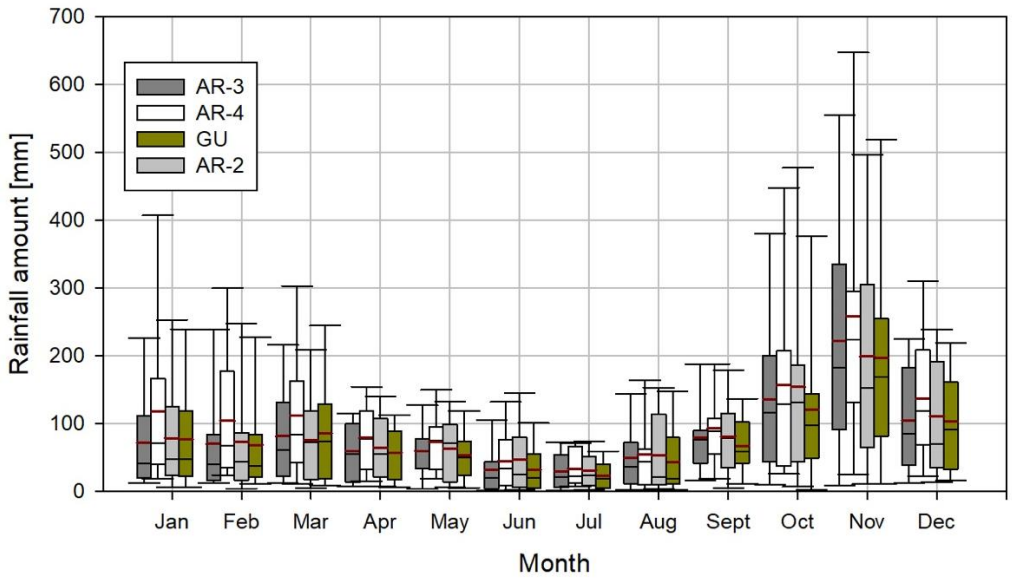

Figure 47. Year-to-year variability of monthly precipitation at the four rain gauge stations studied. Boxes and whiskers cover the central 50% and 80% of the data set, respectively. The mean and median values are indicated in each box by the horizontal red and black lines, respectively. [Source: Loglisci et al., 2024].

Differences in the precipitation regime at the stations considered are also evident for short-duration high-intensity events, as shown in Figure 48 based on the DDF curves calculated at the nearby reference station (DICCA). Short-duration events of 5, 10, 15, 30, 45, and 60 min were considered in the analysis, thus excluding the GU station due to the coarse time resolution (1 h) of the available data set. The mean value of the annual maxima at each station and for each duration can be compared with the reference DDF curve at T = 2.32 years. The percentage relative difference e (%) between such mean values at each of the investigated stations and at the reference station was therefore calculated (see Table 14). The comparison shows that short duration high-intensity events at the AR-3 station are up to 37% lower than the typical events at the reference station for any duration. Meanwhile, the statistics at the AR-4 station are close to the reference station for short-duration events (between 10 and 30 min), while longer-duration events are less intense, at least over the period studied. The AR-2 station shows an intermediate behaviour.

The results show that, for each duration, the mean values of the annual maxima at the AR-3 station are characterized by the same return period T = 1.5 years, while the AR-4 station exhibits the largest annual maxima for short-duration events (up to 15 min) with T = 2.32 years, then the return period decreases with increasing event duration, reaching 1.5 years at a duration of 60 min. For the AR-2 station, the mean annual maxima range from above to slightly below T = 1.5 years with increasing event duration. Note that for events shorter than 15 min, the AR-4 station is the closest to the reference station in terms of the return period of its annual maxima, although geographically it is the most distant.

However, the dispersion of the annual maxima around the mean value for this station reaches the longest return period studied (T = 5 years), with the limits of the interval covering 80% of the sample, which is not the case for any other station in the range of short-duration events. Therefore, a large variability is observed between the investigated stations, especially for short-duration events, which are typically associated with critical conditions in urban drainage systems and/or the occurrence of pluvial flooding.

The variability of extreme value statistics between the investigated rain gauge stations over the period considered reflects the spatial variability of short duration high-intensity events, even at the limited spatial scale of urban catchments.

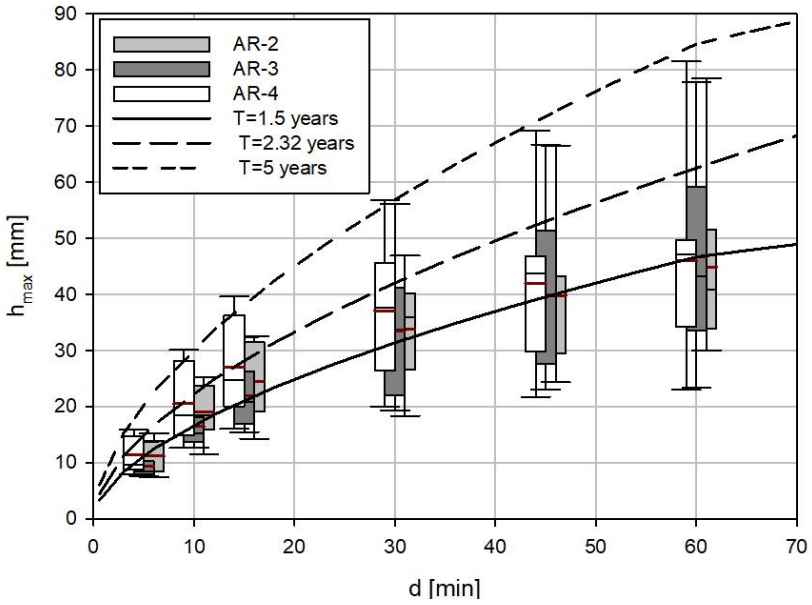

Figure 48. Annual maximum rainfall depth for each duration at the three ARPAL rain gauge stations studied (boxplot), overlaid with the DDF curves derived at the DICCA reference station. Boxes and whiskers cover the central 50% and 80% of the data set, respectively. The mean and median values are indicated in each box by the horizontal red and black lines, respectively. [Source: Loglisci et al., 2024].

Table 14. Percentage relative difference between the rainfall depth at each of the investigated stations and at the reference station (DICCA), for a 2.32-year return period (mean annual maxima).

	d = 5 min	d = 10 min	d = 15 min	d = 30 min	d = 45 min	d = 60 min
e(AR-2) [%]	-36	-15	-14	-20	-25	-28
e(AR-3) [%]	-37	-26	-22	-20	-25	-25
e(AR-4) [%]	-24	-9	-4	-12	-21	-26

3.3.3 Network of met-stations for statistical analysis of meteorological and climatological observations

Today, meteorological and climatological models are becoming increasingly vital, not just for the scientific community but for society as a whole. The demand for precise meteorological and climatic information is growing daily, and the response to this demand is also on the rise. This high demand reflects two main trends: the need for accurate data in a globalized world where industrialization and human activities impact every corner of the planet, and the influence of climate change on ecosystems and populations.

Recent climate studies and reports, such as the Intergovernmental Panel on Climate Change (IPCC) Assessment Report 6 (AR6) (IPCC, 2022), highlight the dramatic negative impacts of human activities and greenhouse gas emissions on Earth's climate. These activities have significantly increased global temperatures. On the other hand, technological advancements are helping meet the demand for climate information. Improved computational power enables more sophisticated meteorological and

climatological models, capable of resolving fine atmospheric and orographic details with horizontal resolutions of just a few kilometers.

Technological innovation has also led to the development of state-of-the-art measuring instruments, which can record high-fidelity temporal and spatial meteorological and climatological data. Lower costs have made it possible for a larger global community to install and use standard measuring systems. This widespread access is crucial for monitoring Earth's conditions and tracking climate change progress, as well as providing essential data for computational models. Climate studies (Faranda et al., 2022; Púčik et al., 2017; Rädler et al., 2018; Taszarek et al., 2019, 2020) indicate an increasing trend in the intensity of extreme events and the rapid alternation of opposing extremes (e.g., heatwaves and cold waves, droughts and heavy precipitation). This trend encompasses various extreme climate variables, such as rain, wind, temperature, and humidity. However, the frequency of extreme events varies depending on the climate parameter and region. For example, the frequency of extreme events in the Mediterranean basin is still debated, though models agree on the intensification of such events. Heatwaves and heavy precipitation are expected to increase in both frequency and intensity.

Given the Earth's surface heterogeneity and the varied impacts of climate change on different locations, regional-scale studies are increasingly important. Modern meteorological and climatological models often use global models' initial and boundary conditions to focus on specific areas.

This chapter presents two different case studies: a network of meteorological stations and of wind-measuring instruments in the municipality of Genoa, Italy.

3.3.3.1 Case Study 1 – Municipality of Genoa

Area of Investigation

The area under investigation is the Municipality of Genoa, located in northwestern Italy. Within and around this area, several meteorological stations provide data for the statistical characterization of key physical quantities, such as wind velocity and temperature. These stations are part of networks managed by the Municipality of Genoa and the Regional Agency for Environmental Protection (ARPAL).

Objective of the Study

To achieve statistical significance, it is crucial to select representative meteorological stations with medium- to long-term datasets. The data from these stations will be processed to calculate extreme value distributions, which will be used to create hazard maps for wind and temperature. These hazard maps can help stakeholders, such as the Municipality, assess potential climatic risks, such as high winds and temperatures, and issue timely alerts to the public. Additionally, the results of the statistical analysis are essential for climate studies and understanding climate change trends.

Map of met-stations

Figure 49 shows the locations of the meteorological stations managed by the Municipality of Genoa, with Table 15 listing the stations. Two types of stations are available: Davis stations, which measure wind speed and direction with resolutions of 0.5 m/s and 1°, respectively, and a sampling rate of 3 minutes; and MTX stations, which measure the 10-minute average wind speed and direction. Similarly, Figure 50 and Table 16 display the locations and list the meteorological stations managed by ARPAL.

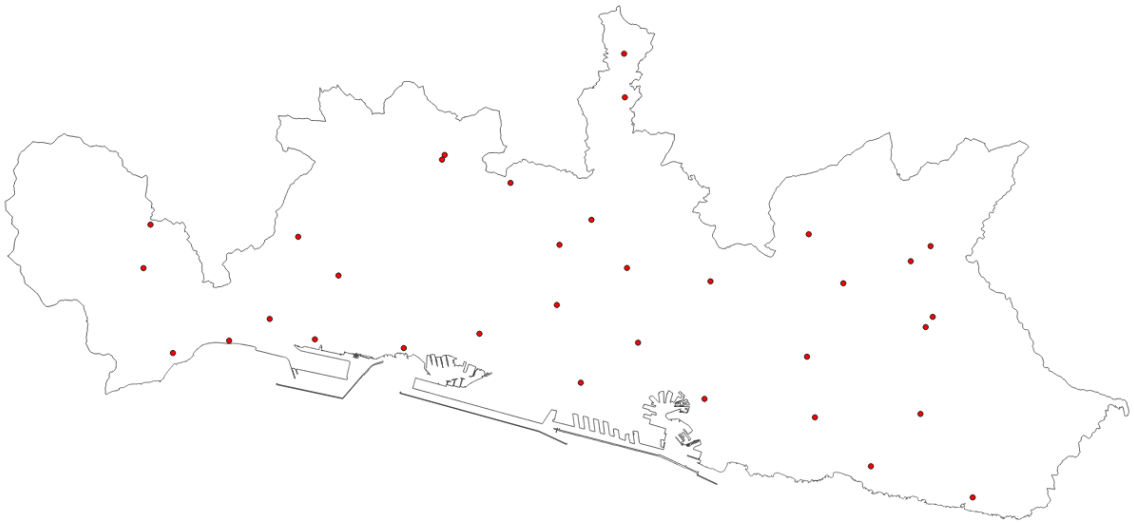

Figure 49. Map of the met-stations belonging to the network of the Municipality of Genoa in the area under investigation (black border).

Table 15. List of met-stations (ID, name, position, and data availability) belonging to the network of the Municipality of Genoa.

ID	Name	Location	Obs avail from
DAVIS			
1	GPRS_fabbriche	Sede I.C. Voltri I - Via delle Fabbriche, 189	28/10/2010
2	GPRS_crevari	Sede I.C. Voltri I P.zza Pissapaola, 48	28/10/2010
3	LAN_voltri	Sede Municipio VII Ponente - P.zza Gaggero, 2	28/10/2010
4	GPRS_pra	UOST I Ponente - Via Martiri del Turchino, 127	26/10/2010
5	LAN_pra	I.C. Pra - Via Villini Negrone, 2/C	28/10/2010
6	LAN_pegli	Centro Civico di Pegli - Via Pallavicini, 5	28/10/2010
7	LAN_sestri	UOST 0/6 II Medio Ponente – Via A. Negro, 6	18/10/2010
8	GPRS_scarpino	Discarica Rifiuti – Via Militare di Borzoli	26/11/2010
9	LAN_borzoli	Scuola Infanzia "Arcobaleno" I.C. Borzoli – Via F.lli di Coronata, 11	18/10/2010
10	LAN_sanpierdarena	Asilo Nido "Mongolfiera" – Liceo Classico "Mazzini" – Via Paolo Reti, 25B	22/09/2010
11	GPRS_murta	Plesso Doge G. da Murta – D.D. Bolzaneto – P.zza Chiesa di Murta, 5A	22/10/2010
12	GPRS_pontedecimo	I.C. Pontedecimo – Via Isocorte, 1B	04/11/2010
13	GPRS_cesino	Centro Riabilitazione Disabili – P.zza Cesino, 4	05/11/2010
14	GPRS_granarolo	UOST 0\6 II – Via S. Marino, 219	26/11/2010
15	GPRS_begato	Sede I.C. Teglia – Via Linneo, 232	22/10/2010
16	LAN_genovacentro	Sede comunale - Palazzo Albini – Via Garibaldi, 9	22/10/2010
17	GPRS_quezzi	Scuola "B. Ball" I.C. Quezzi – Sal. Costa dei Ratti, 6A	26/10/2010
18	GPRS_pino	Scuola Primaria "Pino" I.C. Molassana – Sal. Pino Sottano 20	28/10/2010
19	GPRS_eusebio	Scuola Primaria "S. Eusebio" I.C. Staglieno – Via Valtrebbia, 299-301	30/10/2010
20	LAN_quarto	UOST I Levante – Via C.A. Vecchi, 3	22/10/2010
21	LAN_prato	Biblioteca Campanella – Scuola Primaria "Prato" I.C. Prato – Via Struppa, 214	30/10/2010
22	GPRS_bavari	Scuola Primaria "Gioiosa" C.D. Borgoratti – Via Casale, 11A	26/10/2010
23	GPRS_cosimo	Scuola Vespertina – Via Trossarelli, 68	30/10/2010
24	LAN_nervi	Scuola Primaria "Fermi" D.D. Nervi – P.zza Duca degli Abruzzi, 6	22/10/2010
25	GPRS_carlodicese	Associazione Self-Help - Via S.Carlo di Cese, 59	07/12/2012

26	GPRS_martino	Scuola Primaria "Perasso" I.C. S. Martino Borgoratti – Sal. Superiore della Noce, 78	07/12/2012
MTX			
1	San Carlo di Cese	Via San Carlo di Cese	12/2021
2	Colla di Prà	Via Acquasanta	12/2021
3	Santuario Apparizione	Prossimità del Santuario "piccola città dell'immacolata"	12/2021
4	Bavari cimitero	Via Piani di Ferretto	12/2021
5	Cannellona	Via superiore dei Giovi	12/2021
6	Prà Scogli Neri	Via superiore Torrazza	12/2021
7	Forte Puin	Su sentiero tra forte Sperone e forte Puin	12/2021
8	Costiera	Via della Costiera	12/2021

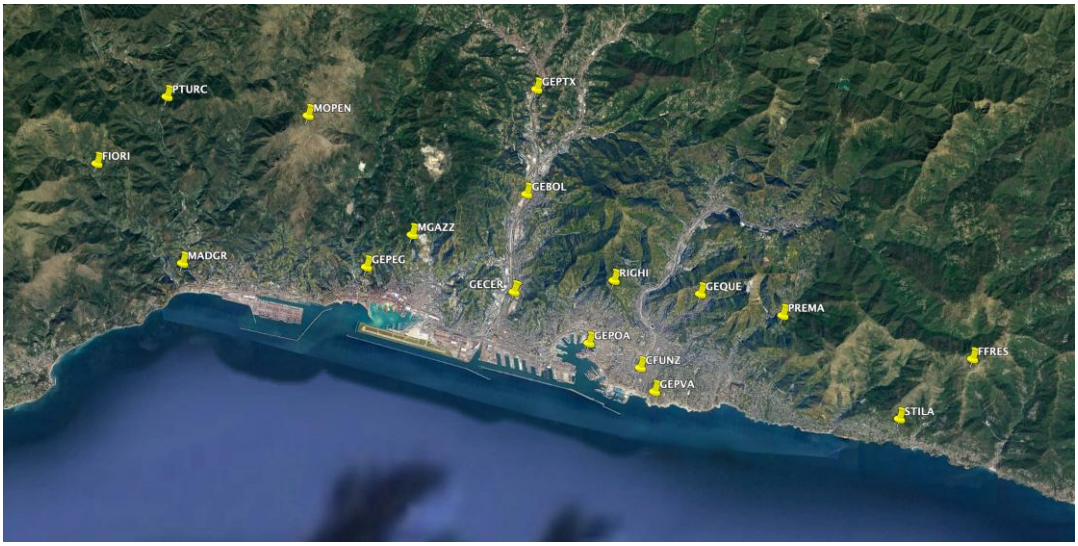

Figure 50. Map of the met-stations belonging to the network of ARPAL in the area under investigation.

Table 16. List of met-stations belonging to the network of ARPAL in the area under investigation. Observations in the last column are temperature (T), humidity (H), and wind velocity (W).

No.	Name	Code	Lat (°N)	Lon (°E)	Height (m ASL)	Observations
1	Fiorino	FIORI	44.46494	8.70493	290	T
2	Bolzaneto	GEBOL	44.45530	8.89561	47	T
3	Castellaccio	RIGHI	44.42797	8.93433	360	T,W
4	Centro Funzionale	CFUNZ	44.40035	8.94591	30	T,H
5	Certosa	GECER	44.42439	8.88997	30	W
6	Pegli	GEPEG	44.43227	8.82460	69	T
7	Pontedecimo	GEPTX	44.48852	8.90010	75	T
8	Porto Antico	GEPOA	44.40816	8.92317	25	T,H,W
9	Quezzi	GEQUE	44.42367	8.97260	200	T,H
10	S. Ilario	STILA	44.38400	9.06066	174	T,H,W
11	Madonna delle Grazie	MADGR	44.43344	8.74299	104	T,H
12	Monte Pennello	MOPEN	44.48017	8.79867	980	T,H,W
13	Premanico	PREMA	44.41681	9.00911	234	T
14	Santuario Monte Gazzo	MGAZZ	44.44247	8.84485	310	T
15	Fontana Fresca	FFRES	44.40290	9.09318	791	T,W
16	Punta Vagno	GEPVA	44.39278	8.95222	10	W
17	Passo Turchino	PTURC	44.48613	8.73602	590	T,W

3.3.3.2 Case Study 2 – harbour anemometric network

Area of Investigation

An extensive anemometric network was recently established for the European projects "Wind and Ports" (WP, 2009–2012) (Solari et al., 2012) and "Wind, Ports and Sea" (WPS, 2013–2015) (Repetto et al., 2018). These projects, financed by the European Territorial Cooperation Objective under the Cross-border program "Italy-France Maritime 2007–2013", have led to the installation of a comprehensive in-situ wind monitoring network in the main commercial ports of the Northern Tyrrhenian and Ligurian Sea, including Savona/Vado Ligure, Genoa, La Spezia, Livorno, Bastia, and L'Ile Rousse.

Objective of the Study

The network has enabled the collection of an unprecedented dataset of wind measurements. This data supports the development of numerical simulations of wind and wave fields, statistical analyses of wind climate, and algorithms for medium-term (1–3 days) and short-term (0.5–2 hours) wind forecasts. The large anemometric network established by the WP and WPS projects has been regularly enhanced with new measuring instruments (Solari et al., 2020).

Map of Instruments

Initially, during the WP project, the network comprised 23 ultrasonic anemometers. This number was increased to 28 during the WPS project. Additionally, three weather stations—each equipped with an ultrasonic anemometer, thermometer, barometer, and hygrometer—along with three LiDAR (Light Detection and Ranging) wind profilers, were installed in the ports of Genoa, Savona, and Livorno. Figure 51 illustrates the entire monitoring network. The instruments were strategically placed throughout each port area to ensure good spatial resolution for the measurements.

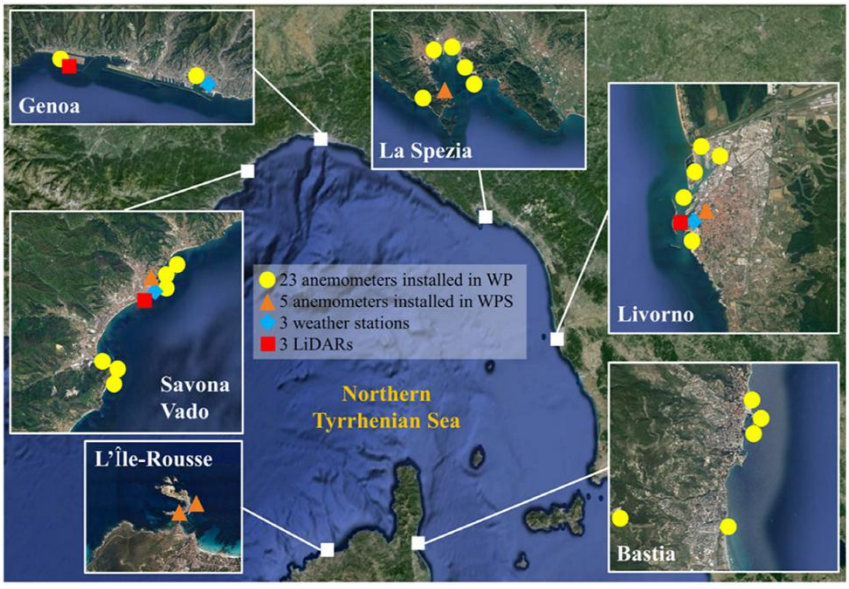

Figure 51. WP and WPS wind monitoring network.

Operational procedure

Local servers at each port authority's headquarters receive data from the monitoring network and calculate basic statistics every 10 minutes, including mean and peak wind speeds and mean wind direction. Each server then systematically sends this information to a central server at the Department of Civil, Chemical, and Environmental Engineering at the University of Genoa, Italy. The data is stored in an internal database through a four-step automatic procedure:

1. raw data is systematically checked and validated.
2. 10-minute statistics are calculated and stored.
3. 1-minute statistics are calculated and stored.
4. An automatic daily report is sent to the port authorities, providing the main data needed for their institutional activities.

Using this process, a continuously updated database is generated and maintained at the University of Genoa. This database includes first- and second-order moment statistics for 10- and 60-minute intervals, as well as maximum wind speeds averaged over a 1-minute interval.

3.3.3.3 Correction of wind databases

To ensure a wind database can be effectively used for probabilistic analysis, it must be representative, reliable, and homogeneous. A representative wind database is acquired over a sufficiently long period by a well-placed anemometric station. A reliable wind database is error-free, and a homogeneous wind database consists of values recorded under consistent conditions.

The representativeness of a wind database is relative, depending on the recording period's duration and the anemometer's location. The required recording duration for a representative database depends on:

- the problem under examination. For example, the safety analysis of a long-lasting structure requires a long-term database.
- The quality of the probabilistic analysis procedure. Using advanced probabilistic techniques can allow for the analysis of shorter databases.
- The desired accuracy. Achieving highly reliable probabilistic analyses necessitates longer databases.
- Finally, the location of the anemometer is crucial (see, for example, Figure 52), especially if the recorded data will be used to derive statistics for other locations. In such cases, the anemometer should be placed in open terrain, at a height of at least 10 meters. The presence of nearby obstacles is acceptable only if the subsequent transformation procedures used to account for these obstacles are effective.

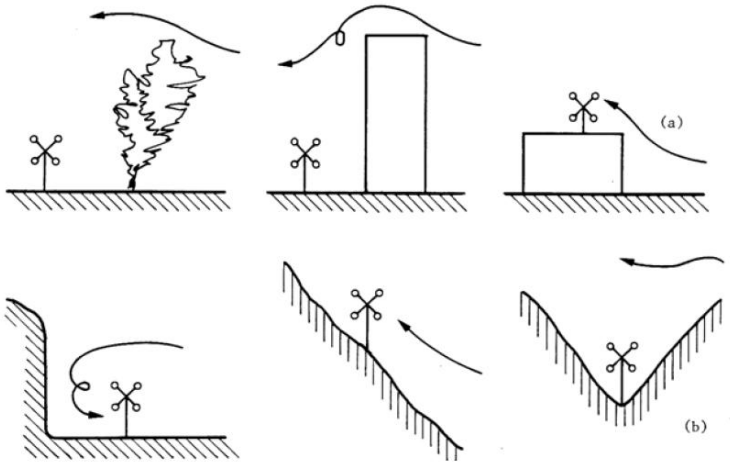

Figure 52. Influence of anemometer positioning.

A wind data base may contain four main classes of errors:

1. measurements made with poor-functioning instruments due, for instance, to lack of maintenance of wear (e.g., Figure 53).

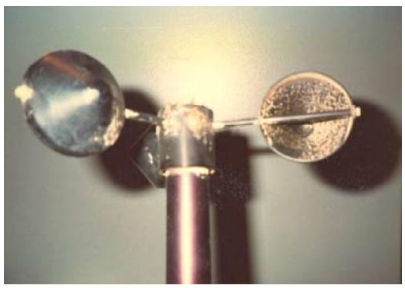

Figure 53. Cup-anemometer with sand that prevents correct functioning.

2. Measurements made outside the reading interval of the anemometer (v1, v2), such as during wind calms ($0 < v < v1 \sim 0.5\text{-}2.0$ m/s) or wind phenomena of exceptional intensity ($v > v2 \sim 50$ m/s).
3. Recording of events extraneous to the problem examined, e.g. airport measures concurrent with aircraft landing or take-off (Figure 54);

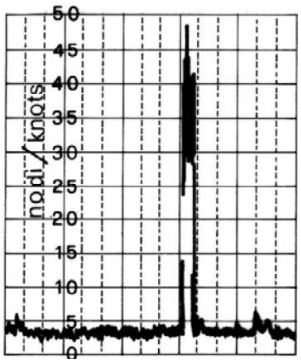

Figure 54. Biased measurement from airport anemometer.

4. Human errors arisen in the transfer of data from graphs to cards or to digital files (Figure 55), as it was typical of the first periods in which data were recorded (around 1950-1975).

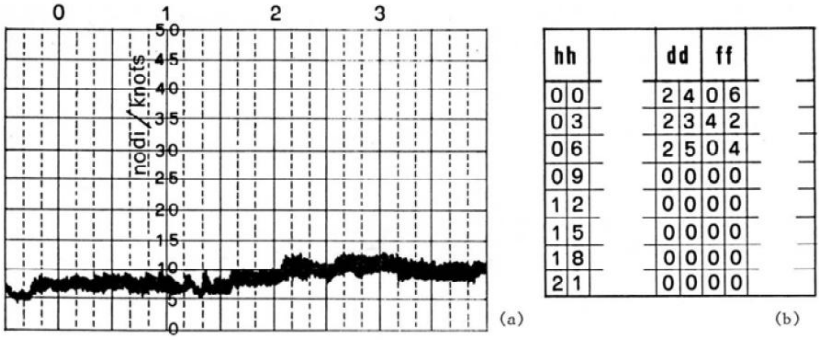

Figure 55. Human errors in the past for transferring data from graphs to cards.

Additionally, a wind database may contain missing data due to instrument shutdowns caused by natural events (e.g., extreme wind speeds or lightning), human factors (e.g., maintenance, replacement, or relocation of anemometers), or suboptimal data acquisition procedures (e.g., mean wind velocity averaged over 10 minutes but recorded every 3 hours, or stations operating only during specific daily periods).

In such cases, correction procedures must be applied based on the following criteria:

- correction of errors in the lower velocity range (e.g., wind calms): this is fundamental for accurately determining the parent distribution.
- Correction of errors in the middle velocity range: this is usually unnecessary as such errors statistically compensate for each other.
- Correction of errors in the high velocity range: this is crucial for determining the extreme distribution (e.g., Figure 56 and Figure 57).

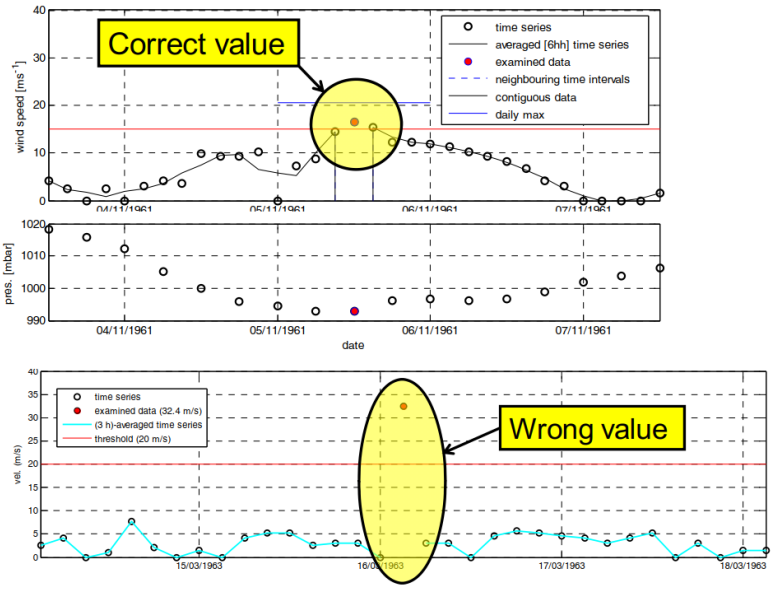

Figure 56. Interpretation of data for possible evaluation of data errors.

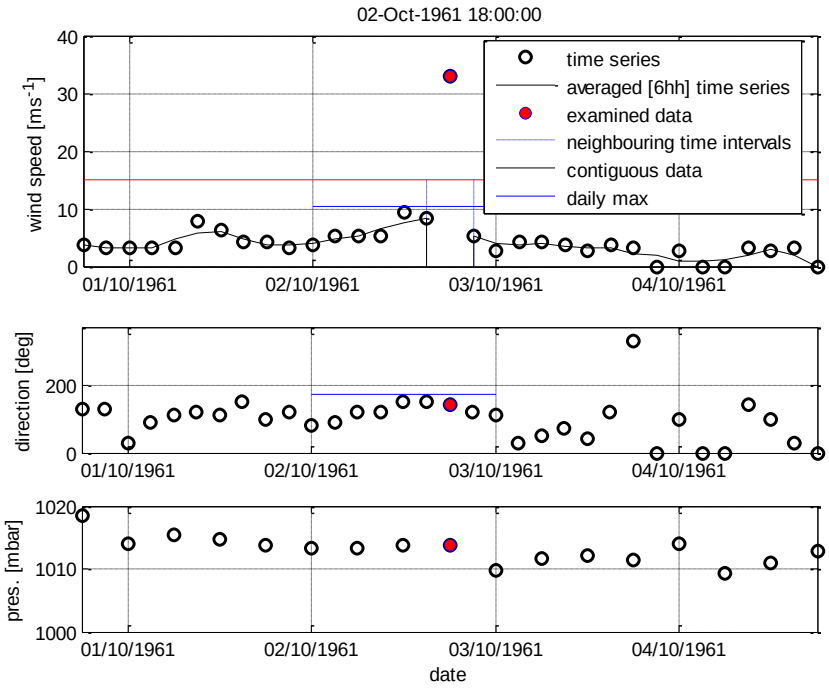

Figure 57. Singular value to be eliminated as it is higher than the daily maximum.

In general terms, a wind data base may contain 3 main classes of heterogeneity:

1. values averaged on different time periods.

2. Shifting of the anemometer or evolution of the terrain surrounding the instrument (e.g., Figure 58).

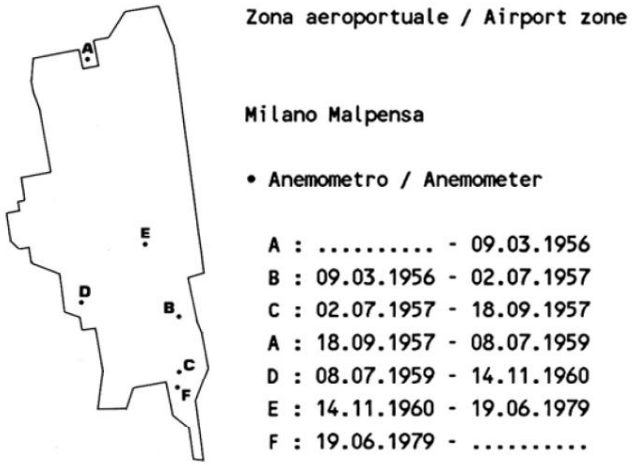

Figure 58. Airport anemometer movement.

3. Data associated with different wind phenomena, e.g. extra-tropical cyclones, gust fronts or tornadoes (e.g., Figure 59).

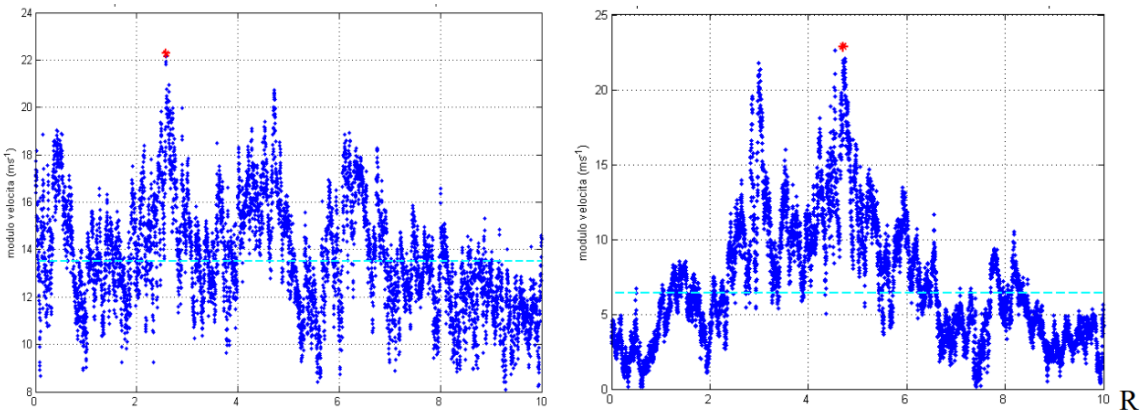

Figure 59. 10-min records of different wind phenomena.

To recap, the recorded datasets may contain errors from five basic categories (Hoaglin et al., 1983):

1. measurements carried out in conditions of instrumental malfunction, for example due to lack of maintenance or wear and tear over time.
2. Measurements outside the reading interval (V_1, V_2), such as wind calms $(0 \leq V \leq V_1 \approx 0.5 - 2\ \mathrm{m/s})$ or wind phenomena of exceptional intensity $(V > V_2 \approx 50\ \mathrm{m/s})$.

3. Recording of events unrelated to the problem addressed, e.g. airport measurements concomitant with aircraft landing or take-off operations.
4. Loss of data due to instrumental arrest caused by natural events (tornadoes, impact phenomena, lightning, ...), or by operator interventions (maintenance, replacement or transfer of the anemometer, prohibitive weather conditions, ...).
5. Manual errors occurred during transfer of data from chart to card, or from card to magnetic support.

A correct dataset is defined as the set of anemometric measurements V_c made reliable by appropriate deletion or correction of incorrect data. The transition from initial to correct datasets involves different interventions depending on the size of the data being dealt with. Operations on the lowest measurements, those below the lower anemometric reading threshold, is significant in the analysis of probability distributions of global data populations. The intervention on the data pertaining to the central body of the initial datasets is generally irrelevant to the results of the statistical analysis and as such not necessary. The intervention on the largest data is a fundamental element in the study of extreme winds and proceeds according to the two sequential phases described in the following. In the first step, potentially incorrect values are identified. The operation involves the preliminary selection of the data that will be used in the statistical analysis of the maxima. This data is compared with the data immediately before and after (e.g., within a day). The data homogeneous with the neighboring measures are assumed as correct; those that are detached from regular trends are considered potentially wrong.

Potentially incorrect data are deleted or corrected in the second step, based on the following technique. First, singular data above the maximum wind speed daily value are removed. Subsequently, the data series comprising the remaining singular values are compared with the corresponding series of atmospheric pressures on the ground (if available); singular data that do not correspond to significant pressure drops are judged to be wrong and as such suppressed (Figure 57).

3.4 Climate hazards

3.4.1 Urban heat waves characterization

The World Meteorological Organization (WMO) defines a heatwave as a period where local excess heat accumulates over a sequence of unusually hot days and nights (WMO, 2024[1]). As for other types of weather extremes, heat wave events occur when air temperatures are extremely high and fall in the rightmost part of the distribution. However, one of the main peculiarities of heat wave events is their persistence along prolonged time periods. As from 2020, the WMO has developed a guideline for defining and characterizing extreme weather and climate events (WMO, 2023). The guideline contains the currently worldwide recognized definition for heat wave as “a period of marked and unusually hot weather persisting for at least two consecutive days”. Similar definitions from the IPCC exist, namely: “a period of abnormally hot weather, often defined with reference to a relative temperature threshold, lasting from two days to months” (IPCC, 2021) or “Marked warming of the air, or the invasion of very warm air, over a large area; it usually lasts from a few days to a few weeks” (WMO, 1992). All these definitions agree to a certain extent and are able to broadly characterize the event in terms of the main

[1] https://wmo.int/topics/heatwave

characteristics being magnitude, duration, extent. For heat waves key are also severity, and timing of the event during the heat season (Global Heat Health Information Network, 2020[2]), although all these characteristics are not sufficient alone to develop practical methodologies and tools for heatwave monitoring systems allowing for comparisons across regional or international borders. As a result and due to the significant variability at sub-national scales caused by influences of geography and topography, built environment and atmospheric and other conditions, currently there is no universal numeric limit to characterize heat waves. As such, national warning systems use a range of diverse indices of multiple combined variables and locally defined thresholds to describe excessive or dangerous heat conditions. Examples of national parameters for heat warnings include for instance the following ones:

- *Canada*: a warning is issued based on specific threshold values set for daytime maximum temperatures and nighttime minimum temperatures and varying for different locations and regions (range of 28-40°C and 13-21°C for daytime maximum and nighttime minimum, respectively), for events of 2 days or longer (Environment and Climate Change Canada, 2019[3]). Some regions also utilize thresholds based on the humidex indicator, which combines temperature and humidity together (see DV 5.2.3 for further information).
- *Switzerland*: MeteoSwiss issues warnings based on daily mean temperatures, an indicator which takes into account by definition the evolution over the entire day and night. Specific thresholds and criteria were derived from a scientific analysis carried out by the Swiss Tropical and Public Health Institute (Swiss TPH Basel), on the basis of which the hazard is categorized into 5 levels from 1 (minimal or no danger) to 5 (very severe hazard) (MeteoSwiss, 2019[4]).
- *United States*: warnings and advisories are issued utilizing various tools and indicators, integrating multiple weather parameters beyond air temperatures, namely: heat index (combining temperature and relative humidity, see DV 5.2.3), wet bulb globe temperature (combining temperature, humidity, wind, solar radiation, and other weather parameters and particularly effective for outdoor workers and athletes, see also DV 5.2.3), daily HeatRisk based on the high resolution national gridded forecast database and calculated for each location from the current date through seven days in the future. In particular, the last indicator takes into account the temperature level compared to the "normal" one and their risk of posing health threats, time of the year, duration (NOAA, 2019[5]).
- *Republic of Korea*: different levels are set for advisory and warnings. In both cases, the indicator used is the daily maximum temperature and the thresholds (respectively, 33 and 35°C) have to be overcome for at least 2 days (KMA, 2019[6])
- *India*: heat waves are considered for maximum temperatures exceeding two fixed thresholds, one for the plain (40°C) and one for the hills (30°C). The departure from normality or the specific values determine the severity level (India Meteorological Department, 2024[7])

[2] https://ghhin.org/
[3] https://www.canada.ca/en/environment-climate-change/services/types-weather-forecasts-use/public/criteria-alerts.html#heat
[4] https://www.meteoswiss.admin.ch/weather/weather-and-climate-from-a-to-z/heat-warnings.html
[5] https://www.weather.gov/safety/heat-index
[6] https://www.weather.go.kr/w/index.do
[7] https://internal.imd.gov.in/pages/heatwave_mausam.php

- *Australia*: heatwave warnings are issued based on the observed and forecast maximum and minimum temperatures for the next 3 days, compared with what could be considered hot for that location and observations of the past 30 days, which in particular determine people's ability to adapt to heat (BOM, 2024[8])
- *UK*: the MetOffice issues weather warnings when severe weather has the potential to bring impacts to the UK. These warnings are given a colour (yellow, amber or red) depending on a combination of both the impact the weather may have and the likelihood of those impacts occurring. This means that not only thresholds are used, but also departures from normality, time of the year, presence of outdoor activities in the area, presence of ongoing sensitivities to weather in the area. In the case of heat waves, weather health alerting system is provided by the UK Health Security Agency (UKHSA) in partnership with the Met Office. It's intended to provide early warning to the health and social care sector, the responder community, the voluntary and community sector and government departments when adverse temperatures are likely to impact on the health and wellbeing of the population (MetOffice, 2024[9]).
- *Germany*: Dangerous heat episodes are identified by means of the criteria "strong heat stress" and "extreme heat stress" according to the 12 Coordinated Universal Time (UTC) prediction of thermal index perceived temperature (PT), an equivalent temperature (dimension °C) referring to a reference environment (see DV 5.2.3). Predictions of "moderate heat load" do not cause warnings in order to prevent "warning fatigue", as these conditions are usually fulfilled 30 to 40 times a year in Germany (Matzarakis et al., 2020).
- *France*: France has four levels of heatwave warning depending on the risks to public health, from green (monitoring ongoing but no risk signaled) to red (exceptionally long-lasting intense and widespread heat). The city of Paris also has its own "heightened yellow" alert, in between levels two and three, when the risk is considered high enough that the council begins calling vulnerable residents to check on them (RFI, 2023[10]). The indicator presenting the best compromise in terms of sensitivity and specificity after a testing was found to be the 3-day rolling average of minimum temperatures (IBMN) associated with the 3-day rolling average of maximum temperatures (IBMX). A threshold for each IBM (IBMN/IBMX) has been defined for each department, close to the 99.5 percentile of the distribution of IBM and reflecting the local climate, to which the populations who live there are accustomed (Santé Publique France, 2024[11]).
- *Italy*: the Health Ministry issues heat alerts for 27 cities (regional capitals or cities with more than 250.000 inhabitants) with 24, 48 and 72 h forecasts based on a color code from green – level 0 to red – level 3. Alerts take into account temperatures values together with humidity and solar radiation (Ministero della Salute, 2024[12]). Heat Health Watch/Warning are city-specific systems that, based on 72-hour weather forecasts, can forecast the occurrence of climate conditions

[8] http://www.bom.gov.au/

[9] https://www.metoffice.gov.uk/weather/learn-about/weather/types-of-weather/temperature/heatwave

[10] https://www.rfi.fr/en/france/20230823-what-is-france-s-heatwave-warning-system-and-how-does-it-work

[11] https://www.santepubliquefrance.fr/docs/definition-of-temperature-thresholds-the-example-of-the-french-heat-wave-warning-system

[12] https://www.salute.gov.it/portale/caldo/bollettiniCaldo.jsp?lingua=italiano&id=4542&area=emergenzaCaldo&menu=vuoto

presenting risks for human health through the associated estimate of mortality increases. Such systems are based on epidemiological models that use analyses of time series of historical data related to daily deaths and meteorological variables, to identify climatic conditions associated with significant increases in mortality for the study population.

- *The Italian regions* have specific subnational services which provide higher spatial details. For instance, the Emilia-Romagna region utilizes the Thom discomfort index, which expresses the bioclimatic temperature perception (see DV 5.2.3) (ARPAE, 2024[13]).

As can be observed, national and subnational weather services utilize a wide variety of diverse indices, both bio-meteorological and holistic, including:

- *Bio-meteorological Indices*: heat index, humidex, apparent temperature, excess heat index, human energy-budget based indices (e.g., standard effective temperature, perceived temperature, physiological equivalent temperature, universal thermal climate index) (Zare et al., 2018).
- *Holistic approach*: wet-bulb globe temperature, health-related assessment of the thermal environment, Heat Stress Index, Excess Heat Index-acclimatization, Excess heat factor (Zare et al., 2018).

Most of these indicators are fully described in other Deliverables, and in particular in DV 5.2.2 and DV 5.2.3, and further examples of metrics and additional information are available in the WMO/WHO joint guidance (WMO and WHO, 2016) and on the Global Heat Health Information Network (GHHIN) website (https://ghhin.org), maintained by the WHO/WMO Joint Office for Climate and Health. In particular, the World Meteorological Organization (WMO, 2023) recommends using indices based on local climatological conditions in order to objectively characterize a heat wave. Such indices, however, can be simply based on one meteorological variable (e.g., minimum or maximum temperature) or computed combining multiple variables which affect thermal comfort (e.g., temperature, humidity, and wind speed). Similarly, to reflect the abnormality of hot conditions and the extremity of the event, thresholds can be defined as fixed or mobile thresholds. Indeed, as shown previously, in Europe the indicator mostly used by warning system for health hazard in heat wave conditions, is the 2-m air temperature (Lowe et al., 2011), although parameters combining 2-m air temperature with relative air humidity, such as the apparent temperature or the heat index, are also adopted. This reflects the fact that environmental conditions that are potentially detrimental to human health (both indoors and outdoors) depend not only on temperature, but also on moisture levels, ventilation, sunlight, altogether affecting the human body's ability to maintain its core temperature within the range of optimal physiological performance (McGregor and Vanos, 2018). For this reason, many indices attempt to assess heat stress from the energy-thermal exchange between multiple environmental factors and the human body (Havenith and Fiala, 2016). Of these, one of the indices that was verified as a health-meaningful threshold for a potential heat-health watch warning system is the UTCI (Universal Thermal Climate Index) (Di Napoli et al., 2019).

Heat waves pose particular risks for human health, particularly in urban areas where heat stress is exacerbated by anthropogenic materials and higher population densities (Chen et al., 2023). In the urban

[13] https://www.arpae.it/it/temi-ambientali/rischio-calore

areas, indeed, temperatures tend to be higher than in the rural surrounding areas, creating a city-specific phenomenon known as the urban heat island (UHI) (Figure 60). This effect, present also at night, depends on the efficiency of the surfaces in each environment not only to absorb and hold heat, but also in evapotranspiration and convection. During the day, in the urban area, most of the heat coming from the sun is stored in the urban fabric materials (brick, stone, concrete, roads, tiles, etc.). In addition, the complex 3D shape of the city with most surfaces in direct contact with the atmosphere, favors heat storage and limits energy loss by radiation upward fluxes (Masson et al., 2020; Figure 61).

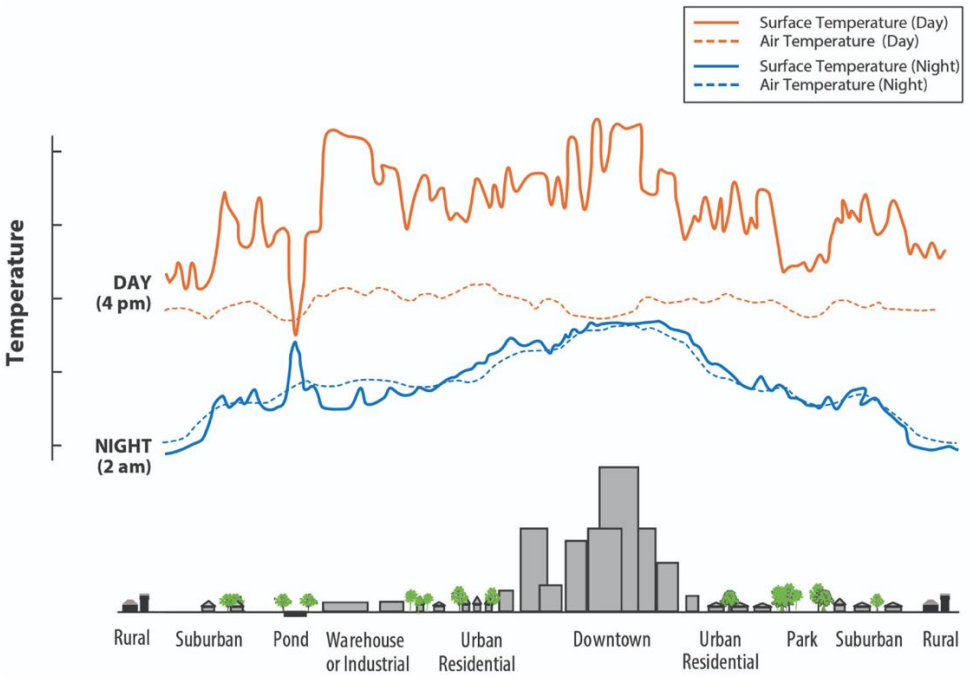

Figure 60. Surface temperatures vary more than atmospheric air temperatures during the day, but they are generally similar at night. The dips and spikes in surface temperatures over the pond area show how water maintains a nearly constant temperature day and night because it does not absorb the sun's energy the same way as buildings and paved surfaces. Parks, open land, and bodies of water can create cooler areas within a city. Temperatures are typically lower at suburban-rural borders than in downtown areas.

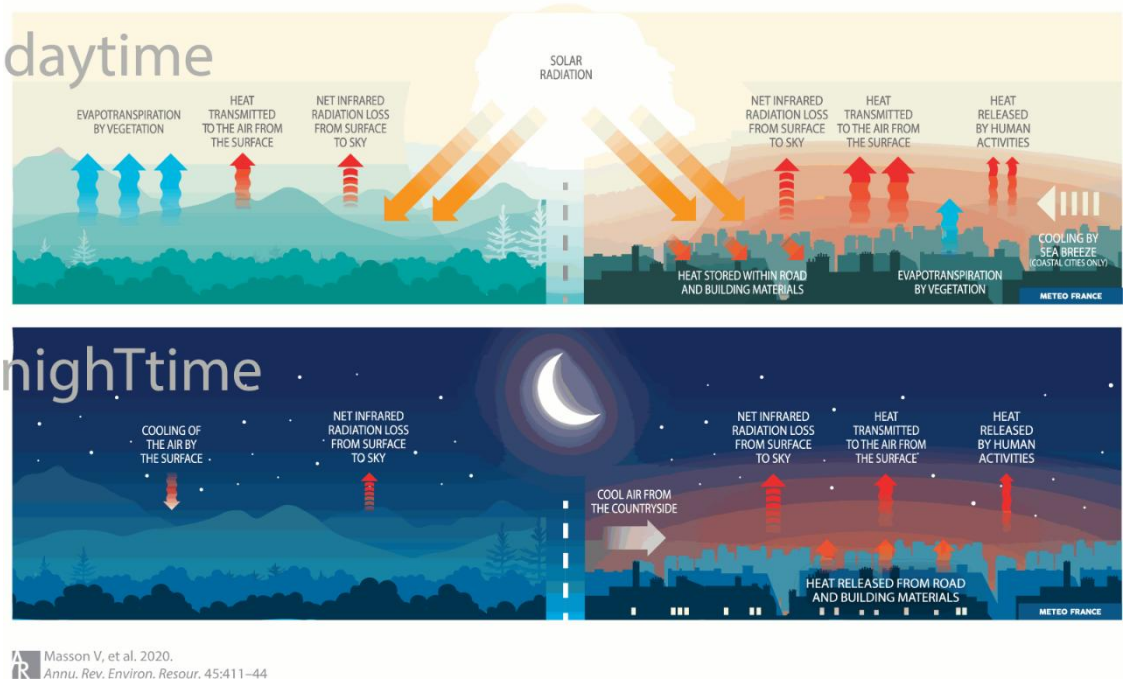

Figure 61. The main processes leading to the urban heat island. Urbanization of the surface and reduction of the vegetation cover strongly modify the energy exchanges. During the day, a large part of the radiation coming from the sun heats the urban materials; this stored heat is released at night, limiting the nighttime cooling of the air in cities and creating the urban heat island. It is also influenced and modulated by the heat released by human activities and the air flow from the countryside and, for coastal cities, from the sea or large lakes. Figure reproduced from Météo-France (2020).

In particular, heat islands form because of the following factors:

Reduced Natural Landscapes in Urban Areas. Trees, vegetation, and water bodies tend to cool the air by providing shade, transpiring water from plant leaves, and evaporating surface water, respectively. Hard, dry surfaces in urban areas – such as roofs, sidewalks, roads, buildings, and parking lots – provide less shade and moisture than natural landscapes and therefore contribute to higher temperatures.

Urban Material Properties. Conventional human-made materials used in urban environments such as pavements or roofing tend to reflect less solar energy, and absorb and emit more of the sun's heat compared to trees, vegetation, and other natural surfaces. Often, heat islands build throughout the day and become more pronounced after sunset due to the slow release of heat from urban materials.

Urban Geometry. The dimensions and spacing of buildings within a city influence wind flow and urban materials' ability to absorb and release solar energy. In heavily developed areas, surfaces and structures obstructed by neighboring buildings become large thermal masses that cannot release their heat readily. Cities with many narrow streets and tall buildings become urban canyons, which can block natural wind flow that would bring cooling effects.

Heat Generated from Human Activities. Vehicles, air-conditioning units, buildings, and industrial facilities all emit heat into the urban environment. These sources of human-generated, or anthropogenic, waste heat can contribute to heat island effects.

Weather and Geography. Calm and clear weather conditions result in more severe heat islands by maximizing the amount of solar energy reaching urban surfaces and minimizing the amount of heat that can be carried away. Conversely, strong winds and cloud cover suppress heat island formation. Geographic features can also impact the heat island effect. For example, nearby mountains can block wind from reaching a city, or create wind patterns that pass through a city.

In general, temperatures are different at the surface of the earth and in the atmospheric air, higher above the city. For this reason, there are two types of heat islands: surface heat islands and atmospheric heat islands. These differ in the ways they are formed, the techniques used to identify and measure them, their impacts, and to some degree the methods available to cool them.

Surface Heat Islands (SUHI). These heat islands form because urban surfaces such as roadways and rooftops absorb and emit heat to a greater extent than most natural surfaces. Surface heat islands tend to be most intense during the day when the sun is shining.

Atmospheric Heat Islands. These heat islands form as a result of warmer air in urban areas compared to cooler air in outlying areas. Atmospheric heat islands vary much less in intensity than surface heat islands.

Being caused at least partially by the different thermal properties of the surfaces exposed to sunlight, the UHI (and in particular the SUHI) is a phenomenon naturally characterized by a multiple-scale nature, whereby besides a temperature difference between the urban and rural areas, also intra-urban UHIs are observed between different neighborhoods in the same city are observed (Di Sabatino et al., 2020).

Many studies have been conducted already on the interaction between heat waves and UHI, with different results depending on the specific climate classification and urban morphology (Harmay and Choi, 2022). Most studies suggest that urban areas are more vulnerable than rural areas during heat wave events, but the opposite is also observed in some studies and is attributed mainly to changes in urban energy budget (Kong et al., 2021). However, it is undoubtful that the thermal stress amplification due to the UHI effect and the fact that it is pronounced also at night, may further amplify the impacts of extremely high temperatures during heat wave events (Zhao et al., 2018). Indeed, many factors in the urban areas tend to increase vulnerability to heat waves, such as population aging and large numbers of people with higher susceptibility due to chronic conditions.

The mitigation of such impacts, projected to increase in the future due to global warming, calls for multidisciplinary research to provide more accurate and explicit guidance to urban planners and policymakers. Mitigation strategies to reduce the UHI (and in particular the SUHI) include for instance the implementation of green and blue Nature-Based Solutions, such as for instance trees, shrubs and grass, surfaces and urban inland water bodies, and use of high albedo materials in external building surfaces (O'Malley et al., 2015). Nature-Based Solutions involve in particular the use of vegetation and water in the components of constructed environments and buildings: examples are green roofs, green walls and green shaded areas, such the use of trees in parkings to realise shaded areas in the urban context. In addition,

also sustainable materials may help to reduce the effect of the UHI, for instance the use of reflective materials to realize streets and pavements, or the utilisation of peculiar coating materials which can absorb less solar radiation (i.e. light-colored paints or color-change materials), or which can change their phase (phase-change materials) helping to boost the thermal capacity of structures. Lastly, also the reduction of buildings emissions through the implementation of proper materials may lead to a mitigation of the UHI phenomenon (Irfeey et al., 2023).

3.4.2 Studies of vulnerabilities and performances of the building envelope related to heat wave in urban context

In recent years, the frequency, intensity and duration of heatwaves is increasing with severe impacts on urban settlements, involving biophysical and socioeconomic subsystems as well, and thus leading to complex and emerging risk condition (IPCC, 2022). To provide an overview of the risk arising from climate change and to assess climate-related risks comprehensively, an integrated approach is essential, considering all aspects contributing to hazards, exposure, and vulnerability.

In this thematic framework, it is important to identify where the effects of single or interconnected hazards and the combination of exposure and vulnerability conditions determine higher risk and, therefore, the factors for which an urban context can be defined critical. Those areas need to be prioritized while considering where to take action with climate resilient strategies (Ho et al., 2015), in order to reduce vulnerability and increase climate resilience. Recognizing hotspot areas within urban critical contexts is essential to support decision makers in complex risk scenarios.

Accounting for the contribution of the built environment to worsening the impacts of heatwaves (Ahmed et al., 2021), it is essential to identify relevant features that determine built-up thermal performance. Such features (i.e. thermal mass and optical properties of building materials) are strongly related to building envelope and allow to characterize the vulnerability of buildings with respect to the heat wave.

3.4.2.1 The Nola study case

In this contribution we analyse the vulnerability to heatwaves of buildings inside Nola's urban critical context (UCC) and in particular in the historical centre (Figure 62). The study case is developed in the framework of the proposal of the new Municipal Urban Plan[14]. According to DV2.2, a UCC can be conceptualized as "a complex system that fails to ensure the expected performances across multiple dimensions". The main goal is to verify the effectiveness of meta-design solutions in Nola's UCC to reduce climate vulnerability to heat waves based on the exposed population.

Nola is a metropolitan urban settlement with specific conditions of vulnerability to climate impacts due to its orographic features, infrastructure system, and geomorphological boundaries, as well as relevant factors of exposure of buildings and outdoor spaces to multiple hazards.

The town has an important infrastructure system around the historic centre and links to residential fabric, a historical and archaeological core, an industrial area in the north ("ZES-CIS" of Nola) and a large

[14] supported by the studies conducted within the framework of "Convenzione DiARC - Comune di Nola per la redazione di preliminare di PUC" (Scientific Responsable proff. M. Russo, M. Losasso, Scientific Coordinators proff. A. Sgobbo, E. Formato).

agricultural and rural heritage. Because of the historic hydrological system – the Regi Lagni system - and a high percentage of sailed urban surfaces, the hazard of heavy rains is among the risk factors.

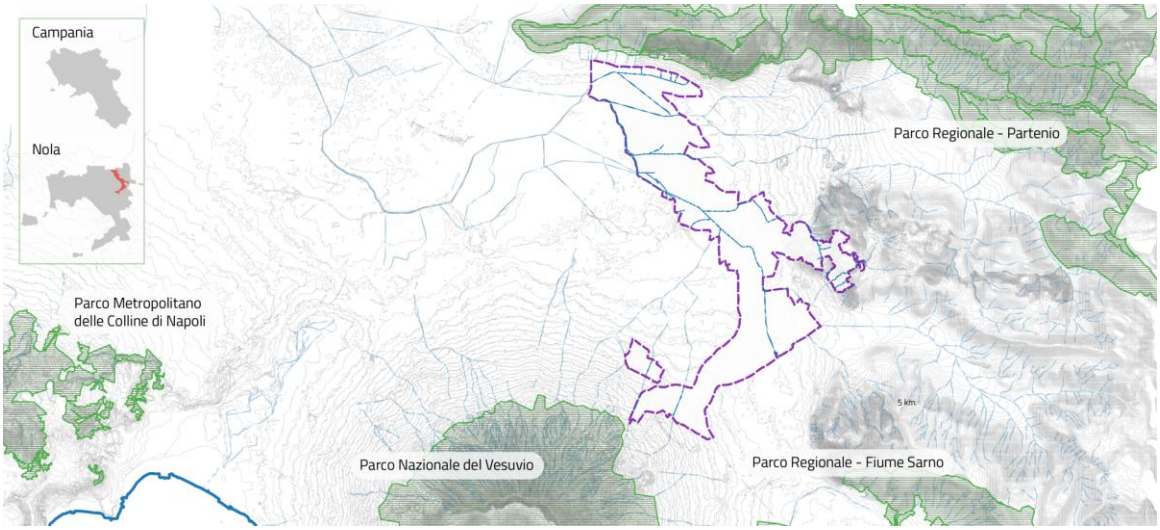

Figure 62. Geographical framework of the case study.

However, the incidence of heatwaves is significant, as made evident by the data (Table 17): several days of peak heat have occurred in the last 5 years as well as a period of dryness from May to August in the last 20 years[15]. Moreover, the built-up fabric of Nola is non-homogenous and dense in some areas, with few outdoor spaces and urban voids and large green areas but unrelated to the town. This can aggravate the impacts of heat waves, along with a non-homogeneous distribution of the population in the city. Moreover, the presence of both hazards - heavy rains and heat-waves - amplifies the risk conditions. Therefore, Nola represents a multi-risk case study.

[15] Such evidence has been made through the Bagnoulus Gaussen diagram, which represents the relationship between average temperatures and average monthly rainfall recorded in Nola from 1991 to 2021.

Table 17. Heat wave days. Data processed from Capodichino weather station data (Fonte: https://www.ilmeteo.it/portale/archivio-meteo/Napoli).

Località	Data	Inizio	Fine	Durata
Nola	2019	23/06/2019	25/06/2019	3
		01/07/2019	04/07/2019	4
		06/07/2019	10/07/2019	5
		25/07/2019	27/07/2019	3
		31/07/2019	02/08/2019	3
		10/08/2019	15/08/2019	6
		20/08/2019	01/09/2019	13
	2020	29/06/2020	03/07/2020	5
		09/07/2020	12/07/2020	4
		29/07/2020	03/08/2020	6
		11/08/2020	26/08/2020	16
		10/09/2020	12/09/2020	3
	2021	05/07/2021	07/07/2021	3
		31/07/2021	02/08/2021	3
		16/08/2021	20/08/2021	5
	2022	22/06/2022	25/06/2022	4
		03/07/2022	07/07/2022	5
		15/07/2022	17/07/2022	3
		21/07/2022	31/07/2022	11
		05/08/2022	07/08/2022	3
		24/08/2022	26/08/2022	3
		06/09/2022	08/09/2022	3
	2023	08/07/2023	15/07/2023	8
		18/07/2023	23/07/2023	6
		30/07/2023	01/08/2023	3
		17/08/2023	19/08/2023	3
		23/08/2023	26/08/2023	4

Due to the non-homogeneous distribution of the population, an integrated vulnerability evaluation method to heat wave's effect based on the exposure of the total population and the weak groups is developed.

For the very variable characteristics of both factors - the physical system (built-up areas, outdoor spaces, and infrastructure) and the distribution of the population - it is important to identify the urban critical context and urban hotspots, i.e. that are most vulnerable and exposed to the heatwave.

To find the vulnerability parameters related to exposure, the study developed some preliminary environmental analyses (map of the green and water system), as well as technological analysis (building's year of construction, surfaces 'albedo) and functional-spatial analysis (Schwarzplan). To calculate the exposure factors, the distribution of the population and of the population groups according to the age is analysed.

Given the evidence that heat waves do not affect the entire population, but susceptibility is greater among the elderly (Hajat S., et al., 2002; Conti et al., 2005; D'Ippoliti D. et al. 2012, Son, 2012) and younger people (Bobb J. et l, 2014), the study considered people over 65 and under 5 years as vulnerable age groups.

Since the method is exposure-based, overlapping the maps shows that the historic centre represents an urban critical context (see Figure 63). In the ZES area the environmental and technological values are critical but the exposure is near to zero. Therefore, the study excludes this area as an urban critical context and considers the historic center.

The urban fabric of the historic center is dense, compact, with limited outdoor spaces and a low presence of green areas, and it has a high percentage of inhabitants in vulnerable age groups.

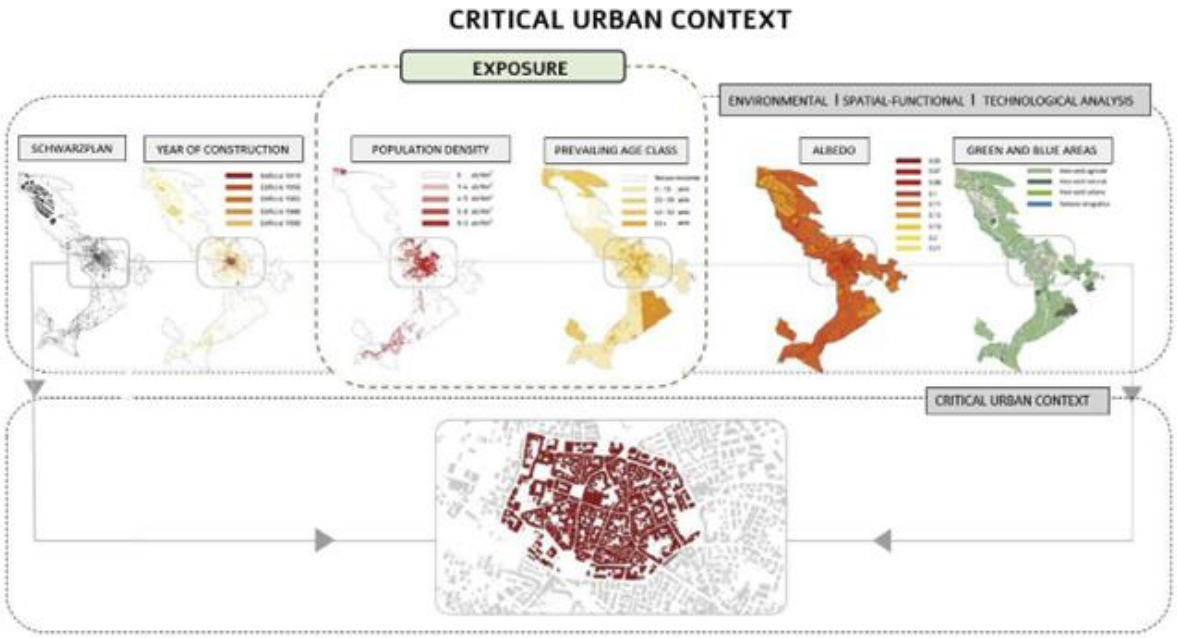

Figure 63. Conceptual framework for urban critical context identification.

3.4.2.2 The vulnerability evaluation method to heat wave's effect

Method description.

The method relies on a framework developed in GIS environment, based on open-source data related to the built-up vulnerability indicators and population features. The method represents an application of the model developed within the research project PLANNER[16], focused on assessing the vulnerability and exposure of urban contexts to heatwave hazard (Bassolino et al., 2021), in particular referring to the aspect of the evaluation of the intrinsic vulnerability.

The method focuses on evaluating the intrinsic vulnerability of the subsystems that constitute the physical system (buildings and outdoor spaces; see Figure 64). The intrinsic vulnerability is hereby defined as the vulnerability of each subsystem caused by its internal features, such as materials with their thermal capacity and surface characteristics, technical and construction solutions, the treatment of outdoor and green spaces, the exposure features of residential buildings, the relationship of buildings to the ground, plant solutions, technological networks, infrastructure systems.

[16] PLANNER-Piattaforma per LA GestioNe dei rischi Naturali in ambiEnti uRbanizzati", POR CAMPANIA FESR 2014/2020 (EET Spa – Lead Partner, Genesis GI, STRESS S.c.a.r.l. - Sviluppo Tecnologie e Ricerca per l'Edilizia Sismicamente Sicura ed ecosostenibile, Scientific Coordinator of the project: prof. G. Verderame; Scientific Responsable DiARC - Departement of Architecture, University of Naples Federico II: prof.sa V. D'Ambrosio

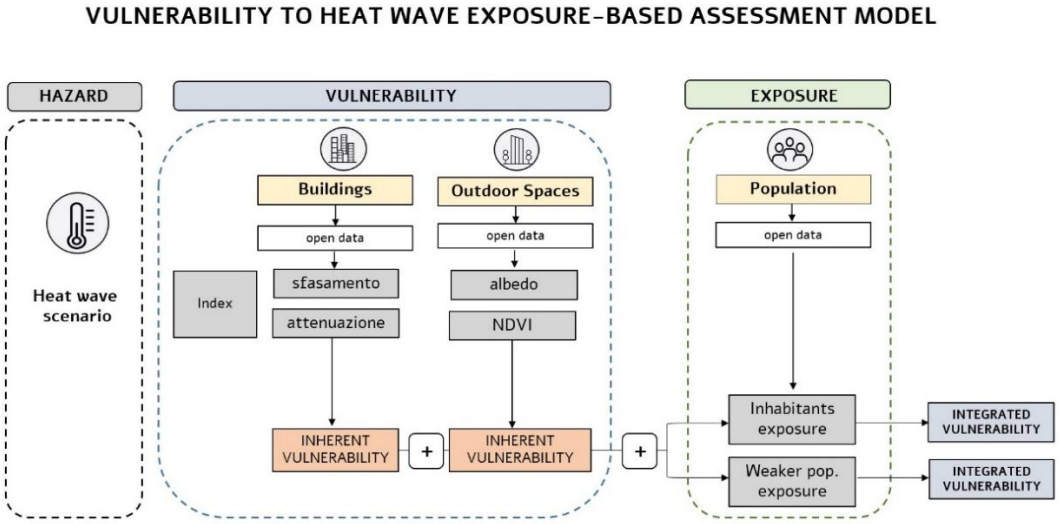

Figure 64. Vulnerability evaluation method to heat wave's effect.

Regarding buildings' features, the study acquired data from the Naples Topographic Database (DBT) to define building height and surface, and from ISTAT regarding prevailing construction techniques and building age, as referred to census cells. The population features (vulnerable groups as weak people and number of inhabitants per census section) have been acquired as well from the 2011 ISTAT census and referred to census sections.

Building intrinsic vulnerability assessment.

The assessment of the intrinsic vulnerability of the subsystems is based on the evaluation of specific features of each subsystem that could affect their response to heatwave effects.

The intrinsic vulnerability of buildings is based on the evaluation of 2 indicators: thermal lag and admittance factor[17]. Both indicators aim to identify the physical properties that describe the behaviour of the building envelope to the heatwave phenomenon. By using the data provided by ISTAT census sections, residential buildings were classified considering the prevalence of construction technique and period of construction. Once acquired, such features were assigned to buildings within each census section.

[17] The thermal lag indicator shows the time difference between the time at which the maximum temperature is recorded on the external surface of a building closure and the time at which the maximum temperature on the inner surface of the building envelope. The admittance factor represents the ratio between the external temperature variation and the flow of thermal energy that needs to be delivered inside an environment to maintain a constant indoor temperature.

BOX 1 - VULNERABILITY ASSESSMENT PROCESS

To the indicators in the vulnerability calculation, each indicator is normalized by partitioning into *n* classes using a thematic classification by range. A thematic classification by value range is a partitioning into *n* classes of equivalence of a set of thematic elements taking into consideration a specific attribute or numeric field of the theme. Each class is identified by the lower and upper extremes of the attribute's value range, called breaks. Each class is then assigned a label and a symbol for display on a map. A thematic classification method for ranges of values is a method that appropriately determines the breaks of each class.

At the end of the calculation process, each indicator is assigned a particular numerical value. The domain of indicator values is partitioned into n classes in the normalization phase. Each indicator is then normalized by partitioning into *n* thematic classes of the elements of the subsystem according to the numerical value of the indicator. A partitioning into 5 classes was chosen and a value from 1 to 5 was assigned to each a value from 1 to 5 to each class, where a lower value corresponds to a greater contribution to the vulnerability of the subsystem element. The following table shows the values and labels assigned to the 5 classes. The process described for this example application have been developed in former research project METROPOLIS* (D'Ambrosio and Di Martino, 2016).

Indicator value	Label
1	High
2	High-medium
3	Medium
4	Low-medium
5	Low

Thus, for each construction technique, five classes of thermal lag and admittance values have been defined (very low, low, medium, high, and very high) and associated with census cells.

, in the present study we calculate thermal lag and admittance for each census cell as follows:

$$Thermal\ lag\ (T) = \frac{(T_{flo} * w_{flo}) + (T_{env} * w_{env})}{w_{flo} + w_{env}}$$

$$Admittance\ (A) = \frac{(A_{flo} * w_{flo}) + (A_{env} * w_{env})}{w_{flo} + w_{env}}$$

Considering:

- T_{flo} and A_{flo} to be respectively the thermal lag and admittance values associated with flooring features of the corresponding construction technique;
- T_{env} and A_{env} to be respectively the thermal lag and admittance values associated with envelope features of the corresponding construction technique;
- w_{flo} and w_{env} to be respectively the weighted values associated with flooring and envelope features of each construction technique.

As previously defined, starting from the thermal lag classes value of the horizontal and vertical envelope associated to the census cells, a weighted average is made between the types of envelopes and flooring according to the indications in the table below.

Altezza (m)	Fforma	peso facciate	peso copertura
< 6	> 0.4	0.5	0.5
≥ 6 e < 12	> 0.4	0.7	0.3
≥ 12	> 04	1	0
<6	≤ 0.4	0.6	0.4
≥ 6 e < 12	≤ 0.4	0.8	0.2
>= 12	≤ 0.4	1	0

Building features classification: envelope and flooring indices weights related to height and form factor values

We considered building volume as an indicator of the capacity to store heat, while we assume that the form factor (defined for each census cell in the critical urban context as the ratio between building surface and volume) might express the heat exchange between buildings and their surroundings (Van Der Hoeven and Wandl, 2018).

To calculate their form factor, data about buildings' surface and volume were acquired from the DBT and elaborated as follows:

$$Form\ factor = \frac{Building\ surface}{Building\ volume}$$

The intrinsic vulnerability value of built-up spaces is the result of a weighted average of the intermediate indicators (phase shift and attenuation values) and to each indicator is given 50% of the weight. Based on the year of construction and construction techniques of the buildings, it is assumed that the building envelope will behave inadequately to heat waves.

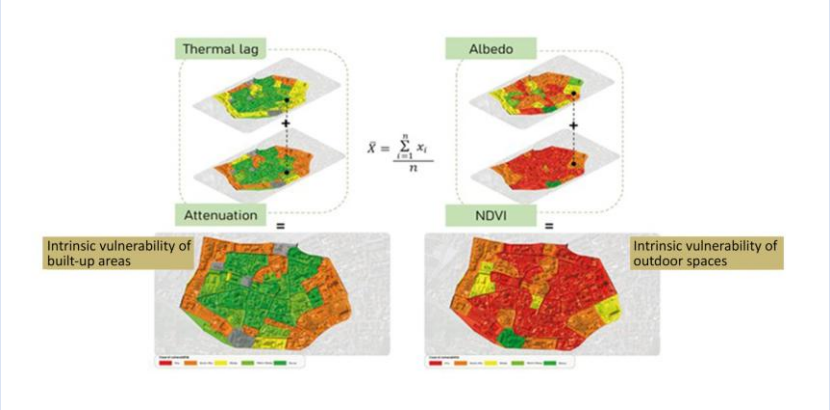

Intrinsic vulnerability assessment process for built-up areas and outdoor spaces.

Integration of exposure and vulnerability to identify urban hotspots.

The exposure is assessed related to the total population of census sections and to the weak groups. The approach to evaluate integrated exposure considers not only individual hazards, such as those related to natural events (earthquakes, floods, storms, heat waves) or anthropogenic events (industrial accidents, terrorist attacks, pandemics), as well as their potential interaction, but also considers the interconnections and interactions between different urban assets, such as transport, critical infrastructure, public health, etc. In the study, the assessment of the integrated exposure has been made considering the exposure of

the population and the exposure of the weak groups, starting from the intrinsic vulnerability values of buildings and outdoor spaces. The integration of those values and integrated exposure allowed, to identify urban hotspots, i.e. the areas within the critical urban context of the historic center that are most vulnerable and exposed to the heatwave (see Figure 65). Here the interventions should be allocated as a priority.

The results showed that the built-up system behaves inadequately to heat waves. The impermeable surfaces are 26% and located in the historic center. About 12% of the population, children and people, are weaker to heatwaves negative effects.

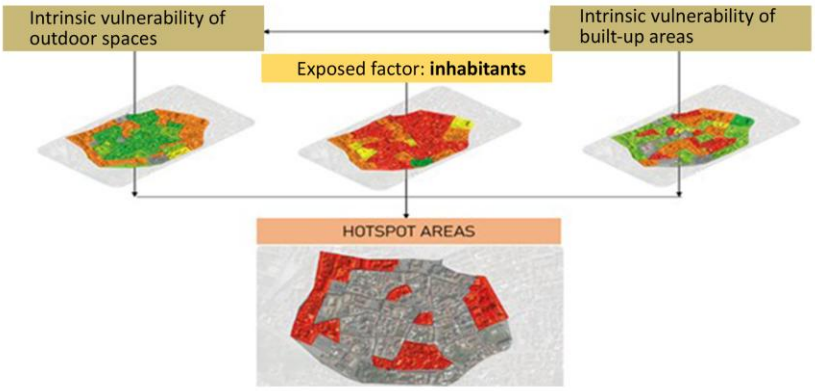

Figure 65. Identification of hotspot areas considering weak people as exposed factor.

3.4.2.3 Design strategies proposal

The testing phase allows to verify the effectiveness of strategic and meta-design solutions, aiming to reduce the climate vulnerability to heatwaves affecting the population.

Therefore, focusing on one of the identified hotspot areas, we propose building retrofitting, greening in the courts, porous and cool pavements, and a cyclo-pedestrian route as design strategies and actions (Figure 66).

Interventions on existing buildings have been planned to improve their performance. Thermal insulation interventions on horizontal and vertical surfaces, both opaque and transparent, have been carried out to improve thermal-hygrometric comfort (Rosweig et al., 2006; Santamouris, 2014). Where possible, green roofs have been installed. Additional interventions include the installation of solar shading systems. In addition, to reduce water and energy consumption (Scherba et al., 2011), photovoltaic systems and rainwater recovery systems have been installed on the roofs.

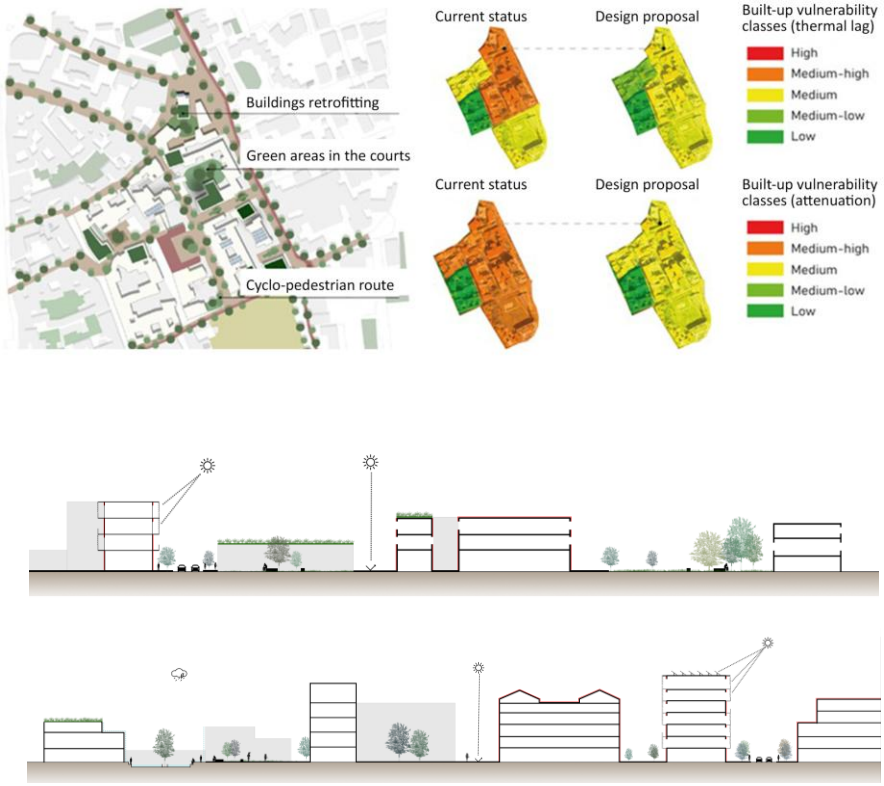

Figure 66. Design proposal contribution to the reduction of built-up vulnerability to heatwaves.

Once simulated, **87%** of hotspot areas **verify a reduction of the vulnerability classes related to attenuation** (from high to medium) and **48% verify a reduction of the vulnerability classes related to thermal lag** (from high to medium). Regarding outdoor spaces, 82% of hotspot areas verify a reduction of the vulnerability classes related to albedo (from medium to low).

In summary, the knowledge of environmental systems in the urban environment - consisting of the interaction between anthropogenic systems and natural systems- as related to emergent risk is complex. It consists of several elements that make the system and the interactions that take place on several urban settlement levels, from morphological to functional-spatial. Understanding these interactions is fundamental for sustainable transformations, capable of tackling the effects of climate-change effects.

High exposure and vulnerability, risks and immaterial assets issues supports the concept of hotspot areas as critical factors in urban contexts, to be verified through index and indicator systems, modelling and simulations. The identification of such areas prioritises the application of strategies and actions for climate adaptation, vulnerability and exposure reduction, and resilience enhancement, also planning efforts and financial resources.

Relying on open-source data and simple calculation operations through GIS-based processes, the vulnerability assessment method is replicable other context, with similar environmental features.

The GIS-based method refers to only one hazard. The further steps will include the assessment of impacts and the identification of multi-risk areas inside the critical urban context.

3.4.3 Coastal hazards driven by climate change: the Liguria region case study

Coastal zones are highly dynamic and complex environmental systems, making them particularly vulnerable to human activities, changes in land cover, sea level rise (SLR), and climate extremes. The impacts of climate change on coastal regions are evident, leading to issues such as erosion, flooding, inundation, and seawater intrusion, which have severe consequences for both natural and socio-economic assets. The Mediterranean region, with its diverse coastal zones, is significantly impacted by extreme climatic events, including storm surges and extreme waves. This region is known for its exceptional biological diversity and socio-cultural richness, spanning three continents. In addition, it is characterized by densely populated coastal areas, between 1960 and 2010, the Mediterranean's population doubled from 240 million to 480 million, with urban populations increasing by 20%. These areas are experiencing not only a rapid demographic change but also, social, economic, and environmental changes. These factors combine to make the Mediterranean's coastal zones particularly vulnerable to future climatic and demographic pressures.

The understading of climate-realted risks in coastal regions requires a complex modelling chain expresed in Figure 67.

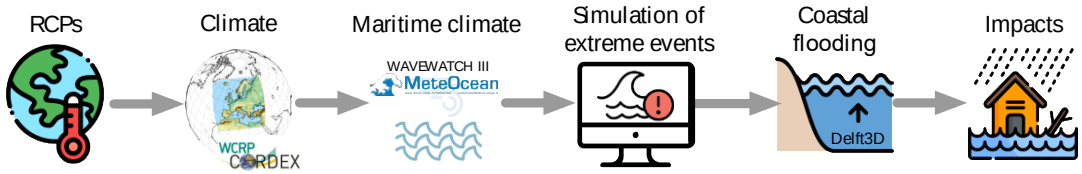

Figure 67. Modelling chain for climate-related coastal risks

Coastal regions face increasing threats from climate change-induced hazards, including sea level rise, storm surges, and extreme wave events. The Ligurian region, with its complex orography, rich cultural heritage, vibrant coastal communities, and economic activities reliant on its marine resources, is particularly vulnerable to these challenges. Understanding and quantifying the risks faced by this region is imperative for informed decision-making and effective coastal management and adaptation strategies.

The CRI, developed in this study, comprises four interlinked components: Coastal Hazard Index (CHI), Coastal Physical Susceptibility Index (PSI), Socioeconomic Susceptibility Index (SSI), and Economic Damage Index (EDI). Each component is aligned with a different set of variables to evaluate the hazards and vulnerability in the present and, based on the different narratives and climate projections, the future.

The Coastal Hazard Index is established based on a Storm Power Index (SPI). The SPI is assembled from a probability distribution of wave power for a specific temporal duration. The wind-wave climate data used in this study was developed by the MeteOcean Research Group of the University of Genoa using the WaveWatch III propagation model enabling high-resolution wave data simulation. The forcing wind data utilized in this study consists of 10-meter wind fields sourced from various Regional Climate Models (RCMs) provided by the EURO-CORDEX framework.

The socioeconomic vulnerability, encompassed in the PSI, SSI and EDI, is captured through variables encompassing population density, land use, infrastructure distribution, cultural heritage sites, GDP, and tourism activities, spatially represented using Geographic Information System (GIS) technology.

Innovatively, by aligning socioeconomic variables with the Shared Socioeconomic Pathways (SSP) scenarios, the thesis explores future vulnerability trajectories.

For this study, given the available data, the scope of the work, the resources at hand, and other constraints, a CRI Framework was selected as the assessment method. This framework is designed to integrate various aspects of coastal vulnerability into a comprehensive assessment tool for the Ligurian region. The index is composed of four main components:

- Coastal Hazard Index (CHI). This component encompasses the hazards to which the coast is exposed. It is evaluated through the wave Storm Power Index (SPI), which measures the frequency, intensity, and duration of storms impacting the Ligurian coast. The SPI is derived from wave climate time series modelled through the WaveWatch III model, forced by wind field reanalysis and projections data.
- Physical Susceptibility Index (PSI). This component reflects the physical characteristics and protective measures of the coast. It is assessed based on the type of coastline (e.g., sandy, rocky) and the presence and condition of coastal defenses (e.g., sea walls, groynes). This index indicates the natural and man-made resilience of the coastal area against hazards.
- Socioeconomic Susceptibility Index (SSI). This index measures the potential impact of coastal hazards on human and economic activities. It comprises variables such as population density, land use, critical infrastructure (e.g., roads, ports), and cultural heritage sites. By assessing these factors, the SSI highlights the social and economic vulnerabilities of coastal communities.
- Economic Damage Index (EDI). This component underscores the economic stakes involved in coastal risk management. It is calculated using GDP and tourism facilities data to relate potential economic losses due to coastal hazards. The EDI provides a quantitative measure of the financial risks associated with coastal hazards.

Each component is calculated based on its specific parameters, applying a square root mean and weighting them according to their number to obtain a final Coastal Vulnerability Exposure Index (CVEI), combining PSI, SSI, and EDI. Each of these indexes is normalized using a five-part quantile distribution, ensuring that the risk values align with the selected risk scale.

The overall CRI is then calculated by multiplying the probability of hazard occurrence (CHI) by the CVEI (Figure 68). This integrated approach ensures a comprehensive and balanced assessment of coastal risk, accommodating various dimensions of vulnerability and exposure

Coastal Risk Index (*CRI*)		*CHI* 1	2	3	4	5
CVEI	1	1	2	3	4	5
	2	2	4	6	8	10
	3	3	6	9	12	15
	4	4	8	12	16	20
	5	5	10	15	20	25

1: very low
2: low
3: medium
4: high
5: very high

Figure 68. Definition of Coastal Risk Index

Figure 69 presents the Coastal Hazard Index for different points (colored in red) in the Ligurian region. More specifically, it depicts the CDF of the storm power index, and the identified risk levels, for the hindcast, GCM-RCM ensemble baseline period (1979-2005), RCP8.5 mid-century conditions (2034-2060) and RCP8.5 end-of-century conditions (2074-2100). Regarding the Coastal Vulnerability and Exposure Index, Figure 70 presents the resulting CVEI and its components (as defined previously) for the historical baseline period for a coastline stretch of Liguria. As for the future Shared Socioeconomic Pathways (SSP), Figure 71 presents the CVEI for a coastline stretch for baseline, SSP3 2050 and 2100 and SSP5 2050 and 2100 showing the future changes in the coastal exposure and vulnerability levels.

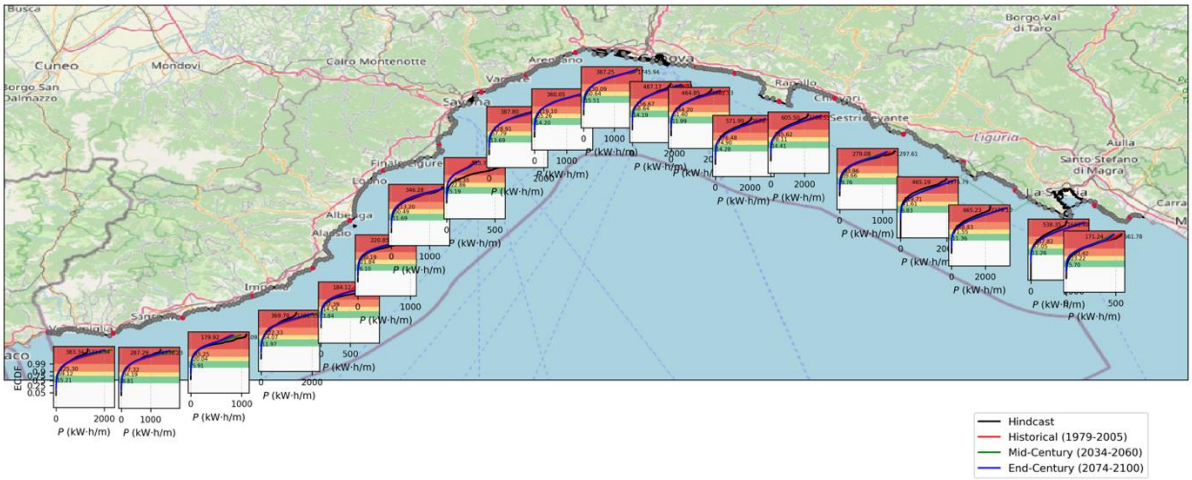

Figure 69. Coastal Hazard Index for the Ligurian Region for the historical and future RCP8.5 Mid-Century and RCP8.5 End-of-century conditions.

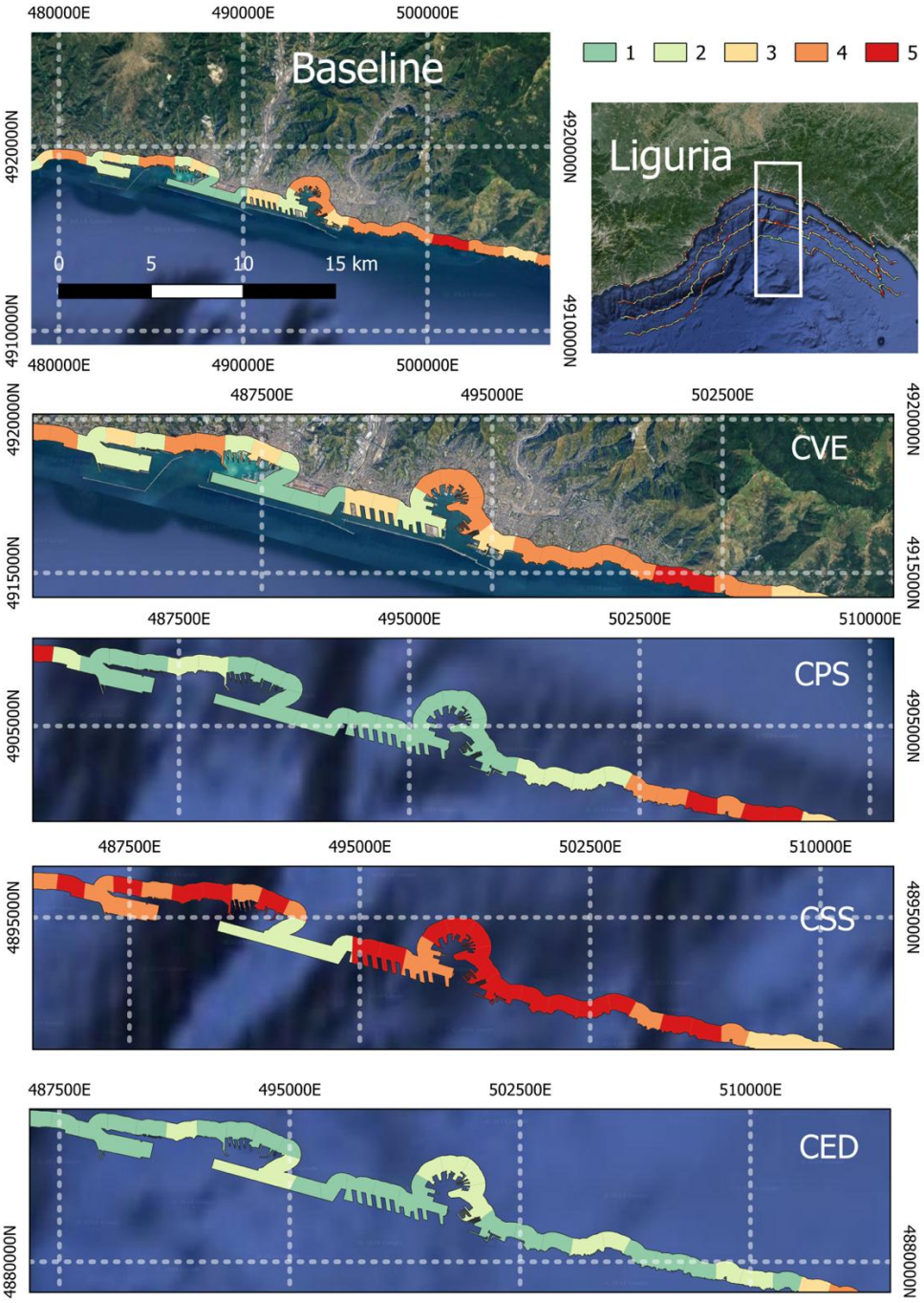

Figure 70. Coastal Vulnerability Exposure Index and its components for the Ligurian Region for the historical baseline conditions.

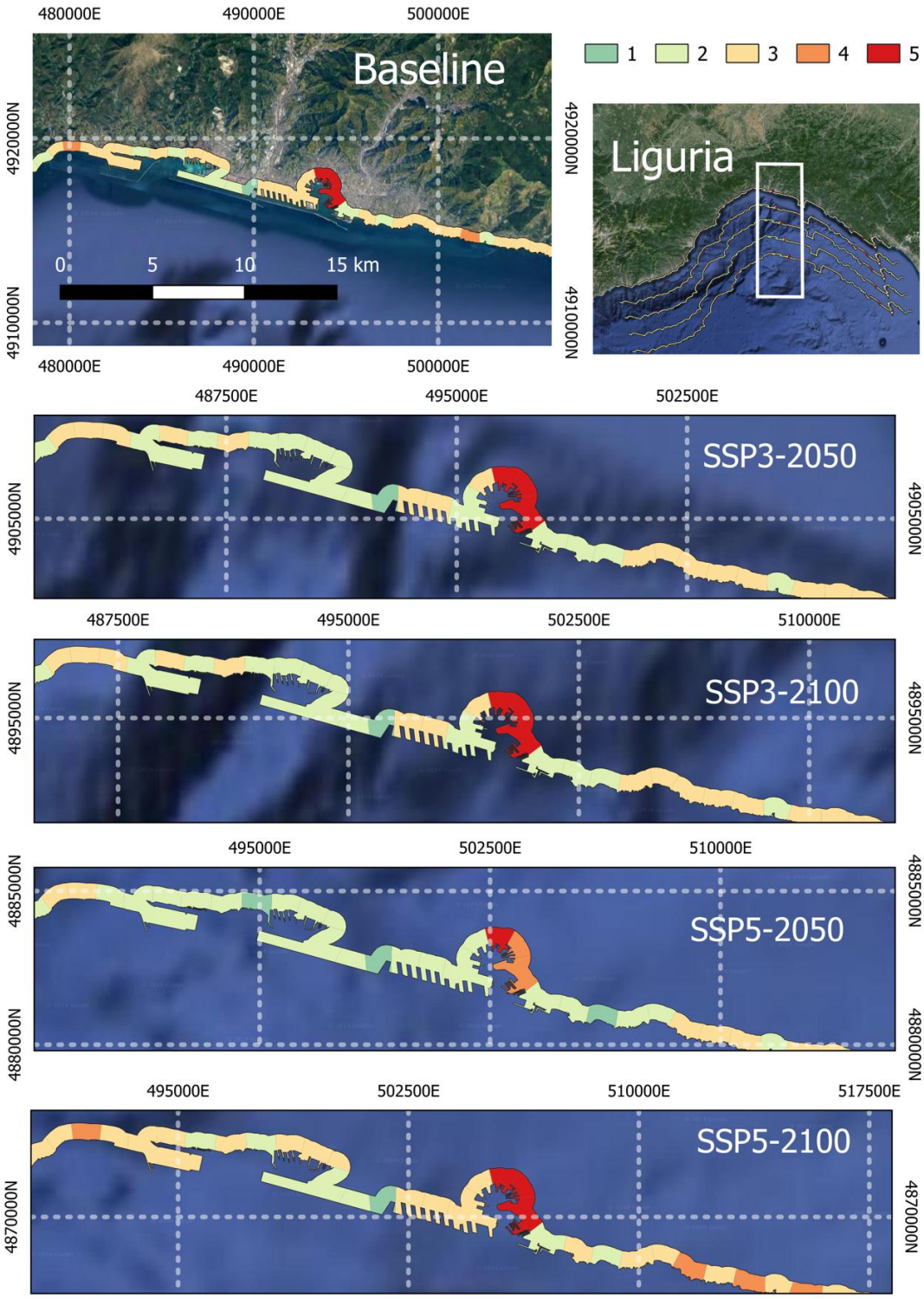

Figure 71. Coastal Vulnerability Exposure Index for the Ligurian Region for the historical baseline and future SSP3 and SSP5 scenarios for 2050 and 2100.

3.5 Chemical hazards

3.5.1 Urbanization, air quality and interactions between urban area and atmosphere

Urbanization is a defining characteristic of the modern era, with over half of the world's population residing in urban areas. This rapid urban growth has significant implications for air quality as the interactions between urban environments and the atmosphere are complex and multifaceted. Understanding these interactions is critical for mitigating air pollution and protecting public health.

According to the World Meteorological Organization (WMO) in 1992, polluted air is air containing dust, smoke, micro-organisms or gases different from those from which it would normally be composed. Air pollution contributes to several health issues including for instance heart disease, stroke, lung cancer and other respiratory diseases. In addition, air pollutants in the atmosphere not only threaten humans but also represent a serious danger to the ecosystem and food security and may damage infrastructures (WMO, 2020) as well as cultural heritage (e.g., Esteban-Cantillo et al., 2024).

To effectively address urban hazard due to air pollution, it is crucial to fully comprehend the entire lifespan of air pollutants within the specific scale of focus. This entails understanding (1) how they are emitted or formed, (2) how they disperse and travel, and (3) how they change and are eventually eliminated from the atmosphere (see sketch of the interaction of air pollutants with the urban environment in Figure 1).

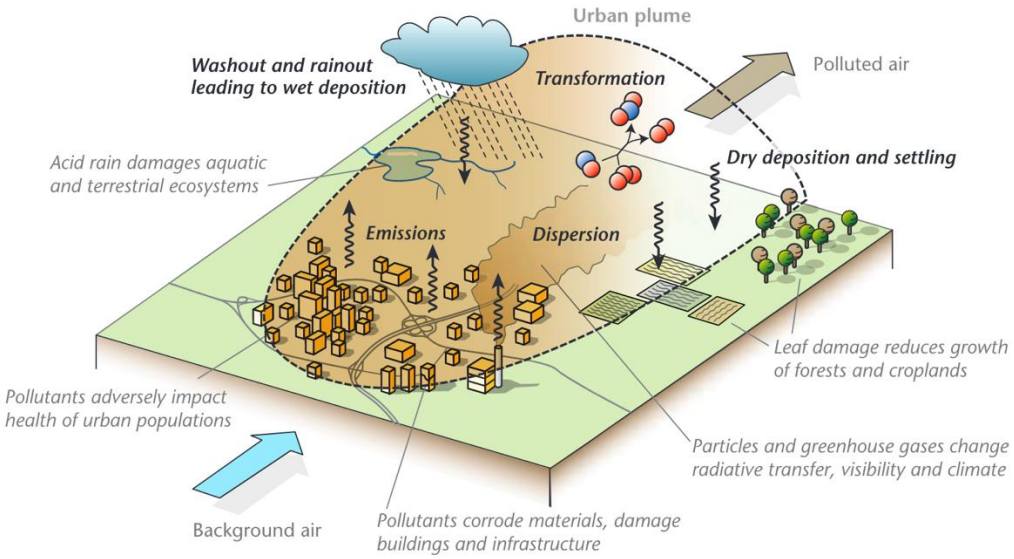

Figure 72. Sketch of the air pollutants in the urban plume, with relevant processes regulating their concentrations in black and impacts of pollutants in grey italics (from Oke et al., 2017).

3.5.1.1 Sources of Urban Air Pollution

Pollutants exist in various states: gaseous, dissolved in droplets, liquid, or solid particulates and are originated by both anthropogenic and natural sources. However, due to the concentration of human activities, in the urban environment anthropogenic sources tend to dominate. The key sources include:

1. Transportation: vehicles emit a variety of pollutants, including nitrogen oxides (NOx), carbon monoxide (CO), volatile organic compounds (VOCs), and particulate matter (PM), both in the fine and coarse modes.
2. Industrial Activities: factories and power plants release sulfur dioxide (SO_2), NOx, PM, and heavy metals.
3. Residential Heating and Cooking: using fossil fuels for heating and cooking contributes to PM, CO, and VOCs.
4. Construction Activities: these can generate significant amounts of dust and PM.

Substances in the atmosphere can be primary or secondary pollutants. Primary pollutants are directly emitted into the atmosphere during combustion or releases, such as leakage from pressurised storage or pipes (fugitive emissions), suspension, or evaporation. Secondary pollutants form in the atmosphere from a series of chemical reactions on primary pollutants, facilitated by incoming solar radiation. It is worth to note that of the key emission sources mentioned above, most of them emit both primary and secondary pollutants. Indeed, for instance, NOx emitted by road vehicles are among the precursors of secondary nitrate; contemporarily, exhaust and abrasion of mechanical components are sources of primary fine and coarse particulate matter, respectively.

Most indoor and outdoor air pollutants are emitted during combustion, the chemical reactions between hydrocarbons and atmospheric oxygen (O_2) that produce heat and light, and release carbon dioxide (CO_2) and water vapour into the atmosphere. Fossil fuels (e.g. natural gas, gasoline, diesel, and coal) and biofuels (e.g. wood, bioethanol, and biodiesel) are the main hydrocarbons. An inadequate oxygen supply during combustion leads to the release of toxic gas carbon monoxide (CO) instead of CO_2. Combustion in very high-temperature environment (typical of internal combustion engines), also causes the formation of nitrogen dioxide (NO_2) and nitric oxide (NO), while other combustion by-products due to impurities of non-carbon and non-hydrogen elements bring to the formation of NO, NO_2 and SO_2.

Combustion also releases aerosols, referred to as particulate matter (PM), which includes solid and liquid particles of various sizes. Among the different sources of PM there are: smoke, diesel exhaust, coal fly-ash, mineral dust, paint pigments. Classification and negative effects on human health depend not only on its chemical composition but also on PM size: PM with aerodynamic diameter[18] less than 10 µm (possibly affecting the upper part of the respiratory system) is defined as PM10, PM with aerodynamic diameter less than 2.5 µm (possibly entering the lower part of the lungs) is defined as PM2.5, while ultrafine particulate matter (UFP) has maximum size of 100 nm (possibly dissolving in the bloodstream).

Fugitive emissions refer to gases' unintended escape from pressurized containers. These may include fugitive hydrocarbon and methane emissions. Moreover, unburned liquefied petroleum gas (LPG) used for cooking or heating in cities can be responsible for substantial emissions that determine O_3 formation

[18] The aerodynamic diameter of an irregular particle is defined as the diameter of a spherical particle with a density of 1000 kg/m³ and the same settling velocity as the irregular particle.

in the lower troposphere, a harmful secondary pollutant and a short-lived climate forcer with a positive (warming) radiative forcing.

Evaporative emissions are due to the evaporation of liquids with low boiling points and are favoured by increasing environmental temperature. VOCs (Volatile Organic Compounds) can originate from several sources, including solvents, paints, vehicle fuelling stations, fuel storage facilities, refineries, and several industrial processes.

The most common air pollutants found in urban contexts are listed in Table 18, where emphasis is given on their major emission sources and their potential impacts on human health and on the environment. As better detailed in the following, the threat of pollutants spans multiple scales, from local to global ones. Their negative effects are different according to the substances considered: the last column in Table 18 indicates the scales of major concern for each listed substance.

Table 18. Major pollutants (in alphabetical order) emitted in cities, their source, impacts on health and structures, and scales of major concern (reproduced from Oke et al, 2017).

Compound	Major emission sources in urban areas	Impact on human health	Impact on environment and infrastructure	Scales of major concern				
				Indoor	Local	Urban	Regional	Global
Carbon dioxide (CO_2)	The major product emitted during all fuel combustion. Also released by respiration of humans, animals, vegetation and soils.	Even high concentrations not toxic, but high density can accumulate in basements and poorly ventilated rooms and reduce / displace oxygen.	Most important long-lived greenhouse gas – alters global radiative forcing and therefore driver of anthropogenic climate change.	○				•
Carbon monoxide (CO)	A primary pollutant from oxygen-limited (incomplete) combustion in motor vehicles, industrial processes and domestic heating.	Interferes with absorption of oxygen by haemoglobin resulting in oxygen deprivation. Low-to-moderate dosages cause headaches, impair brain functions and reduce manual dexterity. At high concentrations death ensues. Heavier than air.	Affects animals the same way as humans. Contributes to formation of the greenhouse gases CO_2 and O_3 when oxidized.	•	•	•		○
Halocarbons and halogenated gases	A class of inert gases including CFC-11, CFC-12 and SF_6. Used as insulating gases, fillings or refrigerants in consumer goods, in the electrical, polymer and metal industry.		Halocarbons and halogenated gases contribute to O_3 depletion in the stratosphere. Many are very long-lived (and hence effective) greenhouse gases.					•
Lead (Pb)	A toxic metal used as petroleum additive in certain countries and released during combustion. Also industrial sources.	Affects nervous system, kidneys, liver and blood-forming organs. Increases blood pressure and disturbs kidney and reproductive functions. Can cause brain damage, impaired mental development and reduced growth.	Persistent when deposited on terrestrial or aquatic ecosystems. Affects ecosystem functioning, animal reproductivity and accumulates in food-chains.		•	•	○	
Methane (CH_4)	By-product of fuel combustion, and fugitive emissions from leaking of natural gas pipes and pipelines. Anaerobic decomposition (e.g. sewage, landfills)		Second most important long-lived greenhouse gas.					•
Nitrogen oxides (NO, NO_2)	Primary and secondary pollutant resulting from fuel combustion in motor vehicles, coal-, oil-, and gas-fired power stations, industrial boilers and waste incinerators. Minor emissions occur naturally from soils.	Acute exposure causes respiratory diseases (coughs, sore throats) and at high concentration inflames airways and reduces lung functioning. Can aggravate bronchitis, asthma and emphysema.	Contributes to the eutrophication of aquatic ecosystems.	•	•	•	○	
Nitrous oxide (N_2O)	Minor combustion by-product of fuel combustion, emitted from soils, primarily managed (fertilized) greenspace.		Important long-lived greenhouse gas.					•
Non-methane volatile organic compounds (VOC)	Gasoline vehicle exhausts, leakage at fuelling stations, paint, manufacturing, solvents. Biogenic emissions from trees.	Some compounds are carcinogenic. Selected VOCs cause eye and mucous membrane irritation, others may cause fatigue and difficulty concentrating.	Selected compounds damage vegetation.	•	•	•		
Ozone (O_3)	Secondary pollutant formed in urban areas primarily from VOCs and NO_x, but also CH_4 and CO can play a role in O_3 formation at larger scales.	Damages respiratory tract and impairs lung function. Physical activity increases the dosage. Long-term exposure may result in decreased lung capacity and premature mortality.	Higher concentration can damage vegetation leading to reduced plant growth. O_3 is a short-lived greenhouse gas changing radiative transfer in the troposphere.			•	•	
Particulate matter (PM10, PM2.5, UFP)	Emitted as primary pollutant during combustion (low-temperature fires, diesel vehicles, waste incinerators, domestic heating and cooking), released during mechanical abrasion (road dust, construction) or formed as secondary pollutant from SO_x, NH_3 and NO_x.	Can reach sensitive parts of the respiratory system. Exposure to fine particulates reduces lung function, increases cardiovascular and respiratory diseases and may cause premature mortality.	Changes radiative transmission in atmosphere (Chapter 5), can impact cloud droplet size distribution (Chapter 10) and alter radiative forcing on global scale. When deposited on snow and ice surfaces, changes their albedo.	•	•	•	•	•
Polycyclic aromatic hydrocarbons (PAH)	Benzene (C_6H_6) and Benzo(a)pyrene (BaP) are the most relevant PAHs and are emitted during incomplete combustion in vehicles, domestic heating, organic material (wood) and oil refining.	PAHs irritate the eyes, nose, throat, and bronchial tubes (BaP). Benzene and BaP are carcinogenic for humans, and harm immune system and central nervous system, blood production. Can cause leukaemia and birth defects.	Many PAHs have acute toxic effects on aquatic life and birds and damage leaves of plants. Selected PAHs bio-accumulate in food-chains.	•	•	○		
Sulphur dioxide (SO_2)	Primary pollutant emitted during combustion of sulphur-containing fuels (coal, diesel, fuel oil), and in industrial processing.	Exacerbates asthma causing wheezing, shortness of breath and coughing and inflammation of respiratory tract. Synergistic effects with exposure to O_3 and particulate matter.	Damages buildings. Causes acidification of soils and aquatic ecosystems downwind of emissions, can damage forests ecosystems. Contributes to the formation of particulate matter.		•	•	•	

Biogenic emissions involve the constant exchange of gases by living organisms as part of their metabolic activity. Specifically, while humans, plants and microbes produce the non-toxic CO_2 greenhouse gas, some microbes and fungi emit toxins, leading to a diminution of indoor air quality. Moreover, many trees are responsible for the emission of specific VOCs that lead to the formation of tropospheric O_3. As will be shown in Section 3.2.1, ozone formation in the lower troposphere depends on the availability of gaseous precursors such as NOx and VOCs and environmental conditions (air temperature and light availability), hence exhibiting a marked diurnal and seasonal pattern.

The layout and structure of a city, along with its economic activities, determine where air pollution is produced. However, the subsequent behaviour of pollution in the atmosphere is very complex, crucially driven by mixing and advection, thus ultimately depending on atmospheric conditions. The urban atmosphere is a dynamic system influenced by various meteorological and topographical factors. Urban areas are often impacted by persistent stability conditions or even temperature inversions, where a layer of warm air traps pollutants close to the ground. Under such situations, dispersion of pollutants emitted in the city is strongly inhibited, and accumulation of primary pollutants together with favored formation of secondary ones lead to high pollution levels. In turn, the layout of a city significantly influences wind movement within the urban canopy layer (UCL), affecting the circulation and distribution of pollutants. In particular, mixing processes are primarily driven by wind intensity, direction, and the height of the mixed layer. Higher temperatures or other characteristics typical of the urban atmosphere can facilitate the formation of secondary pollutants, for instance increasing the production of ground-level ozone. Indeed, urban climate features, such as the urban heat island effect, can also influence these processes, altering local atmospheric circulation patterns and influencing pollutant dispersion. These negative conditions can also be exacerbated in the presence of heat waves, as better explained in Sections 3.4.1 and 4.2.1.

At the microscale, the wind pattern within the UCL is managed by urban form that may help circulate and channel air pollutants. Pollutants are subject to chemical reactions and secondary pollutant formation like ozone (O_3) and secondary organic aerosols (SOAs), which can also occur far from the emission from primary pollutants, and are themselves conditioned by atmospheric conditions both for formations (photochemical reactions depend on the presence of sunlight) and for their dispersal and advection. SO_2 and NOx gases can react with water vapor to form sulfuric and nitric acids, leading to acid rain, possibly damaging ecosystems and infrastructure. Moreover, dispersion scales and residence times of different pollutants can span multiple scales (Figure 73), adding complexity to this framework.

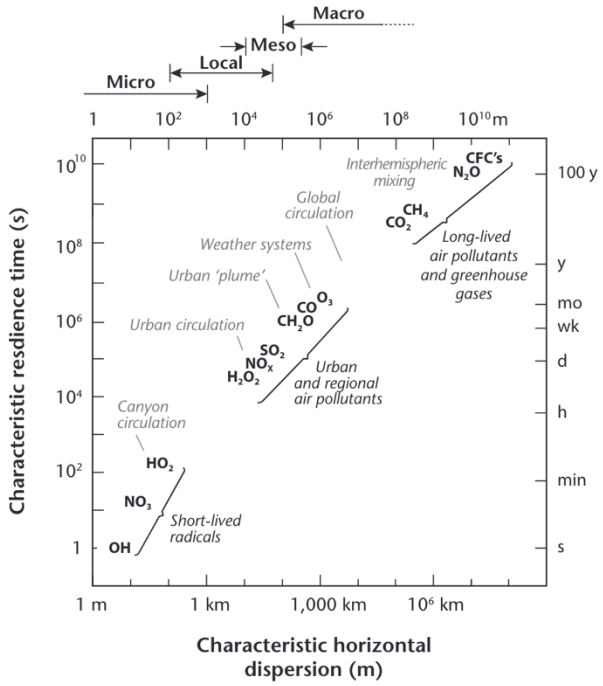

Figure 73. Residence times and dispersion scales of different pollutants shown together with the most important phenomena leading to their dispersion (reproduced from Oke et al., 2017).

3.5.1.2 Air quality and morphometric parameters

A crucial but often underappreciated aspect of the interactions between the urban environments and the atmosphere is the role of urban morphometric parameters, which include the physical and geometrical characteristics of urban landscapes.

The geometry of the built environment and urban canyons influences both the fraction of the surface exposed to radiation and the interaction with the atmospheric boundary layer and ventilation, pollutant dispersion, retention, and chemical transformation processes, making them critical for understanding and managing urban air quality.

Urban Morphometric Parameters

The urban texture can be defined in a more or less complex way depending on the field of application and the data available. The simplest description is the fluid dynamic one, which describes the presence of the urban area as an increase in wall roughness that modifies the vertical velocity profile of the atmospheric boundary layer.

The urban texture can also be described by characterizing its fundamental units, given by the urban canyons. The different descriptions of the urban texture are complementary and not independent of each other. Below the most important descriptive parameters of the different approaches are reported (Grimmond and Oke, 1999; Kent et al, 2019; Steward & Oke, 2012).

1. Aerodynamic parameters:

   z_0: aerodynamic roughness

z_d: displacement thickness

2. Characterization parameters of urban canyons:

   Wc/H: aspect ratio of the urban canyon (Wc width of the canyon, H height of the building)

   Wb/H: aspect ratio of the urban canyon (Wb building width, H building height)

3. Morphometric parameters:

   λ_p: planar area index, ratio between the planimetric area occupied by buildings and the area pertaining to them

   $\lambda_{f:}$ frontal area index, ratio between the frontal area of buildings exposed to the wind and the area pertaining to them (can be defined as a directional average or calculated for a specific direction to avoid anisotropy in the urban texture)

   λ_g: index of green areas, ratio between the planimetric area occupied by vegetation and the reference area (on which the data is calculated)

   The planar and frontal area indices can be calculated at different heights using a 3D digital terrain model to better describe the physiognomy of the buildings through their profiles. In the absence of such a detailed description, some statistical data on the buildings are provided (such as maximum height, average and standard deviation). Apart from geometric characterization of the urban texture, also thermo-physical properties of the exposed surfaces and underlying layers such as albedo, capacity and thermal transmissivity have to be defined

4. Local Climate Zones (LCZ)

   In the absence of advanced digital models, it is difficult to precisely calculate the morphometric characteristics of the urban fabric. For this reason, and also in order to represent urban centres in a standardized and synthetic way, the Local Climate Zones (LCZ) were introduced (Steward & Oke, 2012). LCZs are regions with uniform characteristics in terms of urban texture, type of materials and anthropic activities, which extend from hundreds of meters to several km in a horizontal direction. There are 10 LCZs with different degrees of urbanization and 7 LCZs relating to natural areas.

   The classification of LCZs is accompanied by a table of characteristic parameters of each class. Specifically, the morphometric parameters assumed for urban areas are:

   - Sky View Factor (SVF): solid angle fraction of the view of the sky from a point in urban space.
   - Aspect Ratio (AR): Average value of the aspect ratio of urban canyons (for the most urbanized areas, LCZ 1–7), of the spacing between buildings (for the areas with less dense urbanization, LCZ 8– 10), and among the trees (for rural areas, LCZs A–G)
   - Ratio between impervious surface (paving, rock) and total surface (%)
   - Ratio between permeable surface (bare soil, vegetation, water) and total surface (%)
   - Geometric mean of the heights of buildings (in urban areas) or of plants in green areas
   - Value of aerodynamic roughness according to the classification of Davenport et al (2000)

Influence on Air Quality

The interaction of the morphometric parameters with atmospheric processes is very complex and significantly impacts on air quality:

1. Airflow and Dispersion:
- Building Density and Height: High building density can obstruct wind flow, reducing ventilation and leading to higher concentrations of pollutants. Conversely, tall buildings can create channels for wind, enhancing pollutant dispersion in some areas while causing accumulation in others.
- Street Canyon Effect: Narrow street canyons with high aspect ratios can trap pollutants, leading to elevated concentrations at street level. Turbulence generated within these canyons can either enhance or inhibit vertical pollutant transport.

2. Pollutant Retention and Removal:
- Surface Roughness: Increased roughness due to buildings and vegetation enhances turbulence, promoting mixing and dilution of pollutants. However, excessive roughness can also lead to the formation of eddies and pockets of stagnant air where pollutants accumulate.
- Green Spaces Vegetation can absorb pollutants like PM and CO_2, improving air quality. Green roofs and walls can also moderate the urban heat island effect, indirectly affecting chemical reaction rates and pollutant formation.

3. Microclimatic Effects:
   In addition to determining the formation of the Urban Heat Island (see Chapter 2.4.1 - Urban heat waves characterization), urban morphology can influence local humidity and precipitation, affecting processes such as wet deposition, which removes pollutants from the atmosphere.

3.5.1.3 Impacts on human health

Air pollution in urban areas poses significant health risks, including respiratory and cardiovascular diseases. Assessing human exposure to urban air pollutants is crucial for understanding the public health implications and developing effective interventions. Johnson et al. (2022) conducted an epidemiological study linking long-term exposure to PM2.5 and NO_2 in urban areas with increased incidence of asthma and chronic obstructive pulmonary disease (COPD). Their research emphasized the need for stringent air quality standards to protect vulnerable populations, particularly children and the elderly. Garcia et al. (2023) developed a novel exposure assessment model integrating personal monitoring data and geospatial analysis to estimate individual exposure to urban air pollutants. Their study revealed significant disparities in exposure levels within cities, with low-income neighbourhoods experiencing higher pollution burdens due to proximity to major roadways and industrial sites.

Perez et al. (2021) found that long-term exposure to particulate matter (PM2.5) in cities like Madrid and Milan significantly increased the incidence of cardiovascular and respiratory diseases. Similarly, research by Andersen et al. (2020) in revealed that high levels of nitrogen dioxide (NO_2) in London and Paris were associated with an increased risk of asthma and other respiratory conditions among children. Moreover, a study by Viana et al. (2019) highlighted that residents in highly polluted urban areas such as Barcelona experienced elevated rates of lung cancer and other chronic illnesses. These findings collectively emphasize the urgent need for improved air quality management to protect public health in European urban environments.

3.5.1.4 Mitigation strategies

As the World Meteorological Organization (WMO) acknowledges, although air pollution nowadays represents the greatest environmental threat to health and ecosystems, it is preventable. Meeting the objective of improving air quality in urban areas and mitigating pollution require a synergistic approach involving the active participation of all stakeholders, from individuals to private companies to governments. Effective results can be achieved if a combination of scientific research, and technological, regulatory, and behavioural interventions is applied. Some of these approaches, whose positive effects have been investigated in literature, are described briefly in the following.

Emission Controls

The first step for improving air quality is to regulate the emissions, this issue is thoroughly faced in Chapter 2.5.2 (Air pollution from gases and aerosols: regulated and emerging substances), which also gives a historical overview of how awareness of the risks linked to air pollution has increased and how the regulatory context has changed in parallel.

Implementing stricter emission standards for vehicles and industrial sources can reduce the release of primary pollutants.

Two main types of schemes restricting private vehicle use in urban areas are low emission zones (LEZs), where vehicles exceeding exhaust emission standards are banned or charged, and congestion charging zones (CCZs), where most vehicles are charged, with little or no differentiation by emission standards. Both solutions aim at improving air quality and health by reducing car use and encouraging a shift towards sustainable mobility. Thompson et al. (2021) evaluated the effectiveness LEZs and CCZs in European cities, which lead to significant reductions in NO_2 and PM10 levels, highlighting the potential of these measures to improve urban air quality and reduce traffic-related emissions. Chamberlain et al. (2023) review the positive effect of these regulatory measures on the health.

Public Transportation

Enhancing public transportation systems can decrease reliance on private vehicles, reducing traffic-related emissions. Sharma et al. (2022) assessed that improving the frequency and coverage of public transit reduced CO2 emissions by 15% in urban areas. Similarly, Liu et al. (2021) highlighted that integrating electric buses into public fleets led to a 25% decrease in particulate matter (PM) emissions. Furthermore, García-Sierra et al. (2020) reported that cities with well-developed public transportation infrastructure experienced a significant drop in NOx emissions, emphasizing the environmental benefits of investing in public transit systems.

Urban Planning and Design

Several case studies have demonstrated that designing breathable cities with lower canyon aspect ratios, varied building heights and sufficient spacing, increasing parks and green infrastructures, and planning ventilation corridors can enhance natural ventilation, prevent the trapping of pollutants, and reduce pollutant concentrations.

Specifically, variations in building height and street layout create micro-environments with distinct air quality profiles. High-density areas with tall buildings often exhibit poor air quality due to limited ventilation. For example, Jiang et al. (2018) demonstrated that New York City neighborhoods with taller buildings experienced higher concentrations of NO2 due to reduced wind flow. Wang and Chen (2023) investigated the impact of urban topography and built environments on pollutant dispersion, showing how tall buildings and narrow streets can create microenvironments with poor ventilation, leading to higher concentrations of pollutants in certain urban hotspots. Oke et al. (2022) explored the impact of urban morphology on air quality in European cities, finding that cities with high building density and narrow streets tend to have higher concentrations of pollutants due to limited dispersion. Sánchez et al. (2023) conducted a detailed analysis of how different urban morphometric parameters affect pollutant levels in several European cities. Using computational fluid dynamics (CFD) models, they demonstrated that increased building heights and reduced street widths significantly hinder airflow and pollutant dispersion, leading to higher pollution hotspots in densely built areas. A study by Salim et al. (2023) examined the relationship between urban geometry and air quality in Mediterranean cities. They found that the combination of complex street layouts and high building heights exacerbated air pollution problems, especially in areas with heavy traffic. Their research highlighted the need for considering morphometric parameters in urban air quality management strategies.

The dense urban core experiences severe air pollution episodes, exacerbated by the street canyon effect and limited green space. Efforts to increase urban greenery have shown localized improvements in air quality. A study by Zheng et al. (2019) found that increasing green space coverage by 10% in certain districts reduced PM2.5 levels by up to 15%. Comparative studies across multiple European cities have demonstrated that cities with higher green space coverage tend to have better air quality, emphasizing the role of vegetation in mitigating pollution. For instance, a study comparing Barcelona and Paris found that areas with more parks and green rooftops had significantly lower levels of NO_2 and PM10. An interdisciplinary study by Roberts et al. (2023) explored the role of green infrastructure, such as urban parks and green roofs, in mitigating air pollution. Their research demonstrated that strategic placement of green spaces can enhance pollutant dispersion and provide additional benefits, including reduced urban heat island effects and improved mental well-being for city residents.

Advanced Air Quality Monitoring

Setting up advanced air quality networks, alongside deploying low-cost sensors and IoT smart city technologies, significantly enhances urban air quality monitoring and management in modern cities. For instance, a study by Castell et al. (2021) highlighted the effectiveness of an advanced air quality network in Barcelona, which integrated high-resolution monitoring stations with IoT-enabled low-cost sensors to provide real-time data, leading to more responsive and informed air quality management. Additionally, Schneider et al. (2020) demonstrated how the deployment of low-cost sensors across Berlin improved spatial coverage and detection of pollution hotspots, facilitating targeted mitigation measures. Borrego et al. (2019) emphasized the role of IoT smart city technologies in Lisbon, which enabled the integration of air quality data with traffic and meteorological information, thus enhancing predictive capabilities and decision-making processes. Traditional air quality networks have also proven beneficial, as illustrated by case studies in London (Beevers et al., 2017), Paris (Airparif, 2018), and Milan (Lonati et al., 2018), where extensive monitoring networks provided critical data that informed effective air quality policies and

interventions. These advancements underscore the critical role of modern technologies in promoting healthier urban environments.

Modeling and Simulation

Utilizing mesoscale, urban and microscale models to simulate airflow and pollutant dispersion in urban areas can provide critical insights into the impact of proposed urban developments on air quality. For example, Lin et al. (2021) demonstrated that such models could accurately predict pollutant hotspots and help in urban planning to mitigate adverse air quality effects. Similarly, Borrego et al. (2019) applied mesoscale models to Lisbon, Portugal, highlighting their effectiveness in simulating urban airflow and pollutant dispersion for better urban planning decisions.

Enhancing integrated modeling approaches that combine emission inventories, atmospheric chemistry, and human exposure assessments can offer a comprehensive understanding of urban air quality dynamics. A study by Chen et al. (2020) highlighted the effectiveness of these approaches in identifying pollution sources and evaluating exposure risks. Thunis et al. (2019) demonstrated how integrating these components improved air quality management strategies in several European cities, including Milan and Berlin.

Additionally, investigating the interplay between climate change and urban air quality is crucial, as changing weather patterns and extreme events significantly impact pollutant levels and exposure risks. Wang et al. (2019) showed that climate change-induced shifts in weather patterns could exacerbate urban air pollution episodes, emphasizing the need for adaptive strategies in air quality management. Likewise, Andersson et al. (2020) examined how climate change and heatwaves influenced air quality in European cities, finding increased pollution levels and heightened exposure risks during extreme weather events.

Community Engagement

Promoting community engagement and citizen science initiatives to raise awareness about air quality issues and empower residents to contribute to air pollution mitigation efforts. The positive results of community-led air quality monitoring were shown to increase public awareness and led to policy changes that reduced local pollution levels (Johnson et al. 2021). Similarly, Williams et al. (2020) proved that citizen science projects involving residents in data collection and analysis contributed to identifying pollution hotspots and developing targeted interventions. This demonstrates a close link between community engagement and measures based on the development of low-cost sensor networks (as mentioned above). Also, Brown et al. (2019) highlighted that active community participation in air quality monitoring fostered greater accountability among industrial polluters, leading to a notable decrease in emissions.

In conclusion, **t**he interplay between urban activities and atmospheric processes significantly influences air quality in urban areas. By understanding and monitoring these interactions, regulating emissions, and implementing effective mitigation strategies, it is possible to improve air quality and protect public health. Urban morphometric parameters, green spaces, and smart materials play a critical role in determining air quality in urban areas. Urban planners and policymakers can design cities that promote better air circulation, reduce pollutant concentrations, and enhance overall air quality.

Ongoing research and adaptive policy measures are vital for tackling the dynamic challenges of urban air pollution. Addressing these issues requires a multifaceted approach that not only improves public health and environmental sustainability but also considers the accelerating impacts of climate change. By continuously updating strategies based on new scientific findings and emerging technologies, cities can create healthier, more resilient urban environments while mitigating the long-term effects of climate-related air quality issues.

3.5.2 Air pollution from gases and aerosols: regulated and emerging substances

In today's world, both developed and developing societies face the serious issue of air pollution. This problem has arisen due to the economic and industrial practices of the previous century, which involved the widespread establishment of large industries and the reliance on fossil fuels for transportation. The issue is particularly acute in large cities where the amount of emission sources and the population in a confined area exacerbate the problem.

The Industrial Revolution, which started in the late 18th century and continued into the 19th century, caused major changes in society, economy, and technology. Although it brought significant progress and better living standards for many people, it also posed serious challenges, especially in terms of environmental impact, social inequality, and working conditions. The smog events that occurred after the Industrial Revolution, particularly in urban areas, were often caused by rapid industrialization and the widespread use of coal as the primary energy source. The name smog (a term first used in the early 1900s to describe a mix of smoke and fog) refers to a particulate cloud normally observed over urban areas, where pollutants mix with haze and react chemically to contribute condensed material to the particulate mixture. These events were characterized by a mix of air pollutants, including smoke, soot, sulphur dioxide, nitrogen oxides as well as other gaseous and aerosol pollutants. Since weather plays a major role in the formation and spread of air pollution and conversely, air pollutants can affect the weather (e.g. by promoting cloud formation), specific weather conditions most typical of the cold season and including thermal inversion and prolonged stability trap these pollutants near the ground, exacerbating the problem. One of the most notable smog events of the anthropogenic era has been the Great Smog of London, occurred in this city in 1952. A cold spell in early December 1952 led residents to burn more coal to heat their homes. This increased coal burning released large quantities of smoke, soot, and sulphur dioxide into the atmosphere. Additionally, a temperature inversion trapped these pollutants close to the ground, preventing them from dispersing. The smog led to respiratory problems and illnesses, resulting in an estimated 4,000 direct deaths in the weeks following the event (Logan, 1953). Later research suggests the total death toll may have been closer to 12,000, considering the long-term effects (Bell and Davis, 2001). The smog also caused significant harm to wildlife and vegetation. This environmental disaster profoundly impacted public health and led to significant changes in air pollution regulation: the UK government intervened against air pollution with the Clean Air Act of 1956. The Clean Air Act of 1956 allowed local authorities to establish "smoke control areas" where only smokeless fuels could be burned. This significantly reduced the amount of smoke and soot released into the atmosphere from domestic fires. Factories and industrial plants were required to adopt measures to reduce the emission of black smoke, including the installation of filters and the use of cleaner fuels. Financial incentives and grants were provided to householders and businesses to convert their heating systems from coal to cleaner alternatives such as gas, oil, or smokeless coal. The act also emphasized the importance of educating the

public about the dangers of air pollution and the benefits of using cleaner fuels. The success of the Clean Air Act of 1956 set a precedent for further environmental legislation in the UK and other countries, demonstrating that government intervention could effectively address environmental and public health issues.

The trapping of pollutants in the lower layers of the atmosphere is a recurring problem in densely trafficked urban areas. A recurring danger in certain weather conditions typical of the warm season is the so-called photochemical smog; awareness of this type of risk materialized with what went down in history as the "Los Angeles smog", following the extraordinary event that occurred here starting on July 26, 1943. This type of smog requires neither smoke nor fog since originates from the photoactivated reaction between nitrogen oxides and hydrocarbon vapours emitted by cars and other sources, with the consequent production of aggressive substances such as tropospheric ozone, a highly toxic and a greenhouse gas. The resulting smog causes a slight brownish coloration of the atmosphere, reduced visibility, damage to plants, eye irritation and breathing difficulties (for a more in-depth discussion on this pollutant, see §3.2.1). Until the 1980s, national governments implemented laws to combat air pollution. It wasn't until 1980, with Directive 80/779/EEC[19], that the first attempt was made to establish air quality standards at a European level. Directive 80/779/EEC was implemented to safeguard public health and the environment by establishing specific limits for sulphur dioxide and suspended particulates in the air. This directive marked a major milestone in establishing a cohesive strategy for managing air quality within the European Economic Community (EEC), which later became the EU. The directive set specific limit values for sulphur dioxide and suspended particulates, which were measured over different periods such as daily, monthly, and yearly averages. These limit values were meant to be binding, compelling member states to take appropriate actions to meet them. The directive outlined procedures for sampling and measuring sulphur dioxide and suspended particulate concentrations. Member states were obligated to monitor air quality to ensure compliance with the specified limit values. Additionally, they were required to report any exceedances of the limit values and make air quality information available to the public. Member states were also responsible for implementing measures to control emissions of sulphur dioxide and particulates from different sources, such as industrial processes and vehicles. The impact of Directive 80/779/EEC was significant because it established common air quality standards. This helped harmonize efforts across member states, facilitating cooperation and collective action against air pollution and it contributed to the protection of public health and the environment by addressing two major pollutants known for their harmful effects.

The Directive 80/779/EEC was eventually replaced and integrated into more comprehensive air quality frameworks as the EU's understanding of air pollution evolved. In particular, Directive 96/62/EC[20], also known as the Air Quality Framework Directive, was adopted by the European Union on 27 September 1996. This directive established a comprehensive framework for managing and improving ambient air quality across the EU. It set the stage for the creation of more specific air quality standards through subsequent "daughter directives." The directive introduced new pollutants (Pb, Nitrogen Dioxide, Benzene, Carbon Monoxide, Ozone, Arsenic, Cadmium, Nickel, Benzo(a)pyrene (PAHs)) and replaced suspended particulate with PM10 (the inhalable particulate matter with an aerodynamic diameter less

[19] https://eur-lex.europa.eu/legal-content/EN/TXT/?uri=CELEX%3A31980L0779
[20] https://eur-lex.europa.eu/legal-content/EN/ALL/?uri=celex%3A31996L0062

than 10 µm). The four "daughter" directives set specific limits for various air pollutants and provided detailed requirements for monitoring and improving air quality.

Directive 1999/30/EC[21], also known as the First Daughter Directive, was adopted by the European Union to set specific limit values for air quality. These limits concern sulphur dioxide (SO_2), Table 19, nitrogen dioxide (NO_2) and nitrogen oxides (NO_x), Table 20, particulate matter (PM_{10}), Table 21, and lead in ambient air, Table 22. The main objectives of this Directive are to establish limit values for specific air pollutants in order to protect human health and the environment, define criteria and techniques for assessing concentrations of these pollutants, and ensure that air quality is maintained where it is good and improved in other cases.

Table 19. Limit values for sulphur dioxide.

	Averaging period	Limit value	Margin of tolerance	Date by which limit value is to be met
1. Hourly limit value for the protection of human health	1 hour	350 µg/m³, not to be exceeded more than 24 times a calendar year	150 µg/m³ (43 %) on the entry into force of this Directive, reducing on 1 January 2001 and every 12 months thereafter by equal annual percentages to reach 0 % by 1 January 2005	1 January 2005
2. Daily limit value for the protection of human health	24 hours	125 µg/m³, not to be exceeded more than 3 times a calendar year	None	1 January 2005
3. Limit value for the protection of ecosystems	Calendar year and winter (1 October to 31 March)	20 µg/m³	None	19 July 2001

Table 20. Limit values for nitrogen dioxide and oxides of nitrogen.

	Averaging period	Limit value	Margin of tolerance	Date by which limit value is to be met
1. Hourly limit value for the protection of human health	1 hour	200 µg/m³ NO_2, not to be exceeded more than 18 times a calendar year	50 % on the entry into force of this Directive, reducing on 1 January 2001 and every 12 months thereafter by equal annual percentages to reach 0 % by 1 January 2010	1 January 2010

[21] https://eur-lex.europa.eu/legal-content/EN/TXT/?uri=CELEX%3A31999L0030

2.	**Daily limit value for the protection of human health**	Calendar year	125 µg/m³, not to be exceeded more than 3 times a calendar year	50 % on the entry into force of this Directive, reducing on 1 January 2001 and every 12 months thereafter by equal annual percentages to reach 0 % by 1 January 2010	1 January 2010
3.	**Limit value for the protection of vegetation**	Calendar year	20 µg/m³	None	19 July 2001

Table 21. Limit values for particulate matter (PM10).

		Averaging period	Limit value	Margin of tolerance	Date by which limit value is to be met
STAGE 1					
1.	**24-hour limit value for the protection of human health**	24 hours	50 µg/m³ PM_{10}, not to be exceeded more than 35 times a calendar year	50 % on the entry into force of this Directive, reducing on 1 January 2001 and every 12 months thereafter by equal annual percentages to reach 0 % by 1 January 2005	1 January 2005
2.	**Annual limit value for the protection of human health**	Calendar year	40 µg/m³ PM_{10}	20 % on the entry into force of this Directive, reducing on 1 January 2001 and every 12 months thereafter by equal annual percentages to reach 0 % by 1 January 2005	1 January 2005
STAGE 2 (1)					
1.	**24-hour limit value for the protection of human health**	24 hours	50 µg/m³ PM_{10}, not to be exceeded more than 7 times a calendar year	To be derived from data and to be equivalent to the Stage 1 limit value	1 January 2010
2.	**Annual limit value for the protection of human health**	Calendar year	20 µg/m³ PM_{10}	50 % on 1 January 2005 reducing every 12 months thereafter by equal annual percentages to reach 0 % by 1 January 2010	1 January 2010
(1) Indicative limit values to be reviewed in the light of further information on health and environmental effects, technical feasibility and experience in the application of Stage 1 limit values in the Member States					

Table 22. Limit values for lead.

		Averaging period	Limit value	Margin of tolerance	Date by which limit value is to be met

Annual limit value for the protection of human health	Calendar year	0,5 µg/m³ (1)	100 % on the entry into force of this Directive, reducing on 1 January 2001 and every 12 months thereafter by equal annual percentages to reach 0 % by 1 January 2005, or by 1 January 2010 in the immediate vicinity of specific point sources, of which the Commission must be notified.	1 January 2005, or 1 January 2010 in the immediate vicinity of specific industrial sources situated on sites contaminated by decades of industrial activities. The Commission must be notified of those sources by 19 July 2001 (2). In such cases, the limit value as from 1 January 2005 will be 1,0 µg/m³.

(1) The process laid down in Article 10 for the review of this Directive will include consideration of the possibility of supplementing or replacing the limit value by a deposition limit value in the immediate vicinity of point sources.

(2) Such notification must be accompanied by appropriate justification. The area in which higher limit values apply must not extend further than 1 000 m from such specific sources.

The Directive required Member States to assess air quality for specific pollutants using standardized measurement techniques. Member States were also instructed to establish monitoring stations in urban, suburban, and rural areas to collect representative data on air quality. Additionally, the Directive mandated that the public must be informed about air quality levels and any exceedances of the limit values. This entailed providing timely information on air quality through various means such as the Internet, local media, and other accessible platforms. Lastly, in areas where pollution levels exceeded the limit values, Member States were required to create and execute action plans to reduce pollution. These plans detailed measures to control emissions from sources like industrial facilities, transportation, and residential heating.

The Directive 2000/69/EC[22], the Second Daughter Directive of the European Union's Air Quality Framework Directive (96/62/EC), was adopted to set specific limit values for benzene, Table 23, and carbon monoxide, Table 24, in ambient air. This directive aimed to protect human health and the environment from the adverse effects of these pollutants.

Table 23. Limit values of benzene.

	Averaging period	Limit value	Margin of tolerance	Date by which limit value is to be met

[22] https://eur-lex.europa.eu/legal-content/en/ALL/?uri=CELEX%3A32000L0069

Limit value for the protection of human health	Calendar year	5 µg/m³	5 µg/m³ (100 %) on 13 December 2000, reducing on 1 January 2006 and every 12 months thereafter by 1 µg/m³ to reach 0 % by 1 January 2010	1 January 2010 (1)
(1) Except within zones and agglomerations within which a time-limited extension has been agreed in accordance with Article 3(2).				

Table 24. Limit values of carbon monoxide.

	Averaging period	Limit value	Margin of tolerance	Date by which limit value is to be met
Limit value for the protection of human health	Maximum daily 8-hour mean	10 mg/m³	6 mg/m³ on 13 December, reducing on 1 January 2003 and every 12 months thereafter by 2 mg/m³ to reach 0 % by 1 January 2005	1 January 2005

The Member States had to set up monitoring networks to measure benzene and carbon monoxide concentrations. These networks had to provide accurate data from urban, suburban, and rural areas. Standardized methods were to be used to ensure the data's accuracy and comparability throughout the EU. Additionally, the public had to be informed about air quality levels, including benzene and carbon monoxide concentrations, and any exceedances of the limit values. This information had to be easily accessible through platforms such as the Internet, local media, and other communication channels. Finally, in areas where benzene or carbon monoxide levels exceeded the limit values, Member States were required to create and execute action plans to reduce pollution levels. These plans were to outline specific measures to control emissions from various sources, such as industrial activities, transportation, and residential heating.

The third Daughter Directive of the European Union's Air Quality Framework Directive (96/62/EC), also known as Directive 2002/3/EC[23], was specifically concerned with regulating ozone levels in ambient air. Its main goals were to set target values (Table 25) and long-term objectives (Table 26) for ozone concentrations in ambient air in order to safeguard human health and the environment. Additionally, the directive aimed to outline the criteria and methods for evaluating ozone concentrations.

Table 25. Target values for ozone.

	Parameter	Target value for 2010 (a) (1)
1. **Target value for the protection of human health**	Maximum daily 8-hour mean (b)	120 µg/m³ not to be exceeded on more than 25 days per calendar year averaged over three years (c)

[23] https://eur-lex.europa.eu/legal-content/EN/TXT/?uri=celex%3A32002L0003

2.	**Target value for the protection of vegetation**	AOT40, calculated from 1 h values from May to July	18 000 µg/m³·h averaged over five years (c)

a) Compliance with target values will be assessed as of this value. That is, 2010 will be the first year the data for which is used in calculating compliance over the following three or five years, as appropriate.

b) The maximum daily 8-hour mean concentration shall be selected by examining 8-hour running averages, calculated from hourly data and updated each hour. Each 8-hour average so calculated shall be assigned to the day on which it ends. i.e. the first calculation period for any one day will be the period from 17:00 on the previous day to 01:00 on that day; the last calculation period for any one day will be the period from 16:00 to 24:00 on the day.

c) If the three- or five-year averages cannot be determined on the basis of a full and consecutive set of annual data, the minimum annual data required for checking compliance with the target values will be as follows:

- **i. for the target value for the protection of human health: valid data for one year,**
- **ii. for the target value for the protection of vegetation: valid data for three years.**

1) These target values and permitted exceedance are set without prejudice to the results of the studies and of the review, provided for in Article 11, which will take account of the different geographical and climatic situations in the European Community

Table 26. Long-term objectives for ozone.

	Parameter	Long-term objective (a)
1. Long-term objective for the protection of human health	Maximum daily 8-hour mean within a calendar year	120 µg/m³
2. Long-term objective for the protection of vegetation	AOT40, calculated from 1 h values from May to July	6 000 µg/m³·h

(a) Community progress towards attaining the long-term objective using the year 2020 as a benchmark shall be reviewed as part of the process set out in Article 11.

As per the previous Directives, the 2002/3/EC required the Member States to establish monitoring networks to measure ozone concentrations in ambient air. These networks had to provide representative data for various types of locations, including urban, suburban, and rural areas. All information about the ozone concentrations had to be visible to the public and, in areas where ozone levels exceeded the established target values, Member States were required to develop and implement action plans to reduce pollution levels. These plans outlined specific measures to control emissions of ozone precursors like NO_x and VOCs.

The fourth and last daughter Directive was the 2004/107/EC[24]. The objectives of this Directive were to establish target values for specific heavy metals (arsenic, cadmium, nickel, and lead) and polycyclic aromatic hydrocarbons (PAHs) in ambient air and to define criteria and techniques for assessing concentrations of these pollutants (see, for example, Table 27).

Table 27. Target values for arsenic, cadmium, nickel and benzo(a)pyrene.

Pollutant	Target value (1)
Arsenic	6 ng/m³
Cadmium	5 ng/m³
Nickel	20 ng/m³
Benzo(a)pyrene	1 ng/m³

[24] https://eur-lex.europa.eu/legal-content/EN/TXT/?uri=CELEX%3A32004L0107

([1]) For the total content in the PM_{10} fraction averaged over a calendar year.

Directive 1999/30/EC and its daughters were a pivotal piece of legislation in the European Union's efforts to improve air quality and protect public health and the environment. By setting specific limit values for key pollutants and establishing robust monitoring and reporting requirements, the directive played a crucial role in driving significant improvements in air quality across the EU. In a significant move, PM10 was included in a European Directive for the first time, with the purpose of establishing limit values to safeguard human health and the environment. This decision was based on scientific knowledge and health impact assessments. Leading up to 2000, numerous scientific articles provided substantial evidence of the harmful health effects of PM10. Research conducted in the years preceding 2000 had clearly established a link between PM10 exposure and various health problems, focusing mainly on respiratory and cardiovascular effects. In particular, several studies demonstrated the acute effects of particulate pollution on both lung function and respiratory symptoms (Schwartz, 1993; Dassen et al., 1986; Dockery et al., 1993; Braun-Fahrländer et al., 1992; Johnson et al., 1990) and respiratory morbidity as measured by hospital admissions, health care visits, or other measures of restricted activity due to illness (Lutz, 1983; Ostro, 1983; Sunyer et al. 1991; Ransom et al. 1992). In 1999, The World Health Organization (WHO) published its Air Quality Guidelines[25] to provide evidence-based recommendations for acceptable levels of various air pollutants, including PM10, to protect public health. These guidelines have been developed based on extensive scientific research and were intended to minimize the health risks associated with exposure to air pollutants. The annual mean limit was 20 µg/m^3, aiming to protect against long-term health effects from chronic exposure to PM10, such as respiratory and cardiovascular diseases. The daily mean limit was 50 µg/m^3, established to protect against the acute health effects of short-term exposure to high levels of PM10, including respiratory symptoms, asthma exacerbation, and increased hospital admissions.

In the same years, several studies demonstrated the significant impact of PM10 not only on public health but also on the environment. PM10 altered the optical properties of the atmosphere, and promoted cloud and fog formation, affecting the water cycle (Charlson and Heintzenberg, 1995; Seinfeld and Pandis, 2006). It may also lead to changes in heat distribution and circulation patterns, as well as influence atmospheric chemistry and photochemistry by facilitating heterogeneous reactions. The impact of aerosols on climate was quite challenging to measure accurately. Figure 74 shows the global annual mean radiative forcing (W m^{-2}) for the year 2000, compared to 1750, attributed to various causes. Some argue that the negative climate forcing caused by human-made aerosols, due to increased scattering and indirect cloud effects, was similar in magnitude (but opposite in effect) to the climate forcing resulting from higher concentrations of greenhouse gases (Houghton et al., 2001). As a result, aerosols could be cancelling out a significant portion of the greenhouse effect. It has been suggested that aerosols were masking the true response of the climate system, leading to a higher than observed Earth temperature sensitivity (Schwartz and Andreae, 1996).

[25] https://iris.who.int/bitstream/handle/10665/66537/WHO_SDE_OEH_00.02-eng.pdf?sequence=18

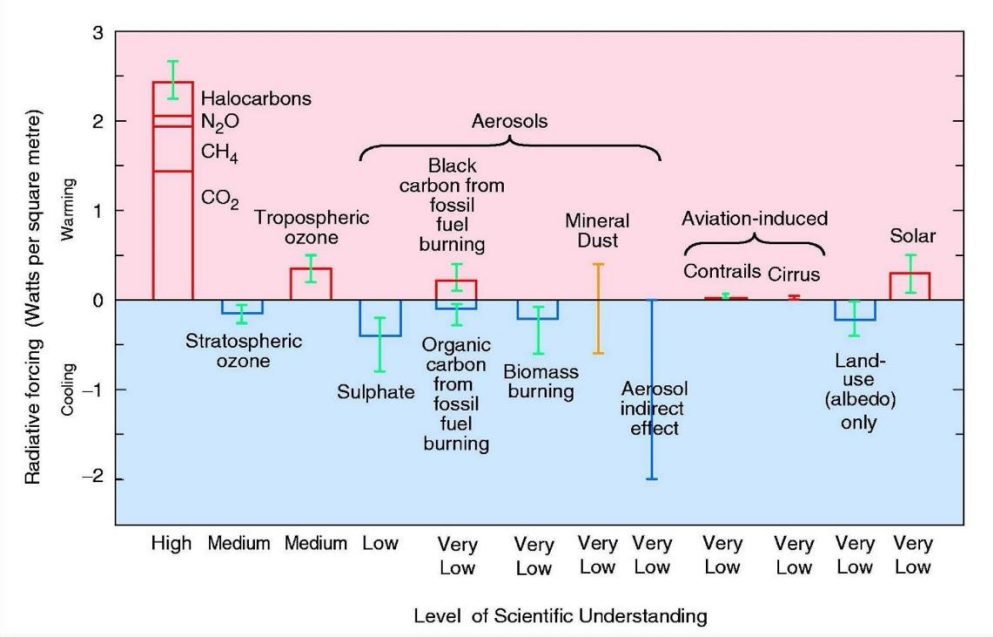

Figure 74. Global annual mean radiative forcing (W m^{-2}) for the year 2000, relative to 1750, attributing to different causes: well-mixed greenhouse gases (CO_2, CH_4, N_2O and Halocarbons); Stratospheric and Tropospheric ozone; various aerosol types (Sulphates, Black and Organic carbon from fossil fuel burning, Biomass burning and mineral dust); aviation-induced cloud formation; albedo variations due to land-use modification; and the variation of the solar flux. This figure has been extracted from the Intergovernmental Panel on Climate Change (IPCC) report (2001).

In 2008, a new directive known as Directive 2008/50/EC[26], or the Ambient Air Quality Directive, was published. This piece of European Union legislation aims to improve air quality across member states by consolidating and updating previous air quality laws. It sets limits and targets for various air pollutants, taking into consideration the increase in knowledge on the effects of atmospheric particulates on health and the environment. The most important change in this Directive was the introduction of PM2.5 (particulate matter with aerodynamic diameter less than 2.5 μm) as a pollutant to monitor. During that time, several studies had already emphasized the harmful impact of PM2.5 on human health, both in the short term and long term. Regarding respiratory effects, research indicated that short-term exposure to PM2.5 could worsen asthma, increase respiratory infections, and reduce lung function. Schwartz and Neas (2000) demonstrated a link between PM2.5 levels and respiratory hospital admissions in children. Prolonged exposure was associated with chronic respiratory diseases such as chronic obstructive pulmonary disease (COPD). The Six Cities Study by Dockery et al. (1993) found that long-term exposure to fine particulate air pollution significantly decreased life expectancy, primarily due to cardiorespiratory mortality. PM2.5 was also shown to contribute to acute cardiovascular events. Pope et al. (1995) discovered that daily fluctuations in particulate matter concentrations were linked to a higher risk of heart attacks and other acute coronary events. Long-term exposure was associated with an increased risk of cardiovascular mortality. The American Cancer Society study by Pope et al. (2003) demonstrated a strong association between chronic exposure to fine particulate air pollution and cardiovascular disease mortality. Multiple studies, including those by Samet et al. (2000), revealed a strong connection between

[26] https://eur-lex.europa.eu/eli/dir/2008/50/oj

PM2.5 exposure and elevated total mortality rates. This research suggested that even low levels of PM2.5 could contribute to premature death, particularly among the elderly and individuals with pre-existing health conditions. Finally, research proposed several biological mechanisms through which PM2.5 could cause harm, including oxidative stress and inflammation, leading to respiratory and cardiovascular damage. Oberdörster (2000) reviewed how ultrafine particles, including PM2.5, could induce oxidative stress and inflammatory responses in the respiratory tract.

The limit values of PM2.5 are reported in Table 28: the Directive only reported an annual average.

Table 28. Limit values of PM2.5.

Averaging period	Limit value	Margin of tolerance	Date by which limit value is to be met
STAGE 1			
Calendar year	25 µg/m³	20 % on 11 June 2008, decreasing on the next 1 January and every 12 months thereafter by equal annual percentages to reach 0 % by 1 January 2015	1 January 2015
STAGE 2(1)			
Calendar year	20 µg/m³		1 January 2020
(1) Stage 2 — indicative limit value to be reviewed by the Commission in 2013 in the light of further information on health and environmental effects, technical feasibility and experience of the target value in Member States.			

Between 2008 and 2024, there were no new limit values for gases and particulate matter in the air. However, in 2015, Directive 2015/1480/EU amended several annexes of Directive 2004/107/EC and Directive 2008/50/EC, which were related to air quality and cleaner air for Europe. This directive primarily aimed to update the reference methods, data validation, and the location of sampling points for assessing ambient air quality.

A new input for a review of the Air Quality Directive came from the updated Air Quality Guidelines of the World Health Organization (WHO, Who Guideline Air Quality 2021[27]) in September 2021; the WHO updated its Air Quality Guidelines, based on a systematic review of the scientific evidence on health effects of air pollution. These guidelines were a significant update from the previous version published in 2005, reflecting the latest scientific evidence on the health impacts of air pollution. The updated guidelines proposed more stringent limits for key pollutants, recognizing the severe health impacts even at lower levels of exposure than previously understood. The pollutants covered were: PM2.5, PM10, Ozone, NO_2, SO_2 and CO. The guidelines suggested the following limit values:

- PM2.5: The annual mean should not exceed 5 µg/m³, and the 24-hour mean should not exceed 15 µg/m³;
- PM10: The annual mean should not exceed 15 µg/m³, and the 24-hour mean should not exceed 45 µg/m³;
- Ozone (O_3): The peak season (6–8 hours mean) should not exceed 60 µg/m³;

[27] https://iris.who.int/bitstream/handle/10665/345329/9789240034228-eng.pdf?sequence=1&isAllowed=y

- Nitrogen Dioxide (NO_2): The annual mean should not exceed 10 µg/m³, and the 24-hour mean should not exceed 25 µg/m³;
- Sulphur Dioxide (SO_2): The 24-hour mean should not exceed 40 µg/m³;
- Carbon Monoxide (CO): The 8-hour mean should not exceed 4 mg/m³.

The guidelines emphasized the connection between air pollution and various health issues, including cardiovascular and respiratory diseases, as well as cancers. They highlighted the disproportionate impact on vulnerable populations such as children, the elderly, and individuals with pre-existing health conditions. Finally, acknowledging that some regions may struggle to meet these guidelines due to differing levels of development and sources of pollution, the WHO encouraged all countries to strive for these standards to protect public health.

A second input arrived from the European Green Deal[28]. The European Green Deal is an ambitious set of policy initiatives by the European Commission aimed at making Europe climate-neutral by 2050. Announced in December 2019, it represents the EU's commitment to comprehensively tackle climate change while stimulating economic growth. The main goal is for Europe to become the first climate-neutral continent by 2050, meaning the EU's greenhouse gas emissions will be balanced by removing equal amounts from the atmosphere. This involves increasing renewable energy sources, improving energy efficiency, and phasing out fossil fuels. The EU aims to achieve 32% renewable energy consumption by 2030, encouraging industries to adopt cleaner technologies and processes, including through the creation of a circular economy, where waste is minimized and resources are used efficiently. Other goals include ensuring a sustainable food system that contributes to climate objectives, reducing pollution, and protecting biodiversity, as well as protecting and restoring biodiversity to halt biodiversity loss in Europe by 2030. Thanks to the push of the European Green Deal and updated WHO guidelines on air quality, the European Parliament approved a new legislative resolution of 24 April 2024 on the proposal for a directive of the European Parliament and of the Council on ambient air quality and cleaner air for Europe (recast) (COM(2022)0542 – C9-0364/2022 – 2022/0347(COD)). The point 2 of the adopted texts sentenced: "*The Commission set out in its communication of 11 December 2019 entitled "The European Green Deal" an ambitious roadmap to transform the Union into a fair and prosperous society, with a modern, resource-efficient and competitive economy, that aims to protect, conserve and enhance the Union's natural capital, and to protect the health and well-being of citizens from environment-related risks and impacts. Specifically on clean air, the Commission committed itself to further improving air quality and to aligning Union air quality standards more closely with the recommendations of the World Health Organization (WHO). The Commission also announced in the European Green Deal a strengthening of provisions on air quality monitoring, modelling and planning."* The point 5 of the adopted texts sentenced: *"In September 2021, the WHO updated its Air Quality Guidelines, based on a systematic review of the scientific evidence on health effects of air pollution. The updated WHO Air Quality Guidelines highlight new evidence about effects occurring at low levels of exposure to air pollution and formulate lower air quality guideline levels for particulate matter (PM10 and PM2,5) and for nitrogen dioxide compared to previous guidelines. This Directive takes into account the latest scientific evidence, including the most up-to-date WHO Air Quality Guidelines."*

[28] https://commission.europa.eu/strategy-and-policy/priorities-2019-2024/european-green-deal_en

The WHO Air Quality document reports specific recommendations on air quality guideline (AQG) levels for the pollutants PM2.5, PM10, ozone, nitrogen dioxide, sulphur dioxide and carbon monoxide, together with the corresponding interim targets. Table 29 below reports the summary of WHO AQG levels and interim targets.

Table 29. Summary of recommended long- and short-term AQG levels and interim targets.

Pollutant	Averaging time	Interim target				AQG level
		1	2	3	4	
PM2.5 (mg m^{-3})	Annual	35	25	15	10	5
	24-hour[a]	75	50	37.5	25	15
PM10(mg m^{-3})	Annual	70	50	30	20	15
	24-hour[a]	150	100	75	50	45
O_3 (mg m^{-3})	Peak season[b]	100	70	-	-	60
	8-hour[a]	160	120	-	-	100
NO_2 (mg m^{-3})	Annual	40	30	20	-	10
	24-hour[a]	120	50	-	-	25
SO_2 (mg m^{-3})	24-hour[a]	125	50	-	-	40
CO (mg m^{-3})	24-hour[a]	7	-	-	-	4

[a] 99th percentile (i.e. 3-4 exceedance days per year).

[b] Average of daily maximum 8-hour mean O3 concentration in the six consecutive months with the highest six-month running-average O3 concentration.

The new limits of the Normative P9_TA(2024)0319 are reported in

Table 30.

Table 30. Limit values for the protection of human health to be attained by 1 January 2030.

Averaging period	Limit value
PM2.5	
1 Day	25 µg/m^3 not to be exceeded more than 18 times per calendar year

Calendar year	10 µg/m³
PM10	
1 Day	45 µg/m³ not to be exceeded more than 18 times per calendar year
Calendar year	20 µg/m³
Nitrogen dioxide (NO_2)	
1 hour	200 µg/m³ not to be exceeded more than 3 times per calendar year
1 Day	50 µg/m³ not to be exceeded more than 18 times per calendar year
Calendar year	20 µg/m³
Sulphur dioxide (SO_2)	
1 hour	350 µg/m³ not to be exceeded more than 3 times per calendar year
1 Day	50 µg/m³ not to be exceeded more than 18 times per calendar year
Calendar year	20 µg/m³
Benzene	
Calendar year	3.4 µg/m³
Carbon monoxide (CO)	
Maximum daily 8-hour mean (1)	10 mg/m³
1 day	4 mg/m³ not to be exceeded more than 18 times per calendar year
Lead (Pb)	
Calendar year	0.5 µg/m³
Arsenic (As)	
Calendar year	6.0 ng/m³
Cadmium (Cd)	
Calendar year	5.0 ng/m³
Nickel (Ni)	
Calendar year	20 ng/m³
Benzo(a)pyrene	
Calendar year	1.0 ng/m³

(1) The maximum daily 8-hour mean concentration shall be selected by examining 8-hour running averages, calculated from hourly data and updated each hour. Each 8-hour average so calculated shall be assigned to the day on which it ends, i.e. the first calculation period for any 1 day shall be the period from 17.00 on the previous day to 1.00 on that day; the last calculation period for any 1 day shall be the period from 16.00 to 24.00 on that day.

For Ozone, target values and long-term objectives to be attained by 1 January 2050 are reported in the following tables (Table 31 and Table 32).

Table 31. Ozone target values.

Objective	Averaging period	Target value
Protection of human health	Maximum daily 8-hour mean (1)	120 µg/m³ not to be exceeded on more than 18 days per calendar year averaged over 3 years (2) (3)
Protection of vegetation	May to July	AOT40 (calculated from 1-hour values) 18 000 µg/m³ × h averaged over 5 years (2)

(1) The maximum daily 8-hour mean concentration shall be selected by examining 8-hour running averages, calculated from hourly data and updated each hour. Each 8-hour average so calculated shall be assigned to the day on which it ends, i.e. the first calculation period

	for any 1 day shall be the period from 17.00 on the previous day to 1.00 on that day; the last calculation period for any 1 day shall be the period from 16.00 to 24.00 on the day.
(2)	**If the 3- or 5-year averages cannot be determined on the basis of a full and consecutive set of annual data, the minimum annual data required for checking compliance with the ozone target values shall be as follows:**
	i. for the target value for the protection of human health: valid data for 1 year,
	ii. for the target value for the protection of vegetation: valid data for 3 years.
(3)	***Until 1 January 2030, 120 µg/m³ not to be exceeded on more than 25 days per calendar year averaged over 3 years.***

Table 32. Long-term objectives for ozone (O3) to be attained by 1 January 2050.

Objective	Averaging period	Long-term objective
Protection of human health	Maximum daily 8-hour mean (1)	100 µg/m³ (1)
Protection of vegetation	May to July	AOT40 (calculated from 1-hour values) 6 000 µg/m³ × h
(1) 99th percentile, i.e. 3 exceedance days per year.		

The normative also recommends beginning to monitor other pollutants that have never been considered in the past. Following the two main interesting ones are reported:

the ultra-fine particle (UFP): UFP means *"particles with a diameter less than or equal to 100 nm, where UFP are measured as the particle number concentrations per cubic centimetre for a size range with a lower limit of 10 nm and for a size range with no restriction on the upper limit"*.

the black carbon: *black carbon or 'BC' means carbonaceous aerosols measured by light absorption.*

The UFPs, or ultrafine particles, are tiny particles with diameters of less than 0.1 micrometers (100 nanometers). They are a significant concern due to their potential impacts on health and the environment. Recent research has investigated how UFP exposure affects respiratory and cardiovascular health, as well as the toxicological mechanisms by which UFPs impact human health at the cellular and molecular levels. Olhwein et al. (2019) suggested adverse short-term associations with inflammatory and cardiovascular changes, which may be at least partly independent of other pollutants. Leikauf et al. (2020) showed how UFPs influenced airway inflammation and discussed several mechanisms that may explain the relationship between particulate air pollutants and human health, particularly respiratory health. Sapienza et al. (2024) showed that UFPs induced the aberrant expression of ER proteins leading to dysmorphic ER, organellar Ca^{2+} dysfunction, ER stress and neurotoxicity, providing putative correlations with the neurodegenerative process occurring in Amyotrophic Lateral Sclerosis (ALS).

Additionally, UFPs have environmental impacts on atmospheric chemistry, such as their interaction with other pollutants and their influence on atmospheric processes (Moreno-Ríos et al., 2022), as well as their role in climate change through their involvement in cloud formation (Sun et al.,2024).

Black carbon (BC) is one of the major components of PM in urban areas and is produced through the incomplete combustion of fossil fuels, biofuels, and biomass. Also, rural/remote areas are heavily affected by this pollutant when agricultural/forest fires occur. It is a significant contributor to air pollution and climate change due to its unique properties and widespread sources. The BC strongly absorbs sunlight (Cappa et al., 2019), contributing to atmospheric warming. When deposited on snow and ice, it reduces

albedo, accelerating melting. It also has a health impact; BC is mainly concentrated in the fine particulate matter and the inhalation of fine particles can lead to respiratory issues, cardiovascular diseases, and other health problems (Janssen et al., 2011).

The process of creating a consistent EU Air Quality directive began in 1980 when the EU started to focus on air quality by issuing directives that targeted specific pollutants such as sulphur dioxide, lead, and particulate matter. In the early 2000s, the directive went through consolidation and expansion phases, addressing additional pollutants and imposing stricter limits. Today, the EU has brought its air quality standards in line with the latest WHO guidelines, which recommend stricter limits for several pollutants. Advances in technology may lead to more comprehensive and accurate air quality monitoring, and future directives may prioritize integrating air quality measures with climate policies, especially in reducing emissions from transportation, energy, and agriculture sectors. According to the European Environment Agency (EEA), in 2021 in Europe, premature deaths due to chronic exposure to fine particulate matter were estimated at about 253,000, to chronic nitrogen dioxide exposure at about 52,000, and to acute ozone exposure at about 22,000 ("Harm to human health from air pollution in Europe"). The evolution of the Air Quality Directive reflects the EU's growing commitment to combating air pollution and safeguarding public health and the environment. Each revision aims to incorporate the latest scientific evidence and address new challenges in air quality management. To allow users to understand more about air quality where they live, work or travel, in 2021 the EEA launched the European Air Quality Index App[29] to provide instant access to up-to-date air quality monitoring data from monitoring stations located in European cities and towns and includes air quality forecasts and health recommendations. The European Air Quality index provides an easily understandable and standardized way to communicate air quality information across Europe. The index aims to raise awareness about air quality and its impact on health, as well as to encourage measures to improve air quality (EAQI[30]).

Though the main sources of air pollutants raising concerns are of anthropogenic nature, most of them present several natural sources. For instance, in the case of particulate matter, besides anthropogenic sources such as vehicular traffic, residential heating and industries, it is also contributed by natural ones such wildfires, volcanoes, seasalt, and mineral dust from the deserts. Of relevance is that climate change may be associated with changes in the contribution from these natural sources. Indeed, currently it is observed an increase in intrusions of mineral dust from neighbouring desert areas particularly in Europe and South America. The intensity and frequency of such episodes in recent years could be related to changes in atmospheric circulation patterns associated with climate change.

In the last months of 2023 and the beginning of 2024, the Copernicus Atmosphere Monitoring Service (CAMS) observed at least four large episodes of transport of Saharan dust over the Atlantic and towards continental Europe. In mid-December 2023, an intense intrusion of Saharan dust occurred in the Canary Islands, causing hazy skies and poor air quality, against a backdrop of unusually high temperatures for the time of year. The Spanish islands saw a new transport of dust during the Christmas period. Traditionally, winter is the season with the least dust transport activity in Europe and the Mediterranean. However, a recent publication highlights a sharp increase in Saharan dust intrusions over the western Mediterranean and the Euro-Atlantic area in the February-March 2020-2022 period, noting that some of them had an

[29] https://www.eea.europa.eu/en/newsroom/news/european-air-quality-index-app
[30] https://ecmwf-projects.github.io/copernicus-training-cams/proc-aq-index.html

unprecedented duration (Cuevas-Agullò et al., 2024). The analysis shows a clear increase in dust concentrations and maximum altitude during the winters of 2022-2022 compared to previous years (2003-2019), while recognizing high variability. The article also examines some of the atmospheric circulation factors that favour winter dust intrusions in the Mediterranean. Cut-off lows, located between the subtropical eastern North Atlantic and the western Mediterranean, and downstream high-pressure systems, trigger a large number of winter dust events over the western Euro-Mediterranean region. A 2021 analysis estimated that the frequency of satellite observations of dust doubled over the period 2005-2019.

Despite the collective efforts of governments and the population themselves, problems related to air pollution are far from being solved, and the risks related to it are potentially increasing due to climate change. In fact, air pollution, responsible for 8.1 million deaths globally in 2021, the second risk factor for death, even for children under 5 years of age, is having an increasingly greater impact on human health. This is the worrying point covered during the fifth edition of the State of Global Air Report, SoGA published in June 2024 by the Health Effects Institute (HEI, an independent non-profit research organization based in the United States, produced for the first time in collaboration with UNICEF). In addition to these deaths, many more millions of people live with debilitating, pollution-related chronic diseases, putting a strain on healthcare systems, economies, and societies. In 2021, exposure to air pollution was linked to more than 700,000 deaths of children under five, making it the second leading risk factor for death globally for this age group, after malnutrition. Of these, 500,000 child deaths were linked to household air pollution from cooking at home with polluting fuels, especially in Africa and Asia. Estimates reveal that nearly 2,000 children under five die every day due to the health impacts of air pollution.

The new SoGA Report offers a detailed analysis of recently released data from the 2021 Global Burden of Disease (GBD - a comprehensive regional and global research program of disease burden that assesses mortality and disability from major diseases, injuries, and risk factors, composed by a collaboration of over 3600 researchers from 145 countries) study, showing the serious impact on human health of pollutants such as outdoor fine particulate matter, PM2.5, household air pollution, ozone, and nitrogen dioxide, worldwide. The GBD report includes data from more than 200 countries and territories around the world, indicating that nearly every person on earth breathes unhealthy levels of air pollution every day, with far-reaching health implications.

As the world continues to warm due to the effects of climate change, areas with high levels of NO_2 can expect higher levels of ozone, with even more serious health effects. For the first time, this year's report includes exposure levels and related health effects of nitrogen dioxide, including the impact of NO_2 exposure on the development of children's asthma. Traffic exhaust is a major source of NO_2, meaning dense urban areas, particularly in high-income countries, often experience the highest levels of NO_2 exposure, resulting in the greatest health impacts. This clearly indicates an opportunity for cities and countries to consider air quality and air pollution as high-risk factors when developing health policies and other non-communicable disease prevention and control programmes.

Air quality measures in all regions of the world such as installing air pollution monitoring networks, implementing stricter air quality policies or offsetting traffic-related air pollution by switching to hybrid or electric vehicles are having a measurable impact on pollution and improving public health. While

progress is being made, more can be done to prevent air pollution from continuing to outweigh other health risks and become a major threat to millions of lives.

3.6 Biological hazards

3.6.1 Climate-change effects on the general and the occupationally exposed population

As reported by Rawat and collaborators in their recent paper (Rawat et al., 2024), climate change is the result of particular human activities, such as burning of fossil fuels, deforestation, and industrial processes. Moreover, the accumulation of greenhouse gases in the atmosphere is a primary driver of these changes, which may significantly alter climatic patterns globally. Climate change can lead to different and various effects, at different levels: these, as reported by the authors, refer to: (i) increased temperatures; (ii) rising sea levels; (iii) more frequent and severe storms; (iv) changes in the pattern of precipitation and sea currents. As a result, these changes have repercussions in various fields, including agriculture, water use, biodiversity and human health.

Global temperatures and heat waves will increase (in terms of frequency and intensity) over the course of this century (as reported by the WHO, World Health Organization). The long-term effects of exposure to high temperatures can cause physiological stress by aggravating respiratory and cardiovascular diseases. The acute effects attributable to heat waves, on the other hand, more often lead to an increase in mortality in the general population. Moreover, heat stress can exacerbate pre-existing health conditions, leading to an overall decline in public health quality. In this regard, it is important to underline that the increase in temperatures affects the entire population, but, at the same time, only some groups result more exposed (e.g., particular types of workers) or more vulnerable to physiological stress (e.g., the elderly, infants and children, pregnant women). Finally, it is important to underline how climate change can directly or indirectly affect environmental quality, introducing pollutants, particles or contaminants through the increase in extreme weather events (Bolan et al., 2024; Borghi et al., 2024).

To investigate the effects (direct and indirect) of climate change (i) on the general population and on the (ii) occupational population, two research query were developed and investigated for carrying out two literature reviews. The main purposes of the reviews on the general population (systematic review of the literature) and on the occupational population (umbrella review) were mainly those of:

1. highlight the most commonly used effect indicators in the scientific field;
2. highlight the categories of subjects/workers most investigated in the scientific field;
3. analyze the effect indicators according to (i) the geographical area considered, (ii) the type of environment considered (urban/non-urban) and (iii) the degree of economic development of the country under consideration.

MATERIAL AND METHODS

For both reviews (systematic literature review and umbrella review), the results obtained from three scientific databases (Scopus, Web of Science and PubMed) obtained from a search query set up as reported in Table 33 will be analyzed. After the removal of duplicate articles, the articles will undergo a two-tier screening process that will involve (i) title and (ii) abstract evaluation. These steps will be conducted independently by two different authors to minimize potential operator-dependent errors. The remaining selected articles will then be analyzed and evaluated with a complete reading of the text.

In particular, regarding the review of the literature concerning the effects of climate change on the general population, articles related to the aims of this work will be selected, excluding scientific articles written not in English, conference proceedings, literature reviews, book chapters, toxicological studies, and in vivo studies. In the case of the umbrella review focused on the evaluation of the effects of climate change on the occupationally exposed population, only systematic reviews of the literature which aim to investigate the effects of climate change on the occupational population will be considered. The exclusion criteria in this case are reported: scientific articles written not in English, conference proceedings, book chapters, toxicological studies, and in vivo studies. To ensure the validity and reliability of the review process, each article was assessed using standardized quality assessment tools relevant to the study design. This included evaluating the methodological rigor and the relevance of findings to the research questions posed.

For the evaluation of the articles, the PRISMA (Preferred Reporting Items for Systematic Reviews and Meta-Analyses) criteria were adhered to, ensuring a systematic and transparent approach to the review process (Moher et al., 2009).

Table 33. Review process on general and occupationally exposed population.

	Review	
	General population **Systematic review of the literature**	**Occupationally exposed population** **Umbrella review**
Review question	Which are the effects of climate change (both in the hot and cold seasons) on the health of the general population.	Which are the effects of climate change (both in the hot and cold seasons) on the health of the occupational population.
Population	General population	Occupationally exposed population
Exposure	General population exposed to heat waves or other events caused by climate change	Occupationally exposed population exposed to heat waves or other events caused by climate change
Outcome	Morbidity and mortality from various causes	
Database	PubMED, Scopus, Web of Science	
Search query	Hazard exposure: "climate change" OR "heat" OR "temperature" OR "cold" OR "global warming" OR "weather" AND	Population: "work" OR "occupant*" OR "employ*" AND Hazard exposure: "climate change" OR "heat" OR "temperature" OR "cold" OR "global warming" OR "weather"

	Effects: "mortality" OR "death" OR "health effect" OR "admission*" OR "morbidity*" OR "reproduction" AND Location: "Albania" OR "Andorra" OR "Austria" OR "Belarus" OR "Belgium" OR "Bosnia and Herzegovina" OR "Bulgaria" OR "Croatia" OR "Cyprus" OR "Czech Republic" OR "Denmark" OR "Estonia" OR "Finland" OR "France" OR "Germany" OR "Greece" OR "Hungary" OR "Iceland" OR "Ireland" OR "Italy" OR "Kosovo" OR "Latvia" OR "Liechtenstein" OR "Lithuania" OR "Luxembourg" OR "Malta" OR "Moldova" OR "Monaco" OR "Montenegro" OR "Netherlands" OR "North Macedonia" OR "Norway" OR "Poland" OR "Portugal" OR "Romania" OR "Russia" OR "San Marino" OR "Serbia" OR "Slovakia" OR "Slovenia" OR "Spain" OR "Sweden" OR "Switzerland" OR "Turkey" OR "Ukraine" OR "United Kingdom" OR "Vatican City" or "Europe*"	
Exclusion criteria	▪ Articles written not in English ▪ Literature reviews; conference proceedings; book chapters ▪ Toxicological studies; in vivo studies ▪ Non-European population	▪ Articles written not in English ▪ Conference proceedings; book chapters ▪ Toxicological studies; in vivo studies

PRELIMINAR RESULTS

Considering the search query set up ad hoc for the general population systematic review, and the number of articles resulting from this (no articles elimination), it is possible to highlight how the number of articles related to this topic increased, starting from the beginning of the 90s (Figure 75), emphasizing the growing interest in this topic.

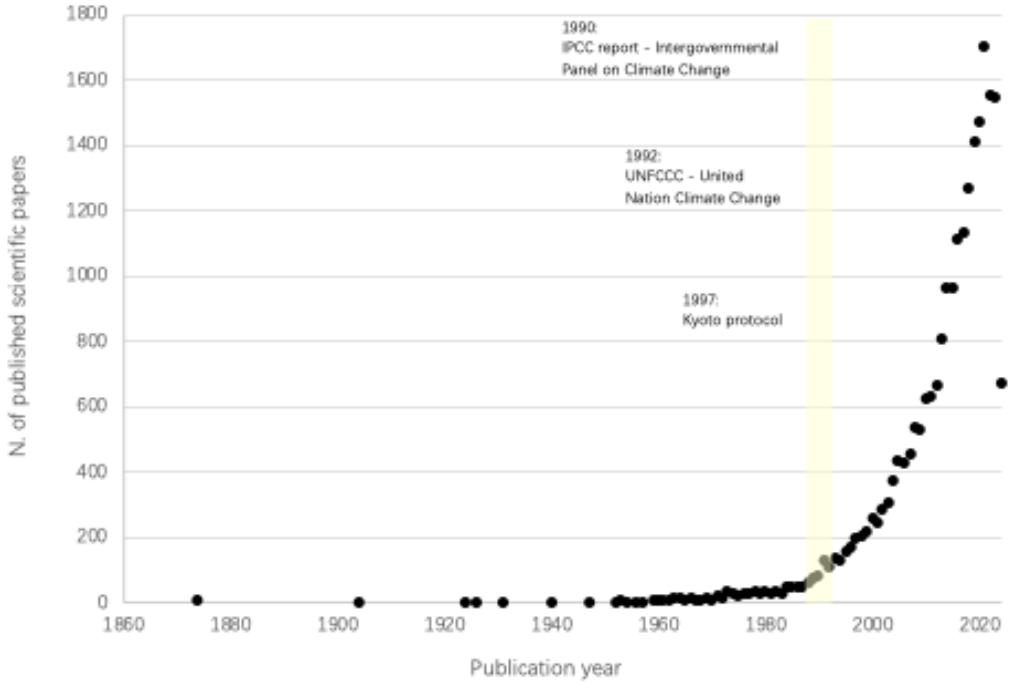

Figure 75. Number of papers resulting from the general population systematic review.

Although the review work is still in progress, some main results can be drawn from an initial analysis of the studies considered, briefly reported below.

Climate change, as is well known, can have adverse effects on the health of the general population, significantly impacting with direct and indirect effects. These effects may manifest in a variety of ways, necessitating a broad and multidisciplinary approach to fully understand and address them. In particular, these effects concern several aspects, such as, but not limited to: (I) effects related to heatwaves and rising temperatures (increased mortality and morbidity, especially considering the most vulnerable population such as children, the elderly and people with chronic diseases); sleep quality; exacerbation of cardiovascular and respiratory diseases; mental health problems); (ii) waterborne infections and infectious diseases (increased in incidence due to changes in climate patterns that can favor the spread of vectors of specific diseases, such as malaria and dengue); (iii) effects on children's health (premature births and low birth weight); (iv) health effects of the elderly (increased vulnerability to heat-related morbidity and mortality; increased respiratory and cardiovascular diseases); (v) reproductive health (increased risk of premature births, low birth weight and stillbirth). In addition, (vi) air pollution, in terms of air quality and the presence of allergens, aggravated by climate change, can affect the health of the population (exacerbating, also in this case, previous respiratory problems).

As reported by the ILO (International Labour Organization), the effects of climate change also have strong repercussions on the health and safety of the occupationally exposed population. In fact, the ILO report (ILO, 2024) highlight that there are numerous workers' health conditions linked to climate change to date, including (i) cancer, (ii) cardiovascular diseases, (iii) respiratory diseases, (iv) kidney dysfunction and (v) mental health conditions, especially for particular categories of workers (i.e., those who work outdoors such as: workers in agriculture, environmental goods and services (natural resource management),

construction, refuse collection, emergency repair work, transport, tourism and sports). In addition to the main health effects reported, high temperatures can also lead to secondary adverse effects, reducing the worker's ability to concentrate and thus increasing the risk of injury in the workplace: for this reason, specific interventions are required to improve worker safety and well-being at work.

The main and preliminary results of this study highlight how the effects of climate change are important and diversified, both considering the general population and the occupationally exposed population. As reported by several studies, in fact, heat waves in addition to aggravating pre-existing health conditions, increase morbidity and mortality in the population, especially in vulnerable individuals (the elderly, children, pregnant women and outdoor workers). In summary, climate change represents a significant threat to the health of the population (general and occupational) and requires multidisciplinary responses involving research, public policies and practical interventions.

3.6.2 Exposure to contaminants in various biological tissues

Climate change directly or indirectly impacts on the environmental quality (e.g., on air and water quality), for example introducing particles or contaminants throughout the increase of extreme weather events (Bolan et al., 2024). Human interactions with exogenous agents would become more frequent over years, as highlighted by recent works analyzing the particles/fibers/pollutants presence in human tissues and their potential health impact (Peters et al., 2020; Visonà et al., 2021; Krause et al., 2024). Thus, reliable and validated procedures are needed to quantitatively detect pollutants and contaminants in human tissues.

Activities

We introduce a step-by-step protocol for mapping, quantitatively evaluating, and chemically characterizing inorganic particles/fibers/pollutants (also considering microplastic particles) present in human tissues.

Among the several potential pollutants we started from well-know and well-characterized ones in order to robustly define the digestion and investigation protocol. Asbestos *is a natural mineral (durable, fireproof and resistant to heat and chemicals) made of fibers commonly used in many industries for decades: especially due to occupation exposure, the asbestos fibers are know to* provoke respiratory system diseases such as asbestosis, mesothelioma and lung cancer (Belluso et al, 2006). Crystalline silica is a natural mineral, highly abundant in the α-quartz form. It is highlighted as a human carcinogen – Group 1, manifesting fibrotic lung diseases pathologically-known as silicosis, and mainly related to occupational exposure (McLean et al, 2017). Recent studies have also reported the correlation of mineral talc, having the following chemical formulation $Mg_3Si_4O_{10}(OH)_2$, with ovarian cancer (Fletcher at al, 2019), for example upon talcum baby-powder (hydrous magnesium silicate, with small amounts of aluminum silicate) intensive use (Johnson et al, 2020).

Microplastics might directly or indirectly trigger inflammations, for example enhancing the prevalence or severity of non-communicable diseases or influencing the uptaking of other environmental pollutants. Owing to the present knowledge gap on microplastics effects (either inhaled or via ingestion), they are currently under study and represent a hot-topic nowadays (Krause et al., 2024).

The digestion protocol is the following. The biological material obtained from biopsies is extracted from the matrix (e.g., paraffin, formalin, simply frozen ice) and digested, soaking them in sodium hypochlorite solution (7% active chloride) or potassium hydroxide (KOH, 1.5M), depending on the pollutants under investigation, at 60°C: 2 to 10 days are needed for the digestion of the biological material. The solution is then filtered on 25 mm diameter, polycarbonate membranes or aluminum coated polyester ones for inorganic/metallic contaminants and microplastics investigation, respectively. Finally, the wet membranes are placed inside a petri dish and dried (50°C) for 20-30 minutes. The digestion protocol proved to be strongly versatile and compatible with several tissues, e.g.:

- lungs
- ovary
- bladder
- ureter
- lymph node
- bone marrow
- prostate

The digestion protocol proved especially effective for biological tissues that were frozen (-20°C or -80°C) or in paraffin matrix, while formalin-stored samples showed worse digestions, which traduced in more residuals observed on the filters during imaging analysis.

For a broaden pollutant investigation, Scanning Electron Microscope (SEM) and Raman spectroscopy were employed for inorganic fibers/particles and microplastics imaging, respectively. A quantitative analysis of the exogenous agents, in terms of dimensions, shape/morphology and concentration per milligrams of dried biological tissue, together with their chemical investigation, enables to extract fundamental information that might be correlated to diseases, inflammations and other direct or indirect impact on tissue/human status.

For the investigation of fiber, for example, the observation of 500 fields at 2000X (magnification) was used for screening the 25 mm diameter membrane filters, using 15kV as electron accelerating voltage and 8.5mm as working distance. A total area bigger than 1 mm2 was investigated by means of the reported protocol analysis: the suspected asbestos fibers were then confirmed or rejected using the Energy Dispersive X-Ray (EDX) chemical analysis. Figure 76 shows an asbestos fiber having length >10 µm and width ≤ 1 µm with its chemical x-ray spectrum, in which Magnesium and Silicon peaks confirm the fiber as asbestos nature.

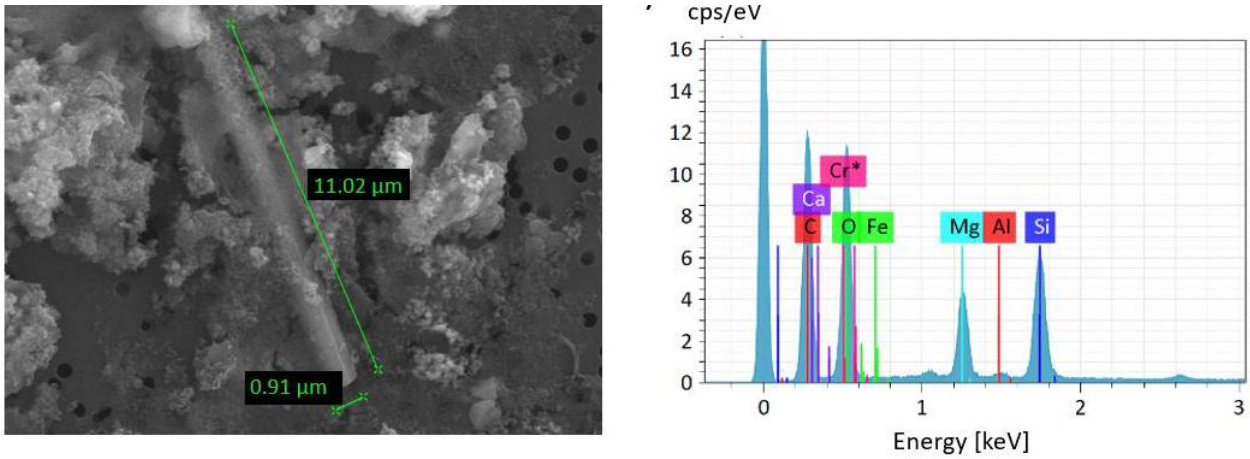

Figure 76. Asbestos fiber on a polycarbonate membrane filter that is visible despite small biological tissue residuals (left) and its chemical x-ray spectrum (right) confirming the Magnesium and Silicon peaks, typical of asbestos-like contaminants.

We similarly proceeded translating our digestion and investigation protocols to other tissues and contaminants, as reported above. Figure 77 represents the search for aluminum pollutants in a human lymph node: EDX chemical mapping analysis allowed for the discrimination of metallic cluster on the filter and biological residuals background.

Related Projects

We are currently assessing and investigating morphology and concentration of asbestos fibers in lungs and talc particles in ovarian tissues. Our aim is the correlation of these pollutants with tumor formation: the information already available stressing the interplay between asbestos fibers and lung tumors will provide the starting point for investigating similar relation or correlation with asbestos/talc with ovarian tumor.

On the other side, we are studying the influence of microplastic particles in placenta on cell metabolomics or as “Trojan horse” for environmental pollutants and contaminants. Our preliminary investigation proved the effectiveness of the digestion protocol, and the high-resolution Raman imaging setup purchase is currently ongoing.

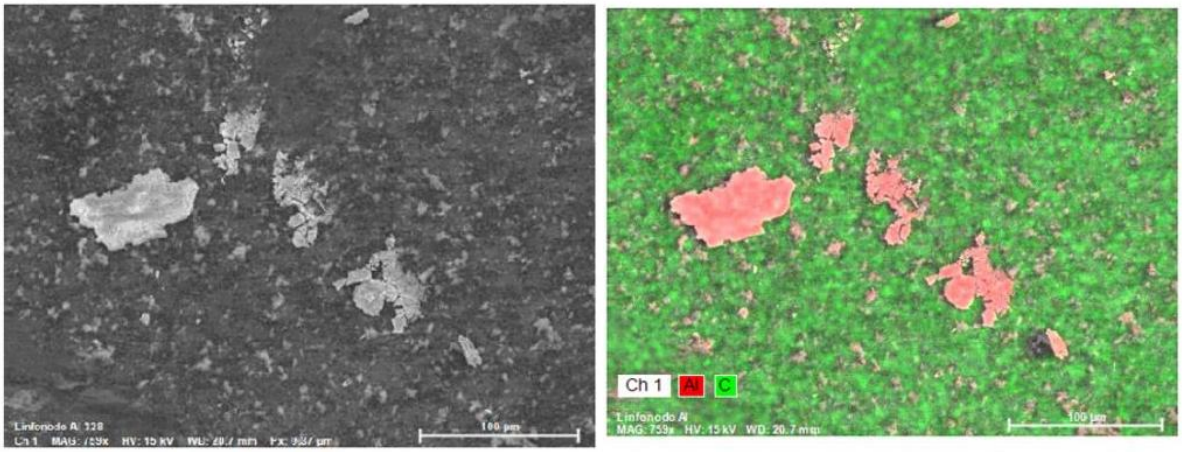

Figure 77. SEM image (left) and correspondent chemical mapping using EDX (right) of a digested, aluminum-contaminated lymph node.

Next steps

Further studies would be directed towards the automatization of SEM-EDX and Raman spectroscopy, comparing the automatic procedure versus a manual one, for saving sampling and analysis time, while maintaining the quantitative and reliable evaluation. In particular, the "counting" and evaluation performed throughout an AI system will be compared to the strict assessment protocol manually taken by two of our skilled lab operators.

4. Multi-hazard analysis for urban and metropolitan areas

Urban and metropolitan areas are increasingly susceptible to a variety of hazards, often characterized by compounding or cascading effects. The complexity of these multi-hazard scenarios necessitates comprehensive analysis and innovative strategies to enhance urban resilience and effectively mitigate risks. Herein, various scenarios and approaches for understanding and managing these risks within the context of densely populated and highly developed environments are explored.

The Section is divided into two main sub-sections, each addressing critical aspects of multi-hazard analysis. The first sub-section focuses on strategies and methodologies for studying and analyzing climate-related hazards, which may not always be cascading or compound. It provides a framework for urban planners and policymakers to anticipate and respond to complex hazard scenarios effectively.

The second sub-section delves into real-world examples where hazards interact, leading to cascading and/or compounding effects. These interactions can amplify the overall impact, making them more difficult to predict and manage. It highlights key cases where the interaction between multiple hazards has resulted in significant consequences for urban and metropolitan areas, offering insights into how such scenarios can be better understood and addressed.

Finally, it is important to note that as the storyline development within Work Package 3 evolves, new multi-hazard cases may be added to this analysis. The initial set of storylines, presented in the following Section 5, will guide the ongoing exploration and refinement of multi-hazard scenarios, ensuring that the strategies discussed in this Section remain relevant and responsive to emerging risks.

4.1 Climate-related multi-hazard

4.1.1 Low-Cost Monitoring Strategies for Measuring Environmental Parameters in a Multi-Hazard Urban Context

The need for effective environmental monitoring has grown in the urban context due to increasing concerns about climate change, urbanization, and associated multi-hazard risks. Traditional monitoring systems are often expensive and limited in spatial coverage, leading to a growing interest in low-cost, wireless sensor networks (WSNs). We discuss the state-of-the-art low-cost monitoring strategies using networks of wireless sensors for measuring environmental parameters such as air temperature, humidity, CO_2, and flood levels. Emphasis is placed on the applicability of these technologies in urban settings for managing and mitigating the impacts of environmental hazards to enhance urban resilience. Case studies from peer-reviewed literature highlighting successful implementations and lessons learned are analysed.

4.1.1.1 Wireless sensor networks (WSNs)

WSNs consist of numerous spatially distributed sensor nodes that communicate wirelessly to collect and transmit data to a central server for analysis. These networks are increasingly used for environmental monitoring due to their key features of WSNs include:

- Scalability: Ability to cover large areas with numerous sensors.
- Flexibility: Easy deployment and reconfiguration.
- Cost-effectiveness: Use of inexpensive sensors and communication technologies.

Multi-hazard monitoring involves tracking various environmental risks simultaneously, such as heatwaves, air pollution, and flooding. Indeed, WSNs can integrate different sensors to provide comprehensive data for hazard assessment and management.

Low Power and Ultra Low Power Sensors

Low Power (LP) and Ultra Low Power (ULP) Sensor Networks are integral to modern smart city infrastructure, leveraging a diverse array of environmental sensors. They are essential for the long-term deployment of WSNs to monitor and manage urban ecosystems efficiently. Technologies such as energy harvesting and low-power communication protocols (e.g., LoRaWAN, Zigbee) are commonly integrated to enhance efficiency.

Key sensors include air quality sensors, which measure pollutants such as CO_2, NO_2, SO_2, and particulate matter (PM2.5 and PM10), providing critical data on air pollution levels. Temperature and humidity sensors monitor climatic conditions, aiding in weather prediction and urban heat island effect analysis. Sound level meters gauge noise pollution, essential for maintaining acceptable urban soundscapes. Light sensors assess ambient light conditions, facilitating adaptive street lighting and energy conservation. Additionally, soil moisture sensors are deployed in green spaces to optimize irrigation systems, promoting water conservation. Flood monitoring sensors, including water level and flow sensors, are crucial for early flood detection and management.

These sensors typically operate on minimal power, often employing advanced energy-harvesting techniques to sustain prolonged operation without frequent battery replacements or external power sources. Solar energy harvesting is a prevalent method, capturing sunlight through photovoltaic cells to power sensors and recharge batteries. Kinetic energy harvesting, which converts vibrations or movements into electrical energy, is another approach, particularly effective in urban environments with constant vehicular or pedestrian motion. Thermal energy harvesting leverages temperature differences between surfaces to generate power, while ambient RF (radio frequency) energy harvesting captures and converts ambient electromagnetic waves from wireless signals into usable electrical energy.

Energy harvesting significantly enhances network sustainability, enabling sensors to draw power from ambient sources such as sunlight, vibrations, and thermal gradients. For instance, Burhan et al. (2018) discuss IoT-based smart irrigation systems utilizing solar energy harvesting to maintain continuous operation of soil moisture sensors. Salman and Liu (2019) emphasize the role of power-efficient transceiver communication in environmental monitoring using wireless sensor networks (WSNs), highlighting the importance of energy harvesting techniques for prolonged sensor life and reliability. Similarly, Kulkarni and Sathe (2014) detail the deployment of water quality monitoring systems where energy harvesting ensures uninterrupted data collection.

Flood monitoring is particularly critical in urban areas prone to heavy rainfall and waterlogging. Afzal et al. (2016) describe an energy-efficient flood detection and evacuation system using WSN technology, which integrates water level sensors powered by energy harvesting to provide real-time alerts and reduce disaster response times. Zhang et al. (2014) present a flood monitoring system that combines wireless sensor networks and GPRS for robust data transmission, employing solar and kinetic energy harvesting to maintain sensor network functionality even during adverse weather conditions.

Integration with Low Power Wide Area Networks (LPWAN) like LoRaWAN and NB-IoT ensures robust, long-range communication with minimal energy expenditure, crucial for widespread urban deployment. These networks facilitate seamless data transmission from distributed sensors to central monitoring systems, enabling real-time environmental monitoring and enhancing urban living conditions through data-driven decision-making. Collectively, these energy-harvesting sensors form a comprehensive network that not only supports sustainable urban development but also ensures resilience against environmental challenges.

4.1.1.2 Case studies on the successful application of low-cost sensors

Case studies on the successful application of low-cost sensors in different applications and geographical contexts are briefly summarized in the following.

- Smart Citizen Project, Barcelona. The Smart Citizen project in Barcelona employs a network of low-cost sensors to monitor air quality, temperature, and humidity across the city. The project aims to engage citizens in environmental monitoring and provide real-time data for urban planning and public health management (Maag et al., 2018).

- Air Quality Monitoring in Beijing. A study in Beijing utilized a network of low-cost sensors to measure PM2.5, CO_2, temperature, and humidity. The data collected helped identify pollution hotspots and temporal patterns, informing public health interventions and urban planning strategies (Liu et al., 2020).

- Heatwave monitoring in Paris. In Paris, a network of low-cost temperature and humidity sensors was deployed to monitor the urban heat island effect during heat waves. The data provided insights into the spatial variability of heat stress, aiding in the development of targeted cooling strategies (Chapman et al., 2017).

- Urban heat island and air quality in Milan. A network of wireless sensors was installed in Milan to monitor environmental parameters such as temperature, humidity, and CO_2 levels. The collected data was used to analyze the urban heat island effect and air quality, leading to the implementation of urban greening projects to mitigate these issues (Bonafè et al., 2018).

- Monitoring in Nairobi, Kenya. A study in Nairobi used low-cost sensors to monitor air quality and temperature across various urban locations. This data was crucial for assessing the impact of traffic and industrial activities on urban air quality, leading to policy recommendations for pollution control (Osano et al., 2019).

- Urban Heat Island Monitoring in Rome. In Rome, a dense network of weather stations was established to measure the urban heat island effect using temperature and humidity sensors. The data was cross-referenced with remote sensing imperviousness data, providing a comprehensive understanding of urban heat dynamics and informing urban planning decisions (Cecilia et al., 2023).

- Heat Island and CO_2 Monitoring in Hong Kong. A study in Hong Kong used a network of low-cost sensors to monitor air temperature, humidity, and CO_2 levels across the city. The data collected helped analyze the impact of urban morphology on heat island effects and CO_2 distribution, supporting urban design and policy-making efforts (Yang et al., 2024).

- Flood Monitoring in Singapore. Singapore has implemented a network of low-cost water level sensors to monitor urban flooding. These sensors provide real-time data to a centralized system, enabling quick response to flood events and enhancing the city's resilience to heavy rainfall and sea level rise (Koo et al., 2018).

- Urban flooding in New York City. FloodNet is a network of low-cost sensors deployed across New York City to monitor flooding events in real-time. The sensors provide data on water levels, helping the city to respond quickly to flood hazards and improving resilience against future flooding events. This initiative showcases the effectiveness of low-cost monitoring in addressing urban flood risks (Hill et al., 2021; Mydlarz et al 2024).

4.1.1.3 Data Loss in urban sensor networks

Data loss in Urban Low Power (LP) and Ultra Low Power (ULP) Sensor Networks is a critical challenge that can undermine the reliability and effectiveness of environmental monitoring and management systems. For instance, Mydlarz et al (2024), when analyzing the FloodNet NYC network, found a high amount of data loss during transmission over LoRaWAN and decided to switch to a cellular network and add onboard flash memory to store data on the sensor, minimising the loss of data packets.

Several factors contribute to data loss in these networks. One major factor is the limited power supply, which can lead to intermittent operation of sensors and communication modules, especially in the absence of effective energy-harvesting mechanisms. Battery depletion or insufficient energy harvesting during periods of low ambient energy availability can cause sensors to fail temporarily, resulting in gaps in data collection. Additionally, the low bandwidth and high latency of LPWAN technologies such as LoRaWAN and NB-IoT, while energy-efficient, can lead to packet loss or delays in data transmission, exacerbating the issue of data loss (Centenaro et al., 2016; Luan et al., 2018). Environmental interferences, such as physical obstructions, electromagnetic interference, and adverse weather conditions, can further degrade the quality of wireless communication, leading to incomplete or corrupted data packets (Akyildiz & Kasimoglu, 2004). Network congestion, especially in densely populated urban areas with numerous interconnected devices, can also cause data collisions and loss (Chouikhi et al., 2015).

However, to mitigate these issues, robust error detection and correction algorithms are crucial. These algorithms can identify and correct errors in transmitted data, ensuring the integrity of the information received (Elsts et al., 2016). Adaptive power management strategies that dynamically adjust the energy consumption of sensors based on their current power levels and the importance of the data being collected can prolong the operational lifetime of the network and reduce data loss (Ma et al., 2020). Redundant sensor deployments, where multiple sensors are used to monitor the same parameter, can provide backup data in case one sensor fails, thereby improving data reliability (Boukerche & Samarah, 2009).

Advanced network protocols that prioritize critical data and optimize communication pathways can also help in reducing the incidence of data loss. For instance, protocols that employ adaptive data compression and efficient routing algorithms can minimize the amount of data that needs to be transmitted, thereby reducing the likelihood of congestion and loss (Elsts et al., 2016). Moreover, edge computing, where data processing is performed closer to the data source, can reduce the amount of data transmitted over the network and allow for faster detection and correction of errors, further enhancing data reliability. These

strategies collectively help maintain the integrity and utility of the sensor network for urban applications, ensuring continuous and reliable environmental monitoring.

4.1.1.3 Data Quality Check in urban sensor networks

Ensuring data quality is critical for the reliability of WSNs in environmental monitoring. Low-cost sensors may be prone to errors and require rigorous quality control measures. Data quality checks involve calibration, validation against reference instruments, and statistical techniques to identify and correct anomalies. A statistically-based quality control method was developed by Napoly et al. (2018) for crowdsourced air temperature data to enhance the reliability of urban climate research. A quality-control framework for crowdsourced air temperature observations, enabling reliable urban climate applications worldwide is provided by the CrowdQC+, a framework that incorporates automated checks and calibrations to ensure data accuracy (Fenner et al., 2021).

These kinds of procedures were applied to a six-year data study from a citizen weather station network in London, revealing horizontal urban heat advection and emphasizing the importance of thorough data validation (Brousse et al., 2022).

In summary, low-cost monitoring networks present many advantages. They are affordable and enable widespread deployment, making it feasible to cover large urban areas. They provide real-time data, which constitutes timely information for prompt decision-making. Moreover, they enhance community engagement, involving citizens in monitoring, raising awareness, and fostering community-driven initiatives.

On the other hand, the development of low-cost monitoring networks also presents challenges and limitations. First of all, they may have lower accuracy and require frequent calibration and quality checks. Moreover, handling large volumes of data from numerous sensors can be challenging and it requires constant care to assure network reliability, since ensuring consistent communication and power supply for sensors is critical.

As described above, low-cost monitoring strategies using wireless sensor networks offer significant potential for enhancing urban resilience against environmental hazards. These systems can inform urban planning and public health interventions by providing real-time, spatially detailed data on air temperature, humidity, CO_2 and flooding levels. Future research should focus on improving sensor accuracy, data integration, and network reliability to fully realize the benefits of these technologies.

4.1.2 Heatwaves and extreme sea level vulnerabilities towards a multi-hazard GIS-based framework

4.1.2.1 The PLANNER and Coast-RiskBySea models for heatwave and extreme sea level rise impact assessment

The PLANNER (D'Ambrosio et al., 2023) and the Coast-RiskBySea (Clemente et al., 2022) methodological frameworks were developed within the environmental design and computer science research group of the Department of Architecture, of the University of Naples Federico II, for support decision makers in the testing of design solutions for risk reduction. In both models, following the IPCC AR5 and AR6 Reports, risk is assessed in a GIS environment taking into account hazard, vulnerability, and exposure.

The PLANNER model (D'Ambrosio et al., 2023) allows the evaluation of the heatwave's effects on urban population. The model is based on the use of remote sensing data and census zones data provided by ISTAT (Italian National Institute of Statistics). The exposed population type and urban vulnerability considering residential buildings and open spaces for census zones, are combined with the heatwave hazard scenarios to implement the impact scenarios. The PLANNER model workflow was schematized in the following Figure 78.

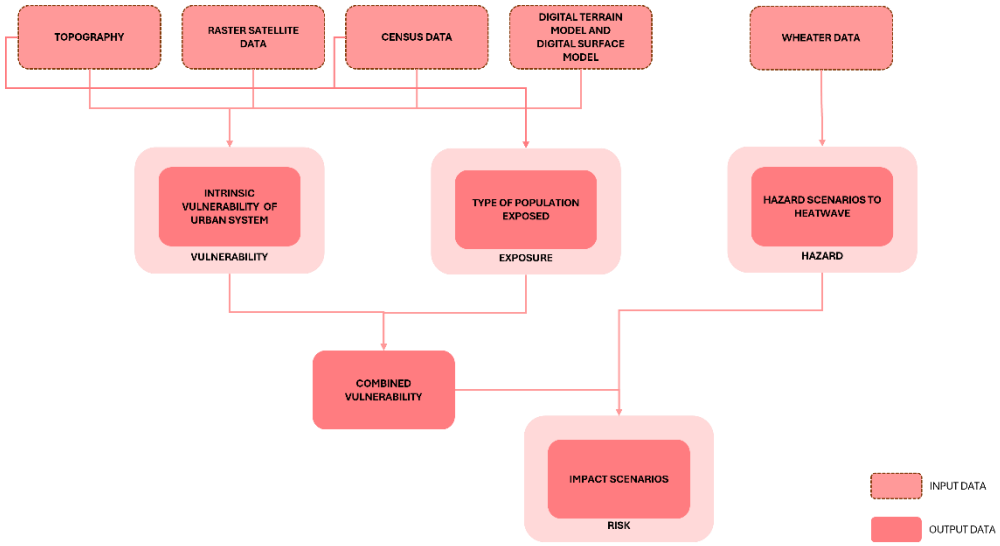

Figure 78. Workflow of the Heatwave model. Source: Clemente et al., 2023.

The Coast-RiskBySea model (Clemente et al.; 2022) allows a simplified assessment of the potential effects of coastal flooding on the built environment due to extreme sea level events. Also in this case, remote sensing data serves as the base data; simulations are performed based on a homogeneous hexagonal reference grid. The combination of the exposed built environment type, the vulnerability considered as the mean elevation above sea level, and the hazard scenarios as potential extreme sea level events (in function of mean sea level, tides, wind-waves, and storm surges), generated impacts scenarios. The Coast-RiskBySea model workflow was schematized in the following Figure 79.

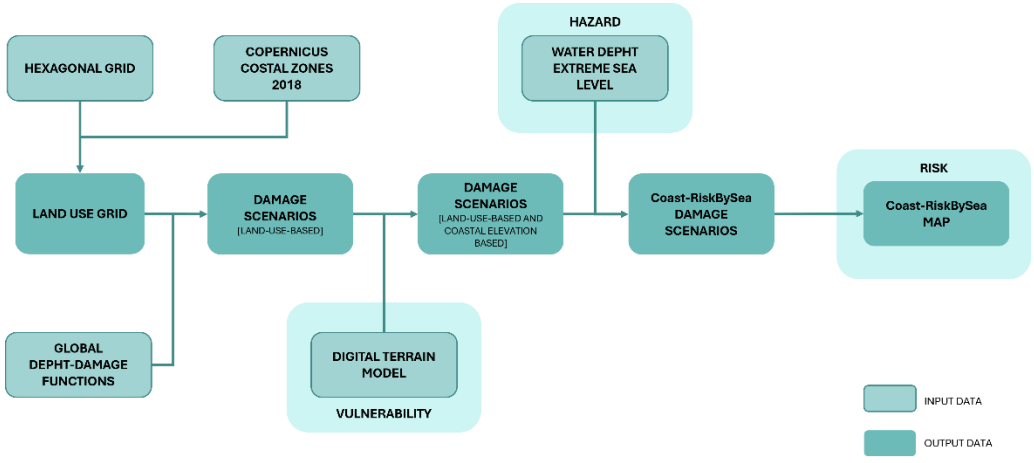

Figure 79. Workflow of the Coast-RiskBySea model. Source: Clemente et al., 2023.

The medium and long-term climate scenarios are the basis for the impact assessment implemented by both models in GIS environment. The main characteristics of each model are synthesized and compared in Table 34.

Table 34. Characteristics of PLANNER and Coast-RiskBySea models.

	PLANNER		Coast-RiskBySea
Hazard/s	Heatwave: – Short-term scenario (2020-2040) – Medium-term scenario (2041-2070) – Long-term scenario (2071-2100)		Extreme Sea Level (ESL)
Exposure and related indicators	Inhabitants: – Population Density – Disadvantaged Population – Fuel Poverty		Physical system of urban areas – Land use classes
Vulnerability and related indicators	Residential building system: – Thermal lag – Solar exposure of building envelope – Thermal decrement factor – Building volume	Open spaces system: – Albedo – NDVI – Solar exposure of open spaces – Sky View Factor indicators	Altimetry – Mean elevation above sea level
Reference unit	Census section		Hexagonal cells
Input data	Topographic database of the study area Census data Satellite data		Copernicus coastal zones DTM EU Joint Research Centre "Global depth-damage function" Extreme Sea Level scenarios
Reference	D'Ambrosio et al., 2023		Clemente et al.; 2022

4.1.2.2 An integration proposal towards multi-hazards simulations

In the framework of urban and metropolitan settlements, urban coastal areas, in Italy and in the Mediterranean region, are among the areas most at risk due to the high exposure of people, activities, goods and services, and due to the intrinsic vulnerability of coastal territories. These areas face multiple hazards, and considering the long-term climate projections, the direct link between rising global average temperatures and sea levels rise will further increase the fragility of these territories (Abadie et al., 2016; Forzieri et al., 2016; Vousdoukas et al., 2017; Prahl et al., 2018; Abadie et al., 2019). Together with coastal-related hazards heatwaves represent a critical issue for national urban settlements and for the public health, moreover, the increase in the global average temperature has a direct impact on the occurrence, frequencies and intensity of this phenomena (Kovats et al., 2006; Molina et al., 2020; Bacciu et al., 2020).

Based on the PLANNER and the Coast-RiskBySea models, a GIS-based framework was elaborated to assess the vulnerabilities for extreme sea level events and heatwaves on the same reference unit, as well as to identify the most critical areas and support design processes oriented towards risk-reduction (Clemente et al.; 2023). The combination of the two models allows a simultaneous assessment of the Extreme Sea Level (ESL) vulnerability (measured as a function of mean elevation above sea level) and the Heatwave (HW) vulnerability (measured as a function of Albedo, NDVI, Solar exposure of open spaces, and Sky View Factor indicators). By combining the two models on the same atomic reference unit, the vulnerability considering the two hazards can be evaluated simultaneously. This means that decision-makers can be

supported by considering more than one phenomenon at the same time, a condition that is crucial to better orient the multi-risk design solutions in order to increase urban resilience face to multiple hazards.

The GIS-based framework is structured in the following steps:

1. the input data collection and the definition of new reference atomic units;
2. the development and implementation of computational processes to assess vulnerability to ESL, applying the Coast-RiskBySea methodology, and vulnerability to HW and applying the PLANNER methodology;
3. the identification of critical areas considering the vulnerability of more than one hazards.

Since the two models were based on distinct reference units, new atomic reference units were elaborated. In fact, if PLANNER is based on ISTAT census zones to have a homogenous distribution of the census data section throughout the whole national territory, Coast-RiskBySea is based on a hexagonal reference grid.

Considering coastal-related hazards, mean elevation above sea level is a crucial component in determining and organizing the new atomic reference units. By giving each elevation interval a distinct class value, the heights Above Mean Sea Level (AMSL) were classed using a method of spatial analysis based on the Digital Terrain Model (DTM) raster data. The thresholds used are the same of that used in the Coast-RiskBySea model (Clemente et al., 2022), which were established based on the threshold of the "global depth-damage functions" (Huizinga et al., 2017) to assess the potential economic damages to the built environment according to land use classes. The obtained values can be then classified through a manual approach.

Following the identification of the AMSLs on the reclassified raster file, the data were transformed into a polygonal shapefile. The polygons are then intersected with the Municipality's Topographic Database (TDB) data. This intersection provides information related to the functional-spatial and dimensional properties of the open spaces. Subsequently, a single polygon can be created by dissolving adjacent features with the same land use and the same ASML class. The assessments focus only on open space systems.

Identifying the new atomic reference unit and the land use classes, according to the analytical framework (Apreda et al., 2019) used in the PLANNER model, the relationship between the four vulnerability indicators – Albedo, Solar exposure of open spaces, NDVI, and Sky View Factor – was taken into to assess the open spaces heatwave vulnerability.

The proportion of light that a surface reflects in every direction is known as its Albedo, and it represents the surface's reflecting power. Its goal is to determine the solar radiation's reflection characteristic, which will reveal the open space's materials and contextual suitability.

The amount of time a surface is exposed to solar radiation during the day is measured by the Solar exposure of open spaces. The condition of the sky and any man-made or natural barriers that block the radiation are also considered. The purpose of this indicator is to measure the quantity of solar radiation that enters an open area.

The primary satellite measure of vegetation's existence and temporal change on Earth's surface, the NDVI evaluates photosynthetic activity. The indicator's purpose is to show whether or not there is any vegetation in a certain open region.

The area of the sky that is viewable from an observation location is indicated by the Sky View Factor (SVF). Greater heat exchange in the atmosphere of a particular surface is indicated by an indicator with a higher value. The indicator's purpose is to measure the open space's breadth in order to determine its capability for heat exchange with the atmosphere and how it affects buildings.

To each indicator a weight was given with which the vulnerability could be summarized through a weighted average (Table 35).

Table 35. Heatwave indicator with each weight.

Subsystems	Indicators	Weights
Open spaces	SVF	5
	Albedo	2
	Solar exposure of open spaces	4
	NDVI	3

At the same time extreme sea level vulnerability is assess according to the mean elevation above sea level. Based on the characteristic of the AMSL derived from the DTM raster, the values were separated and categorized into eight classes, operating also a default approximation of the values to prevent any underestimate of the potential climatic implications (Table 36).

Table 36. Vulnerability classes considering the altimetry Above Mean Sea Level. Source Clemente et al., 2023.

AMSL Class	Vulnerability	Labels
Less than −0.00 m	0	Extremely high
Between −0.25 m and +0.25 m	1	Very high
Between +0.25 m and +0.75 m	2	High
Between +0.75 m and +1.25 m	3	Medium-high
Between +1.25 m and +1.75 m	4	Medium
Between +1.75 m and +2.50 m	5	Medium-low
Between +2.50 m and +3.50 m	6	Low
Between +3.50 m and +4.50 m	7	Very low

Based on these findings, a workflow was therefore developed to assess the vulnerability characteristics for the two types of hazards on the same reference atomic units. The presented workflow is illustrated in Figure 80.

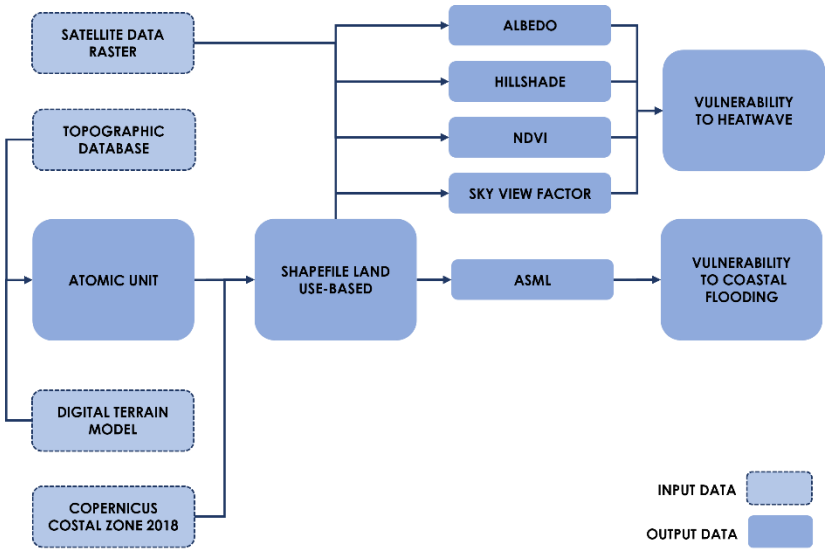

Figure 80. Workflow of the GIS-based framework for multi-hazard vulnerability assessment. Source: elaborate from Clemente et al., 2023.

4.1.2.3 Test on a Case Study area in the city of Naples

The city of Naples, located in the Campania Region in Southern Italy, was identified as a first case study area. The urban-coastal areas would be subject to multiple risks associated with the direct, as well as indirect, effects of climate change. The area of Via Partenope, highlighted in Figure 81, is considered as a critical area because of the recent storm events that impacts the area (Fortelli et al., 2021; Mattei et al, 2021) with significant economic losses.

Figure 81. Case study area: Naples waterfront (Italy). Source: Clemente et al., 2023.

The area is characterized by a dense residential and commercial fabric, as well as its historical and cultural identity, make it as a crucial area. Its high user population, comprising both residents and especially visitors, further adds to the area's relevance.

As mentioned before, the first stage involved gathering the input data collection and the elaboration of the new atomic reference units. The input data for the vulnerability assessment are: the topographic

database (TDB), provided by the Campania Region; the Digital Terrain Model in raster format, provided by the Italian Ministry of Environment and Land and Sea Protection; the raster images processed by the Sentinel2 Satellite, 20 m × 20 m resolution.

Starting with the Naples TDB, all shapefiles that related to this category were chosen and uploaded in GIS, considering that the framework's goal was to provide directed decision support in the design of public open spaces. Polygons belonging to the same class were combined into a single shapefile using a merging tool, and the DTM raster underwent a reclassification in the interim. The shapefile made up of polygons distinguished by the ASML field was created by performing a spatial intersection operation between the new shapefile that came from the DTM and the outcome of the TDB merging. In order to combine all adjacent polygons with the same ASML class (elevation) and land use determined by the TDB, a dissolve operation was lastly carried out. These actions made it possible to create the case study area's atomic reference units.

Apart from the establishment of atomic reference units, the ASML field was utilized to evaluate the vulnerability of open spaces considering ESL events. Eight vulnerability classes were created from the ASLM data. In Figure 82 the ESL vulnerability map and the percentage distribution of vulnerability are presented.

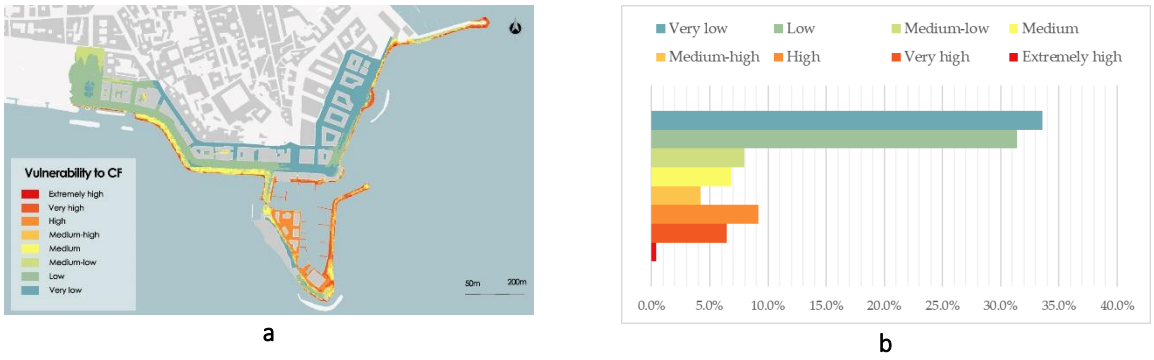

*Figure 82. (**a**) Maps of the vulnerability considering ESL; (**b**) histogram of vulnerability classes distribution. Source: Clemente et al., 2023.*

Due to their low height, the areas close to the sea are the most vulnerable. Just 16% of the open spaces were categorized as High, Very high, or Extremely high, according to the percentage distribution, whereas more than 60% of the open spaces fell into the Low or Very low vulnerability category.

For identify HW vulnerability the data of several satellite rasters have been retrieved and summarized using zonal statistical methods for the four indicators: Albedo, Solar exposure of open spaces, NDVI, and Sky View Factor. The synthesis of these four indicators, as mentioned before, define the HW vulnerability (Apreda et al., 2019). Figure 83 displays the processes' outcomes.

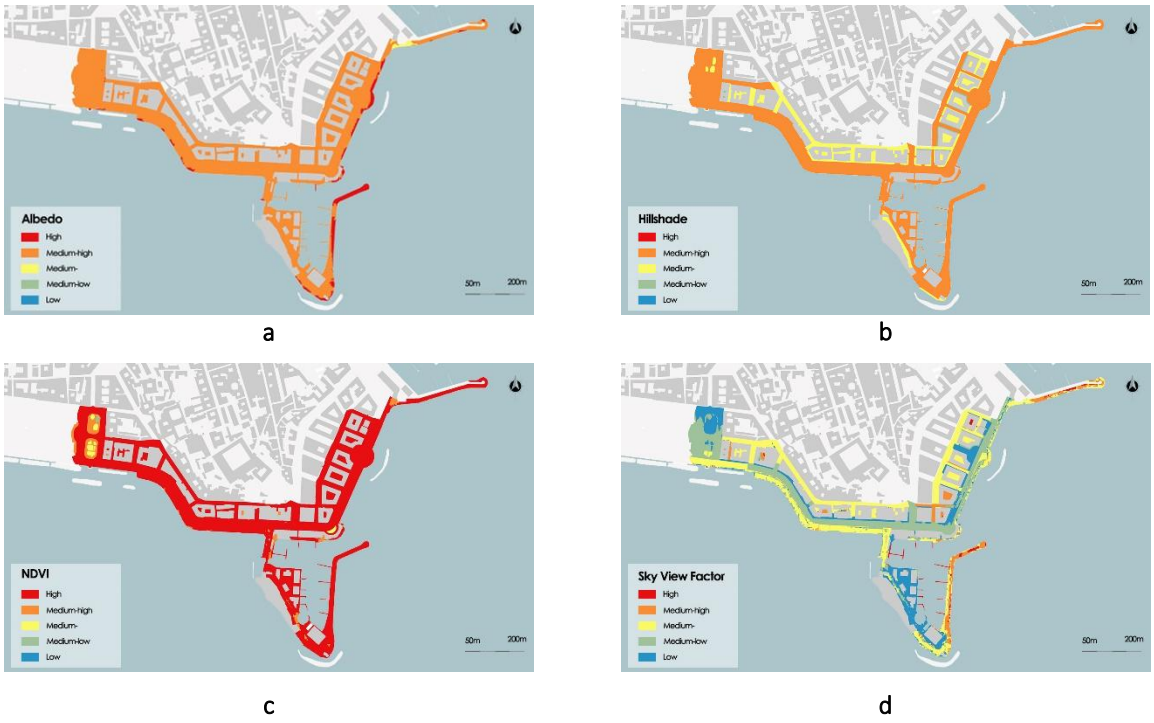

*Figure 83. (**a**) Map of Albedo; (**b**) map of Solar exposure of open spaces; (**c**) map of NDVI; (**d**) map of Sky View Factor. Source: Clemente et al., 2023.*

To each indicator is the given a weight, and a weighted average was computed to summarize the vulnerability to HW. Figure 84 shows the process's outcome.

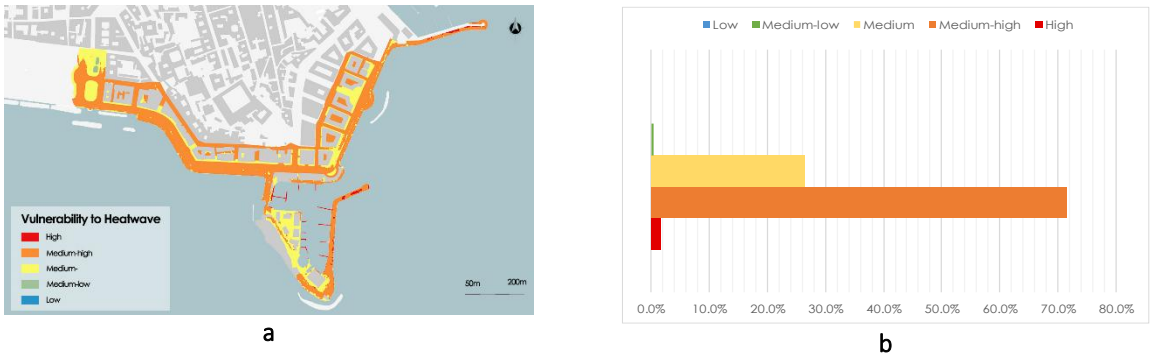

*Figure 84. (**a**) Vulnerability to heatwave phenomenon; (**b**) vulnerability histogram of the areas.*

The case study area shows a medium-high degree of vulnerability to the heatwave phenomena, reaching 71.6%, as can be observed from the histogram (Figure 84b), which was mostly concentrated along the shoreline road infrastructure. The comparison between the two maps shows some similarity. The waterfront road axis, one of the most important city routes, represents an area with high vulnerability considering both the phenomena.

The purpose of the proposed GIS-based framework is the support of decision makers in evaluating urban areas' vulnerability to heatwave and coastal flooding impacts due to extreme sea level impacts. Further steps will include the exposure and impact assessment. The framework can be used by decision makers as a tool to support their decision-making in planning and designing climate resilient solutions.

4.1.3 Studies of vulnerabilities and performance of building envelope components related to complex and emerging hazards and building risk

The building envelope serves as the first layer of protection from environmental hazards for the entire building system. Its technical elements, such as cornices, balconies or finishing, are highly vulnerable, i.e., very prone to reporting damage. Degraded envelopes can trigger structural problems, loss of building functionality and high repair costs (Silva et al., 2016). Also, damaged technical elements can become a risk factor for the urban system, exposing it to potential detachment or obstruction of emergency routes. In this sense, the technical elements of the building envelope play a significant role in the safety, functionality, and economic performance of the entire building and the surroundings. Therefore, developing a model to assess their vulnerability represents a crucial issue.

This research aims to evaluate the vulnerability of some technical elements of the building envelope to certain natural hazards. Examples of damages to building envelope technical elements and related hazards are reported in Table 37. For example, most of the technical elements report damage due to their fragility and poor structural connections in case of an earthquake. Another example of mechanical stress is the wind load, and the extend of its damage depends on the slope and the shape of the roof. Chemical reactions induced by air pollution, rain, humidity, and sunlight induce degradation too and lead elements to failure.

The elements under analysis were retrieved from the building taxonomy proposed by the RETURN project, included in Deliverable 5.2.1. The authors have identified the hazards to which the entire envelope is exposed, i.e., earthquakes, wind, rain, air pollution and environmental conditions, such as humidity and temperature changes. Then, they adopted two approaches for vulnerability assessment, a merely qualitative approach and a quantitative approach. The former is based on available studies and expert opinion; this is aimed at gaining a good preliminary overview of how well different technological solutions can withstand the impact of different hazards. The latter is based on field observation and statistical analysis. Indeed, a data collection phase is conducted to retrieve information on elements characteristics (e.g., technology and age), environmental exposure and the degradation level of technical elements. The Neapolitan context is used as a case study. Given the age of the elements, it is possible to correlate degradation levels to exposure parameters, considering different technological solutions. Eventually, it is possible to identify the technological solutions which can better withstand a set of exposure parameters by comparing their degradation levels.

These results will support decision-making processes by informing risk mitigation policies and promoting proactive rehabilitation measures and design solutions tailored to the specific system of hazards of the relevant context, thereby enhancing the adaptability of both new and existing building systems.

Table 37. Examples of damage reported by the envelope's technical elements due to several natural hazards.

Element	Damage description	Hazard	Reference
Balcony	Collapse of stone slabs, due to their fragility, type of constraint and span.	Earthquake	DPC, 2009
Chimney	Collapse of masonry chimney due to differential deformation of the support.	Earthquake	DPC, 2009
Window	Collapse of the glass due to its fragility. Bigger elements are associated with bigger damage.	Earthquake	DPC, 2009
Roof cornice	Collapse of the element due to poor physical condition and poor structural connections (e.g., stone slabs on metal corbels).	Earthquake	DPC, 2009
Plaster and cladding	Detachment of the element due to in-plane stress and poor connection to the infill.	Earthquake	DPC, 2009
Overall envelope	Damage of the roof terraces and green flat roofs, damage to the connection points between balconies or the pitched roofs of the main buildings, and damage to the basement and exterior basement walls.	Rain	Papathoma-Köhle et al., 2023
Cladding	Claddings with severe or unfavourable exposure to pollution tend to deteriorate faster, since the deposition of atmospheric pollution leads to the degradation of the tiles' surface, promoting staining and other anomalies.	Air pollution	Souza et al., 2018
Buildings' facades	Urban acids (e.g., sulphur dioxide and carbon dioxide) dissolve calcite minerals in marble and limestone facades or in concrete and mortar aggregates. Salts (e.g., chloride) often damage stone through the formation of salt crystals within pores near the stone surface, causing the stone to rupture.	Air pollution	Beasley, 2017
Finishing materials	The temperature rise can directly lead to materials' degradation. Increased temperature can accelerate chemical reactions too. Damages are due to differential thermal expansion and ultraviolet oxidation.	Sunlight and temperature variation	Berdhal et al., 2008
Roof	Pyramidal roofs better withstand wind forces. Roofs made of asphalt shingles are the least resistant to wind force, whereas metal and concrete roofs perform better than clay or slate tiles. Finally, the steeper the roof slope, the lower the vulnerability to wind.	Wind	Papathoma-Köhle et al., 2023
Roof	Of 3194 houses surveyed in the aftermath of a hurricane in Florida, 26% had less than 15% of the roof coverings removed, 18% had between 15% and 40% removed, and 7% had more than 40% removed.	Wind	Sparks et al., 1994

It is well known that damaged technical elements sometimes referred to as "non-structural" elements, can lead to economic losses, safety issues and downtimes (NIST, 2008). These impacts can be part of multi-hazards or multi-risks analysis. The main outcome of this research consists of contributing to vulnerability studies of the technical elements of the envelope, to be included in the "Building Risk" assessment, not only to analyse the effects of hazardous events on buildings themselves but also to consider the hazardous events that the building itself may pose to the surrounding context (Castelluccio et al., 2023). For example, people can be injured by falling bodies from the envelope. Assessing the risk of people being injured by damaged technical element is an issue not yet thoroughly explored, even though it represents the primary concern for Public Administration in ensuring public and private safety. Two studies in this regard propose a risk index evaluation (Ruggiero et al., 2021) and the calculation of the probability of detachment (Ruiz

et al., 2019), both starting from the analysis of a façade's degradation conditions. The studies offer interesting methodological insights, although the results are limited to homogeneous construction techniques and do not account for different factors of environmental exposure.

The issue of escape route obstruction following the collapse of technical elements of the building envelope has been exclusively analysed for seismic events, where the vulnerability of a building to an earthquake of a certain intensity is associated with the volume of debris generated during the event and the subsequent obstruction of escape routes (Bernardini et al., 2022; Santarelli et al., 2018).

The main contribution of this research consists of developing a structured framework for technical elements vulnerability assessment against a set of natural hazards. Starting from this framework, it is possible to evaluate the arising risks for the urban context. Both direct and indirect consequences are investigated, namely, people getting injured and road obstruction due to detached technical elements (Figure 85).

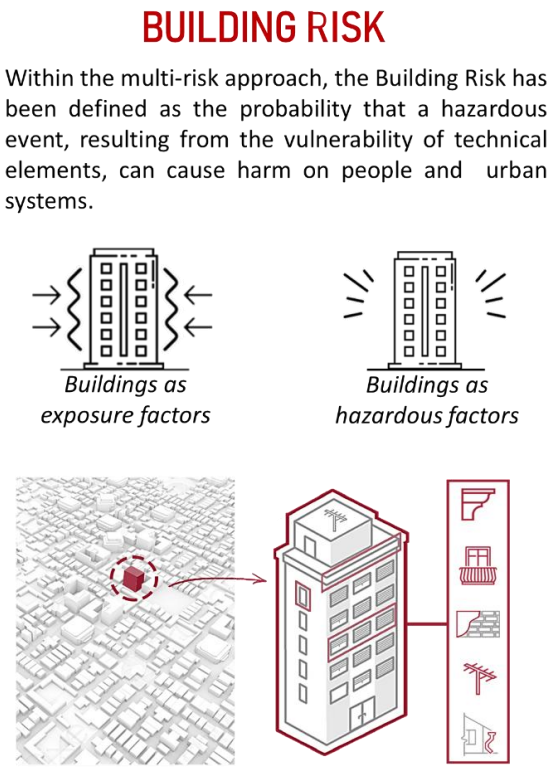

Figure 85. Building risk graphical abstract.

4.2 Multi-hazard interactions

4.2.1 Interactions between heat waves and air quality

Climate and air quality are tightly interconnected. Indeed, not only sources of air pollutants often coincide with sources of greenhouse gases (such as CO_2) (e.g., vehicular traffic, residential heating, industrial sources), but also some of the air pollutants, and in particular the so-called Short-Lived Climate Forcers (SLCFs) such as ozone and black carbon, are capable to alter radiative forcing in different ways. For instance, black carbon can absorb solar radiation, but other aerosol components (e.g., sulfates) are capable to scatter sunlight. In addition, by acting as cloud condensation nuclei, aerosols can change not only clouds optical properties (albedo) but also their atmospheric lifetime (see Section 3.5.2). On the other hand, a changing climate may trigger new phenomena or exacerbate/mitigate usual conditions, therefore changing the current sources, sinks and accumulation/remotion of air pollution. Indeed, global warming is associated with widespread changes in weather patterns, with changes in precipitation and circulation patterns, also leading to more frequent and severe extreme weather events such as heat waves and storms. In particular, climate change is expected to worsen air quality in many polluted regions by reducing ventilation and dilution processes (Fiore et al., 2015).

As concerns heat waves and their connection with air pollution, firstly we need to recall that they occur in the warm (summer) period of the year and are marked by unusually high temperatures persistent for a long period of at least 2 days, as stated in Section 3.4.1. From a meteorological point of view, heat waves are characterized by peculiar synoptic conditions which are marked by strong insulation, reduced wind speeds, reduced precipitation, and air stagnation, all of which ultimately lead to temperature increases. These conditions, at the large scale, are generally linked to the presence of stationary anticyclones, often leading to the establishment of the so-called blocking high (or blocking anticyclones), i.e. any high (or anticyclone) that remains nearly stationary or moves slowly compared to the west-to-east motion "upstream" from its location, so that it effectively "blocks" the movement of migratory cyclones across its latitudes (AMS, 2024).

Those conditions may trigger air quality worsening due to the increased solar radiation and stagnation of air masses, ultimately leading to an acceleration of atmospheric chemical reactions and a general tendency towards ageing of the air mass. In particular, among atmospheric pollutants cited in Section 3.5.2, these processes involve mainly ozone and particulate matter. As an example, heat waves that occurred during 2022 in Europe and America had important consequences on air quality, with observed increases in ozone and particulate matter concentrations. Besides, the heat waves enhance the probability of wildfires and their intensity, contributing to the worsening of air quality and in particular leading to increases in sulphur dioxide and particulate matter concentrations (mainly in the form of fly ashes) (WMO, 2023b).

Ozone (O_3) is a reactive oxidant gas which is naturally produced in the atmosphere. It can be found mainly in the stratosphere and secondarily in the troposphere, with different roles in the two layers because of its different mechanisms of production and removal. Stratospheric ozone (or so-called “good ozone”) is produced through the so-called Chapman mechanism: the solar ultraviolet radiation facilitates the formation of ozone from the stratospheric oxygen creating a cycle in which all the chemical species are

recycled, preventing the UV radiation from reaching the lower atmospheric layers (Seinfeld and Pandis, 2006).

In the troposphere, the production of the so-called "bad" ozone requires sunlight and nitrogen oxides. The process of formation of ozone includes two chemical reactions:

1) $NO_2 + hv\ (\lambda < 420\ nm) \rightarrow NO + O$

2) $O + O_2 + M \rightarrow O_3 + M$

The first reaction is a photochemical reaction in which NO2 dissociates into NO and atomic oxygen (O) due to the absorption of a photon in the lower ultraviolet spectrum. This process is supported by the volatile organic compounds (VOCs) which are oxidised by the OH radical and then react with the NO producing the NO2 required by the reaction (1) to start the ozone production (Seinfeld and Pandis, 2006). The ozone production in the troposphere is summarised in Figure 86. During nighttime in the absence of solar radiation, ozone cannot be produced and it is removed by the troposphere through different reactions involving nitric oxides (Seinfeld and Pandis, 2006). In Figure 87 the daily ozone and temperature trends are shown, note that ozone peaks in the early afternoon (13-15 h) and has a minimum in the early morning (6-8 h) in both heatwave and non-heatwave conditions.

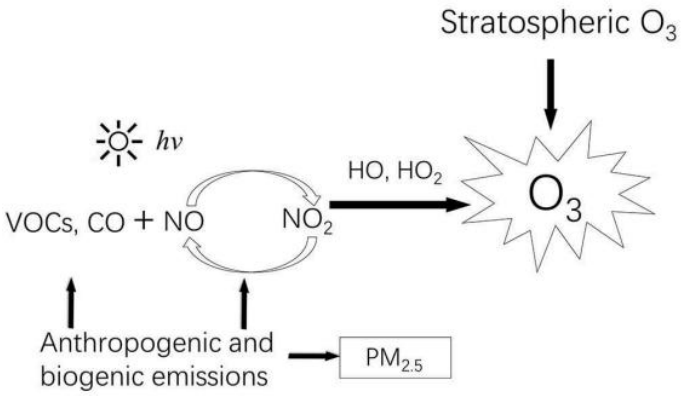

Figure 86. Scheme of tropospheric ozone production, adapted from Zhang et al. (2019).

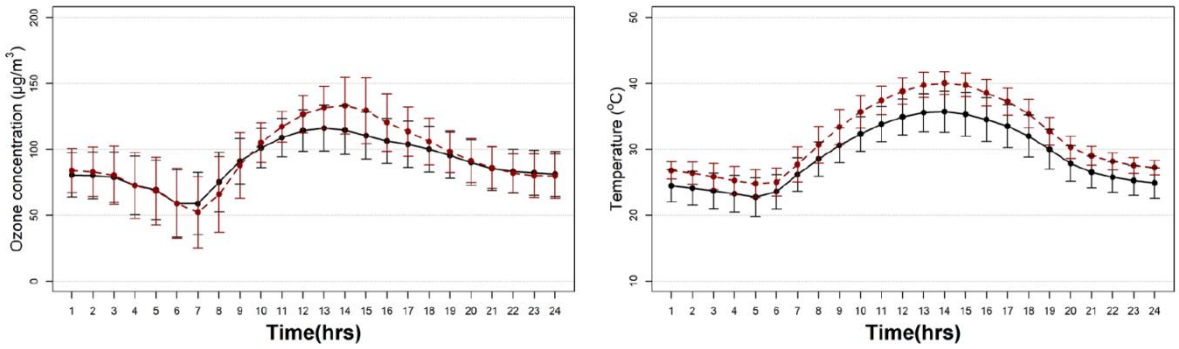

Figure 87. Hourly average ozone concentration (left panel) and temperature (right panel) trend during summer under heatwave (red line) and non-heatwave (black line) conditions in Nicosia (Cyprus), adapted from Pyrgu et al. (2018).

The tropospheric ozone has been among regulated pollutants since September 1992 because of its chemical and physical characteristics. In particular, the high chemical reactivity of this chemical species can cause adverse effects on the respiratory system, such as lung functional decrements, lung inflammation and mild bronchoconstriction (Nuvolone et al., 2018; Zhang et al., 2019). Ozone is indeed associated with morbidity and mortality: the estimated number of deaths in Europe during the warm seasons of the period 2015-2017 is 114,447, approximately 72 annual deaths per one million inhabitants (Achebak et al., 2024). The distributions of ozone concentration and annual deaths attributable to ozone in European subregions are depicted in Figure 88. Furthermore, ozone represents also the third most important greenhouse gas in the atmosphere (Myhre et al., 2013).

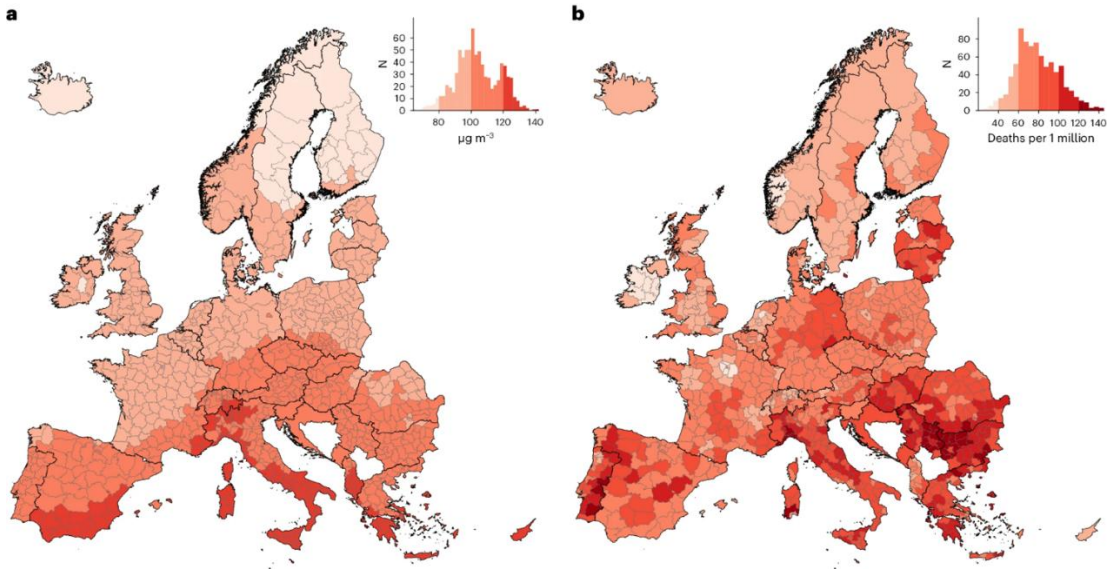

Figure 88. Average daily 8-hour mean ozone (panel a) and mortality (deaths per 1 million population) attributable to ozone (panel b) in Europe during the warm season (May-September) 2015-2017, adapted from Achebak et al. (2024).

As described previously in this section, the tropospheric ozone production is strongly dependent on environmental factors, such as sunlight and the abundance of precursors. In particular, the heat wave

conditions provide the ideal situation for the ozone pile-up. Indeed, stronger insulation supplies more photons for the photo-chemical reactions involved into the ozone production and higher temperatures increase the speed of chemical reactions and pose additional stress on the vegetation which releases more VOCs (WMO, 2023b). In Figure 89 the difference of tropospheric ozone production under normal conditions and heatwave event are summarised. In particular, it is clear that under heat wave conditions, the higher solar radiation and biogenic VOCs emissions lead to more efficient and fast photochemical reactions producing increased ozone concentrations.

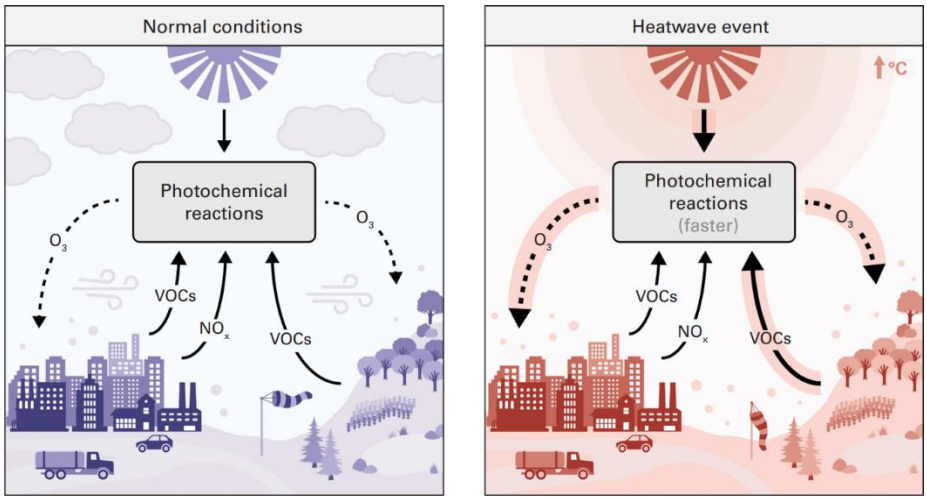

Figure 89. Tropospheric ozone production under normal and heat wave conditions, thicker arrows represent greater fluxes, adapted form WMO Air Quality and Climate Bulletin, No. 3 September 2023 (WMO, 2023b).

In literature, there are various studies which point out the connection between tropospheric ozone and heat waves in several parts of the world:

- Cyprus. Pyrgu et al. (2018) studied the near-surface ozone concentration reported in the city of Nicosia under normal conditions and heat wave events. The study pointed out that heat waves have a profound effect on ozone concentrations: the lowest concentration values were found in the morning, in correspondence with higher NO_X and absolute humidity values, whereas the maxima are observed around noon, when temperatures reached their highest values (Pyrgu et al., 2018). In Figure 87 hourly ozone concentration and temperature trends are shown.
- Korea. Park et al. (2023) found out that surface ozone concentration in Seul increased by 17.2% during heatwaves concerning normal conditions. The daily behaviour of near-surface ozone is like the one observed in Cyprus. During the daytime throughout heat waves higher concentrations are found, with a relative change of 35.0%, with the daily maximum of 8-hour average concentration increasing from 41.0 ppb (80.4 µg/m^3) in normal conditions to 54.2 ppb (106.2 µg/m^3) during heat waves. On the other hand, during the nighttime and throughout heat wave events lower ozone concentrations are reported (Park et al., 2023).
- Morocco. Khomsi et al. (2022) analyzed the concurrent events of heat waves and ozone extremes in Casablanca and Marrakech. The geographical difference in the locations of these two cities

reflects the different occurrences of extreme events. The two cities are subjected to different sunlight exposures: Casablanca (coastal city) is underexposed to sunlight, hence the photochemistry involved in the ozone formation is penalized despite the high NO_2 concentration levels; on the other hand, in Marrakech (inland city) the photochemistry is supported by the strong solar radiation. Concurrent events are observed at the two locations, with ozone concentration peaking at the beginning of the heat wave or with a small offset, with a greater number of events in Marrakech than in Casablanca. These results demonstrate how tropospheric ozone production and the cooccurrence of extreme ozone events and hear waves are impacted by geographical and meteorological features (Khomsi et al., 2022).

- North America. Schnell and Prather (2017) studied the cooccurrence of extremes in temperature and ozone concentration for the eastern North America in order to find temporal and spatial coincidence of those events. The study found out that the ozone extremes are likely to happen about 1 day after the temperature extreme under 40° N, whereas the opposite occurs above that latitude, probably due to an acceleration of photochemistry or a suppression of ozone because of high temperature, with an offset of about 1-2 days (Schnell and Prather, 2017).

In particular, one of the first heat wave events that raised the scientific attention on the synergistic interaction and the deadly impact of ozone and heat waves was the 2003 heat wave impacting severely in southern and central Europe. The event began in June 2003 and continued through July until mid-August, with summer temperatures 20 to 30% higher than the seasonal average (UNEP, 2004). The event was particularly long-lasting (over 20 days) and severe, with extreme maximum temperatures of 35 to 40°C repeatedly recorded in July and to a larger extent in August in most of the southern and central parts of Europe. The event was caused by an anti-cyclone firmly anchored over western Europe holding back the rain-bearing depressions usually entering the continent from the Atlantic Ocean. Many studies focused on the concurrent ozone concentrations extremes occurred in Europe during the heat wave, for example a study carried out at the Frankfurt airport (Germany) pointed out that the high ozone values were the result of several mechanisms which supported the ozone piling up in the atmosphere, such as the increased emission of precursors, the reduced dry deposition due to the drought conditions, the general stagnation of air masses and the biomass burning emissions due to the wildfires affecting Portugal during the heat waves (Tressol et al., 2008). Furthermore, this study characterized the vertical profile of ozone concentration finding that ozone maintained high values in the PBL also during night because of the strength of its daytime production and that the plumes due to the Portugal wildfire were photochemically active for the ozone production in mid troposphere (Tressol et al., 2008). The study performed by Solberg et al. (2008) tried to estimate the contribution of different factors to ozone production during the heat wave by comparing the measured ozone concentrations with the results of a simulation for the same period of the heatwave (August 2003). The comparison pointed out that the most critical parameter for ozone depletion is dry deposition, whose absence may increase ozone concentration by more than 20%. Another important factor is temperature since a 10 °C increase in temperature would result in a 5% increase in ozone concentration. Lastly, biogenic isoprene was considered a significant contributor in the measured ozone concentration, with an estimated potential contribution of 20% increase in ozone concentrations (Solberg et al., 2008). The mortality due to the synergistic effect of heat wave and ozone during 2003 European heatwave was also studied by Filleul et al. (2006) for nine French cities. The combined effect of ozone and higher temperature produced an excess

risk of death ranging from 10.6% of Le Havre to 174.7% of Paris, with different contributions of ozone and temperature according to the characteristics of the city. Results indicated a general heterogeneity in the contribution of ozone with major impacts in urban areas (Filleul et al. 2006). The overall findings, however, pointed out that the contemporary increases in ozone concentrations and in minimum and maximum temperatures contributed significantly and synergically to increasing mortality (Dear et al., 2005; Filleul et al., 2006; Alari et al., 2023).

In the last years ozone and its relationships with heat waves have been deeply studied from different perspectives, but some points may still need some reflections or appropriate studies:

1) Ozone being a short lived climate forcer with a warming effect, there may be a potential positive feedback caused by the increased tropospheric ozone production under heat wave conditions.
2) Increasing green areas in cities is a widespread mitigation strategy for heat waves and in general for improving urban thermal comfort during summer (and in particular to contrast the UHI effect, see Section 3.4.1). However, as commented previously, in general vegetation emits bioVOC which are amongst precursors of ozone. The appropriate choice of species less emissive of bioVOCs may mitigate the risk of further increases in potentially damaging ozone concentrations.

The second, but not less important, major contributor to the worsening of air quality during heat waves, is the atmospheric aerosol. The term atmospheric aerosol indicates a suspension of airborne solid or liquid particles in a gaseous mixture (IPCC, 2021b). Unlike tropospheric ozone, whose origin is found in the photochemistry shown above, atmospheric aerosol sources are widely heterogeneous and so its chemical and physical properties (Seinfeld and Pandis, 2006). Indeed, the main characteristics of atmospheric aerosol, namely size and composition, are mainly dependent on the nature of aerosol sources. Furthermore, aerosol can be classified as “primary” if directly emitted into the atmosphere or “secondary” if it forms in the atmosphere after chemical reactions involving gaseous precursors (Kalberer et al., 2007). Aerosol sources can be divided into natural and anthropogenic. Amongst the former, it is important to cite the sea salt coming from the sea, the mineral dust blown into the atmosphere by winds, volcanic ashes, organic aerosol emitted by vegetation and other biological sources, and secondary sources emitting gaseous precursors such as VOCs. On the other hand, anthropogenic sources include mainly combustion processes, such as biomass burning, fossil fuel combustion and soot (organic aerosols produced after incomplete combustion), and industrial activities such as mining or other manufacturing activities. Many of these anthropogenic sources emit also gaseous precursors such as SO_2, NO_2 and anthropogenic VOCs which contribute to the formation of secondary aerosol of anthropogenic origin (Kalberer et al., 2007).

In terms of air quality, atmospheric aerosol represents an important pollutant to monitor because of its negative effects on human health. How atmospheric aerosol can access the human body are inhalation, ingestion, dermal absorption and injection. Besides, there are also evidences that insoluble ultrafine particles deposit upon the olfactory mucosa and translocate through the olfactory nerve up to the brain. Considering the processes involving dermal deposition and inhalation of aerosol, the daily dose to which many individuals are exposed is few hundred micrograms, which may elicit measurable response to the human body, despite the low quantity (Thompson, 2018). Furthermore, the International Agency for Research on Cancer (IARC) stated that atmospheric aerosol represents a carcinogenic agent for human body (IARC, 2016). The atmospheric aerosol concentration is usually measured through the PM10 and

PM2.5, which are respectively the fraction of atmospheric aerosol having maximum aerodynamic diameter 10 micrometer and 2.5 micrometer; these values represent the average size thresholds filtered, respectively, by human head airways and tracheobronchial regions (Hinds, 1999).

Nowadays the connection between aerosol and heat waves is not clear because of the complexity of this pollutant in terms of sources and meteorological conditions affecting the study site. However, the usual meteorological conditions characterizing heat waves, namely the blocking high, can have a role in the increases of aerosol during these phenomena. For example, studies concerning Korea and North America found out that low winds and slow-moving high-pressure structures supported the accumulation of atmospheric aerosol (Park et al., 2023; Schnell and Prather, 2017; Wu et al., 2019). In addition, this may be further supported by the stagnation of air masses and the reduction or even suppression of wet deposition processes, one of the largest sinks of atmospheric aerosols and especially of fine particles more dangerous to human health. On the other hand, recent studies carried out for the Mediterranean region suggest also the possibility of coincidences between dust transport from North-Africa during heat waves (Papanastasiou et al., 2014; Fernandes and Fragoso, 2021; Ruiz-Páez et al., 2022). Enhancements in particulate matter concentrations under extreme heat can also occur because of wildfire emissions, as well as because of higher anthropogenic emissions for example by air conditioning. The peculiar atmospheric conditions characterized by high solar radiation and high temperatures lead in particular to higher concentrations of secondary particulate matter.

As well documented for ozone, also in the case of particulate matter the combined effect thermal stress and the increase in atmospheric aerosols concentration may have potentially synergistic roles on mortality and morbidity conditions. However, those effects are still less studied and their contribution on adverse effects on human health remains quite unclear.

4.2.2 Wind impact in multi-hazard scenarios

In Section 3.3.1, the primary sources of wind impact on multi-hazard risks in the Mediterranean basin are introduced, focusing on Mediterranean cyclones (including extra-tropical and tropical-like cyclones) and spatially stationary thunderstorms. Mediterranean cyclones are vast systems, extending across thousands of kilometers and persisting for several days. In contrast, thunderstorms are smaller and shorter-lived phenomena. However, when favorable convective conditions persist, these thunderstorms can become spatially stationary and long-lasting, potentially resulting in multi-climatic conditions that interact and produce catastrophic impacts on both the built and natural environments, as well as socio-economic systems. Furthermore, thunderstorms often arise as a consequence of larger atmospheric cyclonic events. This section first summarizes the discussion provided on the topic by Flaounas et al. (2022) who examined the combined climatic effects (climatic multi-hazards) generated by Mediterranean cyclones, with applicability also to thunderstorm phenomena due to their interrelated nature. Subsequently, the discussion broadens to encompass other potential multi-hazard scenarios where wind plays a central role, such as pedestrian wind combined with pollution and wind coupled with hail precipitation—phenomena that are increasingly intensified by climate change.

4.2.2.1 Impacts of Wind and Heavy Precipitation

The significant role of cyclones in triggering heavy rainfall in the Mediterranean was well-documented by Jansa et al. (2001) within the MEDEX framework. They demonstrated that 90% of heavy rainfall events in

the western Mediterranean were linked to cyclones of varying intensities. More recent studies, such as those by Flaounas et al. (2018), have shown that both weak and intense Mediterranean cyclones can produce substantial precipitation. A linear relationship exists between average rainfall and cyclone intensity, with cyclones contributing over 70% of the annual total precipitation in the region (Hawcroft et al., 2012; Pfahl and Wernli, 2012). Extreme rainfall events, which can constitute up to 90% of regional extremes, are primarily associated with intense cyclones (Pfahl et al., 2014; Flaounas et al., 2016).

The mechanisms behind heavy precipitation can vary. Pfahl et al. (2014) indicated that 40% to 50% of regional extremes are attributed to warm conveyor belts (WCBs, feature 5 in Figure 90), while Flaounas et al. (2018) found that WCBs typically yield more than twice the precipitation associated with deep convection (DC, features 6, 7 and 8 in Figure 90). Case studies from the HyMeX SOP1 campaign in October 2012 illustrated these differing processes, with one event characterized by deep convection and another by stratiform rainfall from WCBs.

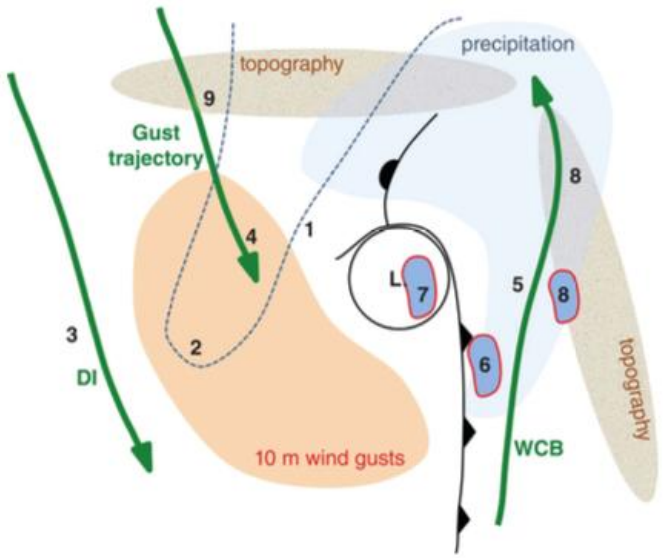

Figure 90. Schematic illustration depicting the potential features associated with combined precipitation and wind impacts of a cyclone in the Mediterranean, based on the five events analyzed by Raveh-Rubin and Wernli (2016). This schematic does not represent any single event but summarizes the various possible significant features. The cyclone center is indicated by the letter "L", with cold and warm fronts also shown. Shaded areas highlight precipitation impact (light blue) and 10-meter gust impact (light red). Regions experiencing both convection and co-located precipitation and wind gust impacts are shaded blue and encircled by a red line. High topography is depicted in grey. The 320 K 2-PVU contour is illustrated as a dashed line, with typical WCB, DI, and gust trajectories marked by green arrows. Numbers indicate the following locations: (1) a notable upper-level feature (PV streamer/trough/ridge), (2) tropopause fold and downward momentum transfer, (3) DI trajectories near high gusts, (4) low-level gust trajectory, (5) WCB slantwise ascent linked with precipitation, (6) convective precipitation at the cold front, (7) convective precipitation at the cyclone center, (8) orography enhancing precipitation and/or convection, and (9) orography accelerating gust trajectories.

Heavy precipitation in the Mediterranean often requires significant moisture at low and mid-tropospheric levels, promoting atmospheric instability and intense rainfall events (Reale and Lionello, 2013; Khodayar et al., 2018b). Composite analyses have shown that heavy precipitation events are linked to instability and moisture from the Mediterranean Sea, transported by low-level jets influenced by synoptic patterns and local orography (Ricard et al., 2012). Similar associations hold for other heavy precipitation hotspots in the western Mediterranean (Khodayar et al., 2018a).

Moisture sources for Mediterranean cyclones include the Mediterranean Sea, the tropical and extratropical Atlantic Ocean, and tropical Africa (Winschall et al., 2014; Chazette et al., 2016; Lee et al., 2017; Raveh-Rubin and Wernli, 2016; Duffourg et al., 2018). Cyclones often steer atmospheric rivers toward regions such as the Alps, leading to severe precipitation events (Davolio et al., 2020). Local evaporation from the sea contributes less moisture compared to transport from the Atlantic (Flaounas et al., 2019; Raveh-Rubin and Wernli, 2016). Cyclones' precipitation efficiency is higher over land than over maritime areas, adding complexity to the relationship between cyclone intensity and precipitation (Flaounas et al., 2019).

Research under the MEDEX project has focused on the societal impacts of flood events, resulting in databases such as FLOODHYMEX and the Mediterranean Flood Fatalities (MEFF) database (Llasat et al., 2013; Papagiannaki et al., 2013; Petrucci et al., 2019). These databases show that flood-related mortality peaks in early autumn in the western Mediterranean and in late autumn and winter in the eastern Mediterranean, correlating with heavy precipitation patterns and cyclone occurrences (Raveh-Rubin and Wernli, 2015). Flash floods are often caused by organized convective systems or orographic precipitation rather than isolated convective cells (Michaelides et al., 2018).

Intense or prolonged rainfall is also a frequent trigger for landslides in the Mediterranean (Trigo et al., 2005; Gariano et al., 2015; Polemio and Petrucci, 2010). Additionally, cyclones contribute to electrical activity, with lightning occurrences peaking during autumn and winter due to intense cyclogenesis (Galanaki et al., 2016).

4.2.2.2 Windstorms, storm surges and sea waves

Strong winds in the Mediterranean, such as Mistral, Tramontana, or Sirocco, are often driven by Mediterranean cyclones. For instance, the intensity of Mistral winds is linked to Genoa cyclones and their upper-tropospheric potential vorticity anomaly (Givon et al., 2021). Similarly, low pressure over the Tyrrhenian Sea caused an exceptional Sirocco storm in the Adriatic basin (Giovannini et al., 2021). Cyclones either enhance local winds or directly cause windstorms through their cyclonic circulation. Nissen et al. (2010) found that cyclones are responsible for most wind extremes in the region, with 42% forming within the Mediterranean and the rest originating from the Atlantic Ocean.

Environmental conditions associated with extratropical cyclones have been linked to tornado and downburst occurrences in Italy, primarily in the warm sector and along the cold front (Tochimoto et al., 2021).

Cyclone-induced windstorms can lead to storm surges and coastal flooding. High wind speeds, significant sea waves, and storm surges, combined with heavy precipitation, increase the risk of compound events

like compound flooding (Bevacqua et al., 2019). Cyclones influence sea level through changes in surface heat flux, heat advection by currents, and climatic variations. These interactions can result in extreme waves and coastal flooding, as seen in Venice's vulnerability to storm surges (Cavaleri et al., 2019; Lionello et al., 2019). Medicanes like Ianos have caused significant storm surges and sea waves in regions like Greece (Smart, 2020; Lagouvardos et al., 2021; see, for example, Figure 91).

Studies on Mediterranean storm surges have linked high sea levels to cyclones from both the Atlantic and within the Mediterranean basin (Lionello et al., 2019). Storm surges depend on surface wind speeds and drag coefficients, with a lack of in situ observations posing challenges for understanding these mechanisms, especially at high wind speeds (Tadesse et al., 2020).

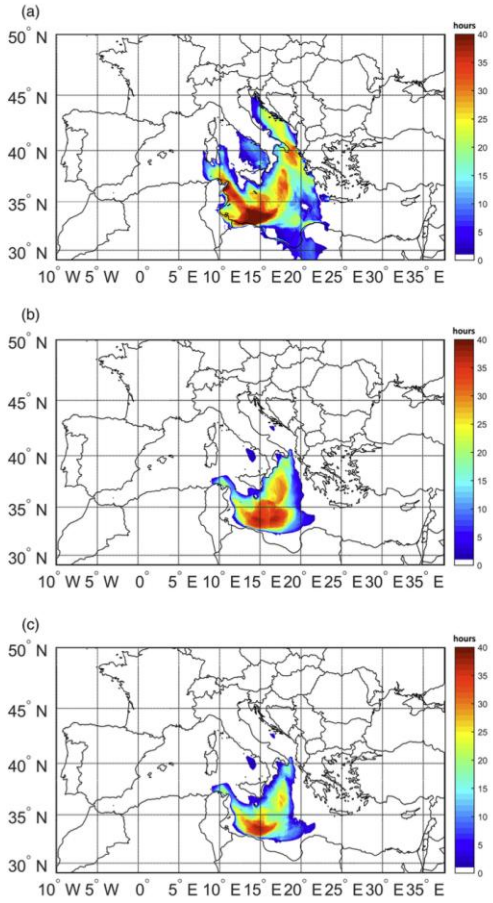

Figure 91. (a) Duration (hours) per grid point where 925 hPa wind speed exceeds the threshold of 17.5 m s^{-1} during medicane Qendresa (2014). Panel (b) same as (a) but for significant wave height exceeding 4 m. Panel (c) same as (a) but for the combined threshold values of both wind speeds and wave height. Contour fields are derived from coupled wave–atmosphere model.

4.2.2.3 Wind and dust transport

Mediterranean cyclones can mobilize and transport mineral dust through strong surface winds associated with baroclinicity and cyclogenesis processes (Schepanski et al., 2009). Cyclones can develop near dust sources, influencing dust events in the eastern Mediterranean (Dayan et al., 2008; Kalkstein et al., 2020). Cyclones contribute to a significant portion of dust transport days and extreme dust events (Flaounas et

al., 2015). Dust transport is often linked to the southerly warm advection ahead of cyclones' cold fronts (Varga, 2020). Severe dust transport events, such as one in March 2016, demonstrate the interaction between cyclones and dust (Rizza et al., 2018). The frequency of dust transport events from the Sahara region throughout the Italian peninsula have been gradually increasing in the recent years.

Cyclones also facilitate the long-range transport of giant mineral dust particles, impacting atmospheric radiation balance, cloud and precipitation processes, and the ocean carbon cycle (Ryder et al., 2013; Van der Jagt et al., 2018). Understanding the size distribution of dust particles under cyclonic conditions remains an important research objective.

4.2.2.4 Pedestrian Wind and Its Interactions with Air Pollution

Urban environments are complex systems where various factors such as architecture, traffic, human activity, and natural elements like wind and weather converge, often resulting in unintended consequences. Among these, the interaction between pedestrian-level wind and air pollution is particularly significant due to its direct impact on public health and comfort. This sub-section explores the phenomenon of pedestrian wind (i.e., wind at the height where pedestrians walk) and its possible relationship with air pollution in urban settings. We will delve into how architectural design, urban planning, and environmental conditions influence these interactions and discuss potential mitigation strategies.

Pedestrian Wind: A Brief Overview

Pedestrian wind refers to the wind experienced at ground level, particularly in areas where people walk and gather. Its behavior is largely influenced by the built environment, including the height, shape, and arrangement of buildings. The main factors influencing pedestrian wind include:

Building Design and Orientation. Tall buildings can channel wind down to the street level, a phenomenon known as the downdraft effect or "wind tunnel" effect. The orientation of buildings relative to prevailing winds can exacerbate or mitigate these effects.

Urban Canyon Effect. Streets bordered by tall buildings on either side can create a "canyon" effect, where wind is funneled through the narrow space, often increasing wind speeds at the pedestrian level.

Open Spaces. Parks, plazas, and other open spaces can either provide shelter from wind or act as channels, depending on their design and location relative to wind patterns.

The local climate, including the direction and strength of prevailing winds, plays a crucial role in determining the pedestrian wind environment. Seasonal changes can also alter wind patterns, affecting pedestrian comfort differently throughout the year also. These effects are also influenced by the daily activities of people using these spaces (Figure 92; see, for example., Pagnini et al., 2023, developed within the framework of the RETURN project).

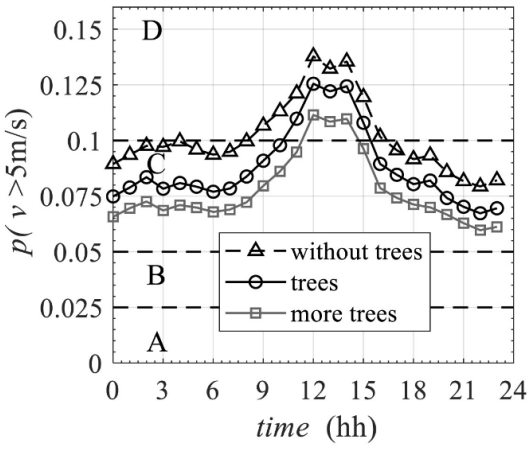

Figure 92. Example of hourly exceedance probability (from Pagnini et al., 2023).

Accurate studies of wind comfort and structural impacts can be achieved by combining statistical meteorological data with aerodynamic insights obtained through either wind tunnel modelling or Computational Fluid Dynamics (CFD) techniques (e.g., Janssen et al., 2013; Zhang et al., 2021). Both methods have their respective strengths and limitations (Blocken et al., 2016; UK WES, 2022). Nowadays, physical and CFD techniques are often used in parallel to leverage their strengths while minimizing their limitations (Adamek et al., 2017; Ricci et al., 2022).

Interaction Between Pedestrian Wind and Air Pollution

Air pollution in urban areas is a pressing concern, with sources ranging from vehicular emissions and industrial activities to construction dust. The pollutants of greatest concern include particulate matter (PM10 and PM2.5), nitrogen dioxide (NO2), sulfur dioxide (SO2), carbon monoxide (CO), and ground-level ozone (O3). These pollutants can have severe health impacts, particularly on the respiratory and cardiovascular systems. Air pollution tends to be most concentrated near its sources, such as busy roads, industrial zones, and areas with poor ventilation due to urban design. The dispersion of these pollutants is heavily influenced by meteorological factors, including wind speed and direction, temperature, and atmospheric stability.

The interaction between pedestrian wind and air pollution is complex and multifaceted. Pedestrian wind can both alleviate and exacerbate air pollution at ground level, depending on various conditions. Key interactions include:

Wind-Induced Dispersion. Wind plays a critical role in dispersing air pollutants. In an ideal scenario, moderate winds can help to disperse pollutants away from street level, reducing concentrations and improving air quality for pedestrians. However, if the wind is too strong, it may stir up dust and other particulates, increasing pollution levels.

Trapping of Pollutants in Urban Canyons. Urban canyons can trap pollutants, leading to higher concentrations at street level. When wind flows through these canyons, it may not have enough strength to disperse pollutants vertically, causing them to accumulate and increasing exposure for pedestrians.

Recirculation Zones. Wind can create recirculation zones, particularly in areas where buildings are irregularly shaped or there are sudden changes in the urban landscape. These zones can trap pollutants, leading to localized pockets of high pollution concentration.

Building architectural features such as overhangs, canopies, and awnings can influence how wind moves at pedestrian level. While these features can provide shelter and reduce wind speeds, they can also disrupt natural airflow patterns, potentially leading to areas where pollutants accumulate. Moreover, the interaction between wind and temperature differences in urban areas can create localized thermal currents. These can either lift pollutants away from the ground or cause them to settle, depending on the specific conditions. For example, on hot days, rising warm air can carry pollutants upwards, but in cooler, stagnant conditions, pollutants may linger at ground level.

Few major cities have implemented regulations concerning wind microclimates. Notably, the City of London has developed a document that outlines general guidelines for wind microclimate assessments, which are required as part of the planning applications for new development proposals. Recent studies (e.g., Keshavarzian et al., 2022) have investigated pollutant dispersion from an experimental perspective, using wind tunnel tests on scaled models to analyze exposure times around buildings and explore the underlying wind-structure interaction mechanisms. The findings indicate that air pollutant exposure time is longer in the side region of a building compared to the windward region. This difference is influenced by the separation-reattachment flow near the side faces and the bifurcating flow near the windward face.

Mitigation strategies for managing pedestrian wind effects and their interactions require an integrated approach involving urban planning, architectural design, and environmental management. While not exhaustive, some key measures include considerations in urban planning and building design, as well as the adoption of new technologies, as briefly discussed below and in other sections of this deliverable.

Wind Corridor Implementation. Designing streets and open spaces to create wind corridors can help enhance natural ventilation and pollutant dispersion. These corridors should be strategically placed to align with prevailing winds.

Building Orientation and Height Management. Orienting buildings to minimize wind tunnelling and managing building heights to avoid excessive downdrafts can help improve pedestrian comfort and air quality.

Incorporating Green Spaces. Green spaces can act as buffers that absorb pollutants and reduce wind speed, mitigating the urban canyon effect. Trees and vegetation also play a role in capturing particulate matter.

Real-Time Monitoring and Modelling. Deploying sensors to monitor air quality and wind patterns in real time can help city planners and architects design more effective interventions. Computational fluid dynamics (CFD) modeling can predict how changes in the urban environment will impact wind flow and pollution dispersion.

Pollution Mitigation Technologies. The use of air filtration systems, both indoors and outdoors, can help reduce the concentration of pollutants in areas where wind patterns lead to accumulation.

In summary, the interaction between pedestrian wind and air pollution in urban environments is a critical issue that affects public health and quality of life. By understanding the dynamics of wind flow and pollutant dispersion, city planners, architects, and environmental engineers can design urban spaces that mitigate the negative effects of these interactions. Through thoughtful design and proactive measures, it is possible to create urban environments that are not only comfortable for pedestrians but also healthier and more sustainable. The ongoing challenge is to balance the needs for urban growth and development with the imperative of maintaining a clean and breathable atmosphere at street level.

4.2.2.5 Combined impacts of Wind and Hail on low-rise buildings

Multi-hazard events, such as those involving thunderstorms and hail, can have significant and complex impacts on the built environment. Thunderstorms are often accompanied by high winds, heavy rainfall, and hail, each of which can independently cause damage to structures, but when combined, their effects can be exacerbated. For instance, strong winds can lift roof materials or break windows, while hail can cause extensive damage to facades and roofing systems, leading to water infiltration and structural weakening.

In urban areas, these hazards can interact in ways that increase the overall risk to buildings. For example, wind-driven hail can strike buildings at high velocities, leading to more severe damage than either hazard would cause alone. Additionally, heavy rainfall during thunderstorms can overwhelm drainage systems, causing flooding that further damages building foundations and infrastructure. The combination of wind, hail, and flooding can compromise the integrity of buildings, increase the potential for cascading failures, and result in significant economic losses and safety risks for occupants.

Understanding the multi-hazard effects of thunderstorms and hail is crucial for developing resilient building designs and urban planning strategies that can mitigate the impacts of these natural events.

Calotescu et al. (2024) explore the effects of an intense thunderstorm on the urban area of Sânnicolau Mare, Romania. The study integrates full-scale meteorological data with a post-event damage survey to analyze wind- and hail-induced damage to low-rise buildings. The findings aim to inform storm-resistant design strategies for buildings in similar environments.

The study collected data from a wind monitoring system on a 50-meter lattice tower and a state-operated meteorological station, both located near the urban area. The monitoring systems recorded various meteorological parameters, including wind speed, wind direction, and temperature, during the thunderstorm event on June 25th, 2021. Video surveillance data provided additional visual insights into the thunderstorm's development and impact. Figure 93 illustrates the 3-h-long records of wind speed and direction collected by the wind and structural monitoring system from 17:00 to 20:00 UTC, which is sufficiently long to fully cover the entire passage of the thunderstorm over the city. The monitoring data revealed that the maximum instantaneous wind speed reached 40.9 m/s, emphasizing the remarkable intensity of the thunderstorm.

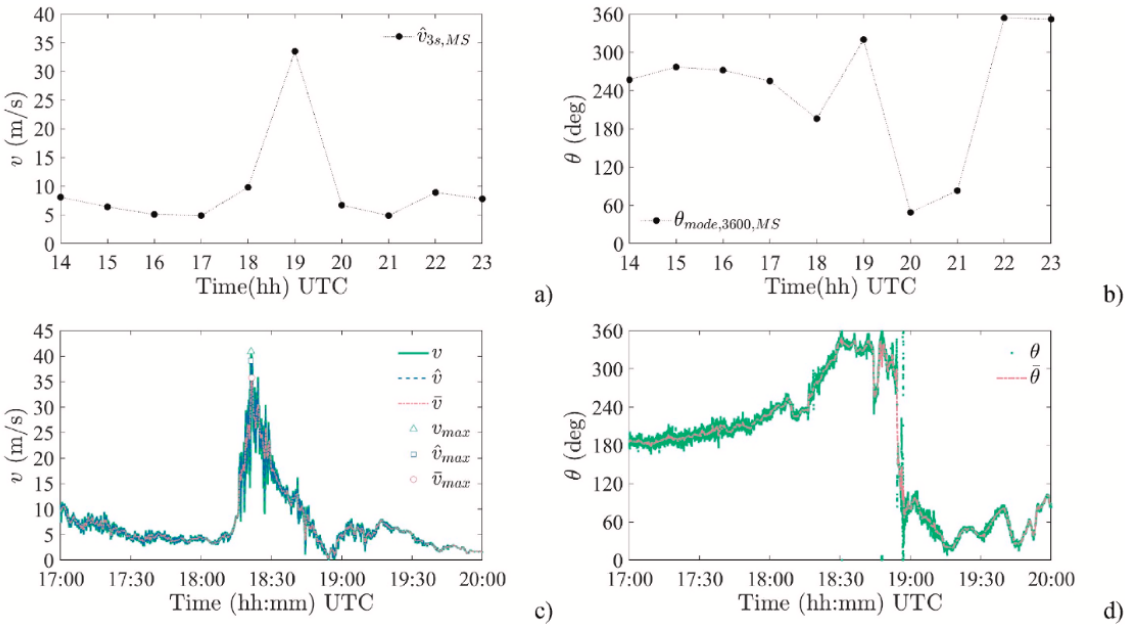

Figure 93. Wind data recorded by the meteorological station (data provided by Meteo Romania): (a) maximum 3-s gust speed and (b) mode of wind direction and by the monitoring system installed on the telecommunication tower: (c) wind speed and (d) wind direction (from Calotescu et al., 2024).

The damage survey, conducted through a combination of in-situ investigation and crowdsourcing, identified 237 cases of damage, predominantly affecting low-rise buildings. The most common type of damage was the partial or complete failure of roofing systems, particularly those made of sheet metal and clay tiles. The study provides a detailed forensic analysis of a church building, referred to as "Building A," which suffered significant roof damage. The analysis, supported by Figure 94, highlights that the roof was uplifted due to the excessive suction forces generated by flow separation near the roof edges.

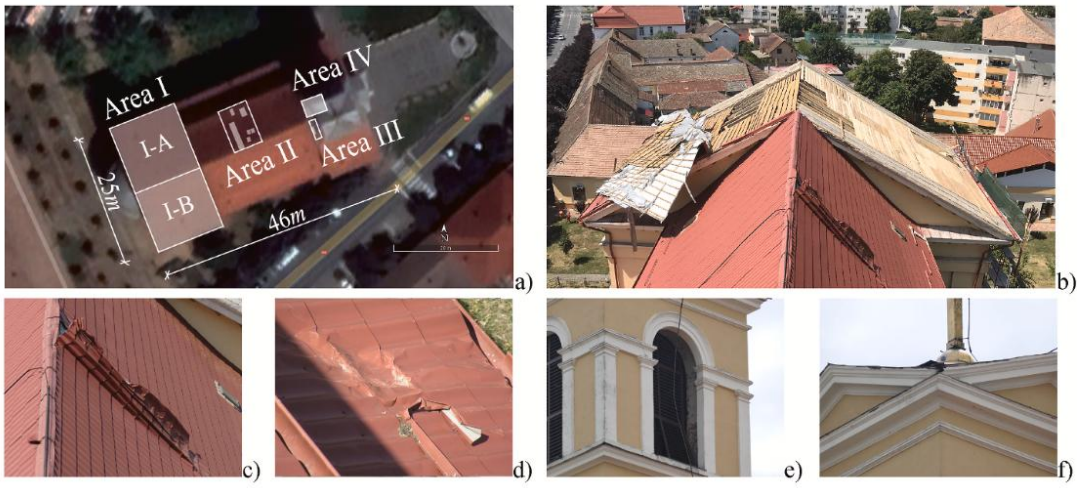

Figure 94. Wind-induced damage to Building A: (a) top view and damage areas; (b) roof damage in Area I (partially restored); (c–d) roof damage in Area II; (e) window damage in Area III; (f) roof damage in Area IV (from Calotescu et al., 2024).

In addition to wind damage, the study also investigated hail-induced damage, which was primarily observed on building facades. The survey identified 220 cases of facade damage, with the majority occurring on thermal insulation layers (TILs) of the buildings. Figure 95 presents examples of hail-induced damage on facades, showing that the intensity of damage varied depending on the presence of a protective top coat on the TILs.

Figure 95. Hail-induced damage patterns: (a) Facade 1; (b) Facade 2; (c) Facade 3 and (d) Facade 4 (from Calotescu et al., 2024).

The study explored the possibility of using hail-induced damage to estimate wind speed and direction. By analyzing the size and distribution of indentations caused by hailstones, the researchers inferred that the horizontal wind speed during the storm was approximately 24 to 28 m/s. This estimate was consistent with the wind speeds recorded by the anemometers, demonstrating the feasibility of using hail damage as a proxy for wind speed. Figure 96 further illustrates the distribution of hail damage intensity on the facade of "Building B," showing that damage was more severe at higher elevations, which correlates with increased wind speeds at those heights.

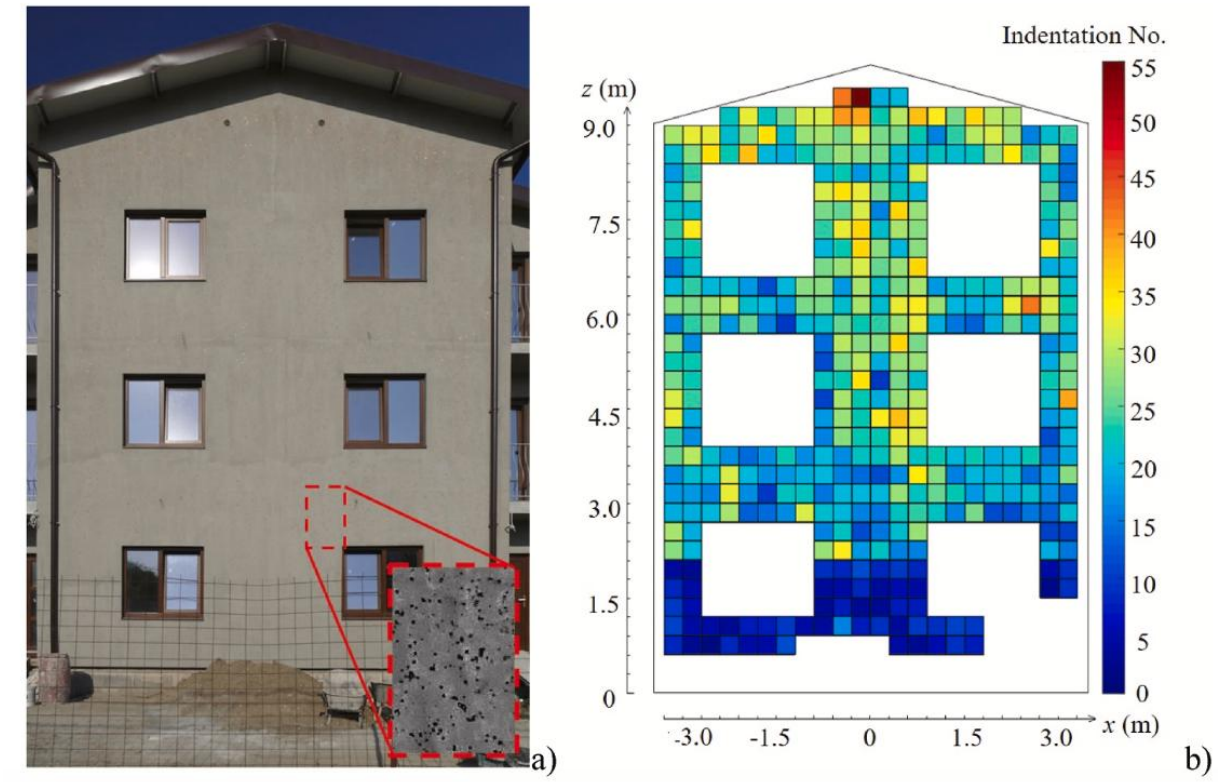

Figure 96. Hail-induced TIL damage to the West facade (middle part) of Building B: (a) high-resolution photo of TIL; (b) distribution of hail damage intensity (from Calotescu et al., 2024).

In summary, this study points out the importance of incorporating wind-resistant design features into buildings, particularly in regions prone to intense thunderstorms. The study validates the use of existing wind speed estimation scales, such as the Fujita and Enhanced Fujita scales, for assessing the intensity of thunderstorm winds. Additionally, it introduces the use of hail-induced damage as a novel indicator for estimating wind speed and direction during such events. Overall, this research provides valuable insights into the mechanisms of thunderstorm-induced damage and offers practical recommendations for enhancing the resilience of buildings in thunderstorm-prone areas.

4.2.3 Earthquake-induced rockfall scenario

The seismically induced rockfalls scenario associated with the May 6th, 1976 Friuli earthquake (M6.5) and its largest aftershocks (M6.1 and M6.0) serves as a specific example of multi-hazard event, or more precisely, of cascading hazards.

Friuli-Venezia Giulia (FVG) is located in northeast Italy, at the convergence of the Adria microplate and the Eurasian plate. This complex seismotectonic setting is the primary reason for the region's high degree of seismic activity. Numerous studies have demonstrated a strong correlation between the spatial distribution of coseismic landslides/rockfalls and ground motion intensities (e.g., Keefer, 2000; Jibson,

2011; Tiwari et al., 2017; Alvioli et al., 2024). In Italy, the most common type of earthquake-induced landslides is rockfalls type.

An approach to rockfalls hazard scenarios based on earthquake ground motion has been developed by OGS researchers for the epicentral area of the 1976 Friuli earthquake. In this work, the spatial distribution of the rockfalls inventory triggered by the FVG 1976 seismic sequence has been considered. Ground shaking scenarios were modeled from the three seismic events composing the earthquake sequence, using point and extended sources, and a representative structural model (Panza et al., 2012). Many realizations or fault rupture patterns for the seismic source have been used to account for the rupture process and the effects of directivity. The available rockfalls inventory, which were triggered by the FVG 1976 seismic sequence, were mapped altogether after the occurrence of these earthquakes. The PGA spatial distribution were computed for several earthquake scenarios, for the main shock and the aggregated earthquake sources, using both point and extended sources, so as to account for increasingly complex scenarios of seismic shaking. Subsequently, the Quantum Geographic Information System (QGIS) tool has been used to compare the spatial distribution patterns of rockfalls and PGAs for the site of interest. The PGA value computed at the center of each grid cell has been assigned to the entire grid cell to perform geo-statistical analyses and relate the landslides distribution with PGA values. Six PGA thresholds were used (namely: 20-40; 40-80; 80-150; 150-300; 300-600; and > 600 gal), which roughly correspond to different macroseismic intensity levels of the Mercalli-Cancani-Sieberg Intensity scale (MCS).

To explore the relation between the spatial pattern of ground motion and its possible effects on rockfall occurrences, we adopted a binary "forecasting" approach of Molchan (1990). Basically, we assess the presence (or absence) of rockfalls within a territory selected according to a specific value of the ground shaking parameter, and then we check whether the number of rockfalls identified based on ground motion is larger than that from a random guess. The results show that the modeled ground shaking predicts the spatial pattern of observed rockfalls better than a random guess and outperforms even predictions based on the slope information.

The obtained results (Figure 97) suggest the opportunity of including topographic effects in the ground shaking simulations and highlight the possibility of further investigating the cumulative effect of complex seismic sequences and their influence on modulating landslide susceptibility (Peresan et al., 2024 and references therein).

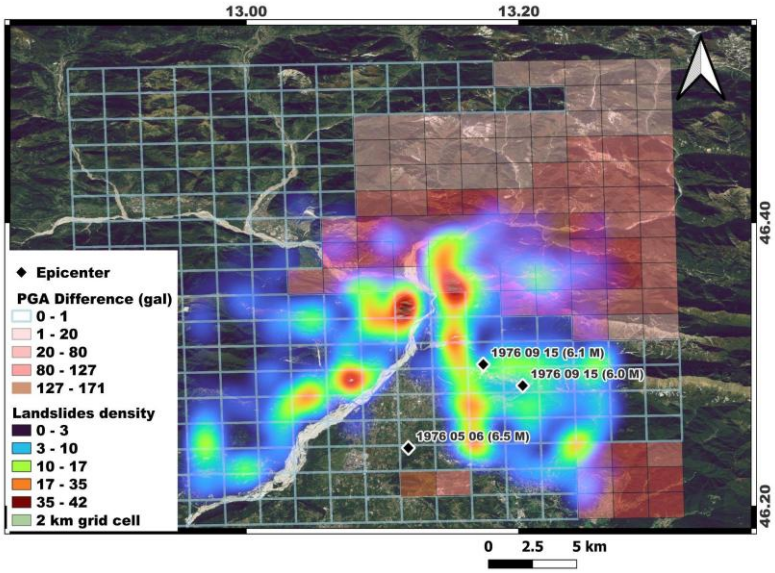

Figure 97. Map of the difference between PGA computed for three earthquake aggregated scenario and one main earthquake for point source model compared with the density of observed landslides.

5. Multi-risk scenarios for informed decision making

As mentioned in Section 1 and Section 2, the concept of risk storylines is introduced within the RETURN Project, referring to a defined, plausible combination of events, their consequences and the factors possibly affecting these elements, as well as the physical, socio-ecological and functional elements at risk (Shepherd et al. 2018; March et al. 1991, Sillmann et al. 2021). It has been proposed as a way of articulating the risk in such cases where there is the need to go beyond a purely probabilistic perspective, with an emphasis on plausibility rather than probability. A storyline-based approach is proposed in the framework of the WP 5.3 activities as a methodology for the multi-risk assessment of urban environments, by including multiple hazards, with their possible interactions, and all the exposed urban assets with the objective of evaluating the socio-economic impacts.

The use of storylines has the multi-fold purpose of:

- Cross-checking and stress-testing the advances in the individual risk-related components (e.g., hazards, exposure and vulnerability) with respect to the needs and expectations of stakeholders.
- Highlighting and exemplifying the cascading mechanisms, the variety of impacts, the different exposed systems and functions possibly affected by compound events, in prototypical settlement types deemed representative of urban areas across the Italian territory or in real urban contexts.
- Designing, co-designing and validating multi-hazard, multi-risk scenarios with a range of stakeholders through simpler, intuitive conceptual representations, even before a more analytical modelling.

The essential elements to be defined within a storyline-based approach are the following (Figure 98):

- Scope of the storyline, which include the description of the urban context, the selection of the time or time interval of interest and the definition of current or future environmental, social and economic conditions.
- Most relevant risks and related factors, namely hazards, exposure, vulnerabilities and the impacts of the hazardous events under investigation.
- Reference stakeholders.
- Other relevant data.

The interrelationships between the different risk components, defined in Section 2, should support the definition of realistic multi-risk scenarios and, consequently, of risk storylines. A storyline should be characterized by a synthetic narrative description, reporting main facts and consequences.

A graphical representation of a risk storyline is an impact chain, highlighting the causal relationships between events and their impacts on the analyzed urban context. In this way, complex multi-risk processes can be considered in a consistent framework for a number of hazards (UNDRR, 2020). As can be seen in the example presented in Figure 99, an impact chain is constituted by elements and connections between them. The element types are: hazard/event, exposure, vulnerability, impact, risk, adaptation or mitigation measures, other external drivers, etc. The possible connections between elements can be classified as: “causes”, “impacts”, “affects”, “relates to”, “mitigates”.

From a methodological point of view, the definition of the vulnerability models and of the possible impacts within a multi-risk perspective, considering all the relevant elements and accounting for the described interrelationships, will be the objectives of the Tasks 5.3.2, 5.3.3 and 5.3.4 of the Work Package 5.3. In the following, a portfolio of storylines is proposed, considering six urban contexts which will be analyzed in the framework of the Transversal Spoke TS1 as case studies towards the Proof of Concept. These contexts are distributed within the Italian territory, as shown in Figure 100.

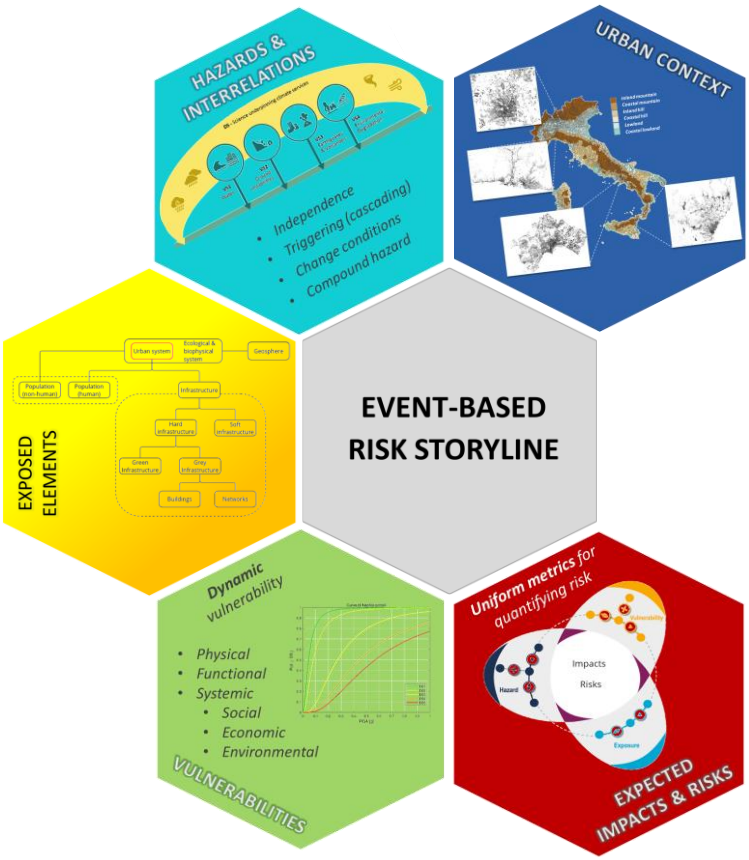

Figure 98. Event-based risk storyline approach

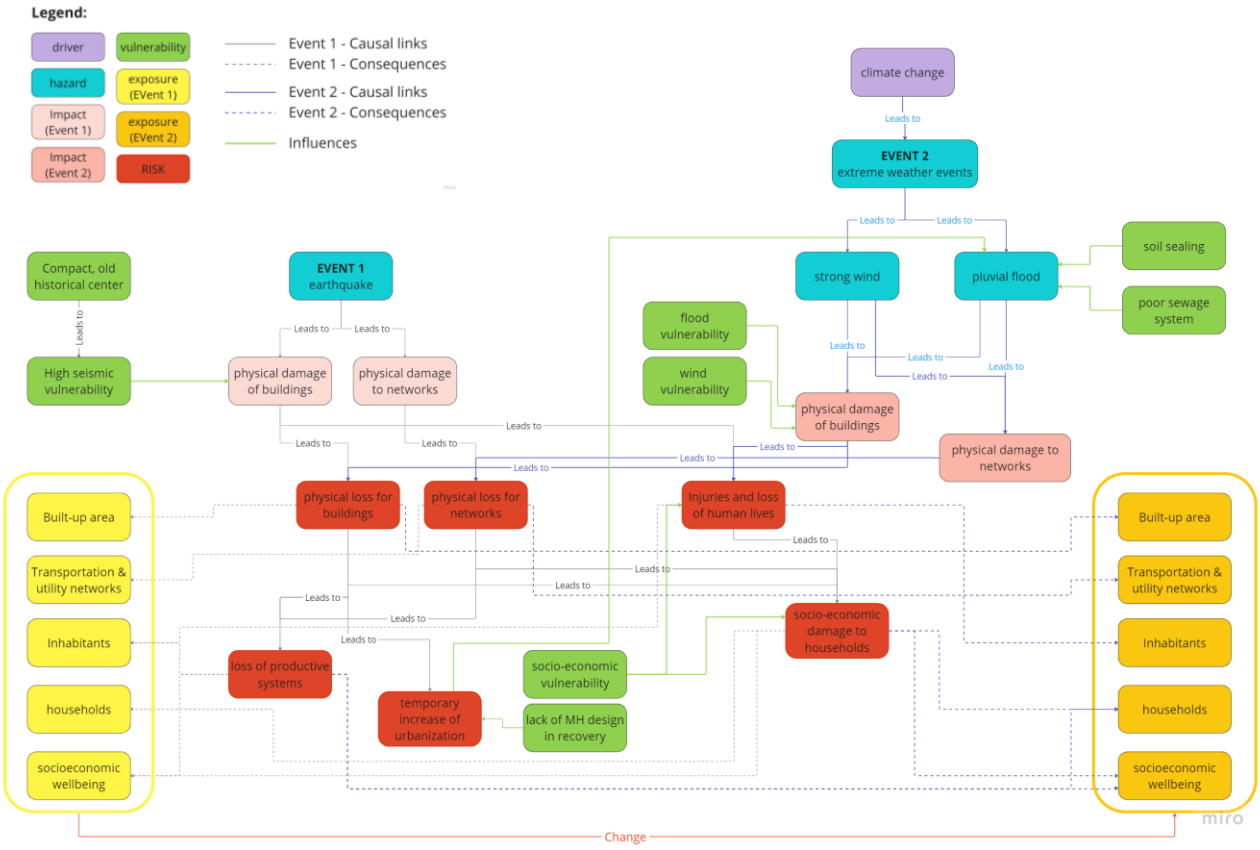

Figure 99. Example of an impact chain

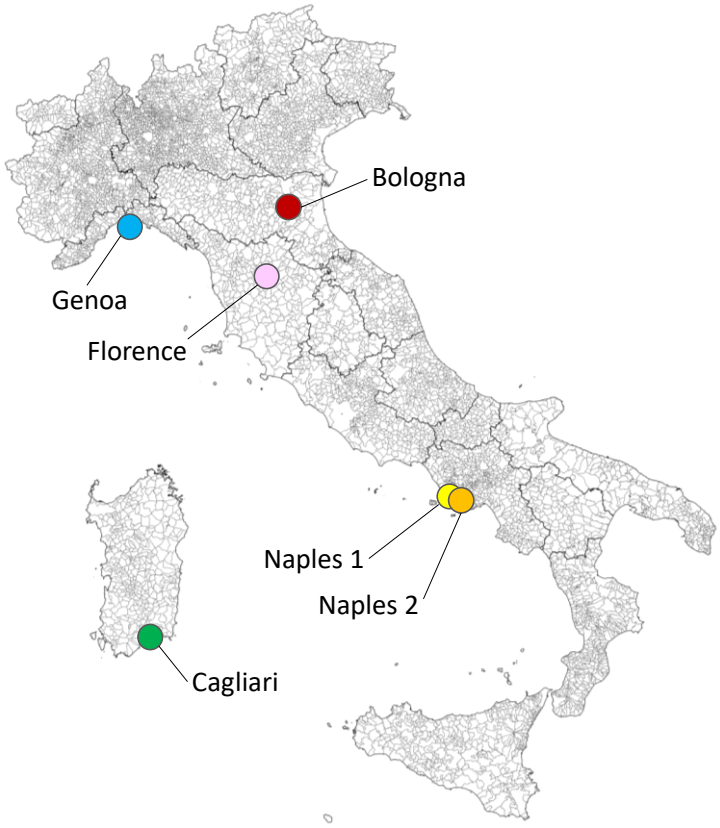

Figure 100. Location of the urban contexts considered for risk storylines

5.1 Storyline 1 - Compounding and independent heatwave and surface water flooding in the context of the Functional Urban Area of Cagliari

5.1.1 Storyline identification

Title	Compounding and independent heatwave and surface water flooding in the context of the Functional Urban Area of Cagliari
Identification code	To be defined
Version	v1.0
Author (s)	Corrado Zoppi, Federica Leone, Sabrina Lai
Date	26.07.2024
Abstract	In the Functional Urban Area of Cagliari, a heatwave occurs in late August, shortly followed by a cloudburst which generates surface water flooding. The impact chain here developed highlights the use of green and blue open spaces as adaptation options through their provision of regulating ecosystem services.

5.1.2 Settlement context

Settlement type	SC_03: Settlement context in the metropolitan area on the coastline
Other info on settlement	none

5.1.3 Description of the urban context

Functional Urban Area (FUA) consisting of a core coastal municipality, Cagliari, and its travel-to-work area, comprising 31 smaller towns.
The core municipality is a Mediterranean city port, whose economy mainly relies on the tertiary sector, and especially on public services, trade, and tourism. The hilly landscape of the core city is bounded by the seaside to the South and by two large coastal wetlands to the East and to the West. Both the seashore and the wetlands have constrained the growth of Cagliari's built-up area; therefore, the core city's urbanization process that has taken place in the last decades has involved its hinterland and, more recently, the inner towns that make up the FUA.
Some of the 31 smaller towns feature large coastal development (for instance, Capoterra to the West and Quartu Sant'Elena to the East), only partly consisting of summer houses. The agricultural sector is a significant contributor to the economy of the inland towns, especially the ones that are closer to the Campidano Plain, hence in the eastern part of the FUA.

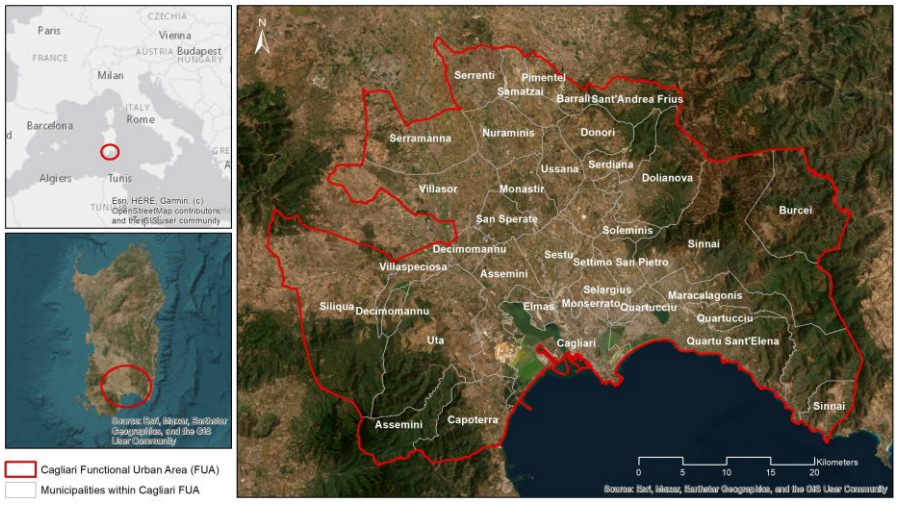

The latest years have been featured by a surge in heat waves; Cagliari is one of the cities included in the national "warning system for the prevention of health effects of heat waves", for which the severity of heat waves is scored on a three-level scale and communicated through a daily bulletin.

5.1.4 Dimension / population

~1950 km^2; ~475000 resident population.

The Functional Urban Area (FUA) of Cagliari comprises 32 local authorities and spans over around 1950 km^2. Resident population in the FUA amounted to 476717 residents as of 2022 (EUROSTAT), of which of which around 30% living in the FUA's core area, i.e., the municipality of Cagliari.
Green spaces, regarded as the combination of ecological systems having various degrees of naturalness, represent 42.06% of the FUA, including green urban areas, which amount to a mere 0.47% of the FUA.
Blue spaces, mostly coinciding with wetlands and saltpans, make up a further 3.87% of the FUA.

5.1.5 Reference hazards

Multi-hazard type	**Compounding and independent** multi-natural-hazard scenario
Hazard interaction type	**Compounding and independent heatwave and surface water flooding**

Individual hazards

Item	***UNDRR-ISC code***[31]	***Individual hazard description***
H1	MH0047	Heatwave
H2	MH0012	Surface water flooding

5.1.6 Main / relevant impacts

Item	***Impacts***
I1	Urban heat island
I2	Functional or physical damages to infrastructure (roads, railroads, and bridges)
I3	Flooded basements and ground floors
I4	Road accidents and injuries
I5	Increase in energy demand for cooling
I6	Increase in morbidity
I7	Damage to agricultural ecosystems
I8	Damage to natural and semi-natural ecosystems (incl. urban green areas)

5.1.7 Exposure types

Item	***Elements at risk***
E1	Residents, Tourists, City users
E2	Road and railroad networks
E3	Buildings
E4	Agricultural sector
E5	Protected areas and urban parks

Other elements, Description	The two main wetlands in the FUA East, Molentargius to the East of the core city and Santa Gilla to the West, enjoy multiple protection regimes (e.g., Natura 2000, Ramsar, Regional Park) because of their relevance in terms of biodiversity, landscape and cultural identity. The presence of the wetlands is important in terms of mitigation of temperature and flood; however, they can also be negatively affected by both rise in temperature (in multiple ways, ranging from decrease in water levels due to evaporation, to increase in alien species, to

[31] See the individual codes here

	eutrophication and subsequent fish die-off) and by floods (for instance due to break of the levees). In the latest decades, the FUA has been affected by some major floods (e.g., 2008, 2013, and 2018) that have caused the loss of human lives, mostly people trapped in their cars or in the basements or ground floor of their houses. During the 2018 event damages to the main road artery that connects Cagliari to Capoterra with the collapse of a bridge resulted in main traffic disruptions.

5.1.8 Vulnerability types

Item	*Vulnerabilities*
V1	High values of soil sealing in the urban settlements
V2	Reduced water infiltration
V3	Wetland environment sensitive to high temperatures
V4	Dense urban fabric with little interspersed greenery
V5	Poor maintenance and irrigation of urban green areas
V6	Residential settlements in flood-prone areas
V7	Limited network redundancy in the southwest area
V8	House basements used as living spaces (in the suburbs and smaller towns, where low-density development and detached houses are common)

5.1.9 Risks

Item	*Risks description*
R1	Loss of human lives
R2	Disruption of utility services (energy)
R3	Disruption of public services (health sector)
R4	Traffic and mobility disruption
R5	Loss of/Damage to the primary productive system (agriculture)
R6	Species & ecosystems degradation and loss

5.1.10 Adaptation options

Item	*Adaptation option description*
A1	Increase in urban greenery
A2	Increase in vegetated land covers, including afforestation
A3	Use of permeable pavements
A4	Flood-related NbS (swales, raingardens…)
A5	Maintenance and enlargement of coastal wetlands

5.1.11 Stakeholders

Stakeholders interested	Civil protection department, municipality, road network managers, railroad managers, transport service providers, water manager, health services, farmers' associations, environmental associations, citizens and city users.
Stakeholder involved (in the description of the storyline)	None

5.1.12 Relevant data

Item	Data type	Hazard Item	Description	Responsible	Link
D01	geospatial	H1	Flood hazard vector map	Regione Sardegna	https://webgis2.regione.sardegna.it/geonetwork/srv/ita/catalog.search#/metadata/R_SARDEG:132322a2-9287-4a38-bfcb-843dfb27d6f4
			Flood risk vector map		https://webgis2.regione.sardegna.it/geonetwork/srv/ita/catalog.search#/metadata/R_SARDEG:f86ae5a0-7b76-47d0-8e35-f55b8515e4a2
D02	geospatial	H2	LST raster maps (Landsat Collection 2 Surface Temperature)	USGS	https://www.usgs.gov/landsat-missions/landsat-collection-2-surface-temperature
D03	geospatial	H2	LST raster maps	EU Copernicus Land Monitoring Services	https://land.copernicus.eu/en/products/temperature-and-reflectance/hourly-land-surface-temperature-global-v2-0-5km

5.1.13 Other relevant notes

None

5.1.14 Risk storyline impact chain

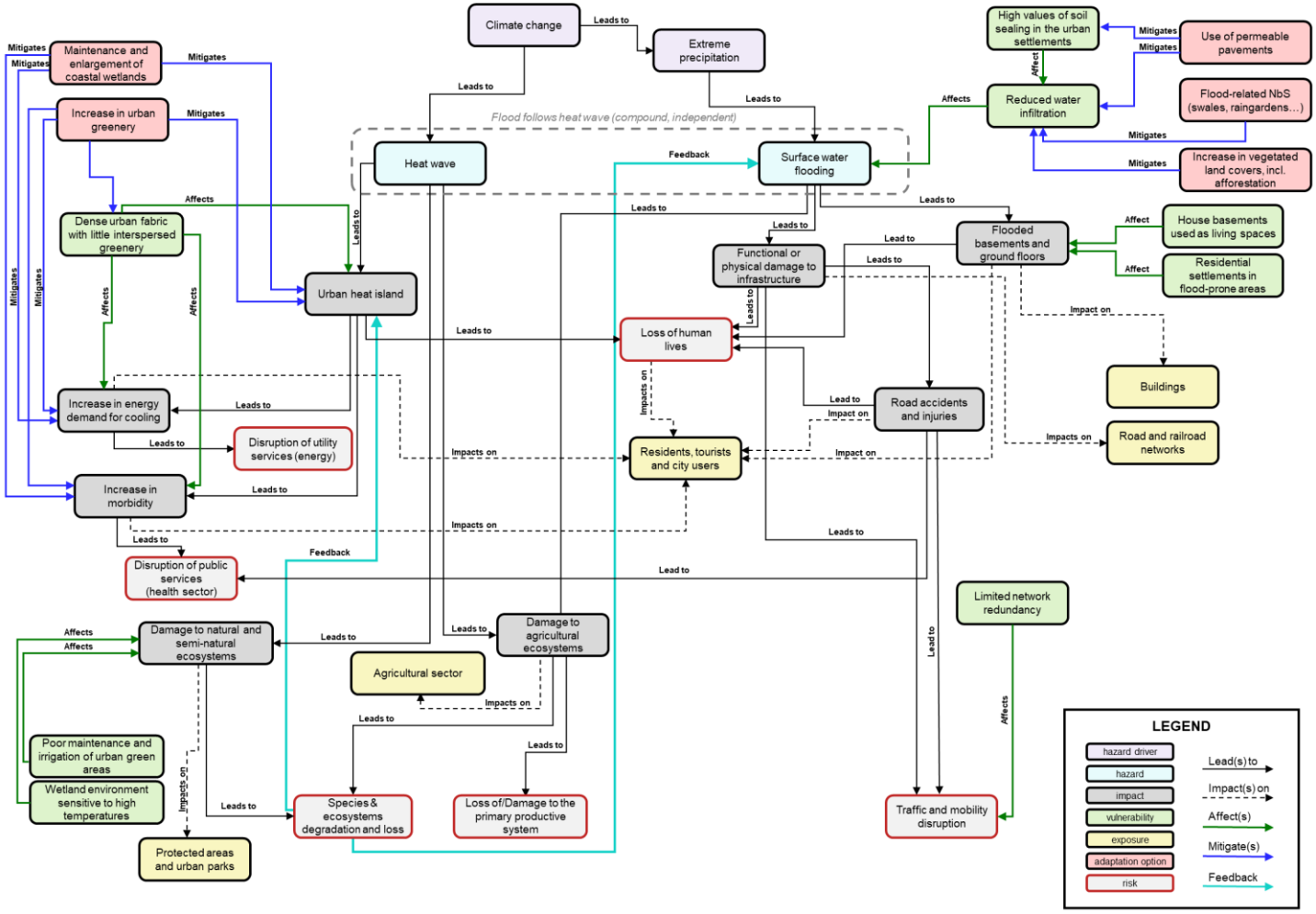

5.2 Storyline 2 – Climate and Geophysical Risks in a polluted coastal settlement in Naples

5.2.1 Storyline identification

Title	Climate and Geophysical Hazards in a polluted coastal settlement
Identification code	To be defined
Version	v1.0
Author (s)	Cristina Visconti (DiARC)
Date	03.08.2024

5.2.2 Settlement context

Settlement type	**SC_03: Settlement context in the metropolitan area on the coastline** / Climatic, biological and na-tech risks
Other info on settlement	Settlement features: settlement in the coastal plain with sandy shore characterized by an industrial area and the presence of rail infrastructures Built-up features: fragmentary fabric of recent construction, articulated along urban roads with a predominantly orthogonal trend to the coastline. Risks: climatic risks from coastal erosion, biological risks from marine pollution and na-tech risks due to the presence of numerous industrial buildings in the coastal area.

5.2.3 Description of the urban context

The urban settlement is located in a coastal plain of a volcanic origin, between a Gulf (North-West) and system of hills (South-East), and it is part of a larger costal urban system densely populated.
The neighborhood is inside an active volcanic field and despite the high environmental value and touristic vocation it has been strongly urbanized and turned in an industrial site for heavy industry of the Italian Government starting from the '60s.
The industries have been dismantled during the 90', creating a large brownfield (250 hectars) declared National Site of Interest due to the high environmental pollution.

The urban fabric is fragmented due to the presence of the former industrial site between the hill and the coastline and a residential area mostly built to dwell the workers of the industries.
The residential area is positioned mainly behind the industrial area and its Northern edge.
The urban fabric is design on an orthogonal grid with a North-South orientation and belongs to the beginning of XXI Century, with most of the buildings built between 1919 and 1976.

The urban form is influenced by a low rate of open spaces, high rate of impermeable surfaces, scarcity of vegetation, compromised biodiversity.
The availability of green areas per capita is lower than the city average (1.2 m2 per capita), with only one public park (14.000 m^2). Most of the beaches are not accessible and there is a bathing prohibition in the whole marine area due to the chemical pollution (heavy metals, hydrocarbons).

Major transportation infrastructures are: one major driveway axis that connects the neighborhood to the other sub-district of the same Municipality and a coastal road that connects the settlement to the area of the Gulf. Two railways axis connect the neighborhood with the city center, the neighboring town situated on the Gulf and other coastal settlements. Demographically the neighborhood presents a high rate of aged population (over 64 years old).

5.2.4 Dimension / population

The considered municipality have 100.000 inhabitants part of a larger city of 1 million (*Naples*). The area (*Municipality 10*) is divided in 2 sub-districts with a total surface of 14, 6 km^2 (sub-district 1 (*Bagnoli)*: 7,96 km^2/ population: 23 333; sub-district 2 (*Fuorigrotta)*: 6,20 km^2/ population: 71 808).

5.2.5 Reference hazards

Multi-hazard type	Climate hazard (heat wave) + Geophysical hazard+ Chemical Hazard and Environmental Degradation
Hazard interaction type	Heat wave period with a sequence of seismic events of small scale (bradyseism) and a major seismic event triggered by volcanic unrest, the area is threatened by chronical environmental and chemical risk (high pollution, environmental degradation, heavy metals) due to a former industrial area. The high chemical pollution and the environmental degradation affects in particular the coastline and the marine area where the industrial settlement was located.

Individual hazards

Item	***UNDRR-ISC code***[32]	***Individual hazard description***
H1	MH0047	Meteorological Hazard, Temperature-related (Heat-wave)
H2	GH0021	Other Geohazard, Ground Shaking (induced earthquake)
H3	GH0015	Volcanogenic Geothermal, Ground Shaking (Volcanic Earthquake)
H4	EN0004	Environmental Degradation (Land Degradation)
H5	EN005	Environmental Degradation (Soil Degradation)
H6	EN006	Runoff / Nonpoint Source Pollution
H7	CH0004	Heavy Metals-Cadmium
H8	CH0005	Heavy Metals-Lead
H9	CH006	Heavy Metals-Mercury
H10	CH0017	Hydrocarbons-Oil
H11	CH0020	Other Chemical Hazards and Toxins- Asbestos
H12	CH0013	Persistent Organic Pollutants (POPs)-Dioxine Dioxin-like Substances

5.2.6 Main / relevant impacts

Item	***Impacts***
I1	Increase of non-communicable diseases
I2	Increase of energy demand
I3	Socio-economic impact (energy costs)
I4	Water/energy shortage
I5	Physical damage of buildings
I6	Physical damage to networks

5.2.7 Exposure types

Item	***Elements at risk***
E1	Population
E2	Built-up area
E3	Open spaces
E4	Transportation and utility network
E5	Social Well-being

[32] See the individual codes here

Other elements, Description	The former industrial area is an exposed element, particularly for the presence of industrial archeology buildings (for the earthquake risk). The area represent also potentiality for climate adaptation as the regeneration as a large green park with nature-based solutions can deliver ecosystem services and mitigate the heat waves effects. Nevertheless, the area with new residential buildings, facilities and services can help for emergency response in case of a major volcanic/seismic event.

5.2.8 Vulnerability types

Item	*Vulnerabilities*
V1	Urban form (building/open spaces relation and quality depending by the age of construction and building typologies)
V2	High population vulnerability depending by age and socio-economic factors
V3	Socio-economic vulnerability (income and productive activities)
V4	Medium/high Seismic vulnerability due to the building typologies, age of construction
V5	Socio-spatial vulnerability due to the lack of green/open spaces and to a reduced distribution of urban services and facilities (e.g. health and educational facilities, public transportation)
V6	Social vulnerability depending by gender and race
V7	Institutional vulnerability

5.2.9 Risks

Item	*Risks description*
R1	Deaths and hospitalizations
R2	Interruption of essential services
R3	Physical loss for buildings
R4	Physical loss for networks
R5	Evacuation routes interruption
R6	Injuries and loss of human lives
R7	Loss of productive systems
R8	Socio-economic damage to households
R9	Chronical Risks for health

5.2.10 Stakeholders

Stakeholders interested	Civil Protection department, municipality, city authorities, citizenships, civic society organizations, NGOs, Special National Authority for the former industrial site (Extraordinary Government Commissioner for the environmental remediation and urban regeneration of the site of national interest), Territorial Authority for the Metropolitan Area, Regional Government, ISPRA (Italian Institute for Environmental Protection and Research), Universities and Research Institutes, Industrial workers committee. Specific stakeholders for the case: City Council of Naples, Bagnoli Futura S.p.A. (the society which led the dismantlement of the industrial area and its transformation process from 2002 to 2014), Invitalia (a joint-stock company of the Ministry of Economy), Bagnoli Assembly, Iskra Collective, Bancarotta Collective (self-organized social movements), Science Centre and Arenile Resort (private bodies), National Research Council of Italy – Institute for Research on Innovation and Services for Development (CNR IRISS), University of Naples Federico II (Department of Civil Engineering, Department of Architecture, PLINIVS Study Center)
Stakeholder involved (in the description of the storyline)	None

5.2.11 Relevant data

Item	Data type	Hazard Item	Description	Responsible	Link
D01	Geospatial	H1	Heat Waves distribution	DiARC, Plinivs	
D02	Geospatial	H1	Building Typologies/Age of Construction	DiARC	
D03	Geospatial	H1	Building Materials	DiARC,	
D04	Geospatial	H1	NDVI (Vegetation)	DiARC, Plinivs	
D05	Geospatial	H1	Population age	DiARC, Plinivs	
D06		H2-H3	Volcanic/Seismic	DIST (???)	
D07		H4-H11		ISPRA, De Vivo &Lima 2018, Albanese 2010, Balzamo 2017	www.isprambiente.gov.it/contentfiles/00004000/4034-c2738-m2-u5.pdf

5.2.12 Other relevant notes

Specific information on the case study:

- Geomorphological characteristics: The Bagnoli-Fuorigrotta plain is an integral part of the Campi Flegrei, an active Quaternary volcanic system, located 10 km W-NW from Naples, characterized by geothermal activities (fumarole and hotsprings) (De Vivo & Lima 2018). The coastal area of Bagnoli is part of a shelf facing the entire shoreline of the Gulf of Pozzuoli (Albanese et al 2010). The groundwater of the plain, resupplied directly by rainfall, is part of a wider groundwater body which spans the whole Campi Flegrei area and that discharges directly to the sea (De Vivo & Lima 2018, Albanese et al. 2010).

- Historical Development of settlement: In ancient times, the area was a thermal site and a fertile agricultural land. Several archeological sites testify the strategic importance of the area during the Roman period as it connected Naples with Campi Flegrei's cities. During the eighteenth century till the beginning of twenty century Bagnoli has been a touristic beach and thermal area. In the first part of the of twentieth century with the implementation of a plan for the industrialization of the city, Bagnoli beaches became an industrial site that after the 60' has been dedicated to heavy national industry. During the 1960s, the steel industry reached its peak employment with 8,800 workers. However, in the 1980s, the demand for Italian steel from foreign markets experienced a continual decline. This downturn led to the closure of the steel factory in 1992, resulting in the abandonment of a significantly polluted coastal area and the loss of jobs for over 2,100 workers. The former industrial site in Bagnoli constitutes 15% of the district, which has a population of 24,000 residents. Efforts to revitalize the former industrial zone in Bagnoli commenced with the factory's closure in 1992 and were still ongoing (Andriello, 2003; Andriello, Belli, & Lepore, 1991; Cento Bull 2006; Cirillo 2016; Ragozzino et al. 2018).

- On-going regeneration process: The area is interested by an on-going remediation project for the former industrial site that will be environmentally regenerated and dedicated to the creation of new green areas, coastal landscape management and protection, transformation of previously derelict areas (Urban Atlas 2021). The Italian government funded the remediation plans with two specific Laws (N. 582—18/11/1996 and N. 388—23/12/2000) for the purpose of reusing the areas of ILVA and Eternit for nonindustrial activities. Possible pollution sources in the area include dust, ash, scum, slag, carbon coke residues, minerals, heavy oils, hydrocarbons, and combustion residues (De Vivo & Lima 2018). The complex process has been blocked for more than 20 years (due to critical economic issue and a governance impasse). Nowadays the process slowly restarted but several issues are still not addressed, such as unresolved issues related to planning, housing, dismantled areas, unemployment, presence of conflicts between political, economic, and social actors (Ragozzino et al. 2018).

5.2.13 Risk storyline impact chain

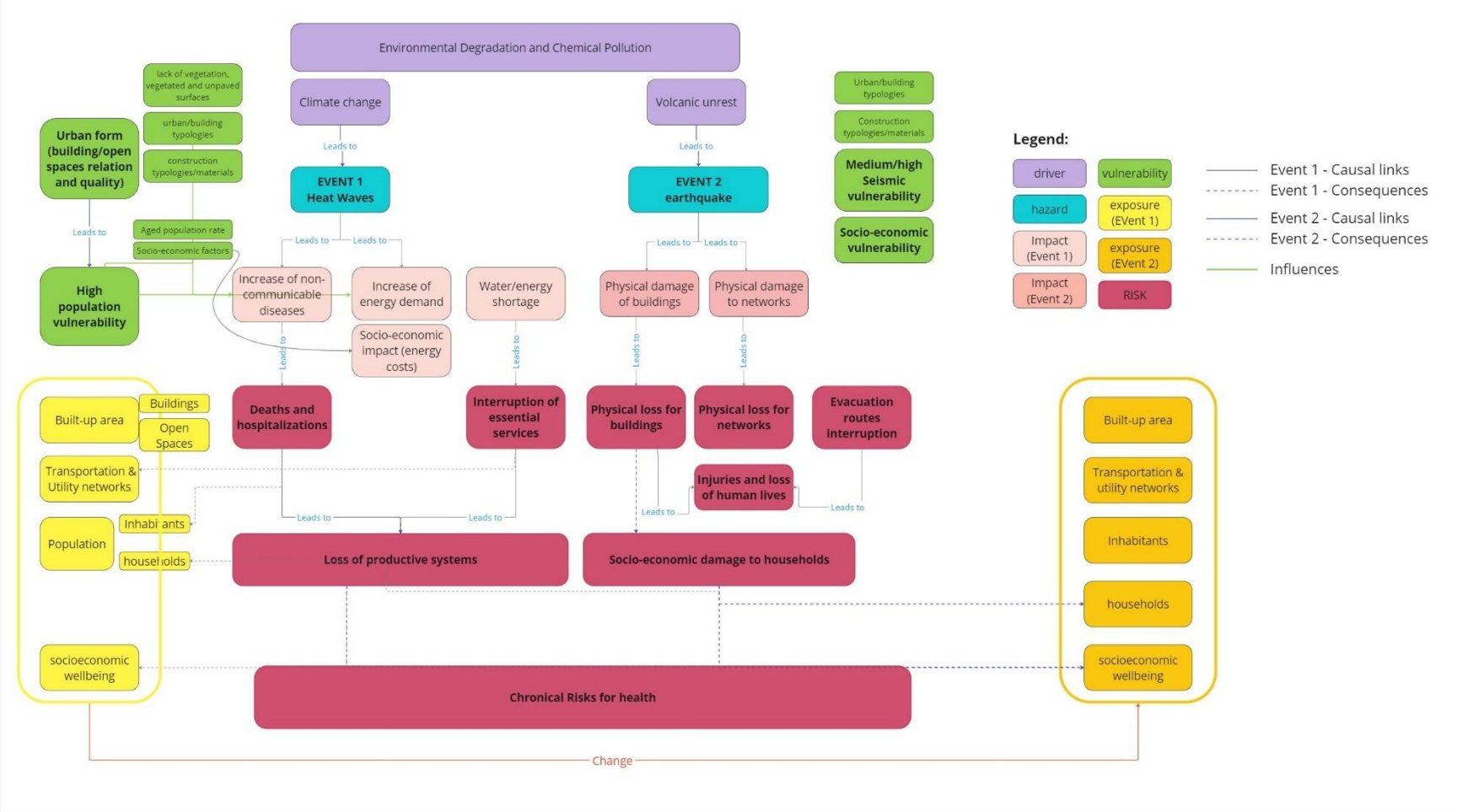

5.3 Storyline 3 - Geophysical risks in the Vesuvian volcanic area

5.3.1 Storyline identification

Title	Geophysical risks in the Vesuvian volcanic area
Identification code	To be defined
Version	v1.0
Author (s)	Gerardo Verderame, Maria Polese, Carlo Del Gaudio, Gabriella Tocchi (UNINA)
Date	25.07.2024
Abstract	A volcanic eruption occurs with the formation of eruptive columns producing the subsequent fall of blocks, ash and lapilli in the surrounding area. The collapse of the eruptive column causes pyroclastic flows. An earthquake of medium-high magnitude is also recorded within a week.

5.3.2 Settlement context

Settlement type	SC_02: Settlement context in metropolitan area in basin of volcanic origin / Geophysical risks
Other info on settlement	The settlement is located on the slopes of an important volcano with a long history of Plinian and sub-Plinian eruptions. In this area there is also a tourist/commercial port.

5.3.3 Description of the urban context

Context consisting of a set of neighboring municipalities characterized by a high population density (about 2000 inhabitants/km^2) and 40,000 residential buildings. Presence of a tourist/commercial port in the area.

5.3.4 Dimension / population

The intermunicipal hubs have 300.000 inhabitants.

5.3.5 Reference hazards

Multi-hazard type	Geophysical hazards (volcanic and seismic)
Hazard interaction type	Independence

Individual hazards

Item	***UNDRR-ISC code***[33]	***Individual hazard description***
H1	GH0010	Ash/Tephra Fall (Physical and Chemical)
H2	GH0011	Ballistics (volcanic)
H3	GH0012	Pyroclastic Density Current
H4	GH0001	Earthquake

5.3.6 Main / relevant impacts

Item	***Impacts***

[33] See the individual codes here

I1	Physical damages to buildings
I2	Physical damages to infrastructures
I3	Traffic/mobility/network disruption
I4	Interruption of port services

5.3.7 Exposure types

Item	***Elements at risk***
E1	Population (inhabitants, tourists)
E2	Built-up area
E3	Open spaces
E4	Transportation and utility network
E5	Tourist/commercial port

Other elements, Description	None

5.3.8 Vulnerability types

Item	***Vulnerabilities***
V1	Physical vulnerability of buildings
V2	Functional vulnerability of buildings
V3	The road network is not redundant enough

5.3.9 Risks

Item	***Risks description***
R1	Injuries and loss of human lives due to damages of buildings
R2	Economic losses related to physical damages of buildings
R3	Economic losses related to physical damages of infrastructures
R4	Road network disruption, determining delays and difficulties both in the emergency phase and post-event
R5	Interruption of business activities generating economic losses (indirect costs)
R6	Costs for temporary shelters due to unusability of buildings

5.3.10 Stakeholders

Stakeholders interested	Civil Protection department, municipality, first responders, road network manager, port authority, citizenships
Stakeholder involved (in the description of the storyline)	University and scientific research organization

5.3.11 Relevant data

Not specified yet

5.3.12 Other relevant notes

None

5.4 Storyline 4 - A multi-risk scenario in hilly morphology area in Florence

5.4.1 Storyline identification

Title	A multi-risk scenario in hilly morphology area in Florence
Identification code	To be defined
Version	v1.0
Author (s)	Gianni Bartoli, Chiara Arrighi, Simona Francalanci, Federico Gusella, Barbara Pintucchi, Marco Uzielli (UNIFI)
Date	21.07.2024

5.4.2 Settlement context

Settlement type	SC_04: Settlement context in a hilly metropolitan area / Geotechnical, hydraulic and seismic risks
Other info on settlement	None

5.4.3 Description of the urban context

The “Piazzale Michelangelo” area, in Florence, is a renowned cultural and historical site, hosting innumerable elements of cultural heritage and attracting numerous visitors year-round. Situated in a zone with varied topographical features and climatic conditions, the area is vulnerable to multiple natural hazards. The territory analyzed corresponds to the left bank of the “Arno River”, between the “alla Vittoria” bridge and “S. Niccolò” bridge. The area includes the historical sites of “Piazzale Michelangelo” and “Boboli Gardens” in addition to the highly populated neighborhood of “Santo Spirito”. The topography of the area is mainly flat, with the exception of the “San Miniato” hill. This storyline considers the interplay and potential effects of four major hazards: earthquake, strong wind, flood, and landslide.

5.4.4 Dimension / population

~4.5 km^2

5.4.5 Reference hazards

Multi-hazard type	Multi-hazard scenario – Wind - Downburst / ThunderStorm - Flood - Landslide - Earthquake
Hazard interaction type	Independent events

Individual hazards

Item	***UNDRR-ISC code***[34]	***Individual hazard description***
H1	GH002	Earthquake
H2	MH0007	Fluvial (Riverine) Flood
H3	GH007	Landslide
H4	MH0060	Wind
H5	MH0001 / MH0003	Downburst / ThunderStorm

[34] See the individual codes here

5.4.6 Main / relevant impacts

Item	*Impacts*
I1	Physical damages to roads/bridges
I2	Physical damages to buildings
I3	Physical damages to green infrastructures
I4	Traffic/mobility/network disruption
I5	Physical damages to natural landscape due to slope instability

5.4.7 Exposure types

Item	*Elements at risk*
E1	Inhabitants
E2	built-up area
E3	road network
E4	underlying utilities
E5	natural slopes

Other elements, Description	The area hosts numerous buildings and manufacts of high cultural and historical value. Moreover, the investigated zone is a tourist area visited by thousands of tourists per year.

5.4.8 Vulnerability types

Item	*Vulnerabilities*
V1	Existing old bridges and buildings designed only for vertical loads
V2	Existing buildings close to the river
V3	Existing roads close to the river and to the hill
V4	Natural slopes constituting the San Miniato hill

5.4.9 Risks

Item	*Risks description*
R1	Loss of human lives because of the impacts of the earthquake, flood and landslide (short-term effect).
R2	Physical damage on the built-up area, including the collapse and/or destruction of some buildings due to earthquakes and landslides.
R3	Interruption of infrastructure network (direct and indirect loss)
R4	Physical damage to natural slopes due to earthquakes and landslides

5.4.10 Stakeholders

Stakeholders interested	Civil Protection department, municipality, road network manager, industrial site manager, citizenships
Stakeholder involved (in the description of the storyline)	None

5.4.11 Relevant data

Item	*Data type*	*Hazard Item*	*Description*	*Responsible*	*Link*
D01	geospatial	H1	e.g., "Raster spatial distribution of macroseismic intensity (EMS-98)"		
D02	geospatial	R4	Comune di Firenze – Sistema Informativo Geologico del Sottosuolo	Comune di Firenze	https://sigs.comune.fi.it/
D03	geospatial	R4	Geoportale Geoscopio	Regione Toscana	https://www.regione.toscana.it/-/geoscopio

5.4.12 Other relevant notes

The activity will focus on the quantitative multi-layer single-risk estimation and zonation of physical and financial risk to a variety of categories of exposed elements from wind, geotechnical, hydraulic, and seismic hazards for an urban area in the Municipality of Florence, Italy. Hazards will be estimated using existing or new hazard type-specific models for a common time period considering the return periods of events of different magnitudes. The vulnerability of the categories of exposed elements will also be estimated relying on existing or new models.

Exposure will be defined in common for all hazards in the physical and financial dimensions. This approach will allow the conduction of quantitative single-risk analyses for all hazard types and for all (shared) categories of exposed elements. Adopting a shared exposure parameter with uniform metrics will allow the merging of the single-risk estimates into multi-layer risk estimates.

5.5 Storyline 5 - Compounding Hazards in Genoa: A Multi-Event Crisis of Heatwaves, Storms, Floods, Landslides, and Earthquake

5.5.1 Storyline identification

Title	Compounding Hazards in Genoa: A Multi-Event Crisis of Heatwaves, Storms, Floods, Landslides, and Earthquakes
Identification code	To be defined
Version	v1.0
Author (s)	Margherita Rago, Sergio Lagomarsino, Serena Cattari (UNIGE)
Date	27.08.2024
Abstract	In the Municipality of Genoa, a series of heatwaves occur in the summer, shortly followed by a thunderstorm which generates surface water flooding in the city and localized landslides/fall of debris in peri-urban areas. Finally, an earthquake of moderate magnitude occurs, with amplified damaging effects due to lack of recovery from previous hazardous events.

5.5.2 Settlement context

Settlement type	SC_06: Settlement context in a metropolitan area on the coastline surrounded by hills/mountains with strong acclivities / Climatic, hydraulic, geophysical risks
Other info on settlement	Settlement developed along the coastline, with recent expansions located on sloping ground along mountainous ridges. Risks include climatic risks with heatwaves and strong thunderstorms, hydraulic risks with flooding events, and geophysical risks with earthquakes and landslides.

5.5.3 Description of the urban context

Urban configuration: The City of Genoa, situated in the Liguria region of Italy and facing the Mediterranean Sea, is a polycentric, dense, stratified, and socially heterogeneous city. Having flourished in the Middle Ages due to its expertise in trade, shipbuilding, and finance, today Genoa is a major port, industrial and touristic city. Despite the proximity to the sea, the territory quickly elevates towards a hilly to mountainous morphology. Therefore, the urban context is bounded by the coastline on the south and the hillside on the north, with very dense and diverse urbanization developing from sea level up to approximately 300m of altitude. Additionally, Genoa is crossed perpendicularly by two main rivers, Polcevera and Bisagno.

Infrastructures: Genoa is well-connected by road, rail, and air. The city's main vehicle infrastructure includes two large freeways, the A10 motorway connecting it to the rest of Italy, and the SS1, allowing the crossing between the Eastern and Western sides of the city. Cristoforo Colombo is the Airport of Genoa, providing domestic and international flights. Due to its challenging topography, Genoa has developed a unique urban infrastructure with extensive use of tunnels, elevators, and funiculars to navigate the steep terrain. The city has undergone various urban renewal projects to modernize and improve living conditions, however Genoa has an ageing infrastructure that requires ongoing maintenance and modernization.

Building typologies: The most common residential building typologies classified among the urban development of Genoa, ranging from the Medieval times (XI-XII century) to the XXI century are: 1) Medieval Aggregate Houses; 2) Renaissance Villas and Palaces; 3) Block Houses; 4) Courtyard Houses; 5) Popular Apartment Buildings; 6) Modern Apartment Buildings; 7) Row Houses.

Multi-hazard framework: Due to its unique morphologic configuration and climate, Genoa is prone to compounding and independent multi-hazard scenarios. Heatwaves, exacerbated by high humidity and the urban heat island effect, create health risks for residents and tourists. The city's location near the Ligurian Alps and Apennines makes it prone to strong winds, particularly the tramontana and mistral, which frequently cause damage to the natural environment, buildings, and infrastructures, especially in the port area. Additionally, when heavy rainstorms occur, Genoa is prone to flooding due to the combined effect of the river basin water levels rising, and the incapacity of the urban drainage system to dispose of the excess. Furthermore, the impermeable soil and hydrogeological instability lead to frequent landslides, especially in suburban areas, causing damage to roads and buildings enhancing residents' risk of isolation from first aid. Finally, Genoa is located in a region that has a moderate seismic risk (zone 3). While it's not in one of the most seismically active zones of Italy, the city is still susceptible to earthquakes being surrounded by the northern Apennine Mountain range.

5.5.4 Dimension / population

Area: The municipality of Genoa covers an area of approximately 240.29 km^2. Resident Population: As of the latest available data (2023), the resident population of Genoa is approximately 550'000 people. This makes it the sixth-largest city in Italy by population. Population Density: The population density in Genoa is about 2'289 inhabitants per km^2, reflecting the relatively dense urban environment of the city.

5.5.5 Reference hazards

Multi-hazard type	Independent and cascading multi-hazard scenario
Hazard interaction type	Thunderstorm TRIGGERING surface water flooding and landslide Heatwave AFFECTING surface water flooding and landslide Earthquake

Individual hazards

Item	***UNDRR-ISC code***[35]	***Individual hazard description***
H1	MH0047	Heatwave
H2	MH0003	Thunderstorm
H3	MH0012	Surface Water Flooding
H4	GH0007	Landslide
H5	GH0001	Earthquake

5.5.6 Main / relevant impacts

Item	***Impacts***
I1	Urban heat island
I2	Increase in energy demand for cooling
I3	Increase in human and animal health issues (e.g. severe dehydration, heat exhaustion, heat stroke)
I4	Functional or physical damage to residential, commercial, public, and industrial buildings
I5	Functional or physical damage to infrastructures (roads, port, railroads, tunnels, and bridges) and energy plants
I6	Business/production interruption and economic loss
I7	Increase in traffic, road accidents and injuries
I8	Increase in morbidity
I9	Damage to agricultural ecosystems
I10	Damage to natural and semi-natural ecosystems (incl. urban green areas)

[35] See the individual codes here

5.5.7 Exposure types

Item	*Elements at risk*
E1	Residents, Tourists, City users
E2	Infrastructures (roads, port, railroads, tunnels, and bridges)
E3	Residential, commercial, public, and industrial buildings
E4	Agricultural sector
E5	Protected areas and urban parks

Other elements, Description	None

5.5.8 Vulnerability types

Item	*Vulnerabilities*
V1	Buildings with poor or lack of retrofitting and maintenance particularly historical/abandoned/old structures.
V2	Ageing infrastructure, including roads, tunnels, and drainage systems.
V3	Dense urban fabric with poor or lack of interspersed greenery.
V4	Poor road network with only one main road connecting the residents across the city in case of emergency.
V5	Peri-urban residential settlements in hilly terrain prone to landslides, with scarce road connection to the rest of the city in case of emergency.
V6	Residential settlements and commercial activities in flood-prone areas, particularly in basements and ground floors.
V7	Residential settlements with no access to cooling devices or natural ventilation living in areas prone to urban heat island formation.
V8	Residential settlements in buildings with poor or lack of retrofitting and maintenance.

5.5.9 Risks

Item	*Risks description*
R1	High population density and urban heat island effect exacerbate heatwave impacts, increasing heat-related health risks and morbidity, particularly for vulnerable populations living in poorly ventilated and older buildings.
R2	Physical damage on buildings with poor or no retrofitting and maintenance due to cumulative impacts from subsequent hazardous events.
R3	Cumulative stress from heatwaves, storms, landslides and potential earthquakes overwhelming public health systems, increasing morbidity and mortality rates.
R4	Poor road network and ageing infrastructure leading to significant delays and difficulties in emergency response and evacuation, especially during landslides in peri-urban residential settlements.
R5	Residential and commercial areas in flood-prone zones, especially basements and ground floors at high risk of severe flood damage, leading to displacement and economic losses.
R6	Interruption of business activities in the port and industrial sectors due to damage to buildings and infrastructural network, generating economic losses.
R7	Environmental and agricultural degradation and loss due to heavy rains and landslides.

5.5.10 Stakeholders

Stakeholders interested	Civil Protection department, first responders & health workers, municipality, road network manager, port manager, citizenship, university & scientific research organizations, policymakers, media.
Stakeholder involved (in the description of the storyline)	University & scientific research organization

5.5.11 Relevant data

Item	*Data type*	*Hazard Item*	*Description*	*Responsible*	*Link*
D01	Geospatial	H1	Copernicus Interactive Climate Atlas	Copernicus	https://atlas.climate.copernicus.eu/atlas
D02	Geospatial	H3	Updated mapping of hydraulic hazards for the city of Genoa	Geoportale Regione Liguria	https://srvcarto.regione.liguria.it/geoviewer2/pages/apps/geoportale/index.html?id=447
D03	Geospatial	H3, H4	VAS indicators of the Municipal Urban Plan - PUC	Geoportale Comune di Genova	https://mappe.comune.genova.it/MapStore2/#/viewer/776
D04	Geospatial	H5	Seismic hazard model MPS04-S1 for the Italian territory	INGV	https://esse1-gis.mi.ingv.it/

5.5.12 Other relevant notes

None

5.6 Storyline 6 - Heat waves and earthquake in the metropolitan area of Bologna

5.6.1 Storyline identification

Title	Heat waves and earthquake in the metropolitan area of Bologna
Identification code	To be defined
Version	v1.0
Author (s)	Francesca Ferretti, Luca Pozza (UNIBO)
Date	20.08.2024
Abstract	In the metropolitan area of Bologna, an earthquake occurs during the summer together with a series of heatwaves, taking place simultaneously and also in the aftermath of the seismic event.

5.6.2 Settlement context

Settlement type	SC_07: Settlement context in a metropolitan area on the flood plain bounded by hills on one side / Climatic and geophysical risks
Other info on settlement	Settlement within a flood plain confining with hills, characterized by a densely populated area and industrial/commercial sites. Risks include climatic risks with heatwaves and geophysical risks with earthquakes.

5.6.3 Description of the urban context

The city of Bologna is located in the Emilia-Romagna Region, in northern Italy, within the "Pianura Padana" flood plain and at the foot of the Apennines. Developing along the Via Emilia, the city has always been a commercial and transportation hub. The historical city center, surrounded by walls and fortifications, remains of which are still visible, is mainly characterized by the presence of masonry buildings, many of which have long porticos at the ground floor. Modern buildings (e.g., reinforced concrete buildings, tall buildings, etc.) are mainly located in the urban expansions outside the walls. The metropolitan area of Bologna is characterized by the presence of many commercial buildings and industrial sites as well.
Concerning infrastructures, Bologna is an important railway and highway hub and hosts an international airport within the urban area.

5.6.4 Dimension / population

The spatial extent of the metropolitan area of Bologna is approximately 3702 km^2, with a number of total inhabitants equal to 1'016'000 (June 2022), with a density of 274 inhabitants per km^2. The municipality of Bologna covers an area of 140.9 km^2, with approximately 391'000 inhabitants (June 2022), with a density of 2776 inhabitants per km^2.

5.6.5 Reference hazards

Multi-hazard type	Climatic (heat waves) and geophysical (earthquake) hazards
Hazard interaction type	Independence: hazardous events overlap in time and space, but they are not correlated with one another in terms of intensity, probability of occurrence, etc.

Individual hazards

Item	***UNDRR-ISC code***[36]	***Individual hazard description***
H1	MH0047	Heatwave
H2	GH0001	Earthquake

[36] See the individual codes here

5.6.6 Main / relevant impacts

Item	*Impacts*
I1	Urban heat island
I2	Increase of energy demand
I3	Physical and functional damages of buildings
I4	Traffic and utility network disruption
I5	Commercial/industrial business interruption

5.6.7 Exposure types

Item	*Elements at risk*
E1	Population (inhabitants, tourists, city users)
E2	Built-up area (residential, commercial, industrial, public buildings)
E3	Open spaces
E4	Transportation and utility network

Other elements, Description	In the aftermath of the earthquake, depending on the damage level of buildings, some people might live in tents/camps or temporary shelters. Presence of an important railway hub (e.g., high-speed train station) and of an international airport.

5.6.8 Vulnerability types

Item	*Vulnerabilities*
V1	Physical vulnerability of buildings, especially the ones built without a proper seismic design
V2	Functional vulnerability of buildings
V3	Urban areas without (or with few) green open spaces
V4	High population vulnerability depending by age and socio-economic factors
V5	Socio-economic vulnerability (income and productive activities)

5.6.9 Risks

Item	*Risks description*
R1	Deaths, injuries and hospitalization
R2	Economic losses related to physical damages of buildings
R3	Economic losses related to physical damages of transport and utility networks
R4	Interruption of business activities generating economic losses (indirect costs)
R5	Costs for temporary shelters due to unusability of buildings
R6	Socio-economic damage to households

5.6.10 Stakeholders

Stakeholders interested	Civil Protection department, first responders & emergency management agencies, municipality, road/train network manager, citizens
Stakeholder involved (in the description of the storyline)	University

5.6.11 Relevant data

To be defined

5.6.12 Other relevant notes

None

References

Abadie, L.M., Galarraga, I., Markandya, A., de Murieta, E.S. 2019. "Risk measures and the distribution of damage curves for 600 European coastal cities." *Environ. Res. Lett.* 14: 064021. https://doi.org/10.1088/1748-9326/ab185c

Abadie, L.M., Sainz de Murieta, E., Galarraga, I. 2016. "Climate risk assessment under uncertainty: An application to main European coastal cities." *Front. Mar. Sci.* 3: 265. https://doi.org/10.3389/fmars.2016.00265

Achebak, H., Garatachea, R., Pay, M.T. et al. 2024. "Geographic sources of ozone air pollution and mortality burden in Europe." *Nat Med* 30: 1732–1738. https://doi.org/10.1038/s41591-024-02976-x

Adamek, K., Vasan, N., Elshaer, A., English, E., Bitsuamlak, G. 2017. "Pedestrian level wind assessment through city development: a study of the financial district in Toronto." *Sustain. Cities Soc.* 35: 178-190.

Afzal, S., Riaz, R.A., and Kim, B.S. 2016. "Energy-efficient flood detection and evacuation system using WSN technology." *IEEE Access* 4: 3285-3296.

Ahmed, I., Esch, M., Hoeven, F. 2023. "Heatwave vulnerability across different spatial scales: Insights from the Dutch built environment." *Urban Climate* 51: 101614.

Airparif 2018. *Evaluation of the air quality monitoring network in Paris and its impact on public health policies*. Airparif Report, 22, 45-57. Retrieved from https://www.airparif.asso.fr/

Akyildiz, I.F., Su, W., Sankarasubramaniam, Y., and Cayirci, E. 2002. "A survey on sensor networks." *IEEE Communications Magazine* 40(8): 102-114. https://doi.org/10.1109/MCOM.2002.1024422

Alari, A., Chen, C., Schwarz, L., Hdansen, K., Chaix, B., Benmarhnia, T. 2023. "The Role of Ozone as a Mediator of the Relationship Between Heat Waves and Mortality in 15 French Urban Areas." *American Journal of Epidemiology* 192(6): 949–962. https://doi.org/10.1093/aje/kwad032

Albanese, S., De Vivo, B., Lima, A., Cicchella, D., Civitillo, D., and Cosenza, A. 2010. "Geochemical baselines and risk assessment of the Bagnoli brownfield site coastal sea sediments (Naples, Italy)." *Journal of Geochemical Exploration* 105(1-2): 19-33.

Aldereguía Sánchez, C., Tubino, F., Bagnara, A., Piccardo, G. 2023. "Experimental Simulation of Thunderstorm Profiles in an Atmospheric Boundary Layer Wind Tunnel." *Applied Sciences* 13(14): 8064. DOI: 10.3390/app13148064

Allamano, P.; Croci, A.; Laio, F. 2015. "Toward the camera rain gauge." *Water Resour. Res.* 51: 1744–1757. https://doi.org/10.1002/2014WR016298

Alvioli, M., Poggi, V., Peresan, A., Scaini, C., Tamaro, A., Guzzetti, F. 2024. "A scenario-based approach for immediate post-earthquake rockfall impact assessment." *Landslides* 21: 1–16. https://doi.org/10.1007/s10346-023-02127-2

AMS 2024. *Glossary of meteorology*. Available online at https://glossarytest.ametsoc.net/wiki/Blocking_high, last accessed 28 June 2024

Andersen, Z.J., Hvidberg, M., Jensen, S.S., Ketzel, M., Loft, S., and Sørensen, M. 2020. "Effects of exposure to nitrogen dioxide on children's respiratory health in European cities." *Environmental Health Perspectives* 128(9): 097001. https://doi.org/10.1289/EHP6146

Andersson, C., Langner, J., and Bergström, R. 2020. "Interactions between climate change and air quality in Europe." *Atmospheric Chemistry and Physics* 20(13): 7671-7693. https://doi.org/10.5194/acp-20-7671-2020

Andriello, V. 2003. “Napoli, Bagnoli e la fabbrica: per una storia dello stabilimento Ilva-Italsider nel territorio”. In: M. E. Roma (Ed.), *Dalle partecipazioni statali alle politiche industriali*.

Andriello, V., Belli, A., and Lepore, D. (Eds.). 1991. *Il luogo e la fabbrica. L’impianto siderurgico di Bagnoli e l’espansione occidentale di Napoli*. Napoli: Graphotonic.

Apreda, C., D’Ambrosio, V., Di Martino, F. 2019. “A climate vulnerability and impact assessment model for complex urban systems.” *Environ. Sci. Policy* 93: 11–26. https://doi.org/10.1016/j.envsci.2018.12.016

Arnell, N.W., and Gosling, S.N. 2016. “The impacts of climate change on river flood risk at the global scale.” *Water Resources Research* 52(7): 5899-5914. doi:10.1002/2015WR018362.

Aronica G.T., Tucciarelli T. & Nasello C., 1998. “A 2D multilevel model for flood propagation in flood affected areas.” *J Water Resour Plan Manage-ASCE* 124(4): 210–217.

Arnoldus H. M. J., 1980. “An approximation of the rainfall factor in the universal soil loss equation.” In: Deboodt M, Gabriels D. (Eds.) *Assessment of Erosion*. Chichester: John Wiley and Sons.

ARPAL, 2013, *Atlante climatico della Liguria*, https://www.arpal.liguria.it/tematiche/meteo/pubblicazioni-bis/analisi-climatologiche/atlante-climatico-della-liguria.html

Bacciu, V., et al. 2020. “Analisi del rischio: i cambiamenti climatici in Italia.” In: Eds. Donatella Spano, and Valentina Mereu. Fondazione Centro euro-mediterraneo sui cambiamenti climatici. https://www.cittaclima.it/wp-content/uploads/2020/11/Presentazione_Spano-25.11.2020.pdf

Baire, Q.; Dobre, M.; Piette, A.-S.; Lanza, L.; Cauteruccio, A.; Chinchella, E.; Merlone, A.; Kjeldsen, H.; Nielsen, J.; Østergaard, P.F.; Porrando M. and Garcia Izquierdo, C. 2022. “Calibration Uncertainty of Non-Catching Precipitation Gauges.” *Sensors* 22: 6413. https://doi.org/10.3390/s22176413

Baker, J.W., Bradley, B.A., and Stafford, P.J. (2021). Seismic Hazard and Risk Analysis. Cambridge University Press.

Balzamo, S., Centioli, D., de Zorzi, P., Potalivo, M. 2017. *Rapporto di convalida dei dati di caratterizzazione del sito Bagnoli – Coroglio*. ISPRA.

Baró, F. et al. 2018. “The role of green infrastructure in air quality improvement: The case of urban trees and green roofs in Barcelona and Paris.” *Science of the Total Environment* 616-617: 113-124. https://doi.org/10.1016/j.scitotenv.2017.11.191

Barreiro, J., Santos, F., Ferreira, F., Neves, R., Matos, J.S. 2023. "Development of a 1D/2D Urban Flood Model Using the Open-Source Models SWMM and MOHID." *Land. Sustainability* 15:707. https://doi.org/10.3390/su15010707

Basili, R., Brizuela, B., Herrero, A., Iqbal, S., Lorito, S., Maesano, F. E., et al. 2020. "The making of the NEAM tsunami hazard model 2018 (NEAMTHM18)." Front. Earth Sci., Sec. Geohazards and Georisks 8: 616594. https://doi.org/10.3389/feart.2020.616594.

Bassolino, E., D’Ambrosio, V. and Sgobbo, A. 2021. “Data Exchange Processes for the Definition of Climate-Proof Design Strategies for the Adaptation to Heatwaves in the Urban Open Spaces of Dense Italian Cities.” *Sustainability* 13: 5694.

Bates, P.D., Marks, K.J., and Horritt, M.S. 2003. "Optimal use of high-resolution topographic data in flood inundation models." *Hydrological Processes* 17: 537–557. https://doi.org/10.1002/hyp.1113

Bates, P.D., Neal, J.C., and Sampson, C.C. 2015. "The Role of Land Use and Land Cover Change in Modifying Flood Risk in the U.S." *Water Resources Research* 51(8): 5844-5862. https://doi.org/10.1002/2015WR017116.

Bazin, P.H., Nakagawa, H., Kawaike, K., Paquier, A., and Mignot, E. 2014. "Modeling Flow Exchanges between a Street and an Underground Drainage Pipe during Urban Floods." *J. Hydraul. Eng.* 140(10): 04014051. https://doi.org/10.1061/(ASCE)HY.1943-7900.0000917

Beasley, K.J. 2016. “Building facades failure in the urban environment.” *Forensic Engineering* 170(1): 8-13.

Beevers, S.D., Kitwiroon, N., Williams, M.L., and Kelly, F.J. 2017. “Air pollution dispersion models for human exposure predictions in London.” *Environmental Modelling & Software* 95: 238-258. https://doi.org/10.1016/j.envsoft.2017.06.019

Bell, M.L., Davis, D.L. 2001. "Reassessment of the lethal London fog of 1952: novel indicators of acute and chronic consequences of acute exposure to air pollution." *Environ Health Perspect* 109(Suppl 3): 389-94. doi:10.1289/ehp.01109s3389

Belluso, E., Bellis, D., Fornero, E. et al. 2006. “Assessment of Inorganic Fibre Burden in Biological Samples by Scanning Electron Microscopy – Energy Dispersive Spectroscopy.” *Microchim Acta* 155: 95–100. https://doi.org/10.1007/s00604-006-0524-y

Berdahl, P., et al. 2008. “Weathering of roofing materials – an overview.” *Construction and building materials* 22: 423-433.

Bernardini, G., Ferreira, T.M. 2022. “Combining Structural and Non-structural Risk-reduction Measures to Improve Evacuation Safety in Historical Built Environments.” *International Journal of Architectural Heritage* 16(6): 820-838.

Bertsch, R., Glenis, V., and Kilsby, C. 2017. "Urban Flood Simulation Using Synthetic Storm Drain Networks." *Water* 9: 925. https://doi.org/10.3390/w9120925

Bevacqua, E., Maraun, D., Vousdoukas, M. I., Voukouvalas, E., Vrac, M., Mentaschi, L., and Widmann, M. 2019. “Higher probability of compound flooding from precipitation and storm surge in Europe under anthropogenic climate change.” *Sci. Adv.* 5: eaaw5531. https://doi.org/10.1126/sciadv.aaw5531, 2019.

Beven, K. 2012. *Rainfall-runoff modelling: The primer*. John Wiley & Sons.

Bianchi, M., Rossi, G., and Mancini, M. 2024. “The 2023 Emilia-Romagna Floods: Hydrological Analysis and Lessons for Future Flood Risk Management.” *Journal of Hydrology* 610: 128500. https://doi.org/10.1016/j.jhydrol.2023.128500.

Birkmann, J., Cardona, O.D., Carreño, M.L., Barbat, A.H., Pelling, M., Schneiderbauer, S., Kienberger, S., et al. 2013. “Framing Vulnerability, Risk and Societal Responses: The MOVE Framework.” *Natural Hazards* 67(2): 193–211. doi: 10.1007/s11069-013-0558-5.

Blocken, B., Stathopoulos, T. , van Beeck, J.P.A.J. 2016. “Pedestrian-level wind conditions around buildings: review of wind-tunnel and CFD techniques and their accuracy for wind comfort assessment.” *Build Environ.* 100: 50-81.

Blöschl, G., Hall, J., Parajka, J., et al. 2020. “Changing climate shifts timing of European floods.” *Water Resources Research* 56(10): e2020WR027639. doi:10.1029/2020WR027639.

Bolan, S., Padhye, L.P., Jasemizad, T., Govarthanan, M., Karmegam, N., Wijesekara, H., Amarasiri, D., Hou, D., Zhou, P., Biswal, B.K., Balasubramanian, R., Wang, H., Siddique, K.H.M., Rinklebe, J., Kirkham, M.B., Bolan, N. 2024. “Impacts of climate change on the fate of contaminants through extreme weather events.” *Science of The Total Environment* 909: 168388. doi: https://doi.org/10.1016/j.scitotenv.2023.168388.

Bonaccorso, B., Cancelliere, A., and Rossi, G. 2017. “The 2016 Arno River Flood in Florence: Hydrological Analysis and Historical Context.” *Hydrology and Earth System Sciences* 21(7): 3367-3382. https://doi.org/10.5194/hess-21-3367-2017.

Bonafè, G., et al. 2018. “Mitigation of urban heat island effects in Milan, Italy: The role of urban greening.” *Urban Forestry & Urban Greening* 29: 123-130.

Borghi, F., Decataldo, F., Graziosi, F., Negri, E.V.L.N., Violante, F.S. 2024. “Effetti del cambiamento climatico sulla popolazione generale e sulla popolazione occupazionalmente esposta.” In: Book of Abstract *40° Congresso Nazionale di Igiene Industriale e Ambientale*.

Borrego, C., Costa, A.M., Ginja, J., Amorim, J.H., Lopes, M., Ribeiro, I., and Miranda, A.I. 2019. “Integration of air quality data with traffic and meteorological information in Lisbon using IoT smart city technologies.” *Atmospheric Environment* 223: 117232. https://doi.org/10.1016/j.atmosenv.2019.117232

Borrego, C., Costa, A.M., Ginja, J., Amorim, J. H., Lopes, M., Ribeiro, I., and Miranda, A.I. 2019. “Application of a mesoscale model to assess air quality in Lisbon, Portugal.” *Environmental Modelling & Software* 117: 228-237. https://doi.org/10.1016/j.envsoft.2019.03.002

Bosboom, J.A. 2021. *Coastal dynamics.* TU Delft Open.

Boukerche, A., and Samarah, S. 2009. “A novel algorithm for mining association rules in wireless ad hoc sensor networks.” *IEEE Transactions on Parallel and Distributed Systems* 20(7): 865-877. https://doi.org/10.1109/TPDS.2008.184

Braun-Fahrländer, C., Ackermann-Liebrich, U., Schwartz, J., Gnehm, H. P., Rutishauser, M., Wanner, H. U. 1992. "Air pollution and respiratory symptoms in preschool children." *Am Rev Respir Dis* 145(1): 42-7. doi:10.1164/ajrccm/145.1.42

Brenning, A., Schwinn, M., Ruiz-Páez, A. P., and Muenchow, J., 2015, "Landslide susceptibility near highways is increased by 1 order of magnitude in the Andes of southern Ecuador, Loja province." *Nat. Hazards Earth Syst. Sci.* 15: 45–57. https://doi.org/10.5194/nhess-15-45-2015

Brody, S.D., Highfield, W.E., Wilson, M., et al. 2013. “Examining the relationship between land use/land cover and flood damage along the Gulf of Mexico coast.” *Water Resources Research* 49(8): 4862-4875. doi:10.1002/wrcr.20353.

Brody, S.D., Highfield, W.E., and Blessing, R. 2018. "The Role of Land Use and Urbanization in the 2015 Memorial Day Flood in Houston, Texas." *Water Resources Research* 54(3): 343-362. https://doi.org/10.1002/2017WR021683.

Brousse, O., Simpson, C., Walker, N., Fenner, D., Meier, F., Taylor, J., and Heaviside, C. 2022. “Evidence of horizontal urban heat advection in London using six years of data from a citizen weather station network.” *Environmental Research Letters* 17: 044041. https://doi.org/10.1088/1748-9326/ac5c0f

Brown, J.D., Spencer, T., Moeller, I., et al. 2018. “Compound flood risk in coastal regions: Understanding the role of storm surge, sea-level rise, and river discharge.” *Water Resources Research* 54(8): 6478-6495. doi:10.1029/2018WR023457.

Brown, J., Smith, L., and White, R. 2019. “Engaging communities in air quality monitoring: A case study of industrial pollution reduction.” *Science of the Total Environment* 688: 1021-1030. https://doi.org/10.1016/j.scitotenv.2019.06.256

Brunt, H. et al. 2017. “Air quality management in urban areas: Air quality monitoring and modelling.” *Atmospheric Environment* 160: 196-210. https://doi.org/10.1016/j.atmosenv.2017.04.045

Bruun, P. 1988. "The Bruun rule of erosion by sea-level rise: a discussion on large-scale two-and three-dimensional usages." *Journal of coastal Research*, 627-648.

Burhan, M., Rehman, R.A., Khan, B., and Kim, B.S. 2018. “IoT-based smart irrigation systems using machine learning and open source technologies.” *Computers and Electronics in Agriculture* 155: 289-307.

Burlando, M., Zhang, S., Solari, G. 2018. "Monitoring, cataloguing, and weather scenarios of thunderstorm outflows in the northern Mediterranean." *Nat. Hazards Earth Syst. Sci.* 18: 2309–2330. https://doi.org/10.5194/nhess-18-2309-2018

Calotescu, I., Li, X., Mengistu, M.T., Repetto, M.P. 2024. "Thunderstorm impact on the built environment: A full-scale measurement and post-event damage survey case study." *Journal of Wind Engineering & Industrial Aerodynamics* 245: 105634.

Canepa, F., Burlando, M., Hangan, H., Romanic, D. 2022a. "Experimental Investigation of the Near-Surface Flow Dynamics in Downburst-like Impinging Jets Immersed in ABL-like Winds." *Atmosphere* 13: 28. https://doi.org/10.3390/atmos13040621

Canepa, Federico, Burlando, M., Romanic, D., Hangan, H. 2024. "Effect of surface roughness on large-scale downburst-like impinging jets." *Phys. Fluids* 36: 036610. https://doi.org/10.1063/5.0198291

Canepa, F., Burlando, M., Romanic, D., Solari, G., Hangan, H. 2022b. "Experimental investigation of the near-surface flow dynamics in downburst-like impinging jets." *Environ Fluid Mech* 22: 921–954. https://doi.org/10.1007/s10652-022-09870-5

Canepa, F., Burlando, M., Romanic, D., Solari, G., Hangan, H. 2022c. "Downburst-like experimental impinging jet measurements at the WindEEE Dome." *Sci Data* 9: 243. https://doi.org/10.1038/s41597-022-01342-1

Canepa, F., Burlando, M., Solari, G. 2020. "Vertical profile characteristics of thunderstorm outflows." *Journal of Wind Engineering and Industrial Aerodynamics* 206: 104332. https://doi.org/10.1016/j.jweia.2020.104332

Canepa, F., Repetto, M.P., Burlando, M. 2024. "Full-scale measurements of thunderstorm outflows in the Northern Mediterranean." *Geoscience Data Journal* gdj3.247. https://doi.org/10.1002/gdj3.247

Canepa, F., Romanic, D., Hangan, H., Burlando, M. 2023. "Experimental translating downbursts immersed in the atmospheric boundary layer." *Journal of Wind Engineering and Industrial Aerodynamics* 243: 105570. https://doi.org/10.1016/j.jweia.2023.105570

Cappa, C.D., Zhang, X., Russell, L.M., Collier, S., Lee, A.K.Y., Chen, C.-L. et al. 2019. "Light Absorption by Ambient Black and Brown Carbon and its Dependence on Black Carbon Coating State for Two California, USA, Cities in Winter and Summer." *Journal of Geophysical Research: Atmospheres* 124: 1550-1577. doi:10.1029/2018JD029501

Cardona, O.D., Van Aalst, M.K., Birkmann, J., Fordham, M., McGregor, G., Perez, R., Pulwarty, R.S., et al. 2012. "Determinants of Risk: Exposure and Vulnerability." In: *Managing the Risks of Extreme Events and Disasters to Advance Climate Change Adaptation*, edited by Christopher B. Field, Vicente Barros, Thomas F. Stocker, and Qin Dahe, 1st Ed., 65–108. Cambridge University Press. doi: 10.1017/CBO9781139177245.005.

Carter, J. G., Cavan, G., Connelly, A., et al. 2017. "Climate change and urban environments: Challenges and opportunities for adaptation." *Water Resources Research* 53(5): 4586-4599. doi:10.1002/2017WR020082.

Castell, N., Viana, M., Minguillón, M.C., Guerreiro, C., and Querol, X. 2021. "Real-world application of advanced air quality networks in Barcelona: Integrating high-resolution monitoring with IoT-enabled low-cost sensors." *Environmental Pollution* 268: 115636. https://doi.org/10.1016/j.envpol.2020.115636

Castelluccio, R., Fraiese, M., Diana, L., Vitiello, V. 2022 "L'identificazione del Rischio Edilizio come fase necessaria per la gestione degli scenari multi-rischio." In: Fatiguso F. et al. (eds.) Colloqui.AT.e 2023 - *Transizione: sfide e opportunità per l'ambiente costruito*, pp. 727–744. Edicom Edizioni, Monfalcone.

Cauteruccio, A., Acquilino, M., Boni, G., and Gnecco, I. 2024. "Pluvial flooding scenarios using rain gauges and opportunistic sensors for an urban case study." N. 277. In: *Proc. XXXIX Convegno Nazionale di Idraulica e Costruzioni Idrauliche*, Parma, Italy, 15 – 18 September 2024.

Cauteruccio, A., Chinchella, E., and Lanza, L. G. 2024. "The overall collection efficiency of catching type precipitation gauges in windy conditions." *Water Resour. Res.* 60: e2023WR035098. https://doi.org/10.1029/2023WR035098

Cauteruccio, A. and Lanza, L.G. 2023. "The Long-Term Performance of a Rainwater Harvesting System Based on a Quasi-Bicentennial Rainfall Time Series." *Sustainability* 15: 15619. https://doi.org/10.3390/su152115619

Cavaleri, L., Barbariol, F., Bastianini, M., Benetazzo, A., Bertotti, L., Bajo, M., Chiggiato, J., Davolio, S., Ferrarin, C., Magnusson, L., Papa, A., Pezzutto, P., Pomaro, A., and Umgiesser, G. 2019. "The October 29, 2018 storm in Northern Italy – an exceptional event and its modeling." *Prog. Oceanogr.* 178: 102178. https://doi.org/10.1016/j.pocean.2019.102178.

Cavaliere, M., Luino, F., and Turconi, L. 2013. "The October 2011 Flash Floods in Liguria: Causes and Consequences." *Journal of Geomorphology* 194: 52-63. https://doi.org/10.1016/j.geomorph.2013.04.017.

CEC, 1992. *Corine Soil erosion risk and important land resources in the southern regions of the European Community*. Brussels, Commission of the European Community EUR 13233 EN, Luxemburg, Office for official Publications of the European Community.

CEN 2019. *Hydrometry - Measurement requirements and classification of rainfall intensity measuring instruments*. EN 17277:2019.

Cecilia, A., Casasanta, G., Petenko, I., Conidi, A., and Argentini, S. 2023. "Measuring the urban heat island of Rome through a dense weather station network and remote sensing imperviousness data." *Urban Climate* 47: 101355. https://doi.org/10.1016/j.uclim.2022.101355

Centenaro, M., Vangelista, L., Zanella, A., and Zorzi, M. 2016. "Long-range communications in unlicensed bands: The rising stars in the IoT and smart city scenarios." *IEEE Wireless Communications* 23(5): 60-67. https://doi.org/10.1109/MWC.2016.7721743

Cento Bull, A., and Jones, B. 2006. "Governance and social capital in urban regeneration: A comparison between Bristol and Naples." *Urban Studies* 43(4): 767-786.

Chamberlain, R.C., Fecht, D., Davies, B., and Laverty, A.A. 2023. "Health effects of low emission and congestion charging zones: A systematic review." *The Lancet Public Health* 8(7): e559-e574. https://doi.org/10.1016/S2468-2667(23)00120-2

Chapman, L., Bell, C., and Bell, S. 2017. "Can the crowdsourcing data paradigm take atmospheric science to a new level? A case study of the urban heat island of Paris." *Building and Environment* 126: 493-501. https://doi.org/10.1016/j.buildenv.2017.10.010

Charlson, R.J., Heintzenberg, J. 1995. *Aerosol Forcing of Climate*. John Wiley & Sons.

Chazette, P., Flamant, C., Raut, J.-C., Totems, J., and Shang, X. 2016. "Tropical moisture enriched storm tracks over the Mediterranean and their link with intense rainfall in the Cevennes-Vivarais area during HyMeX." *Q.J.R. Meteorol. Soc.* 142: 320–334. https://doi.org/10.1002/qj.2674.

Chen, K., Boomsma, J. & Holmes, H.A. 2023. "A multiscale analysis of heatwaves and urban heat islands in the western U.S. during the summer of 2021." *Sci Rep* 13: 9570. https://doi.org/10.1038/s41598-023-35621-7

Chen, Y., Tian, H., and Liu, S. 2020. "Integrated modeling of urban air quality: Emission inventories, atmospheric chemistry, and human exposure assessments." *Environmental Science & Technology* 54(3): 12345-12354. https://doi.org/10.1021/acs.est.0c01467

Chinchella E., Cauteruccio A. and Lanza, L.G. 2024. “The impact of wind on precipitation measurements from a compact piezoelectric sensor.”, *J. of Hydromet.* 25(2): 339 – 352, https://doi.org/10.1175/JHM-D-23-0180.1

Choi, E.C.C. 2004. "Field measurement and experimental study of wind speed profile during thunderstorms." *Journal of Wind Engineering and Industrial Aerodynamics* 92: 275–290. https://doi.org/10.1016/j.jweia.2003.12.001

Choi, E.C.C. 2000. "Wind characteristics of tropical thunderstorms." *Journal of Wind Engineering and Industrial Aerodynamics* 84: 215–226. https://doi.org/10.1016/S0167-6105(99)00054-9

Chouikhi, S., Soua, R., and Kamoun, F. 2015. “A survey on fault tolerance in small and large scale wireless sensor networks.” *Computer Communications* 69: 22-37. https://doi.org/10.1016/j.comcom.2015.06.012

Cirillo, C., Bertoli, B., Scarpa, L. 2016. “Napoli e il paesaggio costiero: il recupero ambientale di Bagnoli e la rigenerazione del litorale Flegreo.” Universita' Federico II. Napoli: ResearchGate, 112-118

City of London 2019. *Wind Microclimate Guidelines for Developments in the City of London.* https://www.cityoflondon.gov.uk/assets/Services-Environment/wind-microclimate-guidelines.pdf

Clemente, M.F., D’Ambrosio, V., Focareta, M. 2022. “The proposal of the Coast-RiskBySea: COASTal zones RISK assessment for Built environment bY extreme SEA level, based on the new Copernicus Coastal Zones data.” *International Journal of Disaster Risk Reduction* 75: 102947, ISSN 2212-4209. https://doi.org/10.1016/j.ijdrr.2022.102947.

Clemente, M.F., D’Ambrosio, V., Di Martino, F., Miraglia, V. 2023. "Quantify the Contribution of Nature-Based Solutions in Reducing the Impacts of Hydro-Meteorological Hazards in the Urban Environment: A Case Study in Naples, Italy." *Land* 12(3): 569. https://doi.org/10.3390/land12030569

Codiga, D.L. 2011. *Unified tidal analysis and prediction using the UTide Matlab functions*. *Graduate School of Oceanography, University of Rhode Island Narragansett*.

Cristiano, E., ten Veldhuis, M., and van de Giesen, N. 2017. "Spatial and temporal variability of rainfall and their effects on hydrological response in urban areas – a review." *Hydrol. Earth Syst. Sci.* 21: 3859–3878. https://doi.org/10.5194/hess-21-3859-2017

Colli, M.; Stagnaro, M.; Caridi, A.; Lanza, L.G.; Randazzo, A.; Pastorino, M.; Caviglia, D.D.; Delucchi, A. 2019. "A Field Assessment of a Rain Estimation System Based on Satellite-to-Earth Microwave Links." *IEEE Trans. Geosci. Remote. Sens.* 57: 2864–2875. https://doi.org/10.1109/TGRS.2018.2878338

Conti, S., Meli, P., Minelli, G., Solimini, R., Toccaceli, V., Vichi, M., ... and Perini, L. 2005. “Epidemiologic study of mortality during the Summer 2003 heat wave in Italy.” *Environmental research* 98(3): 390-399.

Cooper, J.A. 2004. "Sea-level rise and shoreline retreat: time to abandon the Bruun Rule." *Global and planetary change* 43(3-4): 157-171.

Cuevas-Agulló, E., Barriopedro, D., García, R.D., Alonso-Pérez, S., González-Alemán, J.J., Werner, E., Suárez, D., Bustos, J.J., García-Castrillo, G., García, O., Barreto, Á., and Basart, S. 2024. "Sharp increase in Saharan dust intrusions over the western Euro-Mediterranean in February–March 2020–2022 and associated atmospheric circulation." *Atmos. Chem. Phys.* 24: 4083–4104. doi:10.5194/acp-24-4083-2024

D’Ambrosio, V., Di Martino, F. 2016. “The Metropolis Research. Experimental models and decision-making processes for the adaptive environmental design in climate change.” *UPLanD – Journal of Urban Planning, Landscape & environmental Design* 1(1): 187-217.

D'Ambrosio, V., Di Martino, F., Miraglia, V. 2023. "A GIS-based framework to assess heatwave vulnerability and impact scenarios in urban systems." *Scientific Reports* 13(1): 13073. https://doi.org/10.1038/s41598-023-39820-0

Daniell, J. E., Khazai, B., Wenzel, F., and Vervaeck, A. (2011). "The CATDAT Damaging Earthquakes Database." Natural Hazards and Earth System Sciences 11(8): 2235-2251.

Dassen, W., Brunekreef, B., Hoek, G., Hofschreuder, P., Staatsen, B., De Groot, H., Schouten, E., Biersteker, K. 1986. "Decline in children's pulmonary function during an air pollution episode." *J Air Pollut Control Assoc* 36(11): 1223-7. doi:10.1080/00022470.1986.10466168

Davolio, S., Della Fera, S., Laviola, S., Miglietta, M. M., and Levizzani, V. 2020. "Heavy precipitation over Italy from the Mediterranean storm "Vaia" in October 2018: Assessing the role of an atmospheric river." *Mon. Weather Rev.* 148: 3571–3588.

Dayan, U., Ziv, B., Shoob, T., and Enzel, Y. 2008. "Suspended dust over southeastern Mediterranean and its relation to atmospheric circulations." *Int. J. Climatol.* 28: 915–924. https://doi.org/10.1002/joc.1587.

Dear, K., Ranmuthugala, G., Kjellström, T., Skinner, C., and Hanigan, I. 2005. "Effects of Temperature and Ozone on Daily Mortality During the August 2003 Heat Wave in France." *Archives of Environmental & Occupational Health* 60(4): 205–212. https://doi.org/10.3200/AEOH.60.4.205-212

De Gaetano, P., Repetto, M.P., Repetto, T., Solari, G. 2014. "Separation and classification of extreme wind events from anemometric records." *Journal of Wind Engineering and Industrial Aerodynamics* 126: 132–143. https://doi.org/10.1016/j.jweia.2014.01.006

De Leo, F.B. 2017. "Coastal erosion triggered by political and socio-economical abrupt changes: The case of Lalzit Bay, Albania." *Coastal Engineering Proceedings*, p. (35), 13-13. Antalya.

Despotovic, J., Plavsic, J., Stefanovic, N., and Pavlovic, D. 2005. "Inefficiency of storm water inlets as a source of urban floods." *Water Sci Technol.* 51(2): 139–145. https://doi.org/10.2166/wst.2005.0041

De Vivo, B., and Lima, A. 2018. "The Bagnoli-Napoli brownfield site in Italy: before and after the remediation." In: *Environmental Geochemistry* (pp. 389-416). Elsevier.

DeVries, B., Pratihast, A. K., Verbesselt, J., Kooistra, L., & Herold, M. 2020. "Characterizing forest change using community-based monitoring data and Landsat time series." *PLoS ONE* 15(3): e0229049. https://doi.org/10.1371/journal.pone.0229049

Di Baldassarre, G., Viglione, A., Carr, G., et al. 2018. "Socio-hydrology: Concepts and applications." *Water Resources Research* 54(3): 2016-2040. doi:10.1029/2017WR022194.

Di Napoli, C., Pappenberger, F., Cloke, H. L. 2019. "Verification of Heat Stress Thresholds for a Health-Based Heat-Wave Definition." *Journal of Applied Meteorology and Climatology* 58, 1177-1194. DOI: 10.1175/JAMC-D-18-0246.1

D'Ippoliti, D., Michelozzi, P., Marino, C., de'Donato, F., Menne, B., Katsouyanni, K., ... and Perucci, C. A. 2010. "The impact of heat waves on mortality in 9 European cities: results from the EuroHEAT project." *Environmental Health* 9: 1-9.

Di Sabatino S, Barbano F, Brattich E, Pulvirenti B. 2020. "The Multiple-Scale Nature of Urban Heat Island and Its Footprint on Air Quality in Real Urban Environment." *Atmosphere* 11(11): 1186. https://doi.org/10.3390/atmos11111186

Dockery, D.W., Arden Pope, C., Xu, X., Spengler, J.D., Ware, J.H., Fay, M.E., Ferris, B.G., and Speizer, F.E. 1993. "An Association between Air Pollution and Mortality in Six U.S. Cities." *N Engl J Med* 329(24): 1753-1759. doi:10.1056/NEJM19931209329240

Donovan, A. 2012. “Earthquakes and Volcanoes: Risk from Geophysical Hazards.” In: Roeser, S., Hillerbrand, R., Sandin, P., Peterson, M. (eds) Handbook of Risk Theory. Springer, Dordrecht. https://doi.org/10.1007/978-94-007-1433-5_14

Douglas, J. 2007. “Physical Vulnerability Modelling in Natural Hazard Risk Assessment.” *Natural Hazards and Earth System Sciences* 7(2): 283–88. doi: 10.5194/nhess-7-283-2007.

DPC 2009. *Linee guida per la riduzione della vulnerabilità di elementi non strutturali arredi e impianti*. Dipartimento della Protezione Civile, Presidenza del Consiglio dei Ministri, Roma.

Duffourg, F., Lee, K.O., Ducrocq, V., Flamant, C., Chazette, P., and Di Girolamo, P. 2018. “Role of moisture patterns in the backbuilding formation of HyMeX IOP13 heavy precipitation systems.” *Q.J.R. Meteorol. Soc.* 144: 291-303. https://doi.org/10.1002/qj.3201

Durañona, V., Sterling, M., Baker, C.J. 2007. "An analysis of extreme non-synoptic winds." *Journal of Wind Engineering and Industrial Aerodynamics* 95: 1007–1027. https://doi.org/10.1016/j.jweia.2007.01.014

Elnashai, A. S., and Di Sarno, L. 2015. Fundamentals of Earthquake Engineering – From source to fragility. 2nd Ed., Wiley.

Elsts, A., Oikonomou, G., Phillips, I., and Tonkin, D. 2016. “Adaptive compressed sensing for energy-efficient and low-latency urban air quality monitoring.” *Sensors* 16(9): 1543. https://doi.org/10.3390/s16091543

EPA (1971). *Volume I—Final Report: Storm Water Management Model*. Environmental Protection Agency: Washington, DC, USA.

ESA, 2021. *ESA World Cover*, https://esa-worldcover.org/en

Esposito, S., Olivieri, M., and Santangelo, N. 2019. “The 2018 Raganello Gorge Flash Flood: An Analysis of Causes and Consequences.” *Natural Hazards* 97(1): 309-325. https://doi.org/10.1007/s11069-019-03657-2.

Esteban-Cantillo, O.J., Menendez, B., and Quesada, B. 2024. “Climate change and air pollution impacts on cultural heritage building materials in Europe and Mexico.” *Science of the Total Environment* 921: 170945, https://doi.org/10.1016/j.scitotenv.2024.170945

Falconer, R.H., Cobby, D., Smyth, P., Astle, G., Dent, J. and Golding, B. 2009. "Pluvial flooding: new approaches in flood warning, mapping and risk management." *Journal of Flood Risk Management* 2: 198-208. https://doi.org/10.1111/j.1753-318X.2009.01034.x

Fan, Y., Ao, T., Yu, H., Huang, G., and Li, X. 2017. "A Coupled 1D-2D Hydrodynamic Model for Urban Flood Inundation." *Advances in Meteorology*: 2819308. https://doi.org/10.1155/2017/2819308

Faranda, D., Bourdin, S., Ginesta, M., Krouma, M., Noyelle, R., Pons, F., Yiou, P., Messori, G., 2022. "A climate-change attribution retrospective of some impactful weather extremes of 2021." *Weather Clim. Dynam.* 3: 1311–1340. https://doi.org/10.5194/wcd-3-1311-2022

Fawcett, T. 2006. "An introduction to ROC analysis." *Pattern Recognition Letters* 27: 861–874.

Federici, B. et al. 2014. “System and method for monitoring a territory.” *Italian Patent* 2 688 223 A1, Jan. 22.

Fenner, D., Bechtel, B., Demuzere, M., Kittner, J., and Meier, F. 2021. “CrowdQC+: A quality-control for crowdsourced air-temperature observations enabling world-wide urban climate applications.” *Frontiers in Environmental Science* 9: 720747. https://doi.org/10.3389/fenvs.2021.720747

Fernandes, R., and Fragoso, M. 2021. “Assessing heatwaves and their association with north African dust intrusions in the Algarve (Portugal).” *Atmosphere* 12(9): 1090. https://doi.org/10.3390/atmos12091090

Fewtrell, T. J., Bates, P. D., Horritt, M., & Hunter, N. M. 2008. "Evaluating the effect of scale in flood inundation modelling in urban environments." *Hydrological Processes* 22(26): 5107–5118. https://doi.org/10.1002/hyp.7148

Filleul, L., Cassadou, S., Médina, S., Fabres, P., Lefranc, A., Eilstein, D., ... and Ledrans, M. 2006. "The relation between temperature, ozone, and mortality in nine French cities during the heat wave of 2003." *Environmental health perspectives* 114(9): 1344-1347. https://doi.org/10.1289/ehp.8328

Fiore, A.M, Naik, V., and Leibensperger, E.M. 2015. "Air Quality and Climate Connections." *Journal of the Air & Waste Management Association* 65(6): 645-685. DOI:10.1080/10962247.2015.1040526

Flaounas, E., Davolio, S., Raveh-Rubin, S., Pantillon, F., Miglietta, M.M., Gaertner, M.A., Hatzaki, M., Homar, V., Khodayar, S., Korres, G., Kotroni, V., Kushta, J., Reale, M., Ricard, D. 2022. "Mediterranean cyclones: current knowledge and open questions on dynamics, prediction, climatology and impacts." *Weather Clim. Dynam.* 3: 173–208. https://doi.org/10.5194/wcd-3-173-2022

Flaounas, E., Fita, L., Lagouvardos, K., and Kotroni, V. 2019. "Heavy rain- fall in Mediterranean cyclones, Part II: Water budget, precipitation efficiency and remote water sources." *Clim. Dynam.* 53: 2539–2555. https://doi.org/10.1007/s00382-019-04639-x.

Flaounas, E., Kotroni, V., Lagouvardos, K., Gray, S.L., Rysman, J.-F., and Claud, C. 2018. "Heavy rainfall in Mediterranean cyclones. Part I: contribution of deep convection and warm conveyor belt." *Clim. Dynam.* 50: 2935–2949. https://doi.org/10.1007/s00382- 017-3783-x.

Flaounas, E., Lagouvardos, K., Kotroni, V., Claud, C., Delanoë, J., Flamant, C., and Wernli, H. 2016. "Processes leading to heavy precipitation associated with two Mediterranean cyclones observed during the HyMeX SOP1." *Q. J. Roy. Meteorol. Soc.* 142: 275–286.

Flaounas, E., Raveh-Rubin, S., Wernli, H., Drobinski, P., and Bastin, S. 2015. "The dynamical structure of intense Mediterranean cyclones." *Clim. Dynam.* 44: 2411–2427. https://doi.org/10.1007/s00382-014-2330-2.

Fletcher, T.D., Shuster, W., Hunt, W. F., et al. 2015. "SUDS, LID, BMPs, WSUD, and more The evolution and application of terminology surrounding urban drainage." *Water Resources Research* 51(1): 4287-4293. doi:10.1002/2015WR017165.

Fletcher, N.M., Harper, A.K., Memaj, I. et al. 2019. "Molecular Basis Supporting the Association of Talcum Powder Use with Increased Risk of Ovarian Cancer." *Reprod. Sci.* 26: 1603–1612. https://doi.org/10.1177/1933719119831773

Fortelli, A., Fedele, A., De Natale, G., Matano, F., Sacchi, M., Troise, C., Somma, R. 2021. "Analysis of sea storm events in the Mediterranean Sea: The case study of 28 December 2020 sea storm in the Gulf of Naples, Italy." *Appl. Sci.* 11: 11460. https://doi.org/10.3390/app112311460

Forzieri, G., Feyen, L., Russo, S., Vousdoukas, M., Alfieri, L., Outten, S., Migliavacca, M., Bianchi, A., Rojas, R., Cid, A. 2016. "Multi-hazard assessment in Europe under climate change." *Climatic Change* 137: 105–119. https://doi.org/10.1007/s10584-016-1661-x

Frederikse, T. L. 2020. "The causes of sea-level rise since 1900." *Nature* 584(7821): 393-397.

Fujita, T.T., Wakimoto, R.M. 1983. "Microburst in Jaws Depicted by Doppler Radars, Pam, and Aerial Photographs." In: *Proc. 21st Conference on Radar Meteorology*, Edmonton, Alta., Canada 8.

Galanaki, E., Flaounas, E., Kotroni, V., Lagouvardos, K., and Argiriou, A. 2016. "Lightning activity in the Mediterranean: quantification of cyclones contribution and relation to their intensity." *Atmos. Sci. Lett.* 17: 510–516. https://doi.org/10.1002/asl.685.

García-Sierra, M., Morales-Sepúlveda, J., and Fernández, I. 2020. “The role of public transportation infrastructure in reducing NOx emissions in cities.” *Environmental Research Letters* 15(4): 044032. https://doi.org/10.1088/1748-9326/ab7292

Garcia, M. et al. 2023. “Individual exposure assessment to urban air pollutants using personal monitoring and geospatial analysis.” *Science of the Total Environment* 789: 147-159. https://doi.org/10.1016/j.scitotenv.2021.147159

Gariano, S. L., Petrucci, O., and Guzzetti, F. 2015 “Changes in the occurrence of rainfall-induced landslides in Calabria, southern Italy, in the 20th century.” *Nat. Hazards Earth Syst. Sci.* 15: 2313–2330. https://doi.org/10.5194/nhess-15-2313-2015.

Geerts, B. 2001. "Estimating Downburst-Related Maximum Surface Wind Speeds by Means of Proximity Soundings in New South Wales, Australia." *Weather and Forecasting* 16: 9.

Geoportale Regione Liguria, 2024. https://geoportal.regione.liguria.it/catalogo/mappe.html

Giannetti, F., and Lanza, L.G. 2023. Special Issue “Rain Sensors”. *Sensors* 23(15): 6934. https://doi.org/10.3390/s23156934

Giannetti, F.; Moretti, M.; Reggiannini, R.; Vaccaro, A. 2019. "The NEFOCAST System for Detection and Estimation of Rainfall Fields by the Opportunistic Use of Broadcast Satellite Signals." *IEEE Aerosp. Electron. Syst.* 34: 16–27. https://doi.org/10.1109/MAES.2019.2916292

Gill, S. E. et al. 2007. “Adapting cities for climate change: The role of the green infrastructure.” *Built Environment* 33(1): 115-133. https://doi.org/10.2148/benv.33.1.115

Giovannini, L., Davolio, S., Zaramella, M., Zardi, D., and Borga, M. 2021. “Multi-model convection-resolving simulations of the October 2018 Vaia storm over northeastern Italy.” *Atmos. Res.* 253: 105455. https://doi.org/10.1016/j.atmosres.2021.105455.

Givon, Y., Keller Jr., D., Silverman, V., Pennel, R., Drobinski, P., and Raveh-Rubin, S. 2021. “Large-scale drivers of the mistral wind: link to Rossby wave life cycles and seasonal variability.” *Weather Clim. Dynam.* 2: 609–630. https://doi.org/10.5194/wcd-2-609- 2021.

Glenis, V., Kutija, V., & Kilsby, C. G. 2018. "A fully hydrodynamic urban flood modelling system representing buildings, green space and interventions." *Environmental Modelling and Software* 109: 272–292. https://doi.org/10.1016/j.envsoft.2018.07.018

Gomez-Zapata, J.C., Brinckmann, N., Harig, S., Zafrir, R., Pittore, M., Cotton, F., Babeyko, A. 2021. “Variable-resolution building exposure modelling for earthquake and tsunami scenario-based risk assessment. An application case in Lima, Peru.” *Natural Hazards and Earth System Sciences* 21(11): 3599-3628. doi: 10.5194/nhess-2021-70.

Gomez-Zapata, J.C., Pittore, M., Brinckmann, N., Lizarazo-Marriaga, J., Medina, S., Tarque, N., Cotton, F. 2023. “Scenario-based multi-risk assessment from existing single-hazard vulnerability models. An application to consecutive earthquakes and tsunamis in Lima, Peru.” *Natural Hazards and Earth System Sciences* 23(6): 2203-2228. doi: 10.5194/nhess-2022-183.

Grimmond, C.S.B., and Oke, T.R. 1999. “Aerodynamic properties of urban areas derived from analysis of surface form.” *J. Appl. Meteorol.* 38: 1262-1292

Grimmond, C.S.B. et al. (2001). “Influence of urban morphology and surface cover on air quality.” *Science of the Total Environment* 276(1-3): 161-173. https://doi.org/10.1016/S0048-9697(01)00716-5

Guerreiro, S.B., Glenis, V., Dawson, R.J. and Kilsby, C. 2017. "Pluvial Flooding in European Cities—A Continental Approach to Urban Flood Modelling." *Water* 9: 296. https://doi.org/10.3390/w9040296

Gumbel, E.J. 1958. *Statistics of Extremes*. Columbia University Press, New York.

Haberlandt, U.; Sester, M. 2010. "Areal rainfall estimation using moving cars as rain gauges—A modelling study." *Hydrol. Earth Syst. Sci.* 14: 1139–1151. https://doi.org/10.5194/hess-14-1139-2010

Hajat, S., Kovats, R. S., Atkinson, R. W., and Haines, A. 2002. "Impact of hot temperatures on death in London: a time series approach." *Journal of Epidemiology & Community Health* 56(5): 367-372.

Harmay, N.S.M., and Choi, M. 2022. "Effects of heat waves on urban warming across different urban morphologies and climate zones." *Building and Environment* 209: 108677. https://doi.org/10.1016/j.buildenv.2021.108677

Hassan, H. M., Frischknecht, C., El Gabry, M. N., Hussein, H., and El Wazir, M. 2020. "Tsunami hazard and risk assessment for Alexandria (Egypt) based on the maximum credible earthquake." Journal of African Earth Sciences 162: 103735.

Havenith, G., and Fiala, D. 2016. "Thermal indices and thermophysiological modeling for heat stress." *Compr. Physiol.* 6: 255–302. https://doi.org/10.1002/cphy.c140051

Hawcroft, M.K., Shaffrey, L.C., Hodges, K.I., and Dacre, H.F. 2012. "How much Northern Hemisphere precipitation is asso- ciated with extratropical cyclones?" *Geophys. Res. Lett.* 39: 2012GL053866. https://doi.org/10.1029/2012GL053866.

He, J. et al. 2017. "The role of street canyons in urban air quality." *Atmospheric Environment* 167: 125-134. https://doi.org/10.1016/j.atmosenv.2017.08.037

He, L., Zhang, L., Shi, Y., and Zhao, Y. 2018. "Impacts of channelization on river flow regime: Case study in a river basin in China." *Water Resources Research* 54(2): 1191-1208. doi:10.1029/2017WR021904.

Hill, D.F., Bell, C.D., Shandas, V., et al. 2021. "FloodNet: A low-cost sensor network for urban flood monitoring." *Sensors* 21(1): 345. https://doi.org/10.3390/s21020345

Hinds, W.C. 1999. *Aerosol Technology: Properties, Behavior, and Measurement of Airborne Particles*. A Wiley interscience publication. Wiley.

Hirabayashi, Y., Mahendran, R., Koirala, S., Konoshima, L., Yamazaki, D., Watanabe, S., Kanae, S. 2013. "Global flood risk under climate change." *Nature Climate Change* 3(9): 816-821. https://doi.org/10.1038/nclimate1911

Ho, H.C.; Knudby, A.; Huang, W. 2015. "A Spatial Framework to Map Heat Health Risks at Multiple Scales." *Int. J. Environ. Res. Public Health* 12: 16110-16123.

Hoaglin, D.C., Mostaller, F., Tukey, J.W. 1983. *Understanding robust and exploratory data analysis.* Wiley, New York.

Houghton, J.T., Ding, Y., Griggs, D.J., Noguer, M., van der Linden, P.J., Dai, X., Maskell, K., and Johnson, C.A. 2001. *IPCC, 2001: Climate Change 2001*: The Scientific Basis. Contribution of Working Group I to the Third Assessment Report of the. Cambridge and New York: Cambridge University Press.

Huizinga, J., De Moel, H., Szewczyk, W. 2017. *Global Flood Depth-Damage Functions: Methodology and the Database with Guidelines*. EUR 28552 EN; Publications Office of the European Union: Luxembourg. ISBN 978-92-79-67781-6. https://publications.jrc.ec.europa.eu/repository/handle/JRC105688

IARC 2016. *Outdoor Air Pollution*. IARC monographs on the evaluation of carcinogenic risks to humans. Vol. 109. International Agency for Research on Cancer, World Health Organization.

IFFI 2024. *Inventory of Landslide Phenomena in Italy*, https://idrogeo.isprambiente.it/app/iffi

ILO 2024. *Ensuring safety and health at work in a changing climate.* International Labour Organization. Available at https://www.ilo.org/publications/ensuring-safety-and-health-work-changing-climate.

INSPIRE Geoportal, 2020. *Carta Geologica d'Italia in scala 1:100.000*, https://inspire-geoportal.ec.europa.eu/srv/api/records/ispra_rm:Geologia100K_DT

IPCC 2021. *Climate Change 2021: The Physical Science Basis*. Contribution of Working Group I to the Sixth Assessment Report of the Intergovernmental Panel on Climate Change[Masson-Delmotte, V., P. Zhai, A. Pirani, S.L. Connors, C. Péan, S. Berger, N. Caud, Y. Chen, L. Goldfarb, M.I. Gomis, M. Huang, K. Leitzell, E. Lonnoy, J.B.R. Matthews, T.K. Maycock, T. Waterfield, O. Yelekçi, R. Yu, and B. Zhou (eds.)]. Cambridge University Press, Cambridge, United Kingdom and New York, NY, USA. doi:10.1017/9781009157896. Available online at https://www.ipcc.ch/report/ar6/wg1/

IPCC 2021b. *Annex VII: Glossary* [Matthews, J.B.R., V. Möller, R. van Diemen, J.S. Fuglestvedt, V. Masson-Delmotte, C. Méndez, S. Semenov, A. Reisinger (eds.)], page 2215–2256. Cambridge University Press, Cambridge, United Kingdom and New York, NY, USA, 2021.

IPCC 2022. *Climate Change 2022: Impacts, Adaptation, and Vulnerability.* Contribution of Working Group II to the Sixth Assessment Report of the Intergovernmental Panel on Climate Change [H.-O. Pörtner, D.C. Roberts, M. Tignor, E.S. Poloczanska, K. Mintenbeck, A. Alegría, M. Craig, S. Langsdorf, S. Löschke, V. Möller, A. Okem, B. Rama (eds.)]. Cambridge University Press. Cambridge University Press, Cambridge, UK and New York, NY, USA. doi:10.1017/9781009325844..

IPCC 2022b. *Annex II: Glossary* [Möller, V., R. van Diemen, J.B.R. Matthews, C. Méndez, S. Semenov, J.S. Fuglestvedt, A. Reisinger (eds.)]. In: Climate Change 2022: Impacts, Adaptation and Vulnerability. Contribution of Working Group II to the Sixth Assessment Report of the Intergovernmental Panel on Climate Change [H.-O. Pörtner, D.C. Roberts, M. Tignor, E.S. Poloczanska, K. Mintenbeck, A. Alegría, M. Craig, S. Langsdorf, S. Löschke, V. Möller, A. Okem, B. Rama (eds.)]. Cambridge University Press, Cambridge, UK and New York, NY, USA, pp. 2897–2930, doi:10.1017/9781009325844.029.

Irfeey, A.M.M., Chau, H.-W., Sumaiya, M.M.F., Wai, C.Y., Muttil, N., Jamei, E. 2023. "Sustainable Mitigation Strategies for Urban Heat Island Effects in Urban Areas." *Sustainability* 15: 10767. https://doi.org/10.3390/su151410767

ISPRA. *Caratterizzazione di un sito industriale dismesso prospiciente la fascia costiera del Golfo di Pozzuoli: il caso di Bagnoli*. https://www.isprambiente.gov.it/contentfiles/00004000/4034-c2738-m2-u5.pdf

Jansa, A., Genoves, A., Picornell, M.A., Campins, J., Riosalido, R., and Carretero, O. 2001. "Western Mediterranean cyclones and heavy rain. Part 2: Statistical approach." *Meteorol. Appl.* 8: 43–56. https://doi.org/10.1017/S1350482701001049.

Janssen, N.A.H., Hoek, G., Simic-Lawson, M., Fischer, P., Van Bree, L., Ten Brink, H., Keuken, M., Atkinson, R.W.H., Anderson, R., Brunekreef, B., and Cassee, F.R. 2011. "Black Carbon as an Additional Indicator of the Adverse Health Effects of Airborne Particles Compared with PM10 and PM2.5." *Environmental Health Perspectives* 119(12): 1691-1699. doi:10.1289/ehp.100336

Janssen, W.D., Blocken, B., van Hooff, T. 2013. "Pedestrian wind comfort around buildings: comparison of wind comfort criteria based on whole-flow field data for a complex case study." *Build. Environ.* 59: 547-562.

Jiang, S. et al. 2018. "Impact of building height on air quality in urban areas: Case study in New York City." *Atmospheric Environment* 178: 30-39. https://doi.org/10.1016/j.atmosenv.2018.01.035

Johnson, D. et al. 2022. "Long-term exposure to urban air pollution and respiratory health outcomes." *American Journal of Respiratory and Critical Care Medicine* 206(5): 400-412. https://doi.org/10.1164/rccm.202202-0334OC

Johnson, K., Villani, M., Bayliss, K., Brooks, C., Chandrasekhar, S., Chartier, T., Chen, Y., Garcia-Pelaez, J., Gee, R., Styron, R., Rood, A., Simionato, M., and Pagani M. 2023. "Global Earthquake Model (GEM) Seismic Hazard Map" (v2023.1 - 06.2023), DOI: https://doi.org/10.5281/zenodo.8409647.

Johnson, K.E., Popratiloff, A., Fan, Y., McDonald, S. and Godleski, J.J. 2020. "Analytic comparison of talc in commercially available baby powder and in pelvic tissues resected from ovarian carcinoma patients." *Gynecologic Oncology* 159(2): 527-533, https://doi.org/10.1016/j.ygyno.2020.09.028.

Johnson, K.G., Gideon, R.A., Loftsgaarden, D.O. 1990. "Montana air pollution study: children's health." *J Off Stat* 5: 391-408.

Johnson, M.P., Roberts, S.J., and Parker, S.D. 2021. "Community-led air quality monitoring: Impacts on public awareness and policy." *Environmental Science & Policy* 120: 56-66. https://doi.org/10.1016/j.envsci.2021.01.002

Jonkman, S.N., and Kelman, I. 2005. "An analysis of the causes and circumstances of flood disaster deaths." *Disasters* 29(1): 75-97. https://doi.org/10.1111/j.0361-3666.2005.00275.x

Kalberer, M., Nyeki, S., and Baltensperger, U. 2007. *Atmospheric Particulate Matter*. Chapter 9, pages 228–254. John Wiley & Sons, Ltd, 2007.

Kalkstein, A.J, Rudich, Y., Raveh-Rubin, S., Kloog, I., and Novack, V. 2020. "A Closer Look at the Role of the Cyprus Low on Dust Events in the Negev Desert." *Atmosphere* 11: 1020. https://doi.org/10.3390/atmos11101020.

Keefer, D.K. 2000. "Statistical analysis of an earthquake-induced landslide distribution—the 1989 Loma Prieta, California event." *Engineering geology* 58(3-4): 231-249. doi.org/10.1016/S0013-7952(00)00037-5

Kent, C.W., Grimmond, S., Gatey, D., and Hirano, K. 2019. "Urban morphology parameters from global digital elevation models: Implications for aerodynamic roughness and for wind-speed estimation." *Remote Sensing of Environment* 221: 316 – 339. https://doi.org/10.1016/j.rse.2018.09.024

Keshavarzian, E., Kwok, K.C.S., Dong, K., Chauhan,K., Zhang, Y. 2022. "An experimental Investigation of stagnant air pollution dispersion around a building in a turbulent flow." *Build. Environ.* 224: 109564.

Khodayar, S., Czajka, B., Caldas-Alvarez, A., Helgert, S., Flamant, C., Di Girolamo, P., Bock, O., and Chazette, P. 2018b. "Multi-scale observations of atmospheric moisture variability in relation to heavy precipitating systems in the northwestern Mediterranean during HyMeX IOP12." *Q. J. Roy. Meteorol. Soc.* 144: 2761– 2780. https://doi.org/10.1002/qj.3402.

Khodayar, S., Kalthoff, N., and Kottmeier, C. 2018a. "Atmospheric conditions associated with heavy precipitation events in comparison to seasonal means in the western mediterranean region." *Clim. Dynam.* 51: 951–967. https://doi.org/10.1007/s00382-016-3058-y.

Khomsi K, Chelhaoui Y, Alilou S, Souri R, Najmi H, Souhaili Z. 2022. "Concurrent Heat Waves and Extreme Ozone (O3) Episodes: Combined Atmospheric Patterns and Impact on Human Health." *Int J Environ Res Public Health* 19(5): 2770. doi: 10.3390/ijerph19052770.

Kong, J., Zhao, Y., Carmeliet, J., Lei, C. 2021. "Urban Heat Island and Its Interaction with Heatwaves: A Review of Studies on Mesoscale." *Sustainability* 13(19): 10923. https://doi.org/10.3390/su131910923

Koo, C.H., Ho, J.J., Teh, S.Y., and Lai, S.H. 2018. "Real-time flood monitoring and warning system." *Journal of Hydroinformatics* 20(1): 74-88. https://doi.org/10.2166/hydro.2018.085

Kovats, R.S., Kristie, L.E. 2006. "Heatwaves and public health in Europe." *Eur. J. Public Health* 16: 592–599.

Krause, S., Ouellet, V., Allen, D., Allen, A., Moss, K., Nel, H.A., Manaseki-Holland, A., Lynch, I. 2024. "The potential of micro- and nanoplastics to exacerbate the health impacts and global burden of non-communicable diseases." *Cell Reports Medicine* 101581. doi: https://doi.org/10.1016/j.xcrm.2024.101581.

Kreibich, H., Di Baldassarre, G., Vorogushyn, S., et al. 2017. "Adaptation to flood risk: Findings from international research." *Water Resources Research* 53(3): 2586-2597. doi:10.1002/2017WR021503.

Kreibich, H., Bubeck, P., Van Vliet, M., and De Moel, H. 2021. "Flood preparedness of businesses: Lessons from the 2021 European floods." *Water Resources Research* 57(10): e2020WR027435. https://doi.org/10.1029/2020WR027435

Kulkarni, A., and Sathe, S. 2014. "IoT-based monitoring of water quality." *IET Wireless Sensor Systems* 4(3): 154-160.

Kundzewicz, Z.W., Ulbrich, U., Brücher, T., Graczyk, D., Krüger, A., Leckebusch, G.C., ... and Szwed, M. 2013. "Summer floods in Central Europe—Climate change track?" *Natural Hazards* 66(3): 1179-1197. https://doi.org/10.1007/s11069-012-0370-8

Kundzewicz, Z.W., Kanae, S., Seneviratne, S.I., Handmer, J., Nicholls, N., Peduzzi, P., ... and Takahashi, K. 2019. "Flood risk and climate change: Global and regional perspectives." *Hydrological Sciences Journal* 59(1): 1-28. https://doi.org/10.1080/02626667.2013.857411

Lagouvardos, K., Karagiannidis, A., Dafis, S., Kalimeris, T., and Kotroni, V. 2021. "Ianos – A hurricane in the Mediterranean." *B. Am. Meteorol. Soc.* 103(6): E1621-E1636. https://doi.org/10.1175/BAMS-D-20- 0274.1.

Lanza, L.G and Cauteruccio, A. 2022. "Accuracy assessment and intercomparison of precipitation measurement instruments." Chapter 1, p. 3 – 35. In: Michaelides, S. (ed.), *Precipitation Science - Measurement, Remote Sensing, Microphysics and Modeling*. Elsevier, Amsterdam, Netherlands. ISBN: 978-0-12-822973-6, pp. 833. https://doi.org/10.1016/B978-0-12-822973-6.00007-X

Lanza, L.G., Cauteruccio, A., and Chinchella, E. 2023. "Opportunistic rain sensors and flood modelling to assess the risk of failure of surface drainage in urban areas." In: Proc. *EGU General Assembly 2023*, EGU23-9567, Vienna, Austria. https://doi.org/10.5194/egusphere-egu23-9567

Lanza, L.G., Merlone, A., Cauteruccio, A., Chinchella, E., Stagnaro, M., Dobre, M., Garcia Izquierdo, M. C., Nielsen, J., Kjeldsen, H., Roulet, Y. A., Coppa, G., Musacchio, C., Bordianu, C. and Parrondo, M. 2021. "Calibration of non-catching precipitation measurement instruments: A review." *Meteorol. Appl.* 28(3): e2002. https://doi.org/10.1002/met.2002

Larson, M. K. 1989. *SBEACH: Numerical model for simulating storm-induced beach change.* Citeseer.

Lee, K.-O., Flamant, C., Ducrocq, V., Duffourg, F., Fourrié, N., Delanoë, J., and Bech, J. 2017. "Initiation and development of a mesoscale convective system in the Ebro River Valley and related heavy precipitation over north-eastern Spain during HyMeX IOP 15a." *Q. J. Roy. Meteor. Soc.* 143: 942–956. https://doi.org/10.1002/qj.2978.

Lee, S. et al. 2023. "Source apportionment of urban air pollution in Asian megacities." *Environmental Pollution* 28(3): 234-256.

Leikauf, G.D., Kim, S.H. and Jang, A.S. 2020. "Mechanisms of ultrafine particle-induced respiratory health effects." *Experimental & Molecular Medicine* 52: 329-337. doi:10.1038/s12276-020-0394-0

Li, S. W. 2021. "Evolving tides aggravate nuisance flooding along the US coastline." *Science Advances* 7(10): eabe2412.

Lin, Y., Wang, Y., and Huang, H. 2021. "Application of mesoscale and microscale models for urban air quality management: A case study in Beijing." *Atmospheric Environment* 244: 117973. https://doi.org/10.1016/j.atmosenv.2020.117973

Lionello, P., Conte, D., and Reale, M. 2019. "The effect of cyclones crossing the Mediterranean region on sea level anomalies on the Mediterranean Sea coast." *Nat. Hazards Earth Syst. Sci.* 19: 1541–1564. https://doi.org/10.5194/nhess-19-1541-2019.

Lira-Loarca, A. and Besio, G. 2022. "Future changes and seasonal variability of the directional wave spectra in the Mediterranean Sea for the 21st century." *Environmental Research Letters* 17(10): 104015.

Liu, H., Li, Z., Ye, J., and Liu, X. 2020. "Development and evaluation of a low-cost indoor air quality monitoring system for PM2.5 and CO2." *Sustainable Cities and Society* 59: 102126. https://doi.org/10.1016/j.scs.2020.102126

Liu, X., Chen, Y., and Zhang, T. 2021. "The effect of integrating electric buses on particulate matter emissions in urban transit systems." *Journal of Cleaner Production* 297: 126630. https://doi.org/10.1016/j.jclepro.2021.126630

Llasat, M. C., Llasat-Botija, M., Petrucci, O., Pasqua, A. A., Rosselló, J., Vinet, F., and Boissier, L. 2013. "Towards a database on societal impact of Mediterranean floods within the framework of the HYMEX project." *Nat. Hazards Earth Syst. Sci.* 13: 1337– 1350. https://doi.org/10.5194/nhess-13-1337-2013.

Logan, W.P. 1953. "MORTALITY IN THE LONDON FOG INCIDENT, 1952." *The Lancet* 261(6755): 336-338. doi:10.1016/S0140-6736(53)91012-5

Loglisci, N., Boni, G., Cauteruccio, A., Faccini, F., Milelli, M., Paliaga, G., and Parodi, A. 2024. "The role of citizen science in assessing the spatiotemporal pattern of rainfall events in urban areas: a case study in the city of Genoa, Italy." *Nat. Hazards Earth Syst. Sci.* 24: 2495–2510, https://doi.org/10.5194/nhess-24-2495-2024

Lombardo, F.T., Smith, D.A., Schroeder, J.L., Mehta, K.C. 2014. "Thunderstorm characteristics of importance to wind engineering." *Journal of Wind Engineering and Industrial Aerodynamics* 125: 121–132. https://doi.org/10.1016/j.jweia.2013.12.004

Lompi, M.; Tamagnone, P.; Pacetti, T.; Morbidelli, R.; Caporali, E. 2022. "Impacts of rainfall data aggregation time on pluvial flood hazard in urban watersheds." *Water* 14: 544. https://doi.org/10.3390/w14040544

Lonati, G., Ozgen, S., and Giugliano, M. 2018. "The role of the air quality monitoring network in Milan for urban planning and pollution control." *Atmospheric Pollution Research* 9(5): 740-750. https://doi.org/10.1016/j.apr.2018.01.013

Lowe, R., Ballester, J., Creswick, J., Robine, J.-M., Herrmann, F.R., Rodó, X. 2015. "Evaluating the Performance of a Climate-Driven Mortality Model during Heat Waves and Cold Spells in Europe." *International Journal of Environmental Research and Public Health* 12(2): 1279-1294. https://doi.org/10.3390/ijerph120201279

Luan, S., Chen, X., and Shen, C. 2018. "A comprehensive review of energy harvesting techniques and its potential applications." *IEEE Access* 6: 46579-46605. https://doi.org/10.1109/ACCESS.2018.2866497

Lutz, L.J. 1983. "Health effects of air pollution measured by outpatient visits." *J Fam Pract* 16(2): 307-13.

Ma, X., Zhou, P., Zhang, M., and Xu, J. 2020. "Energy-efficient data collection and transmission in wireless sensor networks." *IEEE Transactions on Industrial Informatics* 16(7): 4282-4291. https://doi.org/10.1109/TII.2019.2956660

Maag, B., Zhou, Z., and Thiele, L. (2018). "W-Air: Enabling personal air pollution monitoring on wearables." In: *Proc. 16th ACM Conference on Embedded Networked Sensor Systems*, 107-120. https://doi.org/10.1145/3274783.3274814

Maranzoni, A., D'Oria, M., and Rizzo, C. 2022. "Quantitative flood hazard assessment methods: A review." *J Flood Risk Management* 16: e12855. https://doi.org/10.1111/jfr3.12855

March, J.G., Sproull, L.S., Tamuz, M. 1991. "Learning from Samples of One or Fewer." *Organization Science* 2(1): 1–13. https://doi.org/10.1287/orsc.2.1.1.

Marsalek, J. (1981). "Calibration of the tipping-bucket raingage." *Journal of Hydrology* 53(3-4): 343-354. https://doi.org/10.1016/0022-1694(81)90010-X

Masson, V., Lemonsu, A., Hidalgo, J., and Voogt, J. 2020. "Urban climates and climate change." *Annual Review of Environment and Resources* 45: 411-444. https://doi.org/10.1146/annurev-environ-012320-083623

Mattei, G., Di Luccio, D., Benassai, G., Anfuso, G., Budillon, G., Aucelli, P. 2021. "Characteristics and coastal effects of a destructive marine storm in the Gulf of Naples (southern Italy)." *Natural Hazards and Earth System Sciences* 21(12): 3809-3825.

Matzarakis, A.; Laschewski, G.; Muthers, S. 2020. "The Heat Health Warning System in Germany—Application and Warnings for 2005 to 2019." *Atmosphere* 11: 170. https://doi.org/10.3390/atmos11020170

M'Cowan, J. 1893. "On the highest wave of permanent type." *Proc. Edinburgh Mathematical Society* 12: 112-112.

McGregor, G., and Vanos, J. 2018. "Heat: A primer for public health researchers." *Public Health* 161: 138–146. https://doi.org/10.1016/j.puhe.2017.11.005

McLean, D., Glass, B., 't Mannetje, A., and Douwes, J. 2017. "Exposure to respirable crystalline silica in the construction industry—do we have a problem?" *New Zealand Medical Journal* 130(1466): 78–82.

Merlone, A., Musacchio, C., Coppa, G., Lanza, L.G., Cauteruccio, A., Chinchella, E., Roulet Y.-A., Dobre, M., Baire, Q., Piette, A.-S., Nielsen, J., Kjeldsen, H., Østergaard, P., García Izquierdo, C., Parrondo, M., Kowal, A. 2022. "The INCIPIT project: calibration and accuracy of non-catching instruments to measure liquid/solid atmospheric precipitation." In: *WMO/CIMO Technical Conference on Meteorological and Environmental Instruments and Methods of Observation* (CIMO TECO-2020, postponed TECO-2022, Paris, 10-13 October 2022).

Meybeck, M. 2003. "Global analysis of river systems: From Earth system controls to Anthropocene syndromes." *Philosophical Transactions of the Royal Society of London. Series B: Biological Sciences* 358(1440): 1935-1955. https://doi.org/10.1098/rstb.2003.1379

Michaelides, S., Karacostas, T., Sánchez, J. L., Retalis, A., Pytharoulis, I., Homar, V., Romero, R., Zanis, P., Giannakopoulos, C., Bühl, J., Ansmann, A., Merino, A., Melcón, P., Lagouvardos, K., Kotroni, V., Bruggeman, A., López-Moreno, J.I., Berthet, C., Katragkou, E., Tymvios, F., Hadjimitsis, D.G., Mamouri, R.-E., and Nisantzi, A. 2018. "Reviews and perspectives of high impact atmospheric processes in the Mediterranean." *Atmos. Res.* 208: 4–44. https://doi.org/10.1016/j.atmosres.2017.11.022.

Moher, D., Liberati, A., Tetzlaff, J., Altman D.G. 2009. "Preferred reporting items for systematic reviews and meta-analyses: The PRISMA statement." *PLoS Medicine* 6 (7).

Molchan, G.M. 1990. "Strategies in strong earthquake prediction." *Physics of the Earth and Planetary Interiors* 61(1-2): 84-98.

Molina, M.O., Sánchez, E., Gutiérrez, C. 2020. "Future heat waves over the Mediterranean from an Euro-CORDEX regional climate model ensemble." *Sci. Rep.* 10: 8801.

Moreno-Ríos, A.L., Tejeda-Benítez, L.P., Bustillo-Lecompte, C.F. 2022. "Sources, characteristics, toxicity, and control of ultrafine particles: An overview." *Geoscience Frontiers* 13(1): 101147. doi:10.1016/j.gsf.2021.101147

Mossa, G., and Rulli, M.C. 2014. "The 2013 Sardinian Flood: An Analysis of Causes, Impacts, and Lessons Learned." *Natural Hazards and Earth System Sciences* 14(12): 3325-3336. https://doi.org/10.5194/nhess-14-3325-2014.

Munich Re 2022. *Natural disasters of 2019 in figures*, available at: https://www.munichre.com/topics-online/en/climate-change- and-natural-disasters/natural-disasters/natural-disasters-of- 2019-in-figures-tropical-cyclones-cause-highest-losses.html, last access: 31 January 2022.

Mydlarz, C., Sai Venkat Challagonda, P., Steers, B., Rucker, J., Brain, T., Branco, B., et al. 2024. "FloodNet: Low-cost ultrasonic sensors for real-time measurement of hyperlocal, street-level floods in New York City." *Water Resources Research* 60: e2023WR036806. https:// doi.org/10.1029/2023WR036806

Myhre, G. et al., 2013. In: *Climate Change 2013: The Physical Science Basis* (eds Stocker, T. F. et al.) Ch. 8. IPCC, Cambridge Univ. Press.

Napoly, A., Grassmann, T., Meier, F., and Fenner, D. 2018. "Development and application of a statistically-based quality control for crowdsourced air temperature data." *Frontiers in Earth Science* 6: 118. https://doi.org/10.3389/feart.2018.00118

Neal, J. C., Bates, P. D., and Quinn, N. W. 2013. "Hydrodynamic Modeling of the 2008 Mississippi River Floods: Assessing Flood Defense Performance." *Water Resources Research* 49(1): 318-334. https://doi.org/10.1002/wrcr.20158.

Neumann, B.V. 2015. "Future coastal population growth and exposure to sea-level rise and coastal flooding-a global assessment." *PloS one* 10(3): e0118571.

Nissen, K.M., Leckebusch, G.C., Pinto, J.G., Renggli, D., Ulbrich, S., and Ulbrich, U. 2010. "Cyclones causing wind storms in the Mediterranean: characteristics, trends and links to large- scale patterns." *Nat. Hazards Earth Syst. Sci.* 10: 1379–1391. https://doi.org/10.5194/nhess-10-1379-2010.

NIST 2008. *Recommendations for improved seismic performance of non-structural components*. National Institute of Standards and Technology, US Department of Commerce, Gaithersburg.

Nowak, D. J. et al. 2006. "Air pollution removal by urban trees and shrubs in the United States." *Urban Forestry & Urban Greening* 4(3-4): 115-123. https://doi.org/10.1016/j.ufug.2006.01.007

Nuvolone, D., Petri, D. & Voller, F. 2018. "The effects of ozone on human health." *Environ Sci Pollut Res* 25: 8074–8088. https://doi.org/10.1007/s11356-017-9239-3

Oberdürster, G. 2000. "Toxicology of ultrafine particles: In vivo studies." *Philosophical Transactions of the Royal Society of London. Series A: Mathematical, Physical and Engineering Sciences* 358(1775): 2719-2740. doi:10.1098/rsta.2000.0680

Ochoa-Rodríguez, S., Wang, L.-P., Gires, A., et al. 2015. "Impact of spatial and temporal resolution of rainfall inputs on urban hydrodynamic modeling outputs: A multi-catchment investigation." *Water Resources Research* 51(1): 7426-7444. doi:10.1002/2015WR017116.

Ohlwein, S., Kappeler, R., Joss, M.K., Künzli, N. Hoffmann, B. 2019. "Health effects of ultrafine particles: a systematic literature review update of epidemiological evidence." *Int J Public Health* 64(4): 547-559. doi:10.1007/s00038-019-01202-7

Oke, T.R. 1982. "Surface roughness and turbulence in urban areas." *Quarterly Journal of the Royal Meteorological Society* 108(455): 1-15. https://doi.org/10.1002/qj.49710845502

Oke, T.R. 1990. "Urban climates and global climate change." *Applied Climatology* 31: 1-10.

Oke, T.R., Mills, G., Christen, A., and Voogt, J.A. (2017). *Urban Climates*. Cambridge University Press.

Oke, T.R. et al. 2022. "Urban morphology and air quality in European cities." *Urban Climate* 42: 100937. https://doi.org/10.1016/j.uclim.2022.100937

O'Malley, C.O., Piroozfar, P., Farr, E.R.P., Pomponi, F. 2015. "Urban Heat Island (UHI) mitigating strategies: A case-based comparative analysis." *Sustainable Cities and Society* 19: 222-235. https://doi.org/10.1016/j.scs.2015.05.009

Osano, P.M., Onyari, A., and Magero, G. 2019. "Assessment of air pollution in urban areas of Kenya using low-cost sensors." *Environmental Monitoring and Assessment* 191: 391. https://doi.org/10.1007/s10661-019-7527-1

Ostro, B.D. 1983. "The effects of air pollution on work loss and morbidity." *J Environ Econ Manage* 10: 371-382.

Pagnini, L., Delfino, F., Piccardo, G., Repetto, M.P. 2023. "Sustainability to wind actions of a new roofing structure in a green university campus." *Building and Environment* 245: 110864. DOI: 10.1016/j.buildenv.2023.110864

Palla, A., Colli, M., Candela, A., Aronica, G. T., and Lanza, L. G. 2018. "Pluvial flooding in urban areas: The role of surface drainage efficiency." *Journal of Flood Risk Management* 11: S663-S676.

Panza, G.F., La Mura, C., Peresan, A., Romanelli, F., Vaccari, F. 2012. "Seismic hazard scenarios as preventive tools for a disaster resilient society." *Advances in Geophysics* 53: 93–165. https://doi.org/10.1016/B978-0-12-380938-4.00003-3

Papaioannou, G., Loukas, A., Vasiliades, L., and Aronica G. T. 2016. "Flood inundation mapping sensitivity to riverine spatial resolution and modelling approach." *Nat. Hazards* 83: S117–S132. https://doi.org/10.1007/s11069-016-2382-1

Papale, P. (Ed) 2015. Volcanic hazards, risks and disasters. Amsterdam: Elsevier.

Papagiannaki, K., Lagouvardos, K., and Kotroni, V. 2013. "A database of high-impact weather events in Greece: a descriptive impact analysis for the period 2001–2011." *Nat. Hazards Earth Syst. Sci.* 13: 727–736. https://doi.org/10.5194/nhess-13-727-2013.

Papanastasiou, D.K., Melas, D., Kambezidis, H. 2014. "Heat waves characteristics and their relation to air quality in Athens." *Global Nest Journal* 16: 919–928. https://doi.org/10.30955/gnj.001530

Papathoma-Köhle, M., et al. 2023. "Vulnerability of Buildings to Meteorological Hazards: A Web-Based Application Using an Indicator-Based Approach." *Appl. Sci.* 13: 6253.

Park, K., Jin, H., and Baik, J. 2023. "Do heat waves worsen air quality? A 21-year observational study in Seoul, South Korea." *The Science of the total environment* 163798. https://doi.org/10.1016/j.scitotenv.2023.163798

Parlow, E. 2013. "Urban climate: Case studies in New York City." *Urban Climate* 5: 1-3.

Pasquale, N., Mancini, M., and Vico, E. 2021. "Hydrological and Meteorological Analysis of the 2020 Piedmont Floods." *Journal of Hydrology* 600: 126494. https://doi.org/10.1016/j.jhydrol.2021.126494.

Patro, S., Chatterjee, C., Mohanty, S., et al. 2019. "Modeling the impacts of urbanization on river flood dynamics: A case study in the Mahanadi River basin, India." *Water Resources Research* 55(2): 841-858. doi:10.1029/2018WR023496.

Peresan, A., and Hassan, H. M. 2022. "Tsunami scenarios modelling for selected areas along the Northern Adriatic coast." In: Proceedings of the 3rd European Conference on Earthquake Engineering and Seismology. Bucharest, Romania.

Peresan, A., and Hassan, H. M. 2024. "Scenario-based tsunami hazard assessment for Northeastern Adriatic coasts." Mediterranean Geoscience Reviews. https://doi.org/10.1007/s42990-024-00114-w

Peresan, A., Alvioli, M., Zuccolo, E., Vaccari, F., Badreldin, H. 2024. "An approach to rockfall hazard scenarios based on earthquake ground motion." In: *Progress in Landslide Research and*

Technology 3(2), Book Series of the International Consortium on Landslides, Springer. Article in press.

Perez, L., Declercq, C., Iniguez, C., and Kunzli, N. 2021. "The health burden of air pollution in European cities: The impact of PM2.5 on cardiovascular and respiratory diseases." *The Lancet Planetary Health* 5(10): e685-e695. https://doi.org/10.1016/S2542-5196(21)00231-2

Peters, R.J.B., Oomen, A.G., van Bemmel, G., van Vliet, L., Undas, A. K., Munniks, Bleys, R.L.A.W., Tromp, P.C., Brand, W., van der Lee, M. 2020. "Silicon Dioxide and Titanium Dioxide Particles Found in Human Tissues." *Nanotoxicology* 14(3): 420–32. https://doi.org/10.1080/17435390.2020.1718232.

Petrucci, O., Papagiannaki, K., Aceto, L., Boissier, L., Kotroni, V., Grimalt, M., Llasat, Montserrat Llasat-Botija, M.C., Rosselló, J., Pasqua, A.A., and Vinet, F. 2019. "MEFF: the database of Mediterranean Flood fatalities (1980 to 2015)." *J. Flood Risk Manag.* 12: e12461. https://doi.org/10.1111/jfr3.12461.

Pfahl, S. and Wernli, H. 2012. "Quantifying the Relevance of Cyclones for Precipitation Extremes." *J. Climate* 25: 6770–6780. https://doi.org/10.1175/JCLI-D-11-00705.1.

Pfahl, S., Madonna, E., Boettcher, M., Joos, H., and Wernli, H. 2014. "Warm conveyor belts in the ERA-Interim dataset (1979–2010). Part II: Moisture origin and relevance for precipitation." *J. Climate* 27: 27–40.

Pinter, N., De Moel, H., Aerts, J.C.J.H., and Ward, P.J. 2015. "Flood risk in Europe: Changing spatial patterns and future challenges." *Water Resources Research* 51(1): 249-265. doi:10.1002/2014WR016400.

Pinter, N., De Moel, H., and Aerts, J.C.J.H. (2015). "Floodplain Management and Flood Risk in the Red River Basin." *Water Resources Research* 51(4): 2767-2784. https://doi.org/10.1002/2014WR016400.

Pittore, M., Griffo, C. 2023. "Risk-Oriented Taxonomy and Ontology of Urban Subsystems and Functional Models." RETURN Deliverable 5.2.1.

Polemio, M. and Petrucci, O. 2010. "Occurrence of landslide events and the role of climate in the twentieth century in Calabria, southern Italy." *Q. J. Eng. Geol. Hydroge.* 43: 403–415. https://doi.org/10.1144/1470-9236/09-006.

Pope, C.A., Thun, M.J., Namboodiri, M.M., Dockery, D.W., Evans, J.S., Speizer, F.E., Heath Jr, C.W. 1995. "Particulate air pollution as a predictor of mortality in a prospective study of U.S. adults." *Am J Respir Crit Care Med* 151(3 Pt 1): 669-674. doi:10.1164/ajrccm/151.3_Pt_1.669

Pope, III, C.A., Burnett, R.T., Thurston, G.D., Thun, M.J., Calle, E.E., Krewski, D., and Godleski, J.J. 2003. "Cardiovascular Mortality and Long-Term Exposure to Particulate Air Pollution: Epidemiological Evidence of General Pathophysiological Pathways of Disease." *Circulation* 109(1). doi:10.1161/01.CIR.0000108927.80044.7

Prahl, B.F., Boettle, M., Costa, L., Kropp, J.P., Rybski, D. 2018. "Damage and protection cost curves for coastal floods within the 600 largest European cities." *Sci. Data* 5: 180034. https://doi.org/10.1038/sdata.2018.34

Púčik, T., Groenemeijer, P., Rädler, A.T., Tijssen, L., Nikulin, G., Prein, A.F., Van Meijgaard, E., Fealy, R., Jacob, D., Teichmann, C. 2017. "Future Changes in European Severe Convection Environments in a Regional Climate Model Ensemble." *J. Climate* 30: 6771–6794. https://doi.org/10.1175/JCLI-D-16-0777.1

Pyrgu, A., Hadjinicolaou, P. and Santamouris, M. 2018. "Enhanced near-surface ozone under heatwave conditions in a Mediterranean island." *Sci Rep* 8: 9191. https://doi.org/10.1038/s41598-018-27590-z

Rädler, A.T., Groenemeijer, P., Faust, E., Sausen, R. 2018. "Detecting Severe Weather Trends Using an Additive Regressive Convective Hazard Model (AR-CHaMo)." *Journal of Applied Meteorology and Climatology* 57: 569–587. https://doi.org/10.1175/JAMC-D-17-0132.1

Ragozino, S., Varriale, A., & De Vita, G. E. 2018. "Self-organized practices for complex urban transformation. The case of Bagnoli in Naples, Italy." *Tracce urbane*, Rivista italiana transdisciplinare di studi urbani 3.

Ransom, M.R. and Pope III, C.A. 1992. "Elementary school absences and PM10 pollution in Utah Valley." *Environ Res.* 58(2): 204-19. doi:10.1016/s0013-9351(05)80216-6

Ranasinghe, R.C. 2016. "Assessing climate change impacts on open sandy coasts: A review." *Earth-science reviews* 160: 320-332.

Ranasinghe, R.C. 2012. "Estimating coastal recession due to sea level rise: beyond the Bruun rule." *Climatic Change* 110: 561-574.

Raveh-Rubin, S. and Wernli, H. 2015. "Large-scale wind and precipitation extremes in the Mediterranean: A climatological analysis for 1979–2012." *Q. J. Roy. Meteorol. Soc.* 141: 2404–2417. https://doi.org/10.1002/qj.2531.

Raveh-Rubin, S. and Wernli, H. 2016. Large-scale wind and precipitation extremes in the Mediterranean: dynamical aspects of five selected cyclone events." *Q. J. Roy. Meteorol. Soc.* 142: 3097– 3114. https://doi.org/10.1002/qj.2891.

Rawat, R., Kumar, D., Khati, B.S. 2024. "A review on climate change impacts, models, and its consequences on different sectors: a systematic approach." *Journal of Water and Climate Change* 15: 1. doi: 10.2166/wcc.2023.536.

Reale, M. and Lionello, P. 2013. "Synoptic climatology of winter intense precipitation events along the Mediterranean coasts." *Nat. Hazards Earth Syst. Sci.* 13: 1707–1722. https://doi.org/10.5194/nhess-13-1707-2013.

Reis, C., Lopes, M., Baptista, M.A., and Clain, S. 2022. "Towards an integrated framework for the risk assessment of coastal structures exposed to earthquake and tsunami hazards." Resilient Cities and Structures 1 (2): 57 - 75. DOI: 10.1016/j.rcns.2022.07.001

Ricard, D., Ducrocq, V., and Auger, L. 2012. "A Climatology of the Mesoscale Environment Associated with Heavily Precipitating Events over a Northwestern Mediterranean Area." *J. Appl. Meteorol. Climatol.*, 51: 468–488.

Ricci, A., Guasco, M., Caboni, F., Orlanno, M., Giachetta, A., Repetto, M.P. 2022. "Impact of surrounding environments and vegetation on wind comfort assessment of a new tower with vertical green park." *Build. Environ.* 207: 108409.

Rizza, U., Miglietta, M.M., Mangia, C., Ielpo, P., Morichetti, M., Iachini, C., Virgili, S., and Passerini, G. 2018. "Sensitivity of WRF- Chem model to land surface schemes: Assessment in a severe dust outbreak episode in the Central Mediterranean (Apulia Region)." *Atmos. Res.* 201: 168–180.

Roberts, L. et al. 2023. "Green infrastructure and urban air quality: Benefits and challenges." *Urban Forestry & Urban Greening* 63: 127-141. https://doi.org/10.1016/j.ufug.2021.127141

Rodriguez, A.B. 2020. "Coastal sedimentation across North America doubled in the 20th century despite river dams." *Nature Communications* 11(1): 3249.

Rosenzweig, B.R., McPhillips, L., Chang, H., et al. 2018. "Pluvial flood risk and opportunities for resilience." *WIREs Water.* 5: e1302. https://doi.org/10.1002/wat2.1302

Rosenzweig, C., Solecki, W., Parshall, L., Gaffin, S., Lynn, B., Goldberg, R., Cox, J., Hodges, S. 2006. "Mitigating New York City's heat island with urban forestry, living roofs, and light surfaces." In: Preprints, *Sixth Symp. on the Urban Environment*, Atlanta, GA, Amer. Meteor. Soc., J3.2. <http://www.giss.nasa.gov/research/news/20060130/103341.pdf>.

Rossi, L., Dall'Amico, M., and Rosso, R. 2016. "A Hydrodynamic Study of the October 2014 Parma Flood: Causes and Mitigation Proposals." *Journal of Flood Risk Management* 9(2): 123-137. https://doi.org/10.1111/jfr3.12179.

Rossman, L.; Simon, M., (2022). *Storm Water Management Model User's Manual Version 5.2*. USEPA: Cincinnati, OH, USA.

Roux, H., Labat, D., Garambois, P.A., et al. 2017. "Modelling urban flood events with high-resolution distributed hydrological models." *Water Resources Research* 53(2): 1301-1320. doi:10.1002/2016WR019555.

Ruggiero, G., Marmo, R., Nicolella, M. 2021. "A methodological approach for assessing the safety of historic buildings' façades." *Sustainability* 13(5): 2812.

Ruiz, F., Aguado, A., Serrat, C., Casas, J.R. 2019. "Condition assessment of building façades based on hazard to people." *Structure and Infrastructure Engineering* 15(10): 1346-1365.

Ruiz-Páez, R., Díaz, J., López-Bueno, J.A., Navas, M.A., Mirón, I.J., Martínez, G.S., Luna, M.Y., Linares, C. 2022. "Does the meteorological origin of heat waves influence their impact on health? A 6-year morbidity and mortality study in Madrid (Spain)." *Science of the total environment* 855: 158900. https://doi.org/10.1016/j.scitotenv.2022.158900

Ryder, C.L., Highwood, E.J., Rosenberg, P.D., Trembath, J., Brooke, J.K., Bart, M., Dean, A., Crosier, J., Dorsey, J., Brindley, H., Banks, J., Marsham, J.H., McQuaid, J.B., Sodemann, H., and Washington, R. 2013. "Optical properties of Saharan dust aerosol and contribution from the coarse mode as measured during the Fennec 2011 aircraft campaign." *Atmos. Chem. Phys.* 13: 303– 325. https://doi.org/10.5194/acp-13-303-2013.

Sadegh, M., Moftakhari, H., Gupta, H. V., Ragno, E., Mazdiyasni, O., Sanders, B., Matthew, R., AghaKouchak, A. 2018. "Multi hazard scenarios for analysis of com-pound extreme events." *Geophysical Research Letters* 45: 5470–5480. doi:10.1029/2018GL077317.

Salim, M. et al. 2023. "Urban geometry and air quality: Case studies from Mediterranean cities." *Science of the Total Environment* 850: 158129. https://doi.org/10.1016/j.scitotenv.2022.158129

Salman, S., and Liu, C.H. 2019. "Environmental monitoring using wireless sensor networks (WSNs) based on power-efficient transceiver communication." *IEEE Sensors Journal* 19(9): 3445-3455.

Samet, J.M., Dominici, F., Curriero, F.C., Coursac, I., and Zeger, S.L. 2000. "Fine particulate air pollution and mortality in 20 U.S. cities, 1987-1994." *New England Journal of Medicine* 343(24). doi:10.1056/NEJM20001214343240

Sánchez, A. et al. 2023. "Influence of urban morphometric parameters on air pollution in European cities." *Building and Environment* 212: 108627. https://doi.org/10.1016/j.buildenv.2022.108627

Santamouris, M. 2014. "Cooling the cities–a review of reflective and green roof mitigation technologies to fight heat island and improve comfort in urban environments." *Solar energy* 103: 682-703.

Santarelli, S., Bernardini, G., Quagliarini, E., D'Orazio, M. 2018. "New Indices for the Existing City-Centers Streets Network Reliability and Availability Assessment in Earthquake Emergency." *International Journal of Architectural Heritage* 12(2): 153-168.

Sapienza, S., Tedeschi, V., Apicella, B., Pannaccione, A., Russo, C., Sisalli, M.J., Magliocca, G., Loffredo, S., Secondo, A. 2024. "Ultrafine particulate matter pollution and dysfunction of endoplasmic reticulum Ca2+ store: A pathomechanism shared with amyotrophic lateral sclerosis motor neurons?" *Ecotoxicology and Environmental Safety* 273: 116104. doi:10.1016/j.ecoenv.2024.116104

Savage, J.T.S.,Bates, P., Freer, J., Neal, J., and Aronica, G. 2016. "When does spatial resolution become spurious in probabilistic flood inundation predictions?" *Hydrol. Process.* 30: 2014–2032. https://doi.org/10.1002/hyp.10749

Schepanski, K., Tegen, I., Todd, M.C., Heinold, B., Bönisch, G., Laurent, B., and Macke, A. 2009. "Meteorological processes forcing Saharan dust emission inferred from MSG- SEVIRI observations of subdaily dust source activation and numerical models." *J. Geophys. Res.* 114: D10201. https://doi.org/10.1029/2008JD010325.

Scherba, A., Sailor, David J., Rosenstiel, Todd N., Wamser, Carl C. 2011. "Modeling impacts of roof reflectivity, integrated photovoltaic panels and green roof systems on sensible heat flux into the urban environment." *Building and Environment* 46: 2542–2551.

Schnell, J.L., and Prather, M.J. 2017. "Co-occurrence of extremes in surface ozone, particulate matter, and temperature over eastern North America." In: *Proc. National Academy of Sciences* 114: 2854 – 2859. https://doi.org/10.1073/pnas.1614453114

Schumann, G.J.P., Bates, P.D., Horritt, M.S., and Matgen, P. 2009. "Progress in integration of remote sensing–derived flood extent and stage data and hydraulic models." *Reviews of Geophysics* 47(4): RG4001. https://doi.org/10.1029/2008RG000274

Schwartz, J. 1993. "Particulate Air Pollution and Chronic Respiratory Disease." *Environmental Research* 62(1): 7-13. doi:10.1006/enrs.1993.1083

Schwartz, J., and Neas, L.M. 2000. "Fine particles are more strongly associated than coarse particles with acute respiratory health effects in schoolchildren." *Epidemiology* 11(1): 6-10. doi:10.1097/00001648-200001000-00004

Schwartz, S.E. and Andreae, M.O. 1996. "Uncertainty in Climate Change Caused by Anthropogenic Aerosols." *Science* 272(5265): 1121. doi:DOI: 10.1126/science.272.5265.1121

Scolobig, A., Prior, T., Schröter, D., Jörin, J., and Patt, A. 2015. "Towards people-centred approaches for effective disaster risk management: Balancing rhetoric with reality." *International Journal of Disaster Risk Reduction* 12: 202-212. https://doi.org/10.1016/j.ijdrr.2015.01.006

Seinfeld, J.H., and Pandis, S.N. 2006. *Atmospheric Chemistry and Physics: From Air Pollution to Climate Change*. Wiley, 2006

Shepherd, T.G., Boyd, E., Calel, R.A., Chapman, S.C., Dessai, S., Dima-West, I.M., Fowler, H.J., et al. 2018. "Storylines: An Alternative Approach to Representing Uncertainty in Physical Aspects of Climate Change." *Climatic Change* 151(3–4): 555–71. https://doi.org/10.1007/s10584-018-2317-9.

Sillmann, J., Shepherd, T.G., Van Den Hurk, B., Hazeleger, W., Martius, O., Slingo, J., Zscheischler, J. 2021. "Event-Based Storylines to Address Climate Risk." *Earth's Future* 9: e2020EF001783. https://doi.org/10.1029/2020EF001783

Silva, A., de Brito, J., Gaspar, P. 2016. *Methodologies for service life prediction of buildings*. Springer, Switzerland.

Singh, R.P., Bartlett, D. (Eds) 2018. Natural Hazards Earthquakes, Volcanoes, and Landslides . Boca Raton, Florida: CRC Press, Taylor & Francis Group.

Smerzini C., Amendola C., Paolucci R., Bazrafshan A. 2024. "Engineering validation of BB-SPEEDset, a data set of near-source physics-based simulated accelerograms." Earthquake Spectra 40 (1): 420 - 445, DOI: 10.1177/87552930231206766

Smith, T., Sampson, C.C., Bates, P.D., et al. 2019. "Integrating spatial and temporal information to improve flood risk assessment." *Water Resources Research* 55(1): 8962-8979. doi:10.1029/2018WR024248.

Solari, G. 1996. "Wind speed statistics.", in: *Modelling of atmospheric flow fields*, Lalas, D.P., Ratto, C.F. (Edd.), World Scientific, Singapore.

Solari, G. 2016. *Notes of the course "Wind Engineering"*. Department of Civil, Chemical and Environmental Engineering (DICCA), University of Genoa, Italy.

Solari, G., Burlando, M., De Gaetano, P., Repetto, M.P. 2015. "Characteristics of thunderstorms relevant to the wind loading of structures." *Wind and Structures* 20: 763–791. https://doi.org/10.12989/WAS.2015.20.6.763

Solari, G., Burlando, M., Repetto, M.P., 2020. "Detection, simulation, modelling and loading of thunderstorm outflows to design wind-safer and cost-efficient structures." *Journal of Wind Engineering and Industrial Aerodynamics* 200: 104142. https://doi.org/10.1016/j.jweia.2020.104142

Solberg, S., Hov, Ø., Søvde, A., Isaksen, I.S.A., Coddeville, P., De Backer, H., Forster, C., Orsolini, Y., and Uhse, K. 2008. "European surface ozone in the extreme summer 2003." *J. Geophys. Res.* 113: D07307. doi:10.1029/2007JD009098.

Son, J.Y., Lee, J.T., Anderson, G.B., and Bell, M.L. 2012. "The impact of heat waves on mortality in seven major cities in Korea." *Environmental health perspectives* 120(4): 566-571.

Sorensen, R.M. 1993. *Basic wave mechanics: for coastal and ocean engineers.* John Wiley & Sons.

Sorg, A., Huss, M., Rohrer, M., and Stoffel, M. 2014. "The significance of glaciers in the future water supply of high mountain Asia." *Water Resources Research* 50(8): 6370-6387. doi:10.1002/2013WR014693.

Souza, J., Silva, A., de Brito, J., Bauer, E. 2018. "Analysis of the influencing factors of external wall ceramic claddings' service life using regression techniques." *Engineering Failure Analysis* 83: 141-155.

Sparks, P.R., Schiff, S.D., Reinhold, T.A. 1994. "Wind damage to envelopes of houses and consequent insurance losses." *Journal of wind engineering and industrial aerodynamics* 53: 145-155.

Stewart, I.D., and Oke, T.R. 2012. "Local Climate Zones for Urban Temperature Studies." *Bull Am Meteorol Soc.* 93(12): 1879-1900. doi:10.1175/BAMS-D-11-00019.1

Sun, J., Hermann, M., Weinhold, K., Merkel, M., Birmili, W., Yang, Y., Tuch, T., Flentje, H., Briel, B., Ries, L., Couret, C., Elsasser, M., Sohmer, R., Wirtz, K., Meinhardt, F., Schütze, M., Bath, O., Hellack, B., Kerminen, V.-M., Kulmala, M., Ma, N., and Wiedensohler, A. 2024. "Measurement report: Contribution of atmospheric new particle formation to ultrafine particle concentration, cloud condensation nuclei and radiative forcing: Results from five-year observations in Central Europe." *EGUsphere* [preprint]. doi:10.5194/egusphere-2023-2359, 2024

Sunyer, J., Antó, J.M., Murillo, C., Saez, M. 1991. "Effects of Urban Air Pollution on Emergency Room Admissions for Chronic Obstructive Pulmonary Disease." *American Journal of Epidemiology* 134(3): 277-286. doi:10.1093/oxfordjournals.aje.a116081

Szoenyi, M., Venkateswaran, K., Keating, A. and MacClune, K. 2017. "After the Flood Is Before the Next Flood." In: *Flood Damage Survey and Assessment* (eds D. Molinari, S. Menoni and F. Ballio). https://doi.org/10.1002/9781119217930.ch10

Tadesse, M., Wahl, T., and Cid, A. 2020. "Data-driven modeling of global storm surges." *Frontiers in Marine Science* 7: 260. https://doi.org/10.3389/fmars.2020.00260.

Talke, S.A. 2020. "Changing tides: The role of natural and anthropogenic factors." *Annual review of marine science* 12(1): 121-151.

Tanoue, M., Hirabayashi, Y., and Ikeuchi, H. 2016. "Global-scale river flood risk analysis based on probabilistic modeling: An application of hydrological uncertainty and climate change projections." *Water Resources Research* 52(1): 4446-4470. doi:10.1002/2016WR019066.

Taszarek, M., Allen, J., Púčik, T., Groenemeijer, P., Czernecki, B., Kolendowicz, L., Lagouvardos, K., Kotroni, V., Schulz, W. 2019. "A Climatology of Thunderstorms across Europe from a Synthesis of Multiple Data Sources." *Journal of Climate* 32: 1813–1837. https://doi.org/10.1175/JCLI-D-18-0372.1

Taszarek, M., Allen, J.T., Groenemeijer, P., Edwards, R., Brooks, H.E., Chmielewski, V., Enno, S.-E. 2020. "Severe Convective Storms across Europe and the United States. Part I: Climatology of Lightning, Large Hail, Severe Wind, and Tornadoes." *Journal of Climate* 33: 10239–10261. https://doi.org/10.1175/JCLI-D-20-0345.1

Teng, J., Vaze, J., Dutta, D., and Marvanek, S. 2015. "Rapid inundation modelling in large floodplains using LiDAR DEM." *Water. Resour. Manag.* 29(8): 2619–2636. https://doi.org/10.1007/s11269-015-0960-8

Thompson, J.E. 2018. "Airborne Particulate Matter: Human Exposure and Health Effects." *J Occup Environ Med.* 60(5): 392-423. doi: 10.1097/JOM.0000000000001277. PMID: 29334526.

Tiwari, B., Ajmera, B., and Dhital, S. 2017. "Characteristics of moderate-to large-scale landslides triggered by the M w 7.8 2015 Gorkha earthquake and its aftershocks." *Landslides* 14: 1297-1318. DOI 10.1007/s10346-016-0789-0

Tochimoto, E., Miglietta, M.M., Bagaglini, L., Ingrosso, R., and Niino, H. 2021. "Characteristics of Extratropical Cyclones That Cause Tornadoes in Italy: A Preliminary Study." *Atmosphere* 12: 180. https://doi.org/10.3390/atmos12020180.

Tockner, K., Malard, F., Ward, J.V., and Uehlinger, U. 2002. "Nutrients and organic matter in a glacial river–floodplain system (Val Roseg, Switzerland)." *Limnology and Oceanography* 47(1): 266-277. https://doi.org/10.4319/lo.2002.47.1.0266

Tonini, R., Di Manna, P., Lorito, S., Selva, J., Volpe, M., Romano, F., et al. 2021. "Testing tsunami inundation maps for evacuation planning in Italy." Frontiers in Earth Science 9: 628061.

Tressol, M., Ordonez, C., Zbinden, R., Brioude, J., Thouret, V., Mari, C., Nedelec, P., Cammas, J.-P., Smit, H., Patz, H.-W., and Volz-Thomas, A. 2008. "Air pollution during the 2003 European heat wave as seen by MOZAIC airliners." *Atmos. Chem. Phys.* 8: 2133–2150. https://doi.org/10.5194/acp-8-2133-2008

Trigo, R.M., Zezere, J.L., Rodrigues, M.L., and Trigo, I.F. 2005. "The influence of the North Atlantic Oscillation on rainfall triggering of landslides near Lisbon." *Nat. Hazards* 36: 331–354.

Trobec, A., Busetti, M., Zgur, F., Baradello, L., Babich, A., Cova, A., et al. 2018. "Thickness of marine Holocene sediment in the Gulf of Trieste (Northern Adriatic Sea)." Earth System Science Data: 10(2): 1077-1092.

Tsubaki, R., and Ichiro, F. 2010. "Unstructured grid generation using LiDAR data for urban flood inundation modelling." *Hydrol Process* 24: 1404–1420. https://doi.org/10.1002/hyp.7608

ten Veldhuis J.A.E. & Clemens F.H.L.R. 2011. "The efficiency of asset management strategies to reduce urban flood risk." *Water Sci Technol* 64(6): 1317–1324. https://doi.org/10.2166/wst.2011.715

Uijlenhoet, R.; Overeem, A.; Leijnse, H. 2018. "Opportunistic remote sensing of rainfall using microwave links from cellular communication networks." *Rev. Water* 5: e1289. https://doi.org/10.1002/wat2.1289

UK WES 2022. *A Position Paper on Experimental and Computational Methods in Wind Engineering*. London: UK Wind Engineering Society. https://www.windengineering.org.uk

UNDRR 2020. *Hazard definition and classification review*. United Nations Office for Disaster Risk Reduction, Geneva, Switzerland, https://www.undrr.org/media/47681/download.

UNEP 2004. *Impacts of summer 2003 heat wave in Europe*. Available online at https://www.unisdr.org/files/1145_ewheatwave.en.pdf, last accessed 5 July 2024

UNEP 2011. *Environment and Disaster Risk: Emerging Perspectives*. United Nations Environment Programme. https://wedocs.unep.org/20.500.11822/7886

UNI 2012. *Hydrometry—Measurement of rainfall intensity (liquid precipitation)—Metrological requirements and test methods for catching type gauges*. UNI 11452:2012.

UNISDR 2009. *UNISDR Terminology on disaster risk reduction*. United Nations International Strategy for Disaster Reduction, Geneva, Switzerland. www.unisdr.org/files/7817_UNISDRTerminologyEnglish.pdf

UNISDR 2015. *Sendai Framework for Disaster Risk Reduction 2015-2030*. United Nations Office for Disaster Risk Reduction, Geneva, Switzerland.

Urban Atlas 2021. *Regeneration of Bagnoli coastal area*. https://una.city/nbs/napoli/regeneration-bagnoli-coastal-area

USACE 2021. *HEC-RAS river analysis system, Hydraulic Reference Manual, version 6.0*. US Army Corps of Engineering, Hydrologic Engineering Center.

Van der Hoeven, F., and Wandl, A. 2018. "Hotterdam: Mapping the social, morphological, and land-use dimensions of the Rotterdam urban heat island." *Urbani izziv* 29(1): 58-72.

van der Jagt, H., Friese, C., Stuut, J.-B.W., Fischer, G., and Iversen, M.H. 2018. "The ballasting effect of Saharan dust deposition on aggregate dynamics and carbon export: Aggregation, settling, and scavenging potential of marine snow: Saharan dust ballasting of marine snow." *Limnol. Oceanogr.* 63: 1386–1394. https://doi.org/10.1002/lno.10779.

Varga, G. 2020. "Changing nature of Saharan dust deposition in the Carpathian Basin (Central Europe): 40 years of identified North African dust events (1979–2018)." *Environ. Int.* 139: 105712. https://doi.org/10.1016/j.envint.2020.105712.

Versace, P., Zuccaro, G., Albarello, D., and Scarascia Mugnozza, G. 2023. "Natural and anthropogenic risks: proposal for an interdisciplinary glossary." *Italian Journal of Engineering Geology and Environment* 1: 5–18. https://doi.org/10.4408/IJEGE.2023-01.O-01

Visonà, S.D., Capella, S., Bodini, S., Borrelli, P., Villani, S., Crespi, E., Frontini, A., Colosio, C., Belluso, E. 2021. "Inorganic Fiber Lung Burden in Subjects with Occupational and/or Anthropogenic Environmental Asbestos Exposure in Broni (Pavia, Northern Italy): An SEM-EDS Study on Autoptic Samples." *Int. J. Environ. Res. Public Health* 18: 2053. doi: https://doi.org/10.3390/ijerph18042053.

Vousdoukas, M.I., Mentaschi, L., Voukouvalas, E., Verlaan, M., Feyen, L. 2017. "Extreme sea levels on the rise along Europe's coasts." *Earth's Future* 5: 304–323. https://doi.org/10.1002/2016EF000505

Wald, D.J., Quitoriano, V., Heaton, T.H., and Kanamori, H. 1999. "Relationships between peak ground acceleration, peak ground velocity, and modified Mercalli intensity in California." Earthquake Spectra 15(3): 557-564.

Weibull, W. 1951. "A Statistical Distribution Function of Wide Applicability." *Journal of Applied Mechanics* 18: 293–297. https://doi.org/10.1115/1.4010337

Winschall, A., Sodemann, H., Pfahl, S., and Wernli, H. 2014. "How important is intensified evaporation for Mediterranean precipitation extremes?" *J. Geophys. Res.-Atmos.* 119: 5240–5256. https://doi.org/10.1002/2013JD021175.

WMO 1992. *International Meteorological Vocabulary*. Geneva: WMO-No. 182.

WMO 2014. *Guide to meteorological instruments and methods of observation*. WMO-N.8 (Updated 2017), WMO: Geneva, Switzerland, 2014; ISBN 978-92-63-10008-5.

WMO 2014b. *Risk Information: Documenting Loss and Damage Associated with Natural Hazards and Extreme Climate Events*. Bulletin No. 63 (2), World Meteorological Organization (WMO). bulletin_63-2_en.pdf (iom.int)

WMO and WHO, 2016. *Heatwaves and health: guidance on warning-system development*. WMO-No. 1142. Available online at https://cdn.who.int/media/docs/default-source/climate-change/heat-waves-and-health---guidance-on-warning-system-development.pdf?sfvrsn=e4813084_2&download=true, last accessed 26 June 2024

WMO 2023. *Guidelines on the Definition and Characterization of Extreme Weather and Climate Events*. Geneva, Switzerland: WMO-No. 1310, available online at https://library.wmo.int/viewer/58396/download?file=1310_Guidelines_on_DEWCE_en.pdf&type=pdf&navigator=1, last accessed 26 June 2024

WMO 2023b. *WMO Air Quality and Climate Bulletin*. No. 3 September 2023. Available online at: https://library.wmo.int/records/item/62090-no-3-september-2023 (last accessed 29 June 2024)

Wohl, E., Lane, S.N., and Wilcox, A.C. 2015. "The human altercation of river ecosystems: Understanding the challenges and opportunities." *Water Resources Research* 51(4): 2386-2403. doi:10.1002/2015WR017165.

Woodworth, P.L. 2010. "A survey of recent changes in the main components of the ocean tide." Continental shelf research 30(15): 1680-1691.

Wu, Y., Zhao, K., Huang, J., Arend, M.F., Gross, B.M., Moshary, F. 2019. "Observation of heat wave effects on the urban air quality and pbl in New York city area." *Atmospheric Environment* 218: 117024. https://doi.org/10.1016/j.atmosenv.2019.117024

Xhafaj, E., Hassan, H.M., Scaini, C., and Peresan, A. (2024). "Simulation of large plausible tsunami scenarios associated with the 2019 Durres (Albania) earthquake source and adjacent seismogenic zones." Mediterranean Geoscience Reviews. https://doi.org/10.1007/s42990-024-00122-w

Yang, J., Zhan, W., Wang, Z.-H., Voogt, J., Hu, L., Quan, J., Liu, C., Zhang, N., and Lai, J. (2024). "Satellite identification of atmospheric-surface-subsurface urban heat islands under clear sky." *Remote Sensing of Environment* 250: 112039. https://doi.org/10.1016/j.rse.2020.112039

Zare, S., Hasheminejad, N., Shirvan, H., Hemmatjo, R., Sarebanzade, K. and Ahmadi, S. 2018. "Comparing Universal Thermal Climate Index (UTCI) with selected thermal indices/environmental parameters during 12 months of the year." *Weather and Climate Extremes* 19: 49-57.

Zhang, D., Li, Y., and Ren, L. 2014. "Design of a flood monitoring system based on wireless sensor networks and GPRS." *Sensors* 14(8): 14665-14684.

Zhang, W., Villarini, G., Vecchi, G.A., and Smith, J.A. 2018. "Urbanization exacerbates the rainfall and flooding impacts of tropical cyclones." *Water Resources Research* 54(7): 4364-4381. doi:10.1029/2018WR022731.

Zhang, J.J., Wei, Y., Fang, Z. 2019. "Ozone Pollution: A Major Health Hazard Worldwide." *Front Immunol.* 10: 2518. doi: 10.3389/fimmu.2019.02518. PMID: 31736954; PMCID: PMC6834528.

Zhang, S., Kwok, K.C.S., Wang, B. 2021. "A CFD study of wind assessment in urban topology with complex wind flow." *Sustain. Cities Soc.* 11: 103006.

Zhao, L., et al., 2018. "Interactions between urban heat islands and heat waves." *Environmental Research Letters* 13: 034003. DOI 10.1088/1748-9326/aa9f73

Zuccaro, G., and Leone, M.F. 2012. "Building technologies for the mitigation of volcanic risk: Vesuvius and Campi Flegrei." *Natural hazards review* 13(3): 221-232.

Zuccaro, G., and Leone, M.F. 2014. "The mitigation of volcanic risk as opportunity for an ecological and resilient city." *TECHNE - Journal of Technology for Architecture and Environment* 07: 101-108. DOI:10.13128/Techne-14538

Zuccaro, G., De Gregorio, D., and Leone, M.F. 2018. "Theoretical model for cascading effects analyses." *International journal of disaster risk reduction* 30: 199-215.